University of Southampton

School of Civil Engineering and the Environment

The Effects of Methane Gas Hydrate on the Dynamic Properties of a Sand

by

Jeffrey A. Priest, B.Eng

A Thesis Submitted in Fulfillment of the Degree of Doctor of Philosophy
in the School of Civil Engineering and the Environment of the
University of Southampton

February 2004

This work is dedicated to the three angels in my life,
Debbie, Imogen and Emily.

UNIVERSITY OF SOUTHAMPTON

ABSTRACT

SCHOOL OF CIVIL ENGINEERING AND THE ENVIRONMENT

Doctor of Philosophy

THE EFFECTS OF METHANE GAS HYDRATE ON SOME DYNAMIC PROPERTIES OF A SAND.

by Jeffrey A. Priest

Gas hydrates are solid, ice like, compounds that form in marine sediments and in permafrost regions. The methane gas stored in hydrates is considered by some to be an important future energy resource, whilst others are concerned that it may play a role in global warming, or be a geotechnical hazard during deep offshore oil and gas development. Because methane hydrates occur in deep water and dissociate rapidly when brought to the surface, direct methods of investigation cannot readily be used to assess their global distribution and concentration. Remote seismic geophysical prospecting methods, which depend upon variations in the compressional wave velocity (V_P), the shear wave velocity (V_S), and damping (Q_P^{-1} and Q_S^{-1}), can be of great value in measuring insitu properties. However, a correct interpretation of acquired seismic data requires an understanding of the seismic properties of hydrate-bearing sediments. The aims of this research were therefore to develop a technique for producing synthetic gas hydrates in the laboratory, to construct apparatus allowing measurement of the physical properties of hydrate-bearing sand specimens, and to determine the impact of hydrate content on dynamic properties of a sand.

Thirteen sand specimens with differing volumes of hydrate within the pore space were tested using a specially designed and constructed resonant column apparatus. This allowed the dynamic properties of hydrate-bearing laboratory specimens to be measured under conditions relevant to current seismic methods. Results shows a bipartite relationship between velocity and hydrate content, with a transition zone between 3 - 5 % hydrate content, for both V_P and V_S. Effective stress stiffness dependency reduces rapidly

with increasing but low levels of hydrate cementing, and remains low at higher hydrate contents. These facets of behaviour suggest an initially rapid cementation of sand grain contacts at low methane hydrate contents, followed by infilling of the pore space at higher hydrate contents. It is also shown that damping (Q_P^{-1} and Q_S^{-1}) increases with hydrate content up to the transition zone, and reduces thereafter to a value twice that for non-hydrate-bearing specimens. These results, for the first time, show in detail how methane hydrate cementation affects seismic and geotechnical properties in typical quartz sand.

Contents

List of Figures

List of Tables

List of Symbols

a, b	soil constants
ac	acceleration
b_S, b_L	velocity-stress component for shear and longitudinal waves, respectively
c	damping constant
c_c	critical damping
e	void ratio
e_{max}, e_{min}	maximum and minimum void ratios, respectively
d	specimen diameter
f	frequency of cyclic testing (Hz)
f_r	resonant frequency
$f_{1,2}$	frequency either side of f_r obtained from half-power method
g	acceleration due to gravity
h	height above specimen
$h0_i$,$h1_i$	heights of bottom and top, respectively, of added masses m_i
k	spring stiffness
k	parameter related to plasticity index
l	offset distance of accelerometer from axis of rotation
m	stress component
m_T	mass of specimen (m_i added masses at top of specimen)
n	porosity of rock
r	distance from the neutral axis
t	time
x	elevation from base of specimen
y	horizontal displacement of specimen
y_{ci}	center of gravity of mass m_i measured from top of specimen

y_{meas}	maximum displacement of the specimen (torsional or flexural)
A	dimensionless stiffness coefficient
A	area of specimen
C	grain characteristics
C_m	natural cementation
D	damping coefficient
Dr	relative density
D_{min}	minimum damping coefficient at low strain
E	Young's modulus (E_{flex} Young's modulus from flexural excitation)
$F(e)$	void ratio adjustment factor
F(t)	driving force applied to specimen
G_s	specific gravity of soil particles
G	shear modulus
G_{max}	maximum shear modulus at low strain
I	mass polar moment of inertia of specimen
I_{am}	mass polar moment of added mass
I_b	2nd moment of area of specimen
I_c	ice content
I_0	mass polar moment of inertia of drive plate
I_p	polar moment of inertia of specimen
I_y	area moment of inertia of drive plate
I_{yi}	area moment of inertia of mass m_i
J_a	kinetic energy of added masses
J_S	maximum kinetic energy of specimen
J_U	maximum internal potential energy
J_T	maximum kinetic energy of system
K_2	parameter relating void ratio and strain amplitude to shear modulus
K_0	coefficient of lateral stress at rest
K	saturated bulk modulus of a soil
K_d	bulk modulus of frame
K_f	bulk modulus of fluid
K_i	bulk modulus of mineral
K_m	bulk modulus of matrix

L	length of specimen
N	number of load cycles
N	total number of masses added at the top of specimen
OCR	overconsolidation ratio
Q^{-1}	wave attenuation (Q_P^{-1} compressional, Q_s^{-1} shear, Q_E^{-1} extensional and Q_K^{-1} bulk)
Q	quality factor (Q_P compressional, Q_s shear, Q_E extensional and Q_K bulk)
R	radius of specimen
S_r	saturation ratio
T	torque
V	peak rms voltage from accelerometer
V_{lf}	longitudinal velocity from flexure
V_0	volume of specimen
V_S	shear wave velocity
V_P	compressional wave velocity
X_0	amplitude of vibration
X_{max}	maximum amplitude of vibration
α	constant
ε	strain
ε_{avg}	volume-average axial strain for flexural excitation
ε_v	volumetric strain
ε_z	axial strain
ε_{max}	maximum axial strain
ε_r	residual strain
δ	logarithmic decrement
$\dot{\gamma}$	strain rate
γ_c	cyclic shear strain amplitude
γ_t^e	elastic strain threshold
γ_r	reference strain
γ_h	hyperbolic strain
κ	arbitrary constant
ν	Poisson's ratio
ϕ'	static strength parameter in terms of effective stress
ϕ	phase angle between the displacement and applied force

ω	applied frequency of excitation
ω_n	natural frequency of vibration
ω_d	damped natural frequency of vibration
σ'	effective confining pressure
ρ	mass density of specimen
ρ_d	density of soil frame
ρ_f	density of fluid
ρ_i	density of individual mineral
ρ_m	density of mineral phase
σ'	effective confining prerssure
σ'_0	mean effective principal stress
σ'_V	effective vertical stress
τ_{max}	shearing stress at failure (from triaxial tests)
θ	angular circumferential displacement
$\dot{\theta}$	rotational velocity
$\ddot{\theta}$	rotational acceleration
$\frac{d\theta}{dx}$	angle of twist per unit length
dx	sectional length of bar/specimen

Prefixes

m	milli ($\times 10^{-3}$)
μ	micro ($\times 10^{-6}$)
k	kilo ($\times 10^{3}$)
M	mega ($\times 10^{6}$)

Acknowledgements

The success of this research project was made possible by a wide variety of individuals and the financial support of various organisations.

I therefore wish to acknowledge the financial support of the following organisations:

- EC-European Commission through HYDRATECH-contact No. EVK3-CT-2000-22060.
- EPSRC-Engineering and Physical Sciences Research Council.
- School of Civil Engineering and the Environment, University of Southampton.

I would also like to express my sincere gratitude to the following people:

- Firstly and most importantly my most loving wife Debbie for the sacrifices she has made. Without her I could not of started, without her I could not of finished. To my children for smiling no matter what.
- My supervisors, Prof. Chris Clayton, and Dr. Angus Best, for introducing me to the topic of gas hydrates and giving their unquestionable support and guidance throughout this period of research.
- Jerry Sutton, Karl Snelling and Patrick Hooker from GDS Instruments Ltd who were able to use their expertise to help design and construct the new resonant column which allowed this research project to come to its successful conclusion.

- Prof. Clive McCann and Jeremy Sothcott, both formerly of Reading University, for their insight and help in relation to the geophysical aspects of element testing.
- Harvey Skinner for all his help in the lab, especially with all thing electrical/electronic. The members of the technical workshop: Derek, Dave and Earl for their expertise in making all the bars and things.
- Hannes Gräbe, Martin and Michelle Rust for all the times we shared together: in the office, the lab and the gym.

Chapter 1

INTRODUCTION

1.1 Background

Large seafloor failures have been identified on featureless slopes on continental margins around the world that have gradients, on average, much less than 1^0. Examples include: the Storrega slide off Norway (Bugge et al., 1987); slope failures off the West African coast (Summerhayes et al., 1979); slope failures off the North American Atlantic continental slope (Booth and O'Leary, 1991); and in the North Atlantic (Embly and Jacobi, 1977). It has been hypothesized that these events may be linked to the dissociation of gas hydrate within marine sediment (Ashi, 1999; Berndt et al., 2002; Dillon et al., 1998; Kayen and Lee, 1991; Meinert et al., 1998; Popenoe et al., 1993). Also recent exploration activities by oil companies encroaching on these outer margins have been hampered by the dissociation of gas hydrates. These have included blowouts, casing failures and at the extreme, platform subsidence (Bily and Dick, 1974; Franklin, 1980; Makaogon, 1981).

Gas hydrates are solid, nonstoichiometric, ice like compounds that are formed under certain thermobaric conditions (methane gas hydrate - 3.55MPa @4^0C, Figure 1.1) and with sufficient availability of gas and free water. These conditions naturally occur in high rate deposition marine sediments on continental margins (Figure 1.2(b)) and in terrestrial sediments where permafrost is present (Figure 1.2(a)). Gas hydrates are metastable and become unstable and dissociate if the thermobaric conditions are sufficiently altered, as shown

by the phase boundary in Figure 1.1. This metastability and the change in structure upon dissociation have made gas hydrates a topic of major interest in three separate research fields:

1. Energy resource — 1 m^3 of stable gas hydrate contains $\sim$ 164 m^3 of gas at Standard Temperature and Pressure (STP) (Sloan, 1998)

2. Global warming — in the majority of recovered samples, 99% of the gas contained in gas hydrates is composed of methane which is 20 times more potent as a greenhouse gas than CO_2.

3. Geotechnical hazards — sediment strength and stiffness are affected by inclusions of ice-like compounds that can either cement sediment grains or affect consolidation processes. On dissociation, gas hydrates reduce to water and gas which may give rise to increased pore pressure within the sediments.

1.2 Defining the problem

The link between climate change and submarine landslides, and the activities of oil exploration companies have brought about an increased focus on the geotechnical hazard that gas hydrate dissociation may pose. To assess accurately the potential risk of gas hydrate dissociation, the distribution and extent of gas hydrate bearing marine sediments within the seafloor needs to be quantified. Gas hydrates are found throughout the world's oceans where both the P-T stability conditions exist and where there is a sufficient supply of methane gas to enable hydrate formation. The heterogeneity of hydrates within the sediment column and the cost of spot sampling in such extreme conditions have led to remote sensing techniques being employed to try and identify, and quantify, gas hydrates. At present, the extent of gas hydrates is inferred from seismic reflection surveys (Shipley et al., 1979) where a 'bottom simulating reflector' (BSR) is assumed to mark the base of the gas hydrate stability zone (BHSZ), and hydrate distribution is estimated from certain anomalies associated with the BSR. Recent research (Gettrust et al., 1999;

Holbrook et al., 1996; Paull et al., 1996) has shown that seismic interpretation using assumed geophysical properties is problematic and cannot be relied upon in quantifying either the extent or distribution of gas hydrates.

The recovery of intact samples of marine sediment containing gas hydrate for laboratory characterisation is problematic, since gas hydrates are metastable and dissociate during recovery. The creation of artificial gas hydrates under laboratory conditions either in the bulk phase or within artificial sediment specimens has also proved to be difficult. This has hindered the measurement of the geophysical properties of hydrated sediments, either occurring naturally or grown artificially. Therefore, hypotheses concerned with the effect of gas hydrate on the geophysical properties of marine sediments and how it can be used to assess hydrate concentrations have been unsubstantiated.

The goal of this research is therefore to study the effects of gas hydrate on the geophysical (particularly seismic) properties of granular materials. A methodology was developed and implemented to enable the controlled formation of gas hydrates within artificially reconstituted sand specimens. Subsequent laboratory testing was carried out, using a specifically designed and constructed resonant column, to determine the seismic properties of the resultant material.

1.3 Organisation of the thesis

Chapter 1 presents a brief background to methane gas hydrates and why they have become of interest. It highlights the shortcomings in our current knowledge with regard to gas hydrates and outlines the goals of this research in the context of methane gas hydrate/sediment interaction.

Chapter 2 is a comprehensive review of the current literature relating to methane gas hydrates. Its structure, thermodynamic formation conditions and its growth morphology within sediments are discussed. A summary of published measurements of the acoustic and seismic prop-

erties of pure gas hydrates and hydrate-sediment composites are provided to highlight the shortfalls in current knowledge.

Chapter 3 introduces the resonant column, a laboratory apparatus for measuring key physical properties of specimens. Past research is reviewed and theoretical considerations for the reduction of resonant column data is outlined.

Chapter 4 describes the development of the new resonant column for testing specimens containing gas hydrates. Calibration and testing procedures for the resonant column and associated instrumentation is also discussed.

Chapter 5 outlines the laboratory testing programme. The methodology for specimen preparation, containing sand/ice mixtures, is discussed with the subsequent formation procedure for gas hydrates highlighted. The procedure for resonance testing is described with typical results being shown.

Chapter 6 is devoted to the presentation and discussion of the results from hydrate formation and the subsequent resonant column testing. Models are developed to characterize the influence of gas hydrates on the seismic properties of sand specimens.

Chapter 6 presents the conclusions of this research and offers some recommendations regarding the further development of the resonant column and future testing of gas hydrate bearing sediments.

Finally, the references cited in the report are given in the last section.

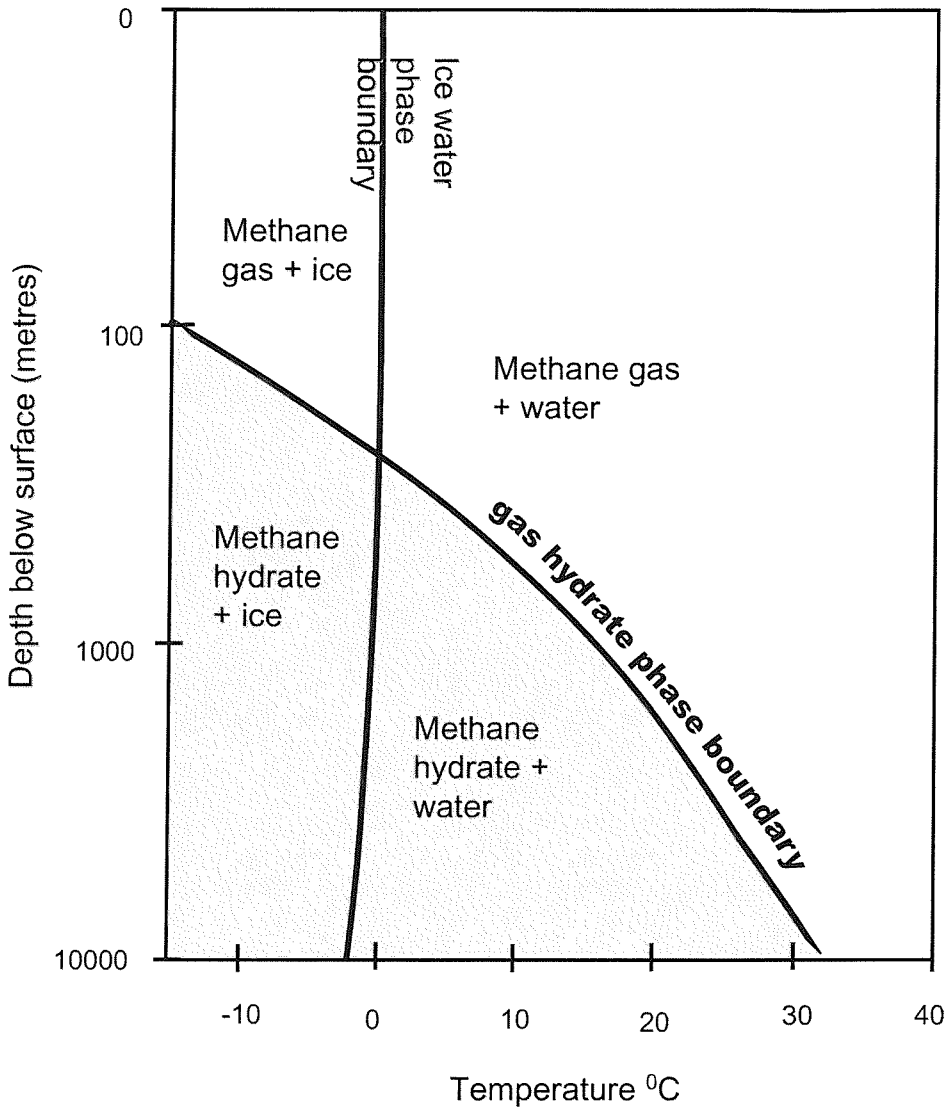

Figure 1.1: *Phase diagram for methane hydrate in pure water showing boundaries between phases. Addition of salt to water moves the phase boundary to the left. Addition of CO_2, C_2H_6, H_2S, C_3H_8 with methane moves the boundary to the right. After Kvenvolden (1998).*

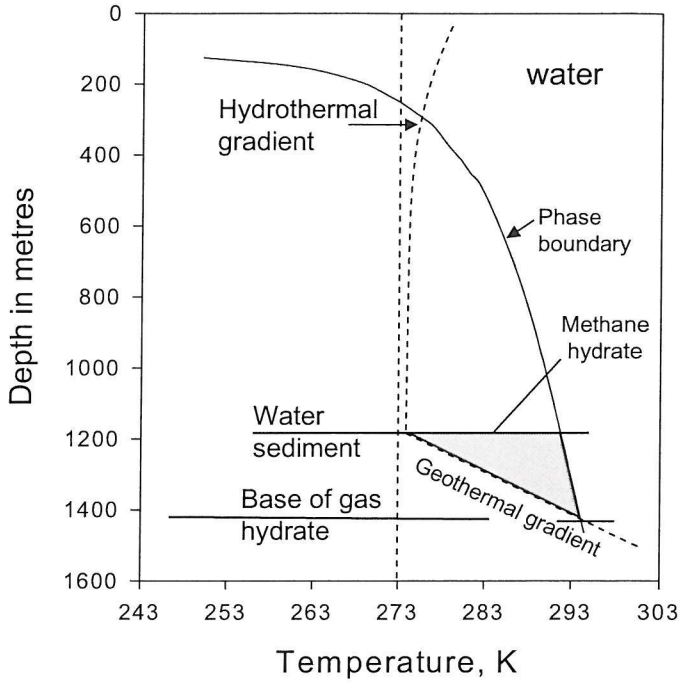

(a)

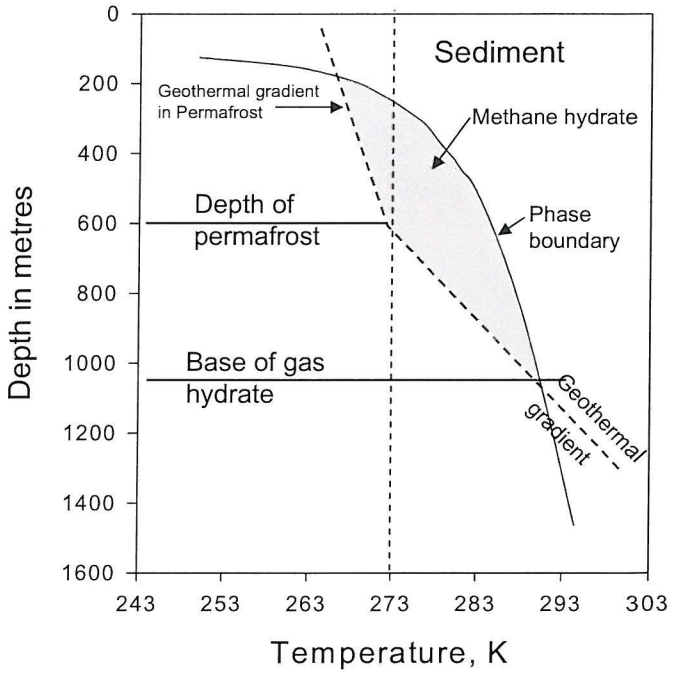

(b)

Figure 1.2: Envelopes of methane hydrate stability for (a) Oceanic sediment and (b) Permafrost. Redrawn from Kvenvolden (1988).

Chapter 2

GAS HYDRATES AND SEDIMENTS

2.1 Introduction

This chapter reviews current knowledge on gas hydrate. The reader is introduced to gas hydrate with a brief outline of its physical structure and the formation criteria for gas hydrate growth. Current hypotheses on hydrate growth within sediments are explained, and the varying techniques currently employed for identifying and quantifying the extent and distribution of hydrates are discussed. Particular attention is paid to laboratory research into the formation and geophysical properties of gas hydrates. The chapter finishes with conclusions drawn from the available literature.

2.2 Gas hydrates - physical structure

When ice forms, individual water molecules (H_2O) are held by hydrogen bonds to four other water molecules to form a 'puckered', non-planar array of hexagonal rings (Figure 2.1(a)). In gas hydrates though, the hydrogen bonds form into more rigid 3-D cages due to the inclusion of a gas molecule at the centre of each cage (Figure 2.1(b)). The formation of the crystal lattice and the size of the cavities of the cages define the structure of the gas hydrate. Three crystal structures have been identified as forming natural

gas hydrates; these are Structure I (sI), Structure II (sII) and Structure H (sH) (Sloan, 1998).

2.2.1 *Structure I*

Structure I (sI) is the simplest gas hydrate structure. This structure is formed by the arrangement of two differing polyhedra which are in themselves formed by the hydrogen bonds of the water molecules forming a cage. The pentagonal dodecahedron is formed from twelve pentagonal faces linking together and labelled 5^{12}. The tetrakaidecahedron is formed by adding two additional hexagonal faces to the 5^{12} cage to form a larger cage labelled $5^{12}6^2$. Both these polyhedra are illustrated in Figure 2.2. The cavities are stabilised by low molecular weight gas molecules such as methane (CH_4), carbon dioxide (CO_2) and hydrogen sulphide (H_2S) residing in the centre of each cage.

The structure of the sI gas hydrate crystal is formed by vertex-linking of the 5^{12} polyhedra together, with the $5^{12}6^2$ polyhedra filling the interstitial cavity (as illustrated in Figure 2.1(b)), with the basic unit crystal containing 2×5^{12} and $6\times5^{12}6^2$ polyhedra. If 100% of the cavities are filled with methane molecules then the unit crystal composition of sI is $8CH_4 : 46H_2O$.

In nature, the great majority of gas hydrates recovered from natural environments have been sI, with about 70% of the cavities being filled. Methane has been found to be the most common gas present ($\approx$ 99% of total gas composition)

vspace1cm

2.2.2 *Structure II*

Structure II (sII) gas hydrate is formed by the replacement of the $5^{12}6^2$ polyhedra with larger polyhedra comprising 12 pentagonal faces and 4 hexagonal faces ($5^{12}6^4$, Figure 2.2) into the crystal lattice. The larger size cavities of the $5^{12}6^4$ polyhedra are stabilised by larger gas molecules such as ethane (C_3H_8) or iso-butane (iso-C_4H_{10}).

In forming this structure the faces of the 5^{12} polyhedra are joined, forming a diamond lattice, with the larger polyhedra forming the interstitial cavity. In

this structure the basic unit crystal contains 16×5^{12} and $8 \times 5^{12}6^4$ polyhedra. The introduction of the larger molecules into the cavities produce a shift in the phase boundary (Figure 1.1) reducing the pressure required to maintain stability of the hydrate at a given temperature.

sII hydrates tend to form in pipelines during oil and gas production or at locations of faulting in oceanic sediments where thermocatalytically derived hydrocarbon gases (propane, ethane, etc, see Section 2.3) in addition to methane, are able to rise into the gas hydrate stability zone (GHSZ).

2.2.3 *Structure H*

Structure H (sH) contains the largest polyhedra with the unit cell containing 3×5^{12}, $2 \times 4^3 5^6 6^3$ and $1 \times 5^{12}6^8$ polyhedra. In sH, small gas molecules (CH_4 etc.) occupy the cavities of the 5^{12} and $4^3 5^6 6^3$ polyhedra while the cavity of the largest polyhedra ($5^{12}6^8$) is stabilised by large gas molecules such as methylcyclohexane, naptha and gasoline (Ripmeester, 1991). Structure sH is the most recently observed hydrate and has been described by Ripmeester et al. (1987) and Mehta and Sloan (1993) . At present, only one example of insitu sH gas hydrate has been recovered and was found in the Gulf of Mexico by Sassen and McDonald (1994) .

2.3 Formation criteria for gas hydrate

2.3.1 *Introduction*

To form gas hydrate sufficient quantities of methane gas and free water must be present under suitable thermobaric conditions. This section therefore outlines the differing methods of gas production and highlights the various models that have been proposed for the formation of hydrate within the sediment column.

2.3.2 *Production of methane gas for hydrate formation*

In oceanic and continental sediments methane is derived from the decomposition of organic matter contained within the sediments. Hesse (1986) modified early work by Claypool & Kaplan (1974) to suggest six stages for the reduction of organic matter to methane by chemical or biogenic processes termed "organic diagenesis" in anaerobic sediments as outlined in Figure 2.3.

Organic matter is slowly reduced via oxidation (Stage 1) then nitrate reduction (Stage 2) and sulphate reduction (Stage 3) to CO_2, which is further reduced to CH_4 (Stage 4). Methane that is produced in Stage 4 is termed biogenic, since it is the presence of bacteria that causes the reduction of the organic matter.

As sediment is progressively buried, the temperature of the bottom sediment rises due to the geothermal gradient. Bacterial production ceases and above 100^0C only thermocatalytic reactions take place, and these are usually associated with hydrocarbon production (Hunt, 1979). Methane produced at stage (6) is termed thermogenic.

2.3.3 *Models for growth of methane gas hydrate*

The amount of gas required to form the volume of methane gas hydrate found in nature exceeds the solubility of methane in water (≈ 0.045vol of CH_4/per unit vol. of water at STP, Yamamoto et al., 1976). Also, the stability zone for gas hydrate formation is above the region where thermogenic methane is produced and within the region of biogenic gas production. Therefore, three models have been suggested to explain in-situ hydrate formation:

1. Diagenetic production of biogenic gas in the zone of hydrate formation - Brooks et al. (1985) and Kvenvolden and Barnard (1983). In this model gas hydrates form when the amount of biogenic methane available from in-situ diagenetic processes exceeds the saturation limit of the pore fluid. At this point gas hydrates crystallize out.

2. Migration of free gas upwards through the hydrate stability zone

(HSZ) - Paull et al. (1994) and Minshull et al. (1994). In this model it is assumed that there is insufficient gas available, from in-situ production of methane, to form free gas and therefore gas hydrates form when gas from below the stability region migrates up through permeable sediment or fissures. Paull et al. (1994) suggested that the free gas could come from the dissociation of previous gas hydrate. This might occur as base of the HSZ moved upwards with progressive sedimentation cycles.

3. Hydrate precipitation from rising methane-saturated water - Hyndman and Davis (1992) and Ginsburg (1998). As the solubility of methane gas in pore water reduces with decreasing depth and temperature, saturated pore water rising through the sediment column could cause precipitation of gas hydrate within the HSZ.

All of these models have limitations, and hydrate formation may result from a combination of all three proposed models. Recent work by Buffett and Zatsepina (2000) has shown that CO_2 gas hydrate can form from dissolved gases, which complicates the three hypotheses mentioned above. Of the gas hydrates that have been recovered (Figure 2.4) the majority of samples have been shown to be produced from biogenic methane gas. Brooks et al. (1994) found samples of thermogenically derived methane gas hydrate in shallow sediments in the Gulf of Mexico while Ginsburg et al. (1992) observed thermogenic hydrate in the Caspian Sea. To date these are the only two sites where such hydrates have been observed.

2.4 Evidence for the extent and distribution of gas hydrates

2.4.1 *Recovery of hydrate samples*

Samples of gas hydrate have been recovered from deep ocean sites during the Deep Sea Drilling Projects (DSDP) and Ocean Drilling Program (ODP) cruises, (Sheridan et al., 1983; von Huene et al., 1985; Westbrook et al.,

1994; Paull et al., 1996) as shown in Figure 2.4. However, only large nodules or cored sections through large sheets of gas hydrates survive the change in thermobaric conditions during recovery. Gas hydrates that are finely disseminated or occur as thin veins within the sediment dissociate during transit from the borehole to the ship deck. Pressure core samplers (Dickens et al., 1997) have had limited success in recovery of samples. Therefore, the extent of gas hydrates has been inferred from geochemical analysis, seismic reflection profiling and downhole logging.

2.4.2 *Geochemistry of gas hydrates*

In the formation of gas hydrate, salt ions are excluded and isotropic fractionation occurs with the heavier water molecules ($H_2^{18}O$ and/or $DH_2^{16}O$) concentrating in the gas hydrate lattice. On dissociation of the gas hydrate, CH_4 gas and 'freshened' heavier pore water are released back into the sediment.

Also, on dissociation of gas hydrate, energy is required to break the hydrogen bonds that form the hydrate lattice. Therefore, the presence of cold spots within recovered cores, directly after their removal from the borehole, have been used to infer hydrate dissociation. These geochemical indicators for the presence of gas hydrate have been noticed at many DSDP and ODP drilling sites (Hesse and Harrison, 1981; Kvenvolden and Barnard, 1983; Jenden and Gieskes, 1983; Kvenvolden and McDonald, 1985; Harrison and Curialle, 1982; Hesse et al., 1995; Kvenvolden and Kastner, 1990; Paull et al., 1996).

2.4.3 *Seismic reflection profiling*

In seismic reflection profiling, the structure of marine sediments is inferred from observing the reflections of acoustic energy brought about by an impedance contrast (change in the product of velocity x density) between differing sediments. The attenuation of the seismic energy due to, i) geometric spreading and ii) absorption of energy by the medium in which it is travelling, generally leads to the depth of penetration of the acoustic pulse within the sediment being inversely proportional to frequency (Keary and Brooks, 1991). Verti-

cal resolution of the seismic survey is between one-quarter and one-eighth the wavelength of the seismic pulse (Telford et al., 1990) and so proportional to frequency. Thus a trade-off exists between the resolution and penetration of the seismic waves. Figure 2.5 highlights the differing sources of seismic/acoustic pulses available and the frequencies at which they operate. Typical deep-sea seismic surveys use air guns/waterguns (low frequency) as the source to enable sufficient penetration into the sediments. From processing of the data obtained during a seismic survey, velocity information can be gained which can help predict differing geological facies within the sediment column.

In the generation of an acoustic pulse, two waveforms are produced. These are:-

1. Body waves that include compressional waves (P-wave) and shear waves (S-waves).

2. Surface waves that include Rayleigh waves and Love waves.

Marine seismic profiling is usually undertaken using hydrophones (streamer) towed behind a boat to detect the reflected seismic pulse, as shown in Figure 2.6. Using this configuration only P-waves, from reflectors within the sea floor, are detected since water does not transmit S-waves (Telford et al., 1990), although it is possible to study mode-converted S-waves using wide angle techniques. In shallow marine sediments the P-wave velocity (V_p) is dominated by the pore water (approximately 1500ms^{-1} (Clayton et al., 1997)) and makes identification of geological features problematic. Recent improvements to marine seismic studies have included multi-component ocean-bottom seismometers coupled to the seafloor that allow S-waves, which are caused by mode conversion of the P wave pulse, to be detected as opposed to hydrophones, which measure pressure waves in the water column.

S-waves are not propagated by the interstitial pore water, therefore any change in velocity is a function of the soil skeleton stiffness. Sea bottom sediments have a typical velocity (V_s) of $100 - 500$ms^{-1}(Pecher and Holbrook, 2000). S-wave reflections help provide greater information with regard to induration and lithification of the geological formation (Whitmarsh et al.,

1990). The compressional and shear wave velocities, V_p and V_s, of pure gas hydrate is about 3300ms^{-1} (Dillon et al., 1994) and 1900ms^{-1} (Waite et al., 2000) respectively. Therefore it is assumed that sediment containing gas hydrates will show a high velocity, with V_s being more sensitive to hydrate inclusion. The parameter, V_p/V_s, has often been used as a diagnostic tool for investigating the lithology of marine sediments (Castagna et al., 1984; Hamilton, 1979; Wilkens et al., 1984). This ratio has also become more effective as a diagnostic tool as advances in geophysical surveying techniques have allowed both S- and P- wave velocities to be measured at the same time.

For geophysical surveys where the strain applied is low ($< 10^{-6}$), the intrinsic attenuation is assumed to be of a viscous nature, rather than frictional (Winkler et al., 1979). In the propagation of a seismic wave differing inertial forces are imposed on the fluid and soil particles leading to viscous shear stresses developing in the fluid. The intrinsic attenuation of a sediment is therefore a function of many components including; frequency of excitation wave, porosity, microstructure of sediment, pore geometry and grain size (Johnson, 1981). The relationship between gas hydrate and attenuation is at present poorly understood. It is assumed that the inclusion of gas hydrate as a cementing agent should reduce attenuation (Dvorkin and Nur, 1993) and Wood et al. (2000) presented results from ODP Leg 164, on attenuation, suggesting that this is true. The study of attenuation derived from geophysical surveys is in its infancy and the effect of using differing techniques to quantify attenuation remains unknown.

At present gas hydrates are inferred from anomalies associated with P-wave reflections. These anomalies (Dillon et al., 1994) are :-

- A reflection from within the sediment column that mirrors the reflection observed at the water/sediment boundary at the sea floor. This anomaly is termed a "bottom simulating reflection" (BSR);
- A reduction in seismic velocity at the base of the BSR;
- A reduction in reflection amplitude above the BSR.

The presence of free gas in the pore space reduces P-wave velocity (Brandt,

1960) and so a strong reflection occurs. The reflections follow the seabed at a constant depth and cut across sedimentary bedding planes (Paull et al., 1996), hence the term BSR. From theoretical extrapolation of the thermobaric conditions that are required for gas hydrate production and dissociation, the BSR is inferred as the 'base of the hydrate stability zone' (BHSZ), where hydrates exist above and only free gas exists below.

The reduction in velocity at the BHSZ causes a phase reversal (Shipley et al., 1979; White, 1979) with the strength of the reflection dependent on the amount of free gas present. Others suggest this anomaly may be due to the concentration of gas between sedimentary layers (Holbrook et al., 1996). Gettrust (1999) showed that the velocity contrast between higher and lower velocity layers, inferred from the BSR on the Cascadia margin off the west coast of America, occurs over several metres and not over tens of metres as suggested by Hyndman & Spence (1992) and Singh et al. (1993) .

The low amplitude reflections above the BSR are assumed to be due to cementation of the sediment grains by the gas hydrate, causing a zone which has low impedance contrast (Anstey, 1991) and no defined boundary, termed blanking. It has been suggested that the volume of gas hydrate within the pore space could be assessed by considering the degree of blanking (Lee et al., 1992; Dillon et al., 1994). However, more detailed geophysical surveys has suggested that the blanking is either the result of homogeneous sediment causing weak reflections, which overly sharp reflections caused by sediments containing free gas (Holbrook et al., 1996), or equally due to attenuation of seismic energy due to scattering and destructive interference (Wood and Ruppel, 2000).

2.4.4 *Downhole logging*

Downhole logging uses a range of geophysical tools that are contained within sondes that are placed down boreholes. The use of downhole logging in the detection of gas hydrates has been applied to five sites. These are the North Slope of Alaska (Collett, 1993), Mackenzie Delta, Northwest Territories, Canada (Winters et al., 1999) and by the shipboard scientific parties

on DSDP Leg 84, ODP Leg 146 and ODP Leg 164. Research undertaken by various authors (Collett, 1993; Collett, 1983; Matthews, 1986) and the results from ODP Leg 164 (Collett and Ladd, 2000) have shown that the Electrical Resistivity Log and Acoustic Transit-time Log produced the most reliable data for measuring the presence of gas hydrates.

The Electrical Resistivity Log measures changes in resistivity along the length of the borehole. As hydrates exclude ions on formation, an increase in resistivity occurs in the presence of hydrate. The Transit-time Log measures the travel time of an acoustic pulse through the formation, within the borehole, between a transmitter and receiver contained within the sonde. This travel time is used to calculate the velocity of the acoustic pulse. The presence of hydrates can therefore be inferred from anomalous variations in velocity measurements.

Guerin and Goldberg (2002) measured attenuation from downhole logging data obtained from the Malik 2L-38 well in the Mackenzie Delta, Canada. Hydrate was found to exist in coarse sand/gravel beds which were water saturated. They found that attenuation increased with increasing volume of the hydrate in the pore space, for both P- and S-waves.

2.5 Morphology of gas hydrate in the sediment column

Malone (1985) suggested that gas hydrates occur in sediments in four ways:

- Finely disseminated within the pore space;
- As nodules;
- As layers between sediment layers;
- As massive hydrates.

Malone suggested that gas hydrates grow from disseminated hydrate through to massive gas hydrate. This view has been supplanted by the notion that the growth of gas hydrates is dependent on the lithology of the

sediment (Brewer et al., 1997; Clennell et al., 1999; Ruppel, 1997). Figure ?? highlights the differing formation of gas hydrates in differing geological settings.

Kraemer (2000) has shown that zones of disseminated gas hydrate within the Blake Ridge area, off the southeast coast of the U.S.A., correspond to diatom rich, coarse, silty sediments. This sediment structure provides nucleation sites large enough for the preferential growth of gas hydrates. In coarse silt sediment, where numerous nucleation sites are available, the hydrate is assumed to grow homogeneously and be disseminated within the pore space (Collett, 1993).

In fine (clay and carbonate rich) sediment the small pore sizes and subsequent high capillary forces reduce the number of nucleation sites available for disseminated hydrate formation (Clennell et al., 1999). Although fine sediments reduce the potential for disseminated gas hydrate, nodules, veins and sheets have been found. Nodules form due to the diffusion of methane gas through the sediment until a pore space of sufficient size is found to allow hydrate growth at in-situ conditions. Veins are formed along fissures and faults within the sediment column through advection of pore fluid and methane gas. Both forms of hydrate will continue to grow, if sufficient methane is present, until the effective confining pressure (σ') and tensile strength (E_s-analogous to c') of the sediment is greater than the phase pressure of hydrate growth (Scherer, 1993). This mechanism is suggested as the origin of the massive gas hydrate found during DSDP Leg 84 at site 570 (Kvenvolden and McDonald, 1985).

2.6 The effect of gas hydrate on geotechnical properties

It was stated in above that gas hydrate can be classified into four differing structures; disseminated, nodule, vein and sheet. Some of the formation classes are analogous to that of ice in freezing soils (Tsytovich, 1975). This has led many researchers to assume the effect of gas hydrate on the physical

properties of sediment are similar to that of ice in frozen soil.

2.6.1 *Physical properties of hydrated sediment*

Disseminated gas hydrates

If the gas hydrate acts as a cementing agent locking the sediment together to form a 'solid, frozen structure' the resulting sediment would have a marked increase in strength and stiffness. The cementation effect would cause a large increase in stiffness at low concentration of hydrate cement (Dvorkin and Nur, 1993; Ecker, 2001). If, however, solid gas hydrate is formed within the pore space and provides no cementation to the sediment grains, then the impact of hydrate formation would be more subtle. An increase in strength and stiffness may occur but may not be noticeable until a high volume of gas hydrate was in the pore space.

In both of these cases, the consolidation process of the sediment may be altered. Recent research (Section 2.7.1) shows gas hydrate to have a higher strength than that of ice and so it may not exhibit plastic flow (Tsytovich, 1975) under given stress conditions. In this case the consolidation and natural cementation process seen in normal marine sediments may be inhibited by hydrate formation as outlined by Kvevolden (1998).

Veins

Hydrate veins tend to occur in clay and carbonate rich sediments, where the formation of disseminated hydrate is suppressed. Hydrate growth occurs due to preferential transport of methane gas and fluid along fissures in the sediment. If the surface area of the hydrate vein is small compared to its volume, and the number of veins in a given area is small, then its impact on sediment strength may be limited. However, if the reverse is true, then a bonded structure may be formed which may have a similar effect to that of disseminated hydrates in terms of strength but with the possibility of a high degree of anisotropy.

Nodules and sheets

The change in physical properties of sediments with nodules and, or, sheets of gas hydrate can be classified (and modelled) more easily. The resultant structural formation is analogous with sediment having inclusions or laminations of a stronger material. Both of these structural formations may give rise to seismic anisotropy.

Clennell et al. (1999) speculated that the growth of hydrate, either as nodules, or as more concentrated layers (sheets), can cause a sequestration of water and gas from the surrounding sediment leading to a 'freeze drying' effect analogous to that in frozen soils. However, they state that this analogy is not perfect due to hydrate formation being dependent on sufficient quantities of methane gas being available as opposed to the thermodynamic undercooling associated with ice formation (Konrad and Duquennoi, 1993). Also, the volume of methane gas needed to cause a freeze drying of the soil is much greater than that which can be generated locally.

2.6.2 *Hydrates and sea-floor stability*

The geotechnical effects outlined above are dependent on the gas hydrate being under stable thermobaric conditions. If these conditions are altered either on a global scale (due to a rise in ocean bottom temperatures or reduction in ocean water depth), or on the local scale (temperature increase due to oil extraction) then the physical characteristics of the gas hydrate can be greatly affected. When gas hydrates dissociate, its ice like structure reverts back to its constituent parts of gas and water. The release of methane gas back into the vapour phase can lead to an increase in pore water pressure (pwp). If there are insufficient pathways to allow quick dissipation of the excess pressure then the structure of the sediment may be altered, resulting in a zone of structurally weak sediment. This weak, gas-charged muddy sediment is thought to be the initiation point for various slides on the world's oceanic margins (Ashi, 1999; Berndt et al., 2002; Bugge et al., 1987; Dillon et al., 1994; Dillon et al., 1998; Maslin et al., 1998; Kayen and Lee, 1991; Meinert et al., 1998; Popenoe et al., 1993; Summerhayes et al., 1979). Figure

2.8 highlights the possible failure mechanism for oceanic slopes. Figure 2.9 shows the Blake Ridge depression, which is attributed to gas hydrate dissociation creating excess pore pressure that mobilised fluid rich sediment (Dillon et al., 1998). These conditions are likely to exist at the base of the HSZ or within the HSZ if the thermobaric conditions are altered. This scenario is also likely to arise locally around oil exploration activities (drilling).

2.7 Experimental research on gas hydrates

Due to the ephemeral nature of gas hydrates and the difficulty of recovering well-preserved samples (Matsumoto et al., 2000), research has focused on characterising laboratory grown gas hydrates. This has included hydrates in the bulk phase as well as hydrates within porous media.

2.7.1 *Laboratory grown gas hydrates - bulk phase*

Gas hydrates that have been recovered from oceanic sites are described by Sloan (1998) as "solid, ice like masses". The growing of hydrates in the laboratory that resemble those found in-situ has proved to be difficult.

As mentioned in Section 2.3 the solubility of methane gas in water is low. This has led most researchers to use a three-phase system where water and free gas is present during the formation of the gas hydrate. Hydrate growth occurs at the interface between the gas and water phases. As the continuation of hydrate growth is dependent on high concentrations of the hydrate forming components at the interface (Makaogon, 1981), a barrier restricting the continued formation of hydrate is formed. To overcome this, researchers have used a variety of techniques to create new initiation points for continuing hydrate growth. Englezos et al. (1987) used agitation of the specimen during formation, whereas Handa (1986) used a grinding action on ice to form initiation points. These techniques have tended to form hydrate having an open and porous structure.

Another technique developed by Stern et al. (1996) formed gas hydrate by slowly heating sieved granular H_2O ice grains (180- to 250μm) in the

presence of cold methane gas within a constant volume reaction vessel. As the sample temperature rose above the liquidus line (0^0C) the melting ice created nucleation sites for hydrate formation. Initially a hydrate skin is formed on the ice surface, with the subsequent conversion of the ice grain interior to hydrate being dependent on the diffusion of methane gas through the formed hydrate rind. To allow for a reasonably fast conversion of ice to hydrate (approximately 8 hours), a partial methane pressure much greater than the equilibrium pressure defined in Figure 1.1 was required (Hwang et al., 1990).

Stern et al. (1996) had assumed that the initial hydrate growth occurred as the ice grain began to melt (sample temperature above 0^0C), and based their assumption on the reduction in methane gas pressure, measured during their tests. Figure 2.10 shows the pressure-temperature (P-T) history for a sample during a test run. it can be noted that formation of hydrate, from melting seed ice, causes a reduction in the thermal expansion gradient of the methane gas as the H_2O liquidus line is passed. This is due to some of the methane gas in the vapour phase being consumed during hydrate formation. Subsequent work (Stern et al., 1998), using an optical-cell, had shown that the initial hydrate rind could actually form whilst the sample temperature was below 0^0C. Salamatin and Kuhs (2002); Staykova et al. (2002) and Satykova et al (2003) were also able to confirm, using images obtained from a field-emission scanning electron microscope, that hydrate growth on ice grains can occur at temperatures below 0^0C and that the rate of hydrate conversion was related to temperature and pressure. It was also demonstrated by Barrer and Edge (1967) that the area of the gas-ice contact area was also a strong factor in the hydrate growth rate.

Studies on bulk hydrates made from seed ice, and naturally occurring hydrates recovered from Hydrate Ridge[1], have shown using a field-emission scanning electron microscope (Salamatin and Kuhs, 2002; Staykova et al., 2003; Suess et al., 2002) that gas hydrate crystals have a sponge-like structure with typical pore sizes of several hundred nanometres (Figure 2.11).

[1]Hydrate Ridge is found in the Cascadia Margin, off the Northwest American coast

2.7.2 *Laboratory grown gas hydrates within porous media*

Most laboratory experiments have been conducted on gas hydrates in the bulk phase. In nature, gas hydrates are dispersed within the sediment. Therefore research has also focused on growing hydrates within a variety of porous media, or soils, to mimic hydrated sediments.

Stoll and co-workers (Stoll et al., 1971; Stoll, 1974; Stoll and Bryan, 1984) were the first to qualitatively assess the impact of gas hydrates on the properties of saturated sands. Initially they formed hydrate by bubbling methane gas through saturated rounded Ottawa sand (average grain size 0.7mm) at an approximate temperature of 3^0C and pressure of 7MPa (Stoll et al., 1971). Unfortunately, they were unable to measure the volume of hydrate produced or control its distribution within the sand. This technique also caused blockages within the sand due to uncontrolled hydrate formation at the base of the sand sample preventing further additions of gas. They tried to overcome this by mixing known volumes of sand, water and gas and then stirring the whole mixture to form gas hydrates before compacting the mixture (Stoll and Bryan, 1984). However, in this method, only propane gas was used and so sII hydrate was formed. It is also worth noting that in their initial tests the potential of forming sII hydrates instead of sI was high due to the use of commercial grade methane gas, containing up to 1% propane, which helps in the formation of sII (Sloan, 1998). They were able to show that sediments containing gas hydrates closely resembled frozen saturated sand (Stoll, 1974).

Handa & Stupin (1992) investigated the thermodynamic properties of methane gas hydrates in silica gel that had an average pore size of $70\dot{A}$, which is much smaller than that typically found in fine-grained sediments. The results show that the small pore size suppresses hydrate formation and so a higher pressure or lower temperature is required than that suggested by the methane phase diagram (Figure 1.1).

Brewer et al. (1997) conducted field tests on separate samples of coarse sand and fine mud on the ocean bottom, by bubbling methane gas through the samples. These tests showed that hydrate infilled the voids in the sand

sample whereas the mud sample showed the injected gas carving out channels through the mud, which infilled with gas hydrates in larger discrete masses. A similar result was reported by Chuvilin et al. (2002) when forming hydrates in clay samples within the laboratory .

Experiments undertaken by the U.S. Geological Survey's Woods Hole Centre using a Gas Hydrate and Sediment Test Laboratory Instrument (GHASTLI) were able to control the formation of gas hydrates at different confining pressures (Winters et al., 2000; Winters et al., 2002) by having a unidirectional cold front moving down the sample. They injected methane gas into the base of the sample and allowed it to percolate up. Although the volume of hydrate could be calculated, by the volume of water ejected, they were unable to control the distribution of the hydrate with the pore space. Although not stated it is probable that the samples were made from granular material whose permeability would allow the easy passage of methane gas. At certain instances, during tests, plugs of hydrate formed at the base of the specimen and prevented further gas injection.

Tohidi (2002) carried out experiments using glass micromodels. These were plates of etched glass where the etching models a two-dimensional porous medium. Hydrates were formed from carbon dioxide and methane gas as well as methane in solution. Video imagery was able to show hydrate formation for the differing solutions. In the formation of hydrate from dissolved gas it was necessary to have silica particles, or ice relics, as initiation points for hydrate growth.

Due to the inherent stability condition required for methane gas hydrate, and its low solubility in water, researchers have used differing hydrate formers to create hydrates. Tetrahydrofan (THF) has been used since it is miscible with water and forms hydrate at atmospheric pressure at 4^0C (Bathe et al., 1984; Kiefte et al., 1985; Pearson et al., 1986; Kunerth et al., 2001) while Berge et al. (1999) used Freon-11 (CCL_3F) as the hydrate former for similar stability considerations.

2.7.3 *Geophysical properties of laboratory grown gas hydrates*

Although significant research has been undertaken in the study of gas hydrate, very little data is available on the geophysical properties of gas hydrate. In the last thirty years only a handful of studies on laboratory measurements of hydrates, with or without sediment interaction, have been published.

Stoll and co-workers (Stoll et al., 1971; Stoll, 1974; Stoll and Bryan, 1984) were the first to measure compressional wave velocity of methane hydrates in saturated sand samples. They reported an increase in velocity from 1830ms^{-1} to 2690ms^{-1} for hydrated sands formed by repeatedly bubbling commercial grade methane gas through the sand (Stoll et al., 1971). Their later work focused on propane hydrates (Stoll and Bryan, 1984) and measured an increase in wave velocity from 1800ms^{-1} to 2260ms^{-1} after the hydrate and sand was compacted and left to age over a twelve day period. In both sets of results the volume and distribution of the hydrate was not quantifiable. The wave velocities were measured using the pulse transmission technique with the fundamental frequencies lying between 100kHz and 300kHz. As the samples were saturated, possible velocity/frequency dispersion effects (Winkler, 1985), due to the ultrasonic frequency applied, may have occurred.

Whiffen et al. (1982) measured the compressional speed for polycrystalline samples of methane and xenon hydrate and presented the data as velocity ratios with that of ice. They used Brillouin spectroscopy to determine the wave velocity and reported a hydrate-ice ratio value of 0.76 and 0.88 for xenon and methane hydrate respectively. Kiefte et al. (1985) extended the work by Whiffen et al. (1982) on methane and xenon hydrate and also included results using other hydrate formers (sulphur dioxide, propane, tetrahydrofuran (THF), Freon 11 (CCL_3F) and sulfur hexafluoride). They showed that the compressional velocity of bulk methane hydrate was 3369ms^{-1}.

Pandit and King (1983) measured both compressional and shear wave velocities on propane hydrate using ultrasonic techniques. However, their methodology allowed the samples to be mixtures of both hydrate and ice. The measured compressional wave velocity reduced sharply, from 3225ms^{-1}

to 2050ms^{-1}, as the sample temperature rose above 0^0C. The shear wave velocity was 1675ms^{-1} below 0^0C while the signal became undetectable above 0^0C. They estimated the ice content to be between 10-20%. Helgerud (2001) suggests that the hydrate samples made by Pandit and King were porous due to the anomalously low density of the samples and that the testing occurred when the hydrate was outside its stability field, inferring that velocity measurements may have been affected.

Bathe et al. (1984) measured both ultrasonic compressional and shear wave velocities of bulk hydrate whilst using tetrahydrofan (THF) as a hydrate former. Values of 3513ms^{-1} and 1663ms^{-1} at -17^0C, for compressional and shear velocities respectively, were reported. From these velocities measurements, the adiabatic bulk modulus (bulk modulus at constant entropy; i.e., with adiabatic exchange of heat) and Poisson's ratio were calculated. However, these results were found to differ from subsequent values obtained by Kiefte et al. (1985) for THF hydrate. Pearson et al. (1986) used THF hydrate to measure the compressional velocities of various hydrated rock samples using the pulse transmission technique. In their tests certain rocks (Berea sandstone and Austin chalk) showed an increase in wave velocity as the sample temperature approached 0^0C from the positive side. They also showed that the rate at which the wave velocity increased was dependent on salinity of the sample, with increased salinity causing a slower increase. Based on these observations, Helgerud (2001) postulated that the velocity rises could have been a function of ice formation since the molar ratio of water-THF used was 18:1, when the ideal ratio is 17:1, suggesting that excess water was available.

Berge et al. (1999) undertook velocity measurements for both hydrate/water samples and hydrate/water/sand samples using Freon-11 (CCL_3F) as the hydrate former. For the hydrate/water samples the maximum ultrasonic compressional wave speed measured was 2500ms^{-1} for 68% hydrate content. Due to poor signal quality no shear wave measurements were obtained. The samples were prepared by vigorously stirring mixtures of Freon-11 and water together and then allowing to age overnight. The hydrate fraction was estimated from conductivity measurements obtained after flushing the sam-

ple with saline solution. For the hydrate/water/sand samples, compressional wave velocity measurements varied from 1700ms^{-1} at low hydrate contents to 3810ms^{-1} for a specimen with 52% of the pore space being filled with hydrate. Shear waves were not detectable until the hydrate content was above 35%, at which point a significant increase in P-wave velocity was observed. The maximum shear wave speed measured was approximately 2250ms^{-1} at 52% hydrate content. Berge et al. (1999) suggested that below the 35% hydrate saturation, termed the critical hydrate concentration, the volume of hydrate is insufficient to cement the sand grains. Above the critical hydrate concentration, the hydrate is mechanically connected to the sand grains changing the state of the sample from unconsolidated to consolidated. In the sand mixtures the hydrate fraction was estimated by a more complicated adaption of the procedure adopted for water/hydrate samples, which could allow significant errors to occur. Also, the distribution of the hydrate phase within the sand mixture could not be accurately defined since in the water/hydrate samples, vigorous mixing was required to form a homogeneous sample.

Apart from the work of Whiffen et al. (1982), which was subsequently extended by Kiefte et al. (1985), the majority of tests have been conducted on sII hydrates with a variety of differing hydrate formers. In nature, the majority of hydrates recovered have been sI with methane gas being the most dominant hydrate former. However the formation of methane hydrates was problematic. The development of the hydrate formation procedure by Stern et al. (1996) allowed polycrystalline methane hydrates to be more readily produced. Waite et al. (2000) used this method to produce hydrate samples, which were then used to measure acoustic properties of the sample using the pulse-transmission method. Waite et al. (2000) were the first to measure the shear wave velocity of laboratory grown structure I methane gas hydrates and reported the velocity to be 1890 ± 30ms^{-1} with the compressional wave velocity being given as 3650 ± 50ms^{-1}.

Stern et al. (2000) have shown that the strength (stress/strain relationship) of laboratory grown methane hydrates to be significantly greater than that of ice at temperatures above 250K (Figure 2.12). Strength tests conducted on samples obtained from the Malik 2L-38 well, using the GHASTLI

apparatus, have shown the impact that hydrate can have on soil strength. Figure 2.13 highlights strength comparisons between a hydrated sample and samples where the hydrate has been allowed to dissociate (Winters et al., 2002). In these tests the volume of the gas hydrate within the sample is not given and so an analysis of strength to hydrate content is unavailable.

2.8 Summary

From the review of the literature concerning gas hydrates it can be seen that our current understanding of the extent and distribution of gas hydrates, and the role they play, within the sediment column is somewhat lacking.

At present, geophysical researchers use estimates of acoustic velocity of gas hydrate bearing sediment based on either empirical-or physics-based approaches (Pecher and Holbrook, 2000). In both cases, uncertainties arise due to lack of knowledge as to whether gas hydrates cement the soil grains together, modify the pore water, or behave as mineral grains themselves. This introduces uncertainties into the estimation of gas hydrate, in-situ, using seismic methods. Although the use of geochemical techniques and downhole logging can be used to estimate hydrate content, they are unable to assess the spatial distribution within the seabed. Also, the cost of invasive techniques is generally prohibitive at such large water depths for practical applications. Therefore, to effectively estimate gas hydrate distribution, a more thorough understanding of the effect of gas hydrate, on the seismic properties of marine sediments is required to allow quantitative estimates of gas hydrate from seismic surveys.

The effective use of inversion techniques and 'effective medium' modelling theories, to improve predictions of hydrate distribution from acquired seismic data, is dependent on validating the models with laboratory measurement of seismic properties from gas hydrate bearing sediment. This has been hindered both by the lack of high quality samples of recovered sediments containing gas hydrates and the limited success of producing well characterized soil specimens containing laboratory grown gas hydrate.

Therefore to fully assess the role of gas hydrate, with regard to either

marine slope stability, global warming or as a possible energy resource, laboratory research must develop methods to create gas hydrate bearing soil specimens where the content and distribution can be controlled.

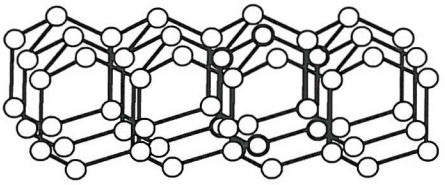

(a) Basic crystal structure of ice Ih

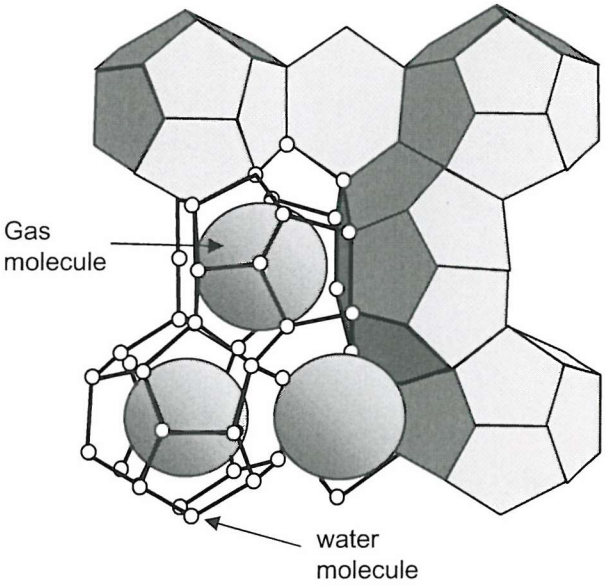

(b) Crystal structure for sI hydrate.

Figure 2.1: *Pictorial view of ice and gas hydrate crystal structure.*

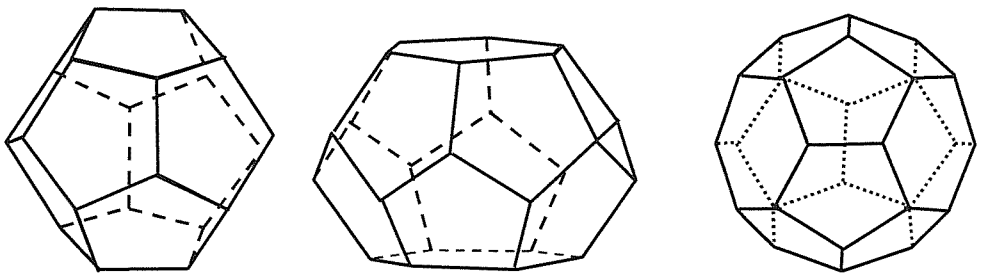

Figure 2.2: *Three cavities in gas clathrate hydrates. (a)* 5^{12} *(b)* $5^{12}6^2$ *(c)* $5^{12}6^4$. *Redrawn from Sloan (1998) after Jeffrey & McMullan (1967).*

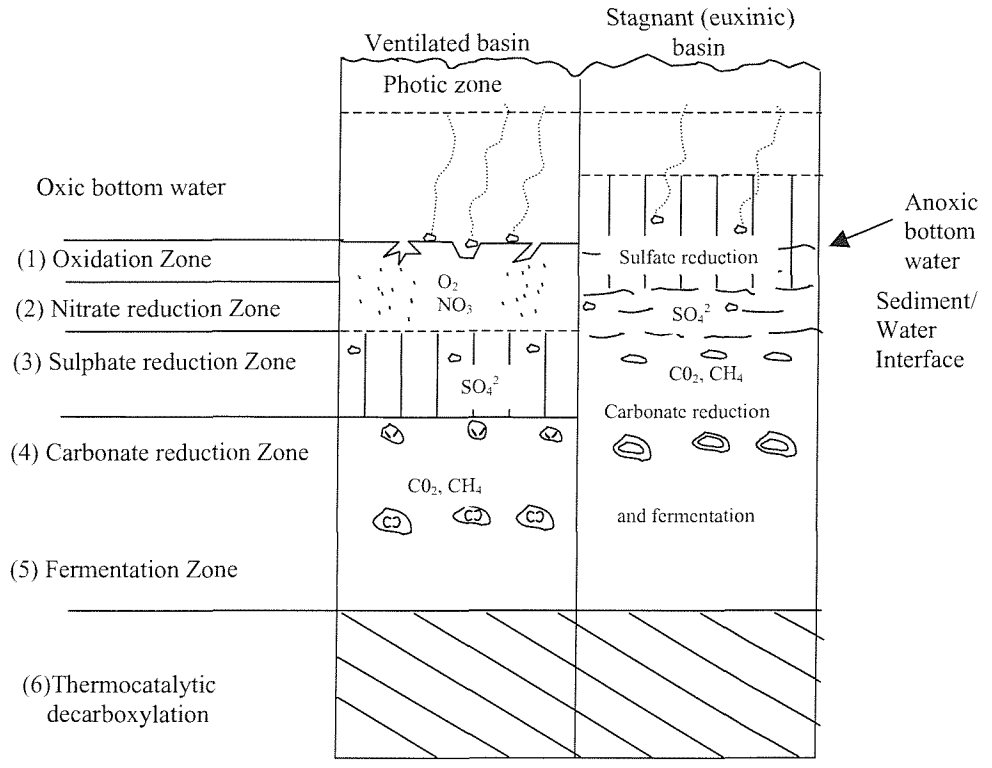

Figure 2.3: *Stages of organic matter oxidation in anoxic sediment. Redrawn from Hesse (1986).*

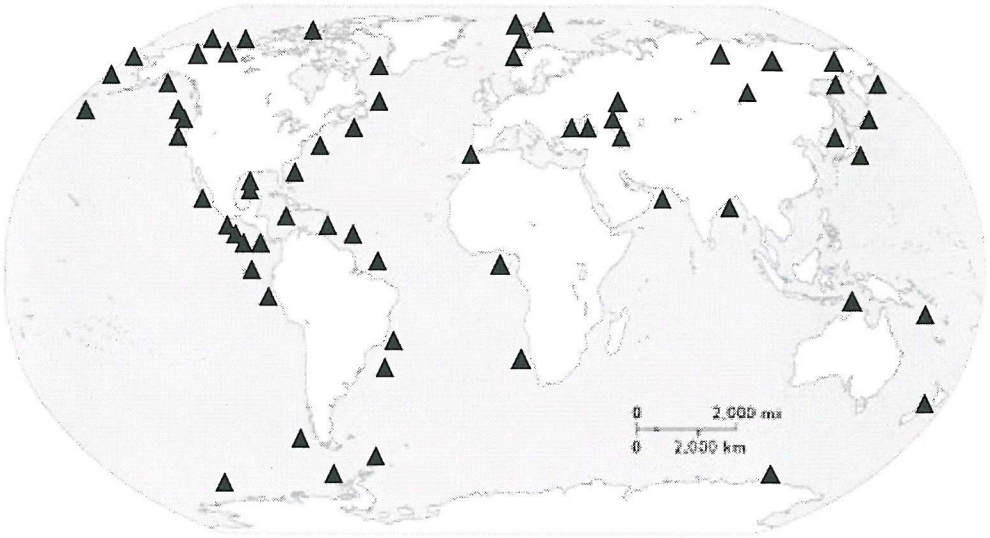

Figure 2.4: *World-wide distribution of recovered samples of gas hydrates. Updated and redrawn from Kvenvolden (1998).*

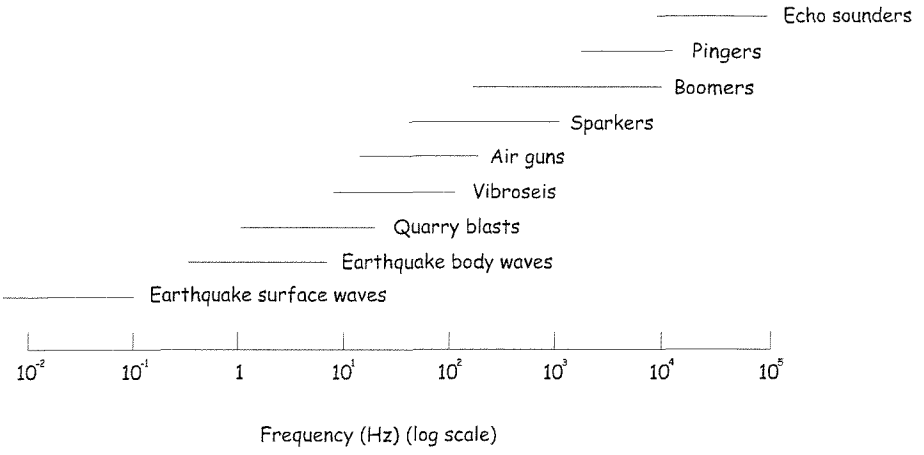

Figure 2.5: *Seismic/acoustic sources and their frequency range. Redrawn from Kearey et al. (2002).*

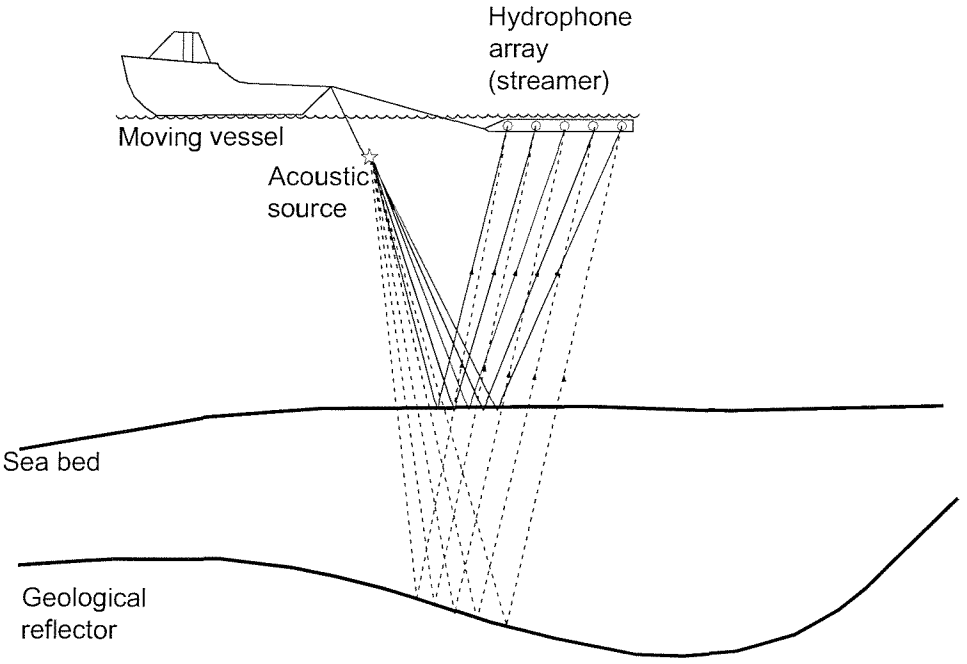

Figure 2.6: *The survey set-up for single-channel seismic reflection profiling. Redrawn from Kearey et al. (2002).*

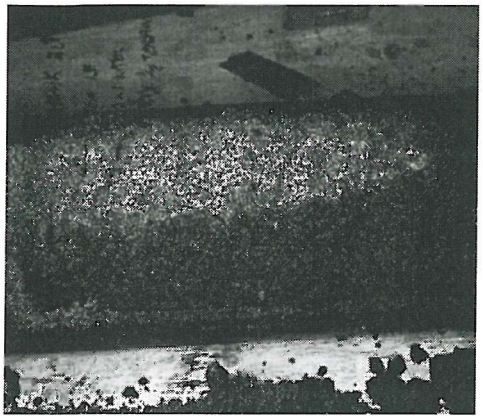

(a) Disseminated gas hydrate in medium grained sand recovered from Malik 2L-38 well. Image courtesy of Natural Resources Canada

(b) Veins and sheet like hydrates recovered from the Cascadia margin, off Newport,Oregon. Images courtesy of Geomar

(c) Nodular gas hydrates in muddy cores recovered from the Black Sea during TTR10 cruise.

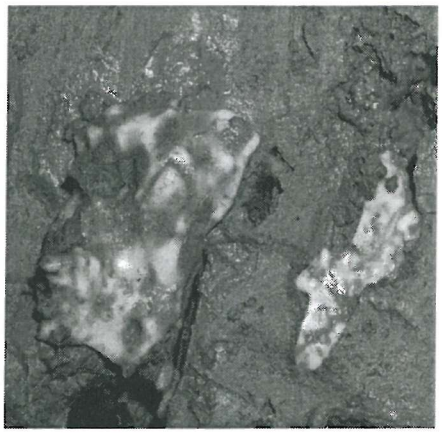

(d) Close up of hydrate nodule recovered from the Black Sea

Figure 2.7: *Differing morphology of recovered gas hydrates*

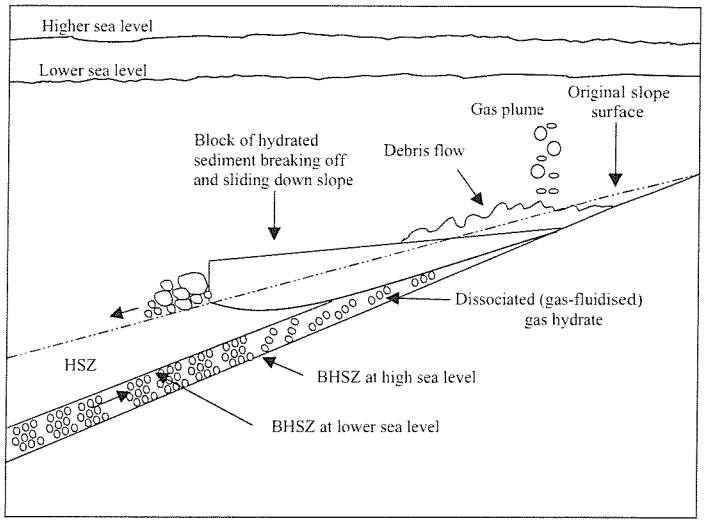

Figure 2.8: *Diagram of slope failure induced by dissociation of gas hydrates as result of falling sea level (or temperature increase). Redrawn from Kvenvolden (1998).*

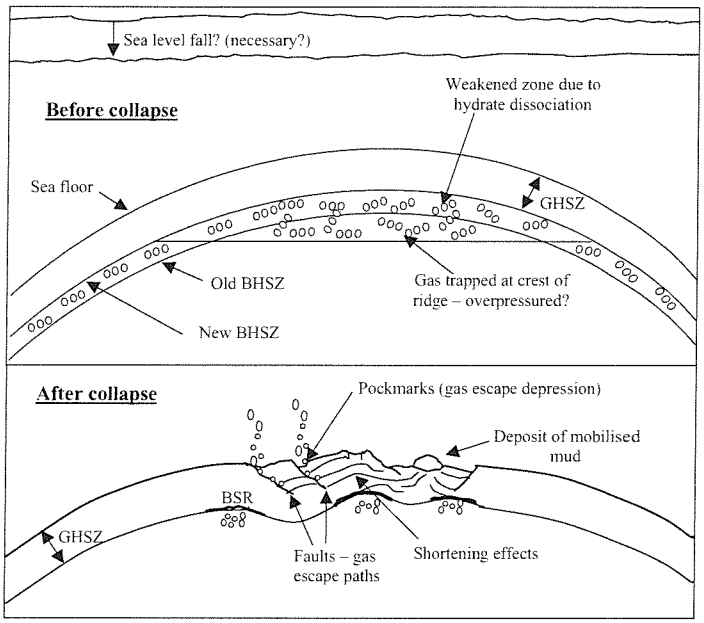

Figure 2.9: *Conceptual drawing for the gas hydrate induced collapse failure of the Blake Ridge crest. Redrawn from Dillon et al. (1998).*

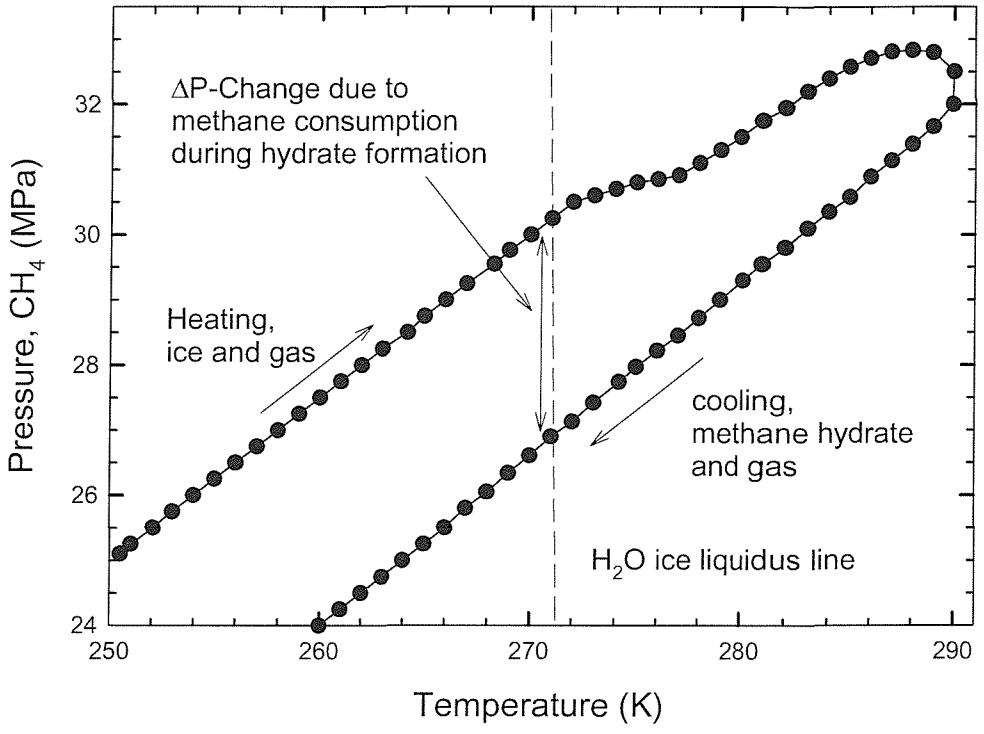

Figure 2.10: *P-T history of a methane hydrate synthesis run. Redrawn from Stern et al. (2000).*

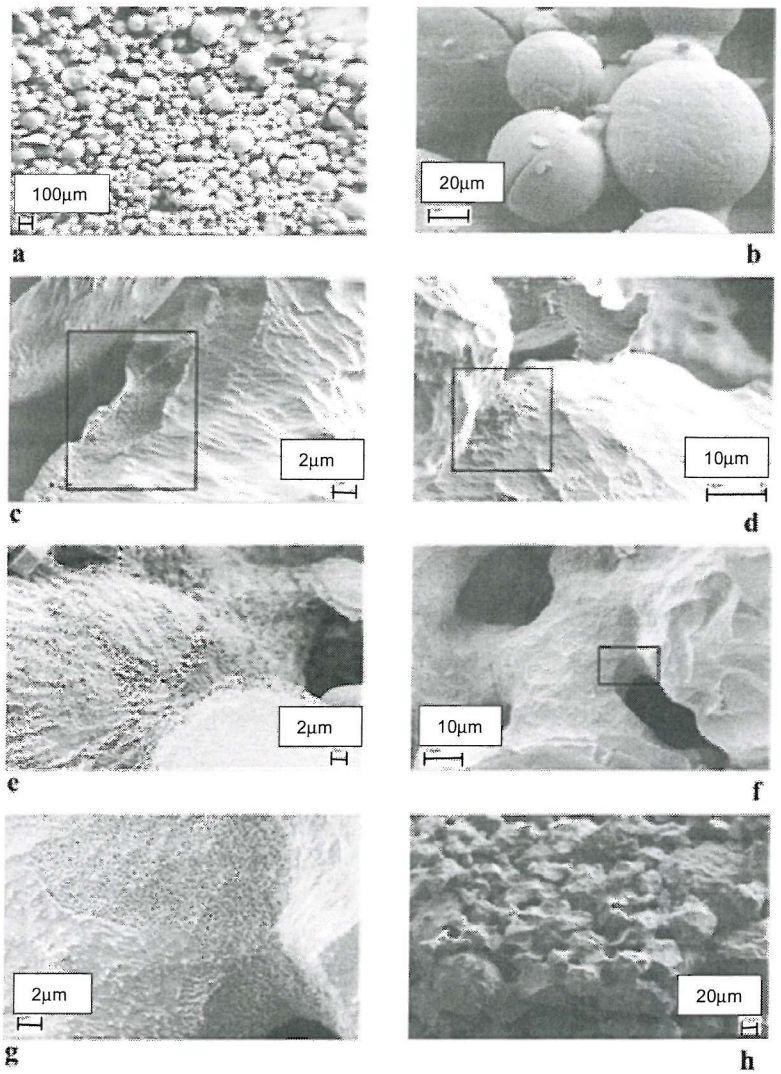

Figure 2.11: *Field-emission scanning electron images showing initial ice-1h material and various stages of the hydrate formation process: (a) initial ice-1h powder, (b) individual spherical 40-60µm ice grains, (c) ice grain crack filled with hydrate film and ice grain contact area (d) covered with hydrate film after 1h of hydrate formation at 60bar and 264K; (e) split grain (lower right) and neighboring grain (left) with the surface covered by porous CH4-hydrate after 10.5h; (f) ice grains completely covered and sintered together by hydrate after 55h; (g) larger magnification of the left-corner area from (f) showing the porous hydrate spreading into the open pore space of the initial ice sample; (h) Overview of a hydrate sample after 80h of reaction in which the original ice grain structure can still be discerned and showing a degree of sintering which leads to a macroscopically consolidated sample. Boxes on the images c, d, and f mark the regions of interest or magnification. Reproduced with kind permission from Staykova et al. (2003).*

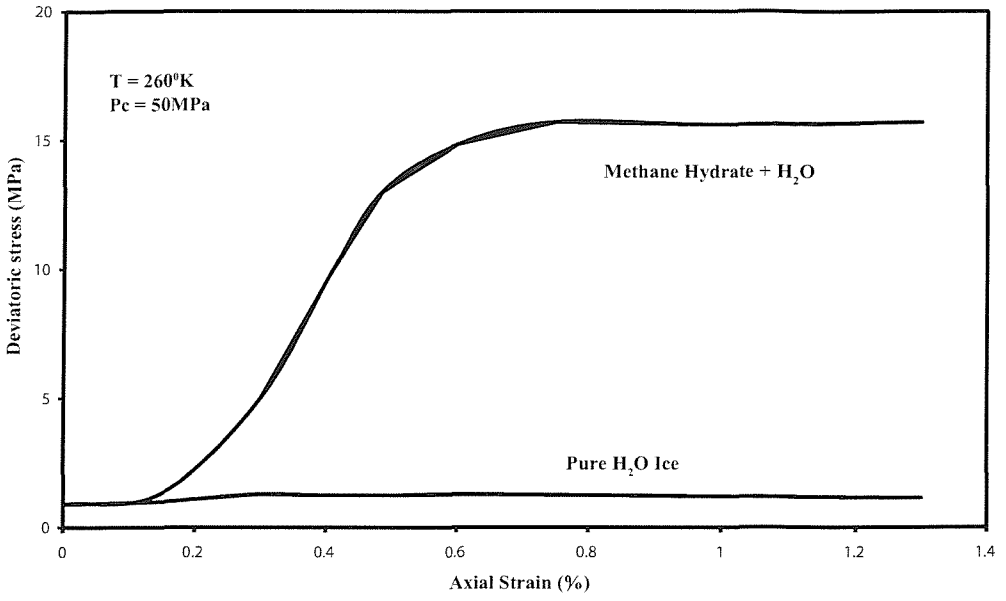

Figure 2.12: *Comparison of stress-strain histories of methane hydrate plus H_2O ice($\approx 3:1$ volume ratio of hydrate to ice) vs pure H_2O ice at 260K and confining pressure of 50MPa and at a constant strain rate of $3.5x10^{-3}s^{-1}$. Redrawn from Stern et al. (2000).*

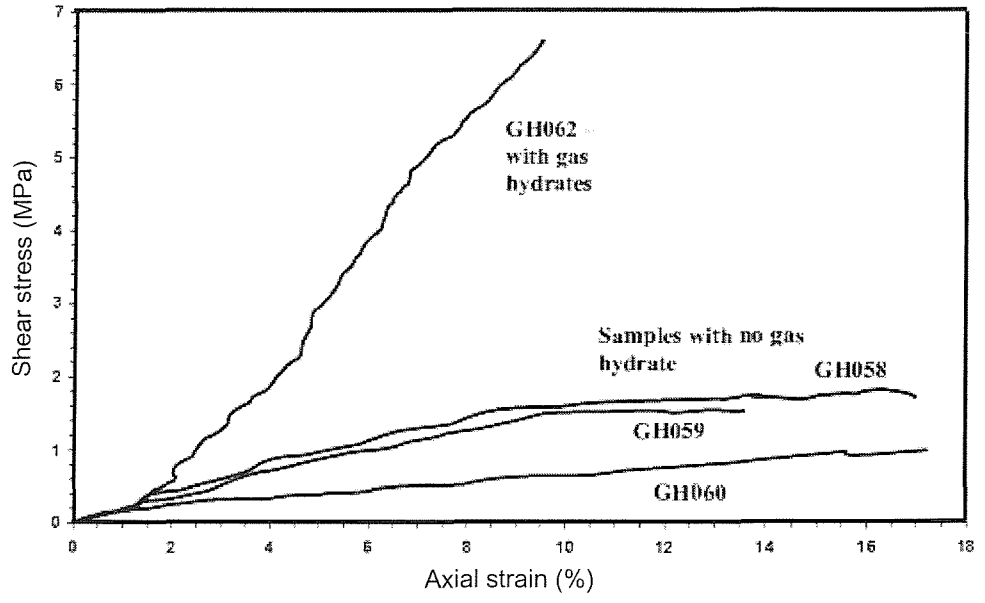

Figure 2.13: *Comparison of triaxial strength plots for sand samples recovered from the Mallik 2L-38 well. Samples were tested after hydrate dissociation except sample GH062 which was tested with gas hydrate in the pore space. Redrawn from Winters et al. (2000).*

Chapter 3

LABORATORY TESTING METHODS - THE RESONANT COLUMN

3.1 Introduction

From Chapter 2 it can be seen that to assess the role of gas hydrate with regard to marine slope stability, global warming or as a possible energy resource, an accurate estimate of its distribution and extent within the sediment column is required. This can be aided by the laboratory measurement of seismic properties (e.g. V_p, V_s, Q_p^{-1}, and Q_s^{-1}) of well characterized soil specimens containing gas hydrate.

The following conditions needed to be achieved if the above objective was to be attained.

- Measurement of dynamic properties of sediments at frequencies and strains that are relevant to current geophysical surveying techniques.
- The proposed methodology for hydrate creation should be incorporated in the laboratory apparatus.
- The experimental techniques should be adapted to allow pressure and temperature conditions for hydrate stability.

- Laboratory tests should be non-destructive so that the effects of hydrate dissociation on the same sample can be assessed.

3.1.1 *Laboratory testing methods*

A variety of laboratory testing methods have been developed for measuring the geophysical properties of soils. These can be classified in groups:

1. Load-deformation: triaxial, cyclic triaxial and simple shear tests;
2. Wave propagation: for example, pulse echo or bender element techniques;
3. Resonance; resonant column and resonant bar techniques.

Of all the testing procedures and laboratory apparatus described, the resonant column was identified as the most suitable method to adopt. It has become a standard laboratory apparatus, used in commercial and academic laboratories to investigate the dynamic response of soils/rocks. The resonant column utilizes the theory of vibration of a linearly visco-elastic cylindrical rod to quantify the velocity of propagation of either a shear wave or compressional wave, depending on the mode of excitation applied to a sample. The velocity of wave propagation is determined from the frequency of vibration, at resonance, of the soil column and attached drive mechanism. The resonant frequency of the soil/drive mechanism system is a function of various factors relating to the sample and can vary from 17-25Hz for soft clay soils (Hardin and Drnevich, 1972a) and up to 400Hz for stiff cemented sands (Avramidis and Saxena, 1990) during torsional vibration, which is within the range employed in deep sea seismic surveys. Also the strain applied to the sample can be controlled so that it is comparable to that applied to the sediment during geophysical surveying.

The majority of the work previously undertaken using the resonant column has been to investigate the effect of torsional vibration on the shear modulus of soil/rock samples. In this chapter, the resonant column is introduced with a brief overview of its development with regard to torsional

vibration (see Section 3.4). The various factors that effect the dynamic response of the soil in torsional mode are highlighted. The assumptions and underlying mathematical theory for the resonant column are introduced. Several authors (Wilson and Dietrich, 1960; Cascante et al., 1998) have investigated the response on Young's modulus using differing excitation modes. Therefore, the chapter concludes with a discussion on recent developments, using the resonant column, to determine Young's modulus E using flexural excitation (Cascante et al., 1998).

3.2 Resonant Column - Overview

The resonant column apparatus has been used to measure the dynamic response of soils since the 1930s, when the resonant column method was first developed by Japanese engineers Ishimoto & Iida (1937). In the 1960s the use of the resonant column apparatus was made popular by the work of authors such as Hall & Richart (1963), Drnevich, Hall & Richart (1967) and Hardin & Black (1968).

The reduction of data from the resonant column apparatus, to obtain the physical properties of the soil, is a function of the boundary conditions. In the majority of cases, research has been undertaken using the fixed-free configuration (Figure 3.1(a)). This configuration is preferred as the mathematical derivation is more straightforward. In the fixed-free test a cylindrical specimen is fixed at its base and excited via a drive mechanism attached to the free end. From measuring the motion of the free end, the resonant frequency for the soil/drive mechanism system is obtained from which the velocity of the propagating wave and the degree of material damping can be derived. The shear modulus is then obtained from the derived velocity and the density of the sample. Theoretical considerations and the constitutive equations for this resonant column apparatus configuration are discussed in Section 3.4. The other type of configuration used is termed free-free. In this configuration both ends of the sample are free to move and resonance is found from the motion of the passive end. In Figure 3.1(b) the free-free model is idealized if the spring is weak relative to the stiffness of the specimen. Menq and Stokoe

(2003) developed a free-free resonant column apparatus by supporting the specimen on soft support springs with the drive mechanism attached to the base of the sample.

In the past 40 years many authors have made improvements and modifications to the design of the resonant column apparatus. These have included the application of anisotropic stresses (Hardin and Music, 1963; Allen and Stokoe, 1982), modifications to the apparatus to allow hollow specimens (Drnevich, 1967) (reduces strain variation in cross section), ability to test at large strains (Anderson and Stokoe, 1978) and testing at high confining stresses (Hardin et al., 1994; Laird, 1994), comparable to those necessary for hydrate stability. Modifications have also been made to extend the tests undertaken to allow torsional shear (Isenhower, 1980; Porovic, 1995). Improvements have been made to the testing procedures that have been adopted. Drnevich has contributed to this subject area extensively and has helped standardise the test procedure (Drnevich, 1978; Drnevich et al., 1978) and provided guidelines to ensure that the assumptions made during the reduction of data are valid during tests. Drnevich was also involved in the development of more complicated mathematical models for use in tests where certain basic assumptions are violated (Min et al., 1990; Ashmawy and Drnevich, 1994).

3.3 Dynamic properties of soils

The past forty years have also seen extensive research being undertaken to identify and quantify the parameters that affect the shear modulus and damping (attenuation) of soils (Hardin and Black, 1968; Seed and Idriss, 1970; Hardin and Drnevich, 1972b; Hardin, 1978; Anderson and Stokoe, 1978; Dobry and Vucetic, 1987). The shear modulus (G) and corresponding damping ratio of soils (D) are now known to be a function of numerous parameters:

$$G, D = f(\gamma_c, \sigma'_0, e, \mathrm{N}, S_r, \dot{\gamma}, OCR, \mathrm{C}, C_m, t) \tag{3.1}$$

where: γ_c = cyclic shear strain amplitude,

σ'_0 = mean effective principal stress,

e = void ratio,
N = number of loading cycles,
S_r = saturation ratio,
$\dot{\gamma}$ = strain rate (frequency of cyclic loading),
OCR = overconsolidation ratio,
C = grain characteristics,
C_m = natural cementation,
t = time.

3.3.1 *Factors affecting Shear Modulus*

Seed & Idriss (1970) compiled results obtained from a variety of laboratory testing procedures, which included triaxial compression, simple shear and the resonant column. They found that by plotting shear modulus, normalised by the small strain shear modulus, G_{max}, as a function of strain amplitude for sands, the stiffness of all soils fell within a narrow band, as shown in Figure 3.2. The very small strain shear modulus, G_{max} was obtained at a small strain amplitude of $3 \times 10^{-4}\%$.

It was shown that the modulus for sands is strongly dependent on

- mean effective principal stress, σ'_0;
- cyclic strain amplitude, γ_c;
- void ratio, e (relative density).

They therefore postulated that a simple equation could be used to relate shear modulus and confining pressure for sands, given as:

$$G = 6.92 K_2 (\sigma'_0)^{\frac{1}{2}} \tag{3.2}$$

where σ'_o is in kPa and K_2 is termed the soil modulus coefficient which relates the influence of void ratio and strain amplitude on shear modulus.

Figure 3.3 shows the importance of void ratio e in the relationship between K_2 and γ_c for sands with an effective vertical stress, σ'_V, = 143.7 kPa, $K_0 = 0.5$ (coefficient of lateral stress at rest) and $\phi' = 36^0$ (static strength

parameter in terms of effective stress). Figure 3.4 shows the variation in normalized shear modulus (G/G_{max}) versus log γ_c at different effective confining pressures (σ') for Leighton Buzzard sand tested by the author as part of this research programme, (G_{max} is taken as the value of G obtained from the linear portion of the graph, $\gamma_c < 10^{-3}\%$). This is the maximum value of shear modulus possible at a given effective stress. Results from Seed and Idriss (1970) show that K_2 varies from 30 for loose sands to 75 for dense sands while later work suggests values from 80-180 for dense gravels (Seed et al., 1986).

Hardin and Black (1968) derived Eq 3.3, subsequently confirmed by Hardin and Drnevich (1972a), to derive G_{max} for all soils with a void ratio less than 2.

$$G_{max} = 1230\frac{(2.973-e)^2}{(1+e)}(OCR)^k\sigma_o'^{\frac{1}{2}}, \tag{3.3}$$

where k is a function of the plasticity index (PI) and both σ_o' and G_{max} are in psi. Eq 3.3 was later adapted by Hardin (1978) to account for higher void ratios and to make the equation dimensionally correct:

$$G_{max} = \frac{A}{F(e)}(OCR)^k Pa^{1-m}\sigma_o'^m, \tag{3.4}$$

where: A = dimensionless stiffness coefficient;
m = stress component,
Pa = atmospheric pressure (same units as σ_0'),
k = parameter related to plasticity index,
σ_0' = mean effective stress,
F(e)= $0.3 + 0.7e^2$ (void ratio adjustment factor).

For most practical situations ($0.4 < e < 1.2$) Hardin suggests values of 625 and 0.5 for A and m respectively. Other researchers have defined different void ratio adjustment factors such as those employed by Shibuya and Tanaka (1996), Lo Presti et al. (1997) and Vrettos and Savidis (1999).

Eq 3.2 is an empirical formula based on the results of a number of laboratory and field tests. Hardin and Drnevich (1972a) proposed a modified

hyperbolic stress-strain relationship to evaluate shear modulus, G, at a cyclic shear strain γ_c. This was termed the 'backbone' curve and is given by:

$$\frac{G}{G_{max}} = \frac{1}{1+\gamma_h}, \tag{3.5}$$

where γ_h is the hyperbolic strain given by

$$\gamma_h = \frac{\gamma}{\gamma_r}[1 + ae^{-b(\frac{\gamma}{\gamma_r})}]. \tag{3.6}$$

γ_r = reference strain = τ_{max}/G_{max},
τ_{max} = shearing stress at failure (from triaxial tests),
a, b = -0.5, 0.16 for clean dry sands, respectively,
a, b = -0.2logN, 0.16 for clean saturated sands, respectively,
a, b = 1+0.25logN, 1.3 for cohesive soils, respectively,
N = number of cycles of loading.

As noted in Eq 3.1, a contributing factor to the shear modulus of soils is time (t). Work undertaken by Anderson and Stokoe (1978) identified two differing phases for the time dependent response of shear modulus for strain less than 0.001%. They classified an initial phase which was due to primary consolidation and a second phase which related to the linear increase in shear modulus with logarithm of time (of confinement), as shown in Figure 3.5. It was shown that fine grained soils exhibited both phases while coarse grained soils usually only exhibited the long term time effect.

Although all soils exhibit a time-dependent effect, the influence of this on the shear modulus of differing samples can be reduced by undertaking measurements at set times after the application of each load step. For cohesionless soils a time of 15mins has been found to be sufficient (Laird, 1994). Stokoe et al. (1999) tested fine grained soils 1000 minutes after the application of the load although for fine grained soils the amount of time required to allow primary consolidation to occur is a function of the soil under investigation and the consolidation process.

3.3.2 *Factors affecting damping ratio*

Studies into the factors affecting damping ratio, D, using the resonant column are not as extensive as those for G. In Eq 3.1 several factors were highlighted as having an effect on damping. It has been shown, using the resonant column, that D is strongly influenced by strain amplitude γ_c and confining stress σ'_0. Figure 3.6 highlights the range of values for D, measured for sands, by a variety of investigators as reported by Seeds and Idriss (1970). Figure 3.7 shows the damping ratios as a function of both effective confining pressure (σ') and cyclic shear strain (γ_c) for Leighton Buzzard sand tested by the author as part of this research programme with the range of values reported by Seed and Idriss (1970) shown for comparison. It can be seen that D reduces for increasing σ' and increases for increasing γ_c. As σ' increases, slippage at particle contacts is restricted thereby leading to a reduction in D, while at higher strains the shear stress at particle contacts is increased, leading to increased frictional losses. Apart from σ' and γ_c, which have a major effect, time of confinement (t), void ratio (e) have only a minor influence on D. The number of loading cycles (N)is important at high strain amplitudes but becomes less important as the induced strains become small.

It can be seen from Figure 3.6 and Figure 3.7 that below a certain strain amplitude the damping ratio is constant and is given the term, D_{min}. The transition from the 'elastic' response to the strain dependent response is termed the elastic threshold, γ_t^e, and occurs for strains less than 0.001% for the Leighton Buzzard sand tested. Therefore, measurements of damping, and also shear modulus, obtained at strains below 0.001% using the resonant column can be directly related to the measurements undertaken in seismic surveys since the values are a minimum and maximum respectively.

The damping that occurs below γ_t^e is thought to be the result of viscous dissipation of energy and not strain-dependent frictional losses (Winkler et al., 1979). Mavko and Nur (1979) developed a model for partially saturated rocks, showing that attenuation ($1/2D$) can be described by fluid flow in partially saturated cracks undergoing compression and dilation, which leads to stress induced fluid flow. This flow causes hysteretic shearing stresses

to develop in the fluid and therefore leads to viscous dissipation of mechanical energy. This flow mechanism, in geophysical literature (Mavko and Nur, 1979; Palmer and Traviola, 1980; Dvorkin et al., 1995) has been referred to as 'squirt flow' which implies a jet of water. Murphy (1982) suggested the term 'squish flow' as a less provocative term and described it as 'the compression of grain contacts and fine capillaries generates a local pore pressure field which drives dissipative fluid flow'. The model developed by Mavko and Nur (1979) suggests that attenuation increases monotonically, for both Q_E and Q_S, with increasing saturation and predicted that Q_K will be twice that of Q_S; the model also predicted that flat pores have a higher dissipative effect than equant pores. Work by Winkler and Nur (1979) on dry, partially saturated and fully saturated Berea sandstone supports this model for attenuation.

Work by Toksöz et al. (1979) showed that attenuation significantly reduced for frozen sandstones. However, the attenuation measurements made by Toksöz et al. (1979) were made at ultrasonic frequencies while measurements of attenuation on frozen soils by Al-Hunaidi et al. (1996), using the resonant column, showed that at seismic frequencies the attenuation value almost doubled. .

3.4 Theoretical considerations for the resonant column

The resonant column method utilizes the theory of elasticity and in particular the propagation of stress waves in a solid cylindrical rod to obtain the dynamic response. The specimen is idealized as an isotropic elastic medium and the equations of motion are developed from the assumption that the specimen obeys Hooke's Law; that is, the observed strains are proportional to the applied stresses.

Within a solid cylindrical bar, three independent types of waves can be propagated. These are termed *dilational* (longitudinal-compressional(V_{rod})), *distortional* (torsional-shear(V_s)) and flexural. The velocity of compressional and shear waves is governed by the wave equation (Eq 3.12) while flexu-

ral waves are dispersive and are therefore dependent on frequency of excitation (Kolsky, 1953). As the resonant column has been primarily used in torsion, the solution for torsional vibration is developed here. To measure the material damping in the resonant column the system is idealized as possessing a single degree of freedom, and two differing methods are available to obtain a solution.

3.4.1 *Equation for torsional vibration in a resonant column test*

The theory of torsional vibration of an elastic cylindrical rod was originated by the French mathematician C. A. de Coulomb (1736-1806) and further developed by T. Young (1773-1829)(Timoshenko, 1953). Let us consider a circular bar (Figure 3.8(a)) subject to torsional vibrations. At this point it is assumed in the following derivation that the rotation is small and each transverse section remains plain and rotates about its centre. Taking a small section of the bar of length dx (Figure 3.8(b)) at a distance x from the origin subject to a torque T which gives a corresponding rotation of θ; the torque and angle of rotation at a further distance of dx along the bar will be $T+(\partial T/\partial x)$dx and $\theta+(\partial\theta/\partial x)$ dx respectively. The equation for the angular motion of the section of bar can be derived by applying Newton's second law of motion:

$$-T + (T + \frac{\partial T}{\partial x})dx = \rho I_p dx \frac{\partial^2\theta}{\partial t^2} \tag{3.7}$$

or

$$\frac{\partial T}{\partial x} = \rho I_p \frac{\partial^2\theta}{\partial t^2}. \tag{3.8}$$

where: ρ = density of sample,
I_p = polar moment of inertia,
$\frac{\partial^2\theta}{\partial t^2}$ = angular acceleration.

For a linearly elastic circular bar the torque $T(x,t)$ acting on a cross-section of the bar at any time t is

$$T(x,t) = \int_A Gr^2 \frac{\partial\theta}{\partial x} \tag{3.9}$$

where: G = shear modulus,

r = radius of cross section,

$\frac{\partial\theta}{\partial x}$ = angle of twist per unit length.

Integrating Eq 3.9

$$T = GI_p\frac{\partial\theta}{\partial x}. \tag{3.10}$$

Differentiating Eq 3.10 with respect to x and substituting into Eq 3.8 gives

$$GI_p\frac{\partial^2\theta}{\partial x^2} = \rho I_p\frac{\partial^2\theta}{\partial t^2} \tag{3.11}$$

or

$$\frac{\partial^2\theta}{\partial t^2} = V_s^2\frac{\partial^2\theta}{\partial x^2} \tag{3.12}$$

where

$$V_s^2 = \frac{G}{\rho}. \tag{3.13}$$

V_S = shear wave velocity.

The wave equation (Eq 3.12) is a linear partial-differential equation (p.d.e.). There is no general solution for Eq 3.12, only particular ones, which consequently depend on the boundary conditions that apply to the specimen in a fixed-free resonant column. Therefore some function $\theta(x,t)$ must be found which satisfies the boundary conditions and reduces Eq 3.12 to an identity. A method that is commonly employed to solve p.d.e.s is the 'separation of variables'. This involves splitting the function $\theta(x,t)$ into two independent functions, each a function of x and t only

$$\theta(x,t) = F(x).H(t). \tag{3.14}$$

To find a solution to Eq 3.14 the equations for F(x) and H(t) are needed. If we substitute Eq 3.14 into Eq 3.12 then

$$\frac{\partial^2\theta}{\partial t^2} = \frac{\partial^2}{\partial t^2}[F(x).H(t)] = F(x).\frac{\partial^2 H(t)}{\partial t^2}$$

and

$$\frac{\partial^2\theta}{\partial x^2} = \frac{\partial^2}{\partial x^2}[F(x).H(t)] = \frac{\partial^2 F(x)}{\partial x^2}.H(t)$$

therefore

$$F(x).\frac{\partial^2 H}{\partial t^2} = V_s^2 \frac{\partial^2 F}{\partial x^2}.H(t). \tag{3.15}$$

Rearranging Eq 3.15 gives

$$\frac{1}{H(t)}.\frac{\partial^2 H}{\partial t^2} = \kappa = \frac{V_s^2}{F(x)}.\frac{\partial^2 F}{\partial x^2}, \tag{3.16}$$

where κ is an arbitrary constant. Both sides of Eq 3.16 are equal to the constant κ. Therefore Eq 3.16 can be expressed as two ordinary, second order, linear differential equations which are much easier to solve.

$$\frac{\partial^2 H(t)}{\partial t^2} - \kappa.H(t) = 0 \tag{3.17}$$

$$\frac{\partial^2 F(x)}{\partial x^2} - \frac{\kappa.F(x)}{V_s^2} = 0 \tag{3.18}$$

By trial and error it can be shown that κ must have a negative value otherwise the solution of F(x)= 0. From the general theory of 2nd order, linear, differential equations it can be shown that the solution to Eq 3.17 and 3.18 can be written as;

$$F(x) = C_1 \cos\frac{\omega_n x}{V_s} + C_2 \sin\frac{\omega_n x}{V_s} \tag{3.19}$$

$$H(t) = C_3 \cos\omega_n t + C_4 \sin\omega_n t \tag{3.20}$$

where ω_n is the natural frequency of vibration of the system and C_1, C_2, C_3 and C_4 are constants.

By substituting Eq 3.19 and Eq 3.20 into Eq 3.14 it can be seen that the solution to Eq 3.14 is:

$$\theta(x,t) = [C_1 \cos\frac{\omega_n x}{V_s}x + C_2 \sin\frac{\omega_n x}{V_s}][C_3 \cos\omega t + C_4 \sin\omega t]. \tag{3.21}$$

To find the particular solution to Eq 3.21 the appropriate boundary conditions relevant to the resonant column need to be applied. If we consider the fixed end where

$$\theta(0,t) = 0 \tag{3.22}$$

then applying this to Eq 3.19 and resolving, we can achieve a non-trivial answer when $C_1 = 0$. Therefore Eq 3.19 can be rewritten as

$$F(x) = C_2 \sin\frac{\omega_n x}{V_s} \tag{3.23}$$

and in turn Eq 3.21 can be written as

$$\theta(x,t) = C_2 \sin \frac{\omega_n x}{V_s}[C_3 \cos \omega t + C_4 \sin \omega t] \tag{3.24}$$

A sinusoidal torque is applied by the drive mechanism at the free end. If this is idealized as a rigid mass (Figure 3.1(a)), and considering Eq 3.10, the torque applied by the drive mechanism can be written as

$$(T)_{x=L} = I_0 \left(\frac{\partial^2 \theta}{\partial t^2} \right)_{x=L}. \tag{3.25}$$

where I_0 is the mass polar moment of inertia of the drive plate and L is the length of the specimen. If the R.H.S. of Eq 3.25 is evaluated from Eq 3.24 then

$$I_0 (\frac{\partial^2 \theta}{\partial t^2})_{x=L} = I_o \omega_n^2 \theta(x,t)_{x=L} \tag{3.26}$$

This torque, given by the R.H.S. of Eq 3.25, must be equal to that given by Eq 3.10, therefore

$$I_o \omega_n^2 \left(\theta(x,t)\right)_{x=L} = G I_p \frac{\partial \theta}{\partial x} \tag{3.27}$$

Evaluating Eq 3.27 using the general solution given by Eq 3.24 and cancelling through gives the particular solution

$$I_o \omega_n^2 \sin \frac{\omega_n L}{V_s} = \frac{G I_p \omega_n}{V_s} \cos \frac{\omega_n L}{V_s}. \tag{3.28}$$

Substituting $I/\rho h$ for I_p where I is the mass polar moment of inertia for the specimen and rearranging gives

$$\frac{I}{I_0} = \beta \tan \beta, \tag{3.29}$$

where

$$\beta = \frac{\omega_n L}{V_s}. \tag{3.30}$$

Eq 3.29 and Eq 3.30 are the basic equations for the fixed-free resonant column. Once V_s is obtained, then rearrangement of Eq 3.13 can be used to derive G. Of the terms expressed in Eq 3.29, only ω_n is not a function of the geometric properties of the specimen. The resonant frequency that is measured in the resonant column is the damped natural frequency (ω_d) but is sufficiently close to ω_n so not give give significant error (see Section 3.5.2).

3.5 Damping in a single degree of freedom system

The theory for material damping in the resonant column is based on the assumption that the vibrating system can be idealized as a single-degree-of-freedom system (the position of any part of the system can be described by just one variable at any point in time) subject to viscous damping (Figure 3.9).

The equation of motion for the system shown in Figure 3.9 can be written as

$$I\ddot{\theta} + c\dot{\theta} + \mathrm{k}\theta = \mathrm{F(t)}, \tag{3.31}$$

where: θ = rotational displacement from equilibrium position
$\dot{\theta}$ = rotational velocity,
$\ddot{\theta}$ = rotational acceleration,
I = mass polar moment of inertia of system,
k = stiffness of spring,
c = damping constant,
F(t) = driving force.

The solution to Eq 3.31 depends on the function F(t).

3.5.1 *Damping during harmonic excitation*

If the function F(t) from Eq 3.31 is a harmonic force, $\mathrm{F}_0 \sin\omega t$ (= force applied by drive mechanism), then the particular solution to the equation is a steady state oscillation with a circular frequency equal to ω. The solution can be assumed to be of the form

$$\theta = \mathrm{X}_0 \sin(\omega t - \phi), \tag{3.32}$$

where X_0 is the amplitude of vibration and ϕ is the phase angle between the displacement of the system and the applied harmonic force. If Eq 3.32

is substituted into Eq 3.31 then X_0 and ϕ can be found and expressed in non-dimensional form as (Thompson, 1988):

$$\frac{X_0 \mathrm{k}}{F_0} = \frac{1}{\sqrt{[1-(\frac{\omega}{\omega_n})^2]^2 + [2D(\frac{\omega}{\omega_n})]^2}}, \tag{3.33}$$

$$\tan\phi = \frac{2D(\frac{\omega}{\omega_n})}{1-(\frac{\omega}{\omega_n})^2}, \tag{3.34}$$

where: $\omega_n = \sqrt{\frac{\mathrm{k}}{I}}$ = natural frequency of vibration,
D $= \frac{c}{c_c}$ = damping coefficient,
$c_c = 2I\omega_n$ = critical damping.

These equations show that $X_0\mathrm{k}/F_0$ and ϕ depend only on the ratio between the excitation frequency, the natural frequency of the system, and on the damping coefficient, D. These equations are shown graphically in Figure 3.10.

From Figure 3.10 it can be seen that as the frequency of excitation approaches the natural frequency of the system, a condition, termed resonance, occurs. At resonance the amplitude of vibration is inversely proportional to damping factor (D). Also, the frequency of excitation approaches the natural frequency of vibration at resonance when D approaches 0. For soils with γ_c less than 0.01%, material damping is less than 10% (Seed et al., 1986; Vucetic and Dobry, 1991). Therefore, it can be inferred that at low strain the applied frequency of excitation (ω) approximates the natural frequency of vibration of the specimen at resonance (ω_n) and with a phase difference between the two of 90^0. This result suggests two differing methods for estimating the natural frequency of vibration of the system by monitoring;

1. The amplitude of vibration of the specimen through a range of frequencies, at constant amplitude. The frequency at peak amplitude will equate to the natural frequency of the specimen (for soils at low strain and damping).

2. The phase angle between the excitation force amplitude and the strain amplitude response of the system. The natural frequency occurs when the phase angle is 90^0.

Although a continuous dynamic system (test specimen) has a multitude of resonant frequencies, the fundamental frequency ω_n produces the maximum system amplitude at resonance for a given force and so it is easily identifiable when a sweep of frequencies is applied.

The material damping for the specimen during forced vibration can be estimated by considering the strain amplitude frequency response curve generated during a test as shown in Figure 3.11. This is the response curve for a pluviated specimen of Leighton Buzzard sand tested by the author. At resonance when $\omega/\omega_n = 1$, the peak amplitude $X_{max} = (F_0/\mathrm{k})/2D$. By choosing frequencies either side of the natural frequency, where their amplitude is $0.707X_{max}$ (half power points), and letting $X = 0.707X_{max}$ in Eq 3.33, it can be shown (Thompson, 1988)

$$D = \frac{f_2 - f_1}{2f_r}, \tag{3.35}$$

where f_2 and f_1 are frequencies either side of resonant frequency (f_r), corresponding to $0.707X_{max}$.

3.5.2 *Free vibration decay*

If F(t) is set to zero then the system is vibrating freely (i.e. after the power to the drive mechanism is shut off at the resonant frequency). Three solutions to the homogeneous differential equation, Eq 3.31, are possible depending on the relationship between c, k and I (Thompson, 1988). If $D > 1$ the system is termed overdamped and no oscillations occur (Figure 3.12(a)). If $D = 1$ then the system is critically damped (Figure 3.12(b)) and it is underdamped if $D < 1$ (Figure 3.12(c)). All soils exhibit underdamping (Lodde, 1982) and the solution to Eq 3.31 gives

$$\theta = e^{-\omega_n Dt}(A \sin \omega_n t\sqrt{1 - \mathrm{D}^2} + B \cos \omega_n t\sqrt{1 - D^2}), \tag{3.36}$$

where A and B are arbitrary constants.

It can be seen from Figure 3.12(c) (graphical representation of Eq 3.36) that the motion of an underdamped single-degree-of-freedom system is oscillatory with an exponential decay. It can be seen from Eq 3.36 that the

damped circular frequency for free vibration, ω_d, in terms of the natural circular frequency of an undamped system, ω_n, can be expressed as;

$$\omega_d = \omega_n \sqrt{1 - D^2}. \tag{3.37}$$

This suggests that at low strains ω_d is within 1% of ω_n. Therefore, in the resonant column method ω_d can be equated to ω_n without any significant error.

The material damping from the resonant column, using free vibration, is obtained by considering the peak amplitude of successive vibrations as the sample oscillates freely as shown in Figure 3.12(c). By evaluating Eq 3.36 at time t_1 and t_2 (which corresponds to θ_1 and θ_2) it can shown that ratio of the amplitude at successive peaks θ_1, θ_2 is given by

$$\frac{\theta_1}{\theta_2} = e^{\frac{2\pi D}{\sqrt{1-D^2}}}. \tag{3.38}$$

By taking the natural logarithm of both sides of Eq 3.38 it can be rewritten as;

$$\delta = ln\frac{\theta_1}{\theta_2} = \frac{2\pi D}{\sqrt{1 - D^2}}, \tag{3.39}$$

where δ is termed the *logarithmic decrement.*

Rearranging

$$D = \sqrt{\frac{\delta^2}{4\pi^2 + \delta^2}}. \tag{3.40}$$

It can also be seen from Figure 3.12(c) that the decay in the amplitude of vibration of any two successive peaks is a constant ratio. Therefore δ can be found from any two peak amplitudes θ_n and θ_{n+1} from the relationship (Richart et al., 1970):

$$\delta = \frac{1}{n-1} ln\frac{\theta_n}{\theta_{n+1}}. \tag{3.41}$$

Figure 3.13 shows a typical free vibration curve obtained with the resonant column for pluviated specimens of Leighton Buzzard sand. The value for δ is usually found from plotting the peak amplitude of each cycle on a logarithmic scale against the cycle number on an arithmetic scale as shown in Figure 3.14. This procedure can also be used to verify the assumption that

the damping is viscous as defined in Eq 3.31, since the locus of points plotted should fall on a straight line if the damping is viscous.

The free vibration method for determining damping can be influenced by background noise during data acquisition at low strains. However, as the strain applied to the specimen increases during a resonant column test, the frequency response curve becomes less symmetrical about the resonant frequency and can introduce errors into the determination of D. Therefore, the two methods described above allow independent determination of D.

Although the emphasis for the measurement of damping has been on torsional vibration, the governing equations are valid for any mode of vibration which can be described as a single degree of freedom system.

3.5.3 *Attenuation parameters and their relationships*

Various parameters can be used to express the attenuative properties of soils. In the field of geotechnical engineering the measure of attenuation generally used is the damping ratio, D. However, in geophysical sciences the measure of attenuation is normally given by either the logarithmic decrement δ, or more usually by the quality factor Q, or even its inverse Q^{-1} (Q is defined as the ratio between stored energy and dissipated energy). These are related to each other by:

$$\frac{1}{Q} = \frac{\delta}{\pi} = 2D. \tag{3.42}$$

It is also worth noting that different attenuation values are obtained for different measurement techniques. Therefore, dynamic methods using the resonant column can measure shear wave attenuation Q_S^{-1}, while extensional (and flexural) excitation can provide values for Q_E^{-1} (anelasticity of the Young's modulus, Johnson and Toksoz, 1981), whereas seismic surveys provide compressional P-wave attenuation Q_P^{-1}. Also, the bulk compressional attenuation, Q_K^{-1}, (derived from hydrostatic stress and dilational strain measurements) can help evaluate attenuation mechanisms.

These can be related to each other by the following relationships (Winkler

and Nur, 1979);

$$\begin{aligned} \frac{(1-\nu)(1-2\nu)}{Q_p} &= \frac{(1+\nu)}{Q_E} - \frac{2\nu(2-\nu)}{Q_S}, \\ \frac{3}{Q_E} &= \frac{(1-2\nu)}{Q_K} + \frac{2(\nu+1)}{Q_S}, \\ \frac{1+\nu}{Q_K} &= \frac{3(1-\nu)}{Q_P} - \frac{2(1-2\nu)}{Q_S}, \end{aligned} \tag{3.43}$$

where ν is Poisson's ratio. For these equations to be valid it is assumed that the soil is isotropic.

Winkler and Nur (1979) also showed that one of the following relationships must hold true for attenuation in soils and rocks:

$$\begin{aligned} & Q_S > Q_E > Q_P > Q_K \\ \text{or} \quad & Q_S < Q_E < Q_P < Q_K \\ \text{or} \quad & Q_S = Q_E = Q_P = Q_K \end{aligned}$$

3.6 Measurement of Young's Modulus

In the previous sections, discussion was restricted to the use of the resonant column in torsional mode, as this had been extensively researched and reported in the literature. The use of the resonant column to measure the Young's Modulus (E) of soils has been mainly ignored in geotechnical work, although it has long been recognised that the comparison of both V_p and V_s, and their associated attenuation measurements, Q_p^{-1} and Q_s^{-1} is a useful aid in the lithological and stratigraphical characterisation of soils (Dutta, 1987; Eastwood and Castagna, 1987). This has led recent researchers to explore wave parameters in multi-modal vibrations. Cascante et al. (1998) adapted a standard 'Stokoe' torsional resonant column to allow flexural excitation of a specimen from which E could be measured and subsequently V_p and Q_p^{-1} could be computed.

3.6.1 *Flexural Vibration*

In a standard 'Stokoe' resonant column four pairs of coils are connected in series so that a net torque is applied to the sample (Figure 3.15). In Cas-

cante's modified version, the coils are reconnected so that only two magnets are used producing a horizontal force to the specimen and inducing flexural excitation. This allows the same coil and magnet arrangement to be used in both flexural and torsional vibration. Flexural vibration produces a frequency dependent dispersive wave. Unlike for torsional data, the reduction of flexural data does not measure the wave velocity but uses 'Rayleigh's energy method' to compute the fundamental resonant frequency of the system from which the longitudinal wave velocity can be computed.

In the reduction of data for flexural excitation, the specimen and drive mechanism shown in Figure 3.16 can be idealized as an elastic column with a rigid point mass at its free end as depicted in Figure 3.17. As the behaviour of the system is assumed elastic, this implies that no energy is lost in the system and the total energy is constant. This is the basic premise that allows the application of 'Rayleigh's energy method'. Rayleigh's method equates the maximum internal potential energy J_U to the maximum kinetic energy J_T

$$J_T = J_U. \tag{3.44}$$

These energies are computed from an assumed displacement shape for the resonant column. Cascante et al. (1996) assumed the displacement of a cantilevered beam y, at an elevation x, to be in the of a third order polynomial:

$$y(x) = a_0 + a_1 x + a_2 x^2 + a_3 x^3. \tag{3.45}$$

where a_0, a_1, a_2 and a_3 are constants By considering the boundary conditions at the base where deflections $y(0) = 0$, and the tangent $y'(0) = 0$ it can shown that $a_0 = 0$ and $a_1 = 0$. By assuming there is no moment at the free end caused by the rigid point mass $x = L$, $EIy''(L) = 0$ and

$$y''(L) = 2a_2 + 6a_3 L. \tag{3.46}$$

For a non trivial answer, $y''(L) = 0$, therefore $a_2 = a_3/3L$. Substituting into Eq 3.45 and rearranging:

$$y(x) = \alpha x^2[3\mathrm{L} - x] \quad for \quad x < \mathrm{L}, \tag{3.47}$$

where α is a constant given by $\alpha = (a^2/3\mathrm{L})$. J_U of the system is found by considering the strain energy stored in the specimen. In theory this should

include the bending and shear strain energy. However, in the following derivation for J_U (Cascante, 1996), only the bending strain energy is considered and the shear strain energy is disregarded, as it is assumed to be only a few percent of the bending strain energy (Gere and Timoshenko, 1991). The strain energy of a beam in bending is given by

$$J_U = \frac{1}{2} E I_b \int_0^L y''(x)^2 dx \tag{3.48}$$

where E is the Young's Modulus, and I_b is the 2nd area moment of inertia of the beam. Substituting Eq 3.47 into Eq 3.48 and solving:

$$J_U = 6 E I_b \alpha^2 L^3. \tag{3.49}$$

To derive J_T, the value for both the specimen and the added masses need to be computed. The value for the specimen (J_S) is computed from

$$J_s = \frac{1}{2} \rho \omega_f^2 \mathrm{A} \int_0^L y(x)^2 dx. \tag{3.50}$$

Therefore substituting Eq 3.47 into Eq 3.50 and solving gives

$$J_s = \frac{33}{70} \omega_f^2 \alpha^2 L^6 m_T \tag{3.51}$$

where m_T is the mass of the specimen ($= \rho \mathrm{A} L$, where ρ is the density, and A the area of the specimen) and ω_f^2 is the resonant frequency in flexure. To compute the value for the rigid mass (J_a), the additional horizontal displacement of the mass above the specimen needs to be considered (Fig 3.17). The deflection at $y(L)$ can be found from Eq 3.47 which gives

$$y(L) = \alpha L^2 (2L). \tag{3.52}$$

The slope between any two points along the the deflected specimen is given by differentiation of Eq 3.47,

$$y'(x) = 2\alpha x(3L - x) - \alpha x^2. \tag{3.53}$$

The slope at the end of the specimen, y(L) is therefore

$$y'(L) = 3\alpha L^2. \tag{3.54}$$

The additional deflection, dy, is then given as

$$dy = 3\alpha L^2(x - L). \tag{3.55}$$

The total deflection is then given by the addition of Eq 3.52 and Eq 3.55 which leads to

$$y + dy = \alpha L^2 \left[2L + 3(x - L)\right]. \tag{3.56}$$

The value of J_a, for a rigid mass at a distance h above the specimen can be evaluated by substituting Eq 3.56 into Eq 3.50, where $h = (x - L)$, and solving to give

$$J_a = m\alpha^2 L^6 \left[2 + 6\frac{h}{L} + \frac{9}{2}\left(\frac{h}{L}\right)^2\right]. \tag{3.57}$$

Finally, the resonant frequency can be computed by equating J_U and J_T $(J_s + J_a)$ and solving for ω_f to give

$$\omega_f^2 = \frac{3EI_b}{\left\{\frac{33}{140}m_T + m\left[1 + 3\frac{h}{L} + \frac{9}{4}\left(\frac{h}{L}\right)^2\right]\right\}L^3}. \tag{3.58}$$

Eq 3.58 is exact for a rigid point mass. This can be extended for N masses whose masses, m_i are uniformly distributed between $h0_i$ and $h1_i$ when measured from the top of the sample (Figure 3.16). Therefore Eq 3.58 can be rewritten

$$\omega_f^2 = \frac{3EI_p}{\left[\frac{33}{140}m_T + \sum_{i=1}^{N} m_i h(h0_i, h1_i)\right]L^3}, \tag{3.59}$$

where

$$h(h0_i, h1_i) = 1 + \frac{3(h1_i + h0_i)}{2L} + \frac{3}{4}\frac{(h1_i^2 + h1_i h0_i + h0_i^2)}{L^2}. \tag{3.60}$$

Eq 3.60 allows the Young's modulus for flexural excitation, E_{flex}, to be estimated based on the geometric properties of the specimen and apparatus, and the measurement of the circular frequency of flexural vibration (using the technique described for torsion). The derivation of this equation is based on engineers beam formula and some assumptions are made with regard to assumed deflected shape, no bending moment or shear flow at the free end. The implications for these assumptions are investigated in Section 4.4.2.

The form of the equation for longitudinal wave velocity in a bounded medium, V_{lf}, is identical to Eq 3.13 with E_{flex} replacing G and V_{lf} replacing V_s. Therefore,

$$V_{lf} = \sqrt{\frac{E_{flex}}{\rho}}. \tag{3.61}$$

The relationship between the body P-wave velocity, V_p, (in an infinite medium) and V_{lf} for a bounded single phase isotropic medium is given by

$$V_p = V_{lf}\sqrt{\frac{1-\nu}{(1+\nu)(1-2\nu)}}, \tag{3.62}$$

where Poisson's ratio, ν can be found (again assuming the soil is isotropic) from,

$$\nu = \frac{1}{2}\frac{V_{lf}^2}{V_s^2} - 1. \tag{3.63}$$

The relationship between V_p and V_{lf} for a two-phase material (water-saturated) is discussed in Section 6.3.3.

As the flexural excitation can be described by a single-degree-of-freedom system, the methods previously described for measuring attenuation can be employed. In flexural excitation the attenuation is related to the inelasticity of the Young's Modulus and provides measurements of Q_E^{-1}. The attenuation value Q_P^{-1} can then be derived from the relationships defined in Eq 3.43 (assuming the material is isotropic).

3.6.2 *Anisotropy*

In the this chapter the behaviour of soils using the resonant column, and the derivation of the constitutive equations governing the use of the resonant column, have been discussed with the assumption that the soil behaves as an isotropic material. However it has been recognised that the small strain stiffness of soils is cross anisotropic, that is $G_v \neq G_h$ and $E_v \neq E_h$, where the subscript v and h relate to the vertical and horizontal direction in which the measurements are made. This elastic anisotropy can be categorized as inherent anisotropy and stress-induced anisotropy. Inherent anisotropy is that which develops during deposition of the material due to particles becoming aligned with the plane of deposition (Powrie, 1997). The degree of anisotropy

is greater in clay rich soils (flat particles) than in sands (round particles). Stress induced anisotropy occurs when an anisotropic loading is applied to the soil. It has been shown that for sands the degree of anisotropy is low when subjected to an isotropic stress at small strains (Kuwano and Jardine, 2002; Tatsuoka and Kohata, 1995) but increases as the strain increases and the loading conditions become anisotropic (Bellotti et al., 1996; Kuwano and Jardine, 2002).

The effect of cross anisotropy is that the isotropic relationship between E, G and ν are no longer strictly valid and additional elastic constants are required. However, these additional constants cannot be measured in the standard resonant column. Since the standard resonant column only applies an isotropic stress and the applied strain are low, the inherent anisotropy is assumed to be low and ignored. Therefore the derived values for ν and its influence on differing attenuation parameters as previously described may not be totally valid and should be viewed with caution.

3.7 Strain amplitude measurements

3.7.1 *Introduction*

It has been shown (Section 3.3.1) that strain amplitude has a major influence on the shear modulus of soils and therefore by association that of Young's Modulus. This section describes the two differing methods of measuring the strain amplitude for torsional and flexural vibrations.

3.7.2 *Torsional strain*

In torsional vibration the cyclic shear strain, γ_c, applied to the sample is calculated from the maximum rotation that the specimen is subjected to during each applied cycle. In a specimen subjected to pure torsion (Figure 3.8(a)) the strain can be defined as:

$$\gamma = \frac{R.\theta}{L}, \tag{3.64}$$

where θ is the angle of rotation in radians, and R is the radius of the specimen.

It can also be seen from Figure 3.8(a) that the magnitude of shear strain varies from zero at the axis of rotation to a maximum value at its outer surface. Drnevich et al. (1978) suggest that the value for average strain in the specimen be taken at the point where R is equal to two-thirds the radius of the specimen. Analytical studies, however, have shown that for a solid specimen in the resonant column a value of 0.8R should be taken as point where average strain occurs (Chen et al., 1979). Therefore the average strain can be found by using a value of 0.8R in Eq 3.64 to give

$$\gamma = \frac{0.8R.\theta}{L}, \tag{3.65}$$

The angle of rotation in the resonant column is calculated from the resonant frequency, the maximum acceleration of the drive system and specimen geometry. The acceleration of the drive system is measured by the accelerometer mounted on the drive system. The accelerometer generates a high impedance charge signal, proportional to the imposed acceleration, which requires conditioning to a low impedance voltage suitable for measurement. This is achieved by a charge amplifier. The charge amplifier used in this research had a transducer sensitivity control that allows the sensitivity of an accelerometer[1] to be set on the charge amplifier so that a 5 volt peak to peak output is achieved for the given input excitation that is indicated on the range control. The transducer sensitivity control can be locked, once set, to prevent the accidental changing of the sensitivity scale. The range control buttons allow a range gain of 1, 10, 100g (where g is the gravitational acceleration at the earth's surface) and can be set depending on the input excitation. In tests that were performed at low strain, a gain setting of 1 was found to be sufficient.

With the charge amplifier adjusted, its output can be used determine the acceleration of the accelerometer, *ac*. The acquired output voltage from the accelerometer is acquired by a computer and converted to *rms* voltage (this helps to smooth spikes in the acquired readings). To convert back to peak output voltage the peak *rms* voltage is multiplied by $\sqrt{2}$. As the amplifier is set to give 5 volts peak to peak output for +/- 1g, the peak output is divided

[1]The accelerometer used in this research had a sensitivity of 62.7pC$_{Peak}$/g$_{Peak}$

by 5/2 to give volts per g. Finally to convert the peak output per g to ms^{-2} the peak output is multiplied by 9.81. Therefore;

$$ac = 5.594 V ms^{-2}, \tag{3.66}$$

where V is the peak rms voltage output from the charge amplifier.

The displacement of the accelerometer, y_{meas} is related to the angular acceleration by

$$ac = \omega^2 y_{meas}, \tag{3.67}$$

where $\omega = 2\pi f$ and f is the resonant frequency.

Therefore the maximum displacement of the accelerometer at resonance is

$$y_{meas} = \frac{5.594V}{4\pi^2 f^2} = 0.141 V/f^2. \tag{3.68}$$

From simple geometry it can be seen that the angle of rotation of the sample, θ (see Figure 3.8(a)) is related to the displacement of the accelerometer and the distance that the accelerometer is offset from the axis of rotation,l, by $\theta = x/l$. Therefore,

$$\theta = \frac{0.141V}{0.03625 f^2} = 3.89 V/f^2, \tag{3.69}$$

where 0.03625 is the offset of accelerometer from the axis of rotation (in metres) used in this research (new GHRC, Chapter 4).

Finally, using Eq 3.65 and considering the specimen geometry, γ_c can be found from

$$\gamma_c = 0.8 R\theta/L = 1.56 Vd/f^2 L, \tag{3.70}$$

where: d = diameter of sample,
L = length of sample.

3.7.3 *Flexural strain*

In flexural excitation the axial strain imposed on a specimen is directly related to the shape of the deflection curve, y(x) formed when the specimen is under load. Using the theory of elasticity it can be shown that the strain in

a beam subject to pure bending at an elevation x and a distance r from the neutral plane in the y-direction (Figure 3.17) is

$$\varepsilon = \frac{d^2y}{dx^2} \cdot r = 6 \cdot \alpha(L - x) \cdot r \tag{3.71}$$

Therefore the average strain for a cylindrical column of radius R and volume V_0 can be determined by summing all the strains in the beam along its length and cross section. In bending of a circular beam the strains above the neutral axis of the beam are positive and those below are negative. Therefore, the average strain in either the side in compression or in tension can be defined as,

$$\varepsilon_{avg} = \frac{2}{V_0} \int_{V_0/2} \varepsilon \cdot dA \cdot dx. \tag{3.72}$$

This can be written as a multiple integral with constant limits by expressing dA in terms of dr (dA=$2\sqrt{R^2 - r^2}dr$), therefore Equation 3.72 can be rewritten as

$$\varepsilon_{avg} = \frac{2}{V_0} \int_0^L \int_0^R 6 \cdot \alpha(l - x) \cdot r \cdot \left(2\sqrt{R^2 - r^2} \cdot dr\right) \cdot dx. \tag{3.73}$$

Integrating with respect to x, and then with respect to r, the solution to Equation 3.73 is

$$\varepsilon_{avg} = \frac{4}{\pi} \cdot R \cdot L \cdot \alpha. \tag{3.74}$$

The maximum strain at the base of the specimen, at its outer edge, can be found by setting $x = 0$ and r=R in Equation 3.71 to give

$$\varepsilon_{max} = 6 \cdot \alpha \cdot L \cdot r. \tag{3.75}$$

By rearranging Equation 3.75 in terms of α and substituting into Equation 3.74, ϵ_{avg} can be related to ϵ_{max} by

$$\varepsilon_{avg} = \frac{2}{3\pi}\epsilon_{max}. \tag{3.76}$$

The value of α is calculated by rearranging Equation 3.56 using the maximum displacement of the accelerometer, y_{meas} (using the value given in Equation 3.68) and its elevation, x from the base of the specimen, such that

$$\alpha = \frac{0.141 \cdot V}{f^2 \cdot L^2 \left[2L + 3(x - L)\right]}. \tag{3.77}$$

The average strain on the sample can then be defined in terms of the measured voltage by substituting Equation 3.77 into Equation 3.74 to give

$$\varepsilon_{avg} = \frac{0.18V \cdot R}{f^2 \cdot L \left[2L + 3(x - L)\right]}. \tag{3.78}$$

3.8 Summary

It can be seen from the the preceding discussion in this chapter that the resonant column is a popular and well used piece of laboratory apparatus for measuring the dynamic properties of soils. Research has focused on dynamic shear measurements and have shown that the shear modulus and damping are mainly influenced by strain rate and confining pressure with void ratio, time of confinement and number of stress cycles also contributing, although to a much lesser degree.

It has been shown that during testing, using induced strain below the elastic threshold, the dynamic properties are considered to be elastic and as such the test is deemed non-destructive. The theoretical discussions have shown that a simple test procedure can be adopted which allows system resonance to be measured, from which G and D can be computed. The wave propagation velocity in a resonant column is a function of the resonant frequency of the specimen and can range from 50-300Hz depending on confining pressure and stiffness of the specimen (Laird, 1994; Hardin et al., 1994; Avramidis and Saxena, 1990). This is within the range of frequencies that are used for geophysical surveys of ocean bottom sediments.

Finally, simple modifications to the resonant column have been outlined that will allow V_p as well as V_s, and their corresponding attenuation (Q_P^{-1} and Q_S^{-1}), to be measured during a single test.

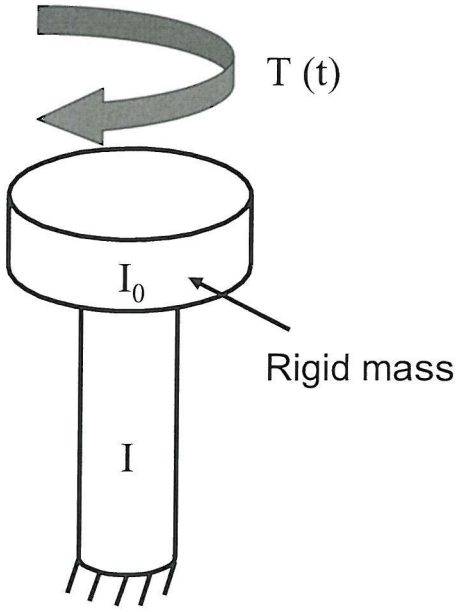

(a) Idealised model of fixed-free resonant column.

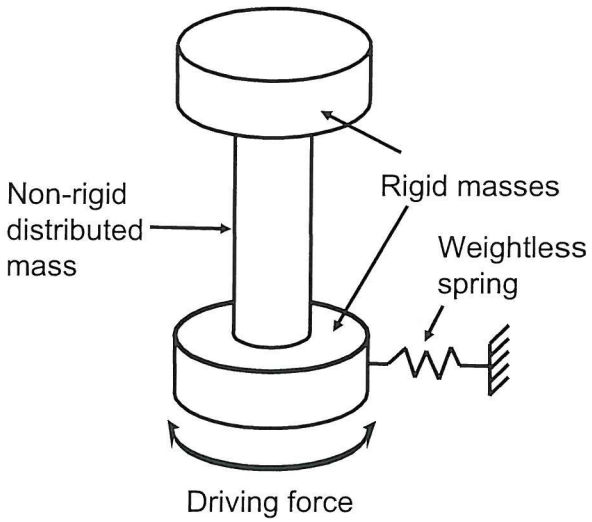

(b) Idealised model of spring base resonant column.

Figure 3.1: Idealised models for the resonant column.

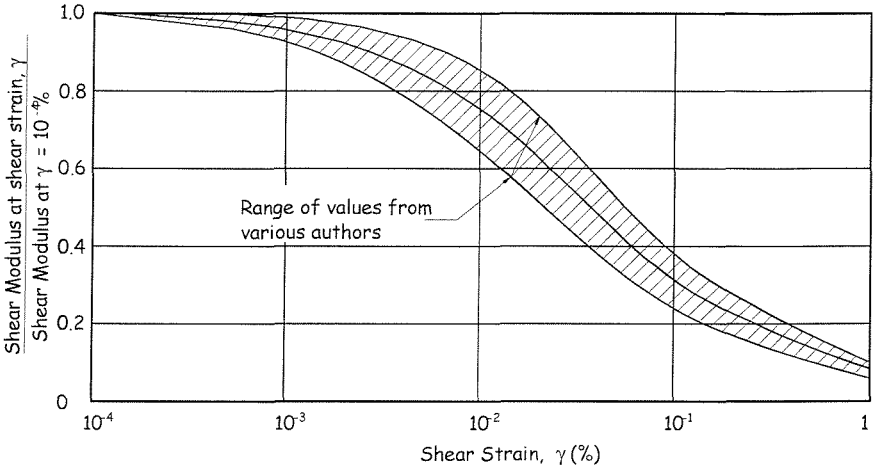

Figure 3.2: *Variation of shear modulus with shear strain for sands. Redrawn from Seed and Idriss (1970).*

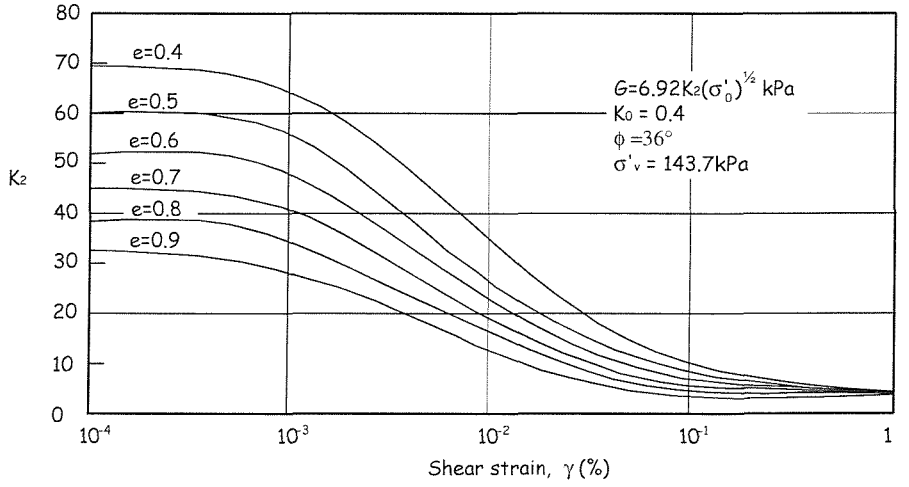

Figure 3.3: *Influence of void ratio, e on shear moduli of sands. Redrawn from Seed and Idriss (1970).*

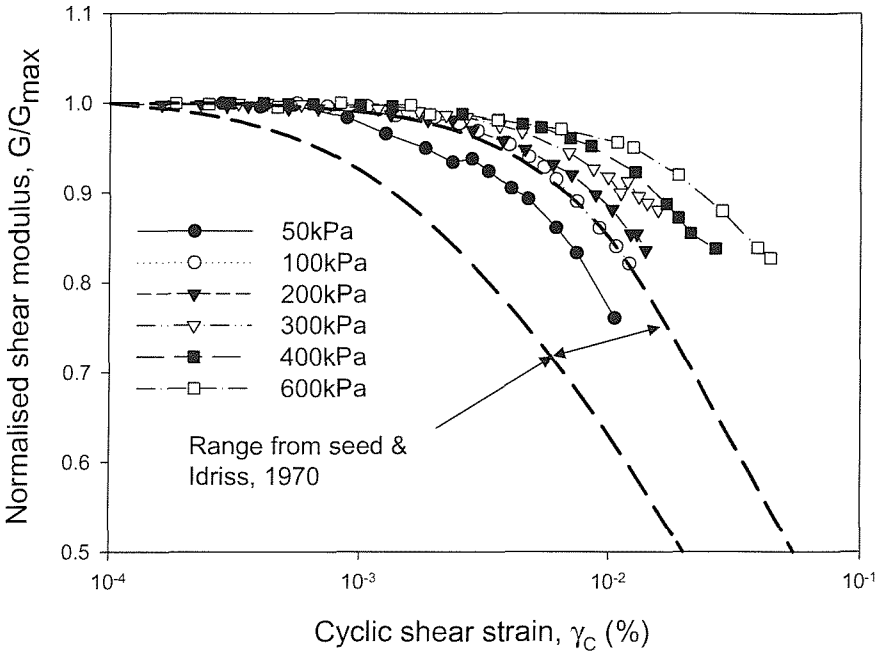

Figure 3.4: *Variation in normalised shear modulus of Leighton Buzzard sand with shearing strain at different effective confining pressures in the resonant column.*

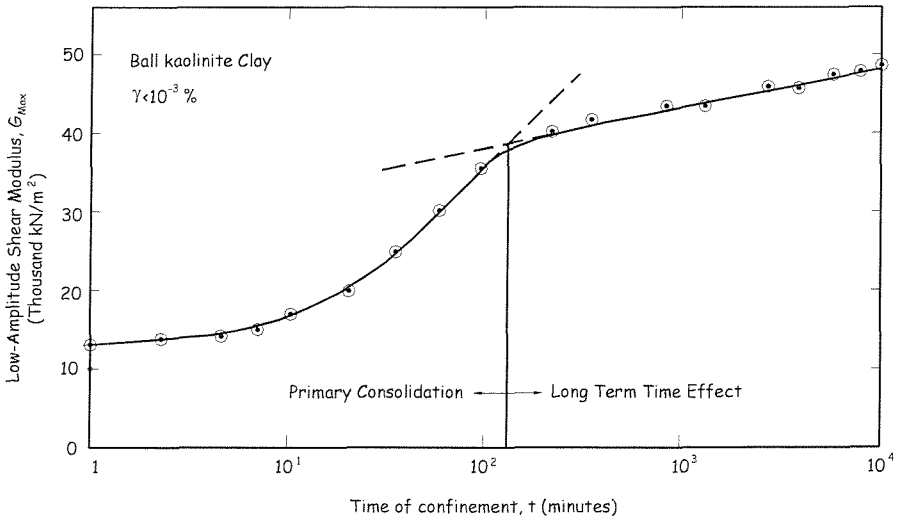

Figure 3.5: *Variation in shear modulus with time of confinement. Redrawn from Anderson and Stokoe (1978).*

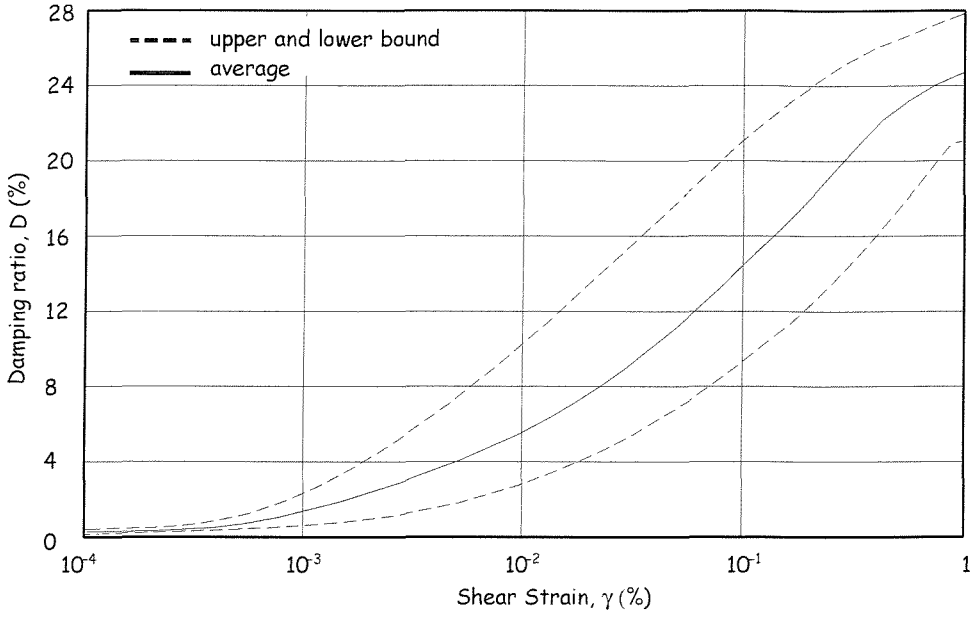

Figure 3.6: *Range of damping ratios measured for sands by a variety of investigators. Modified from Seed and Idriss (1970).*

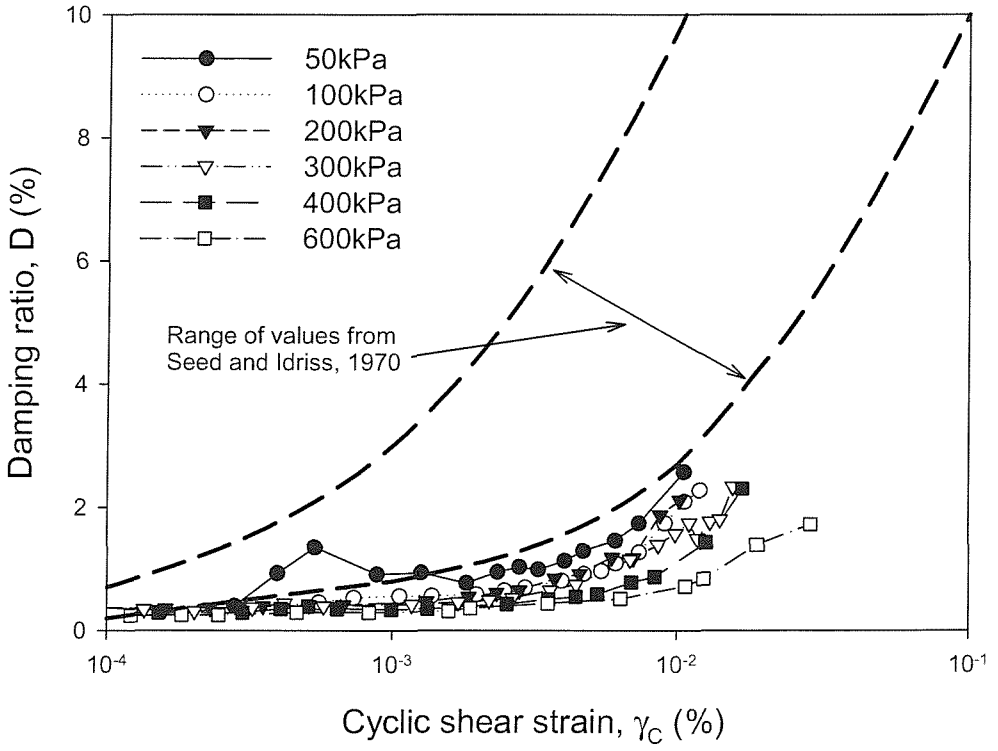

Figure 3.7: *Influence of confining pressure and strain on damping ratio of dry pluviated Leighton Buzzard sands at differing effective confining pressures in the resonant column.*

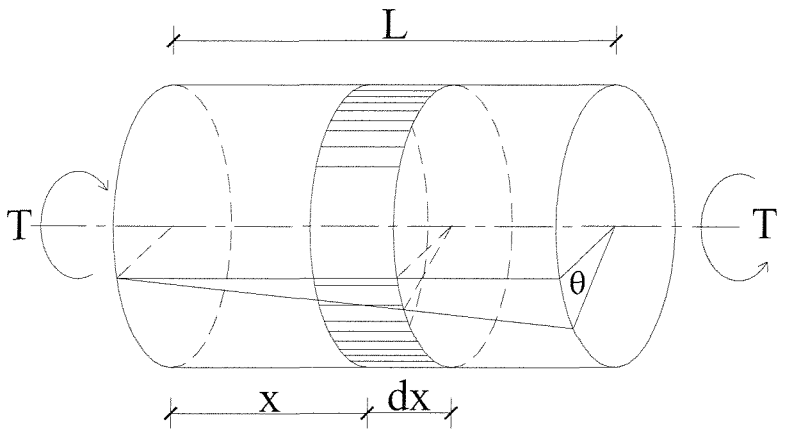

(a) Circular bar in pure torsion.

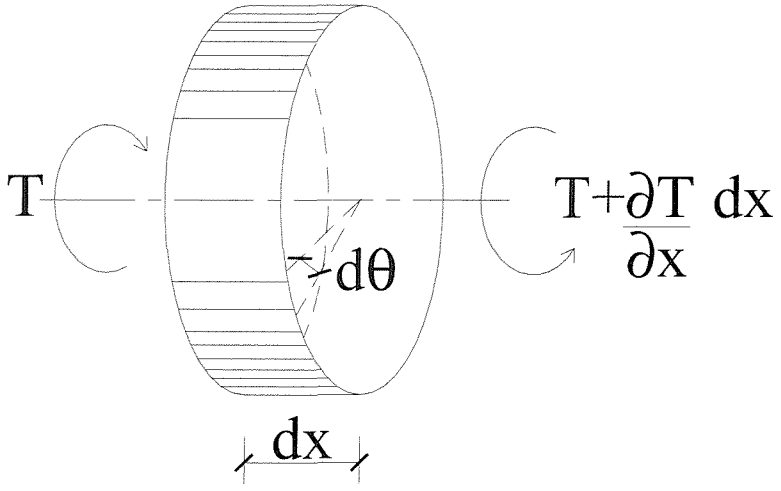

(b) Section of bar.

Figure 3.8: *Diagrammatic view of bars subject to torsion.*

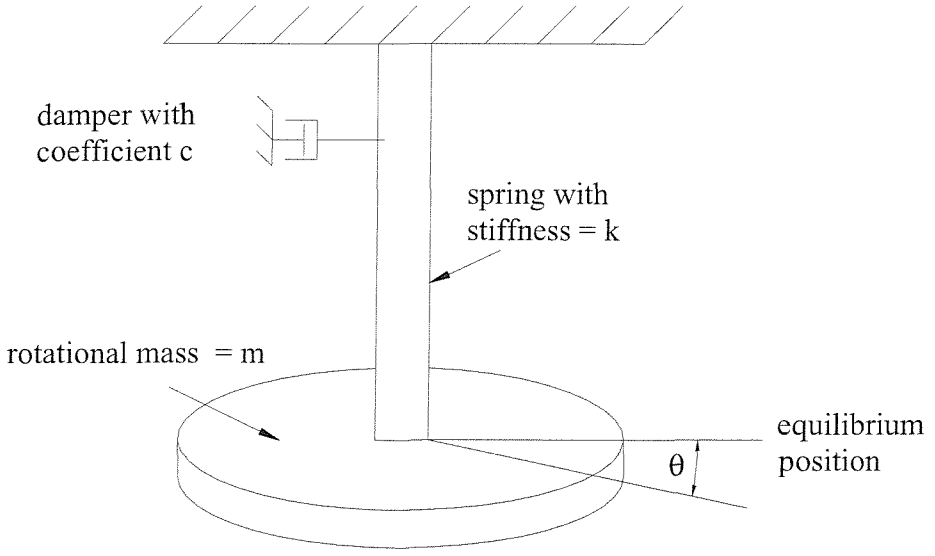

Figure 3.9: *Idealized model of a visco-elastic, single-degree-of-freedom, system.*

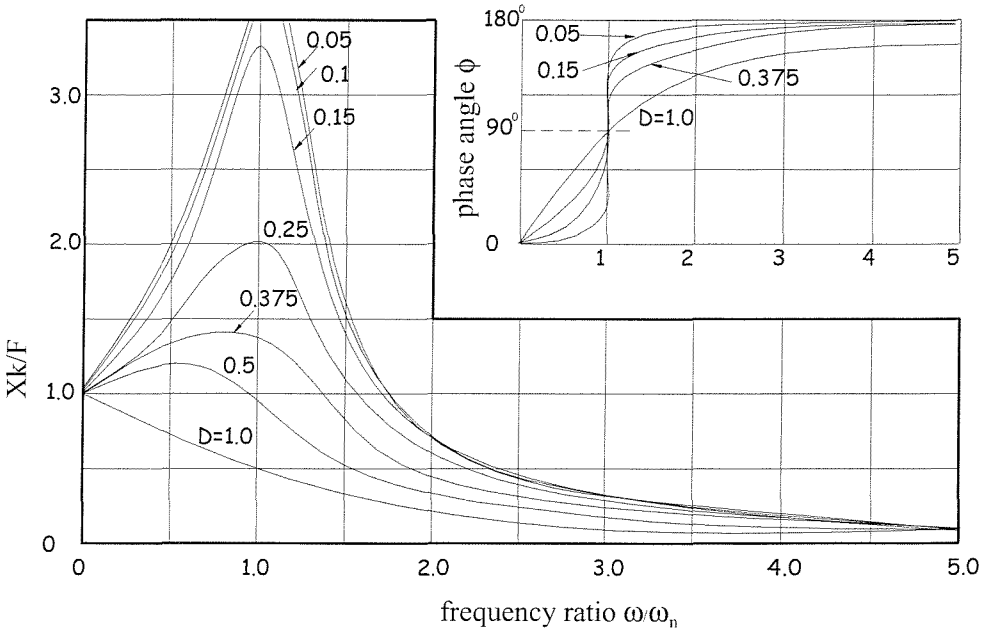

Figure 3.10: *Plot of equations 3.33 and 3.34. Redrawn from Thompson (1988).*

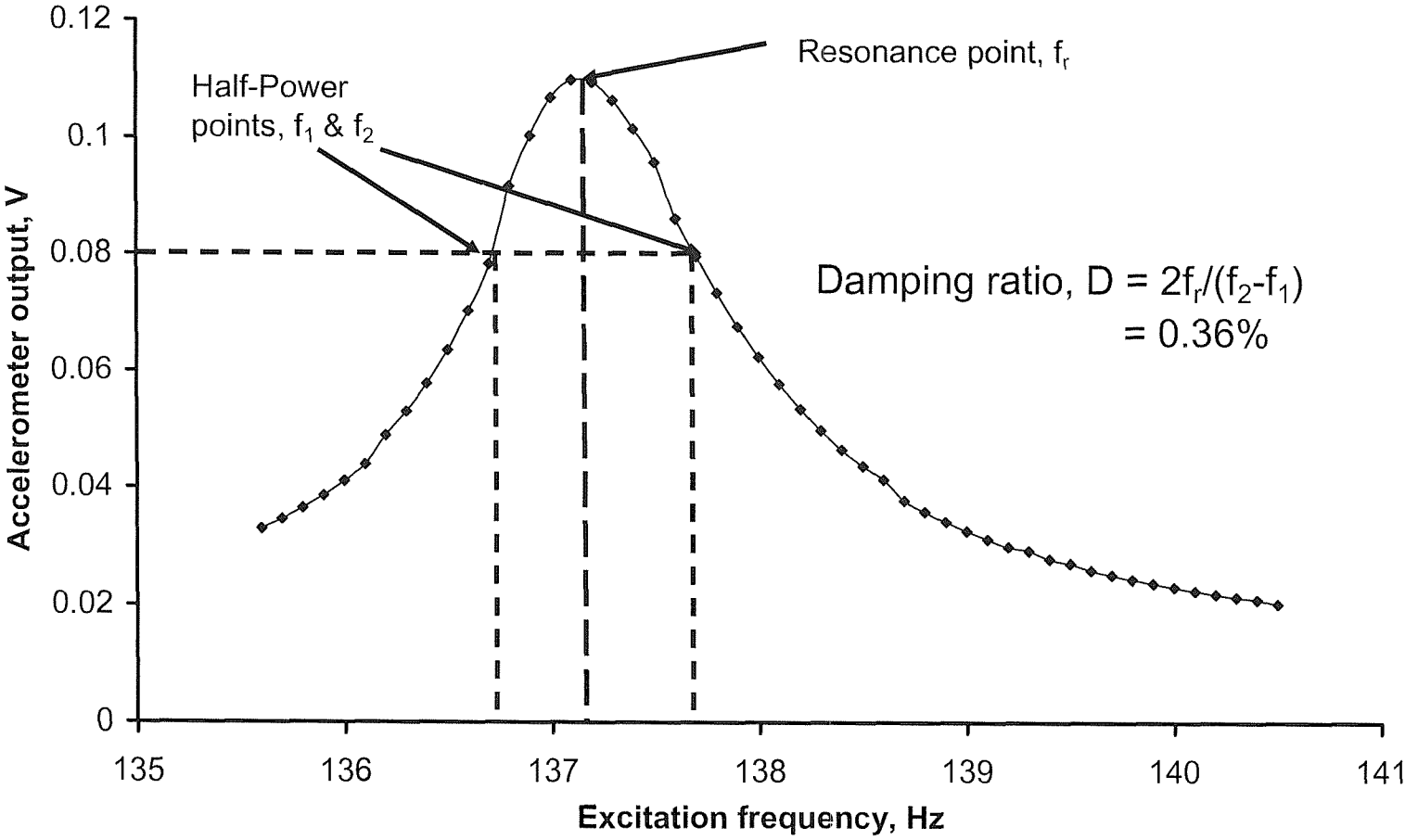

Figure 3.11: *Frequency response curve for a pluviated specimen of Leighton Buzzard sand tested at an effective confining pressure of 200kPa.*

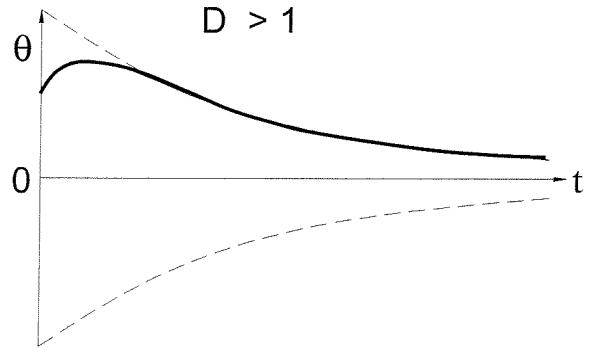

(a) Overdamped system.

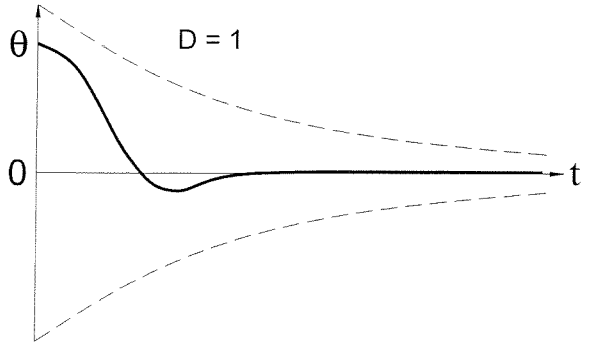

(b) Critically damped system.

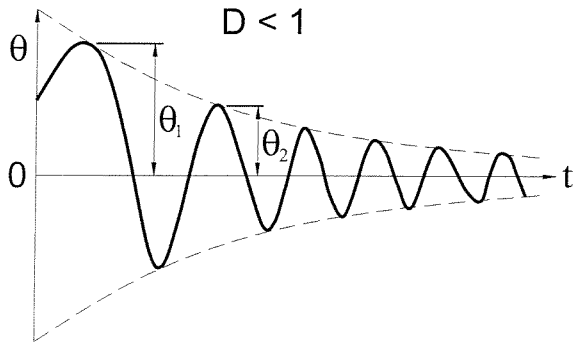

(c) Underdamped system.

Figure 3.12: Graphical representation of damped systems.

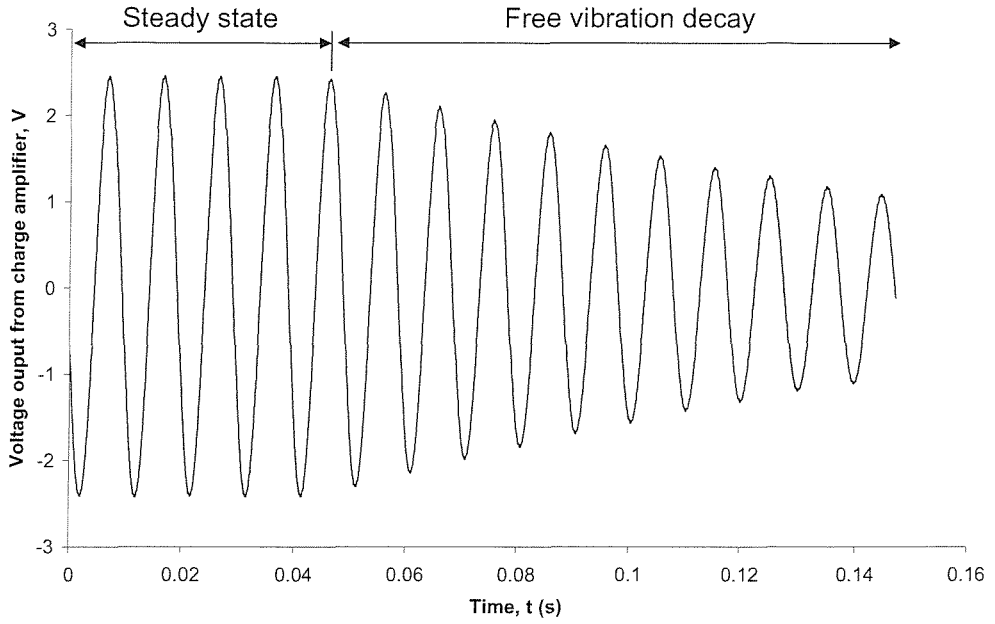

Figure 3.13: *Typical free vibration decay curve obtained from the resonant column for Leighton Buzzard sand.*

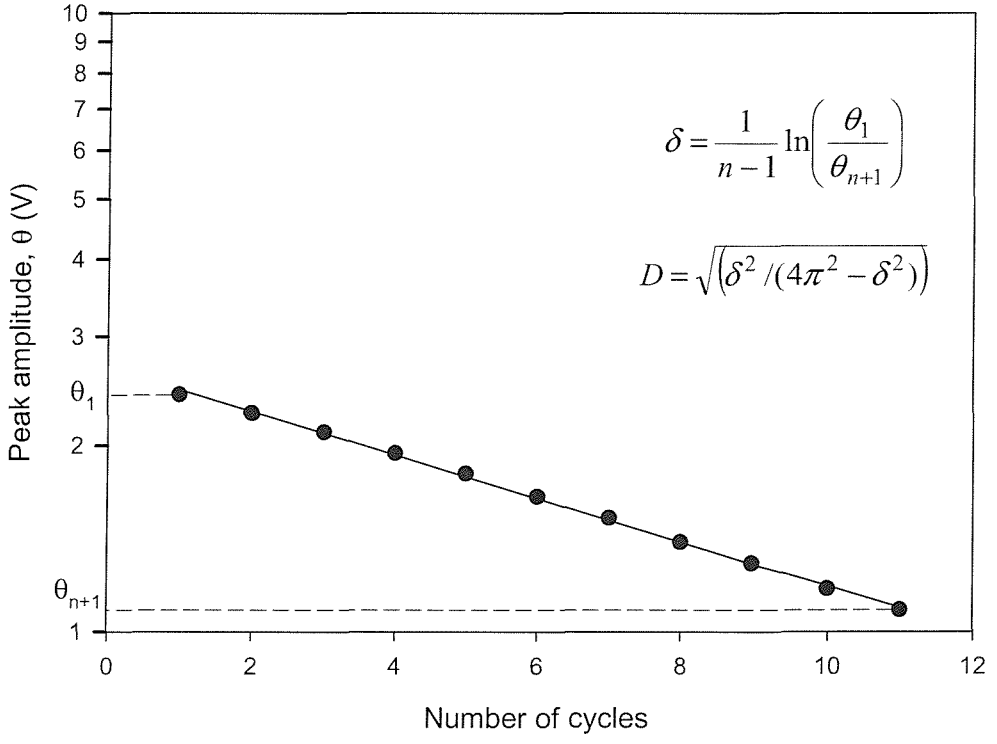

Figure 3.14: *Determination of logarithmic decrement, δ and damping ratio, D, from free vibration curve.*

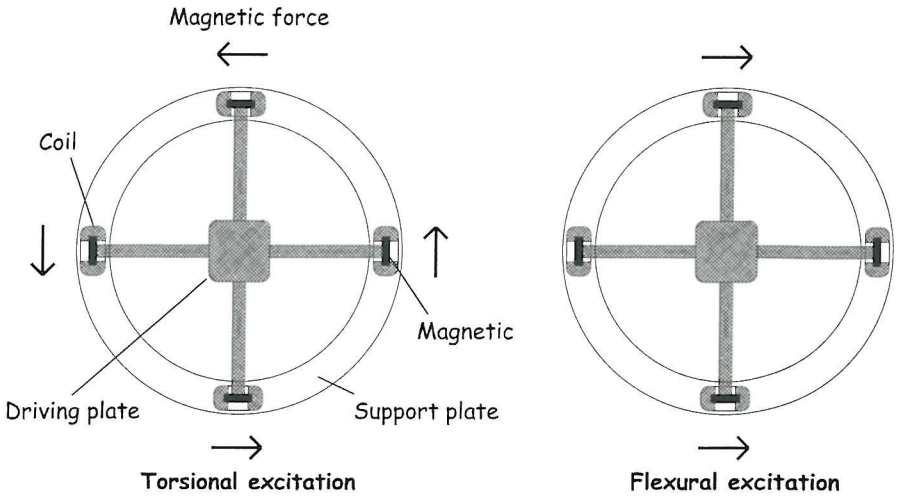

Figure 3.15: *Magnet and coil setup for torsional and flexural excitation. Redrawn from Cascante et al (1998).*

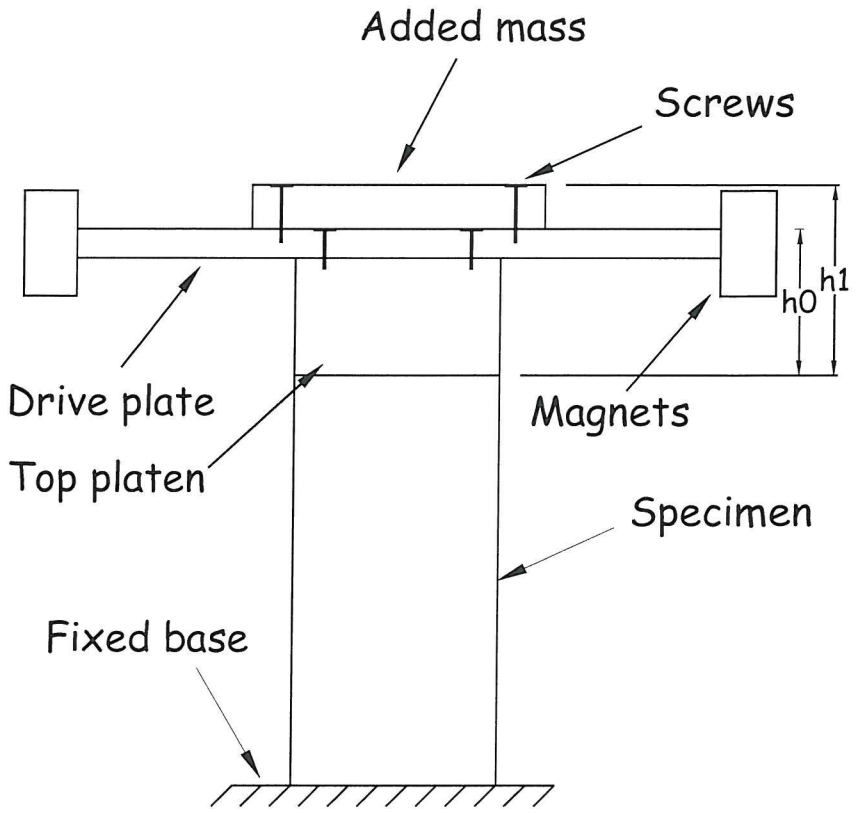

Figure 3.16: *Diagram of specimen and drive plate for resonant column.*

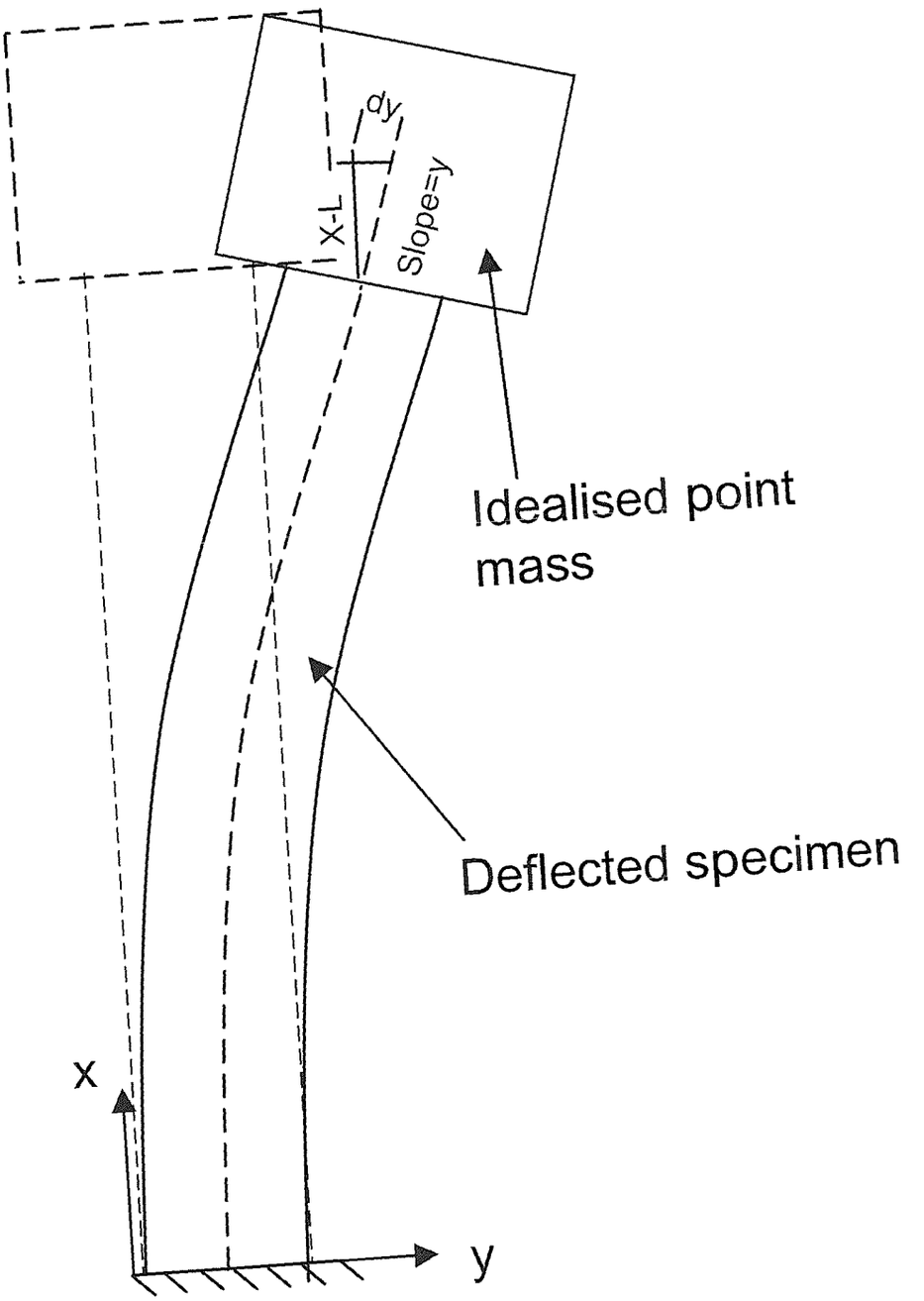

Figure 3.17: *Exaggerated view of deflected column for an idealized system.*

Chapter 4

CALIBRATION AND TESTING OF THE NEW GAS HYDRATE RESONANT COLUMN APPARATUS

4.1 Introduction

The quantification of gas hydrates within the world's oceans using geophysical exploration methods requires a knowledge of the geophysical properties of these sediments. As discussed in the literature review on hydrates (Chapter 2), the recovery of naturally occurring sediments to test in the laboratory is problematic. A technique was identified by Stern et al. (1996) (Section 2.7) which could be modified to form gas hydrates in sand specimens within the laboratory.

The resonant column apparatus was identified in (Chapter 3) as a means of measuring physical parameters of specimens at frequencies and strains relevant to current geophysical surveying techniques. However, the need to combine both the formation and testing of hydrated specimens required the development of a dedicated Gas Hydrate Resonant Column (GHRC). High pressure and low temperature is required during formation as is the applica-

tion of both torsional and flexural excitation during testing. To familiarize the author with the resonant column test method, and the general apparatus set up, tests were performed on a standard 'Stokoe' resonant column (SRC) (Lodde, 1982; Laird, 1994; Stokoe et al., 1999). During the calibration and testing of this apparatus various issues arose which facilitated the design of the GHRC.

This chapter therefore introduces the SRC and discusses the issues arising from its calibration. As the GHRC essentially consists of two independent systems, the design and operating principles are separated and discussed for each part. Therefore, the pressure and temperature systems and their software control are initially introduced. Modification made to the SRC drive system to increase its apparent stiffness, the application of differing vibration modes and improvement in attenuation measurement methods are highlighted. The results of, and improvements to, the calibration of the drive system are discussed. Finally, the calibration of the various transducers and the methodology adopted is described with examples of typical results given.

4.2 The standard 'Stokoe' resonant column

In a 'Stokoe' resonant column (SRC) the drive system, which is attached to the specimen, consists of a four arm bracket with permanent magnets fitted to the end of each arm. The support ring, clamped to the support cylinder, has four pairs of wire coils (Figure 4.1).

During sample preparation the drive plate is connected to the specimen and the height of the support cylinder is adjusted to allow the magnets to be positioned centrally within the wire coils. A torque is applied to the specimen by applying a sinusoidal voltage to the coils, which produces an oscillatory motion in the drive plate due to the resultant magnetic field. By controlling the frequency and amplitude of the applied voltage, the resonant frequency of the specimen and attached drive mechanism can be found. This is achieved by monitoring the output of an accelerometer that is attached to the drive plate (Figure 4.2) as the drive frequency is increased incrementally through a pre-defined frequency range (frequency sweep). By plotting the output of

the accelerometer against the frequency of the applied voltage, the resonant frequency can be easily identified as shown previously in Figure 3.11.

4.2.1 *Calibration of SRC*

From Eq 3.29, it can be seen that the mass polar moment of inertia of the drive system (I_0) is required to reduce resonant column data. As the drive system has a complex shape, I_0 is difficult to derive from geometry, so its value is found experimentally. This may be achieved by calibrating the drive mechanism by substituting, for the specimen, metal calibration bars of known mechanical properties. By modelling the system as a torsional pendulum with a single degree of freedom, where the drive system is the pendulum mass and the calibration bar is the torsional spring, the equation of motion for the system can be written as:

$$\omega_n = \sqrt{\frac{k}{I_0}}, \tag{4.1}$$

where: ω_n = natural circular frequency of vibration of the calibration bar,
k = stiffness of the bar,
I_0 = mass polar moment of inertia of drive mechanism.

To derive I_0 experimentally, a test is performed on a calibration bar to compute its resonant frequency. The test is then repeated with additional masses being added in turn to the drive system with the new resonant frequencies being found. By rearranging Eq 4.1 a linear equation expressing the mass polar moment of inertia of the additional masses (I_{am}) in terms of ω_n can be derived

$$I_{am} = \frac{k}{\omega_n^2} + I_0. \tag{4.2}$$

A variety of brass calibration bars, using brass tubes of differing internal and external diameters were made (Figure 4.3) and tested, Figure 4.4 shows the results of these tests, plotting I_{am} against $1/\omega_n^2$, where I_0 is defined by the y-axis intercept and k is the stiffness of the bar represented by the gradient of the last-squares straight line fitted to the data.

It was assumed that on reduction of the test data, the value of I_0 would be constant, since it is a geometric property of the drive plate that should not alter. However, it was found that the value of I_0 (as derived using the previously described method) increased with bar stiffness. The brass tube, which the calibration bars were made from, was found to be non-uniform. Therefore, further bars were manufactured from solid billet, of different materials (aluminium and nylon, Figure 4.5), and to a higher standard, to investigate the discrepancy in I_0. Using the same bar design allowed for not only the stiffness of the bars and its effect on I_0 to be assessed but also other properties of the bars like mass (m) and polar moment of inertia I_p.

The results of all the tests undertaken are given in Table 4.1. The results show that as the resonant frequency of the bars increases, a corresponding increase in I_0 can be observed as shown in Figure 4.6. Static tests were undertaken, using a torsional loading frame (Figure 4.7), in an attempt to define the true stiffness and shear modulus of the materials used. The results of these tests are also given in Table 4.1. It can be seen that as the torsional stiffness of the bars increases, the resonant column increasingly overestimates the stiffness when compared to the static values. No correlation was found between m, or I_p, of the bar and I_0 (Figures 4.8 and 4.9).

4.2.2 *Compliance Issues*

The results from the calibration tests show that I_0 increases with stiffness of the bars, although it is a geometric property of the drive plate and should be a constant. It can be seen from Eq 3.29 and Eq 3.30 that the value for I_0 is fundamental to the evaluation of V_s and hence G. In tests conducted on dry sand the value of G would have over 40% increase if the largest derived value of I_0 was used rather than the lowest. The validity of the reduced data, using Eq 4.2, is therefore dependent on the apparatus and specimen fulfilling the basic assumptions used when defining the equations of motion. These are:

1. During resonance only the sample and attached devices are vibrating;

2. The apparatus behaves as a single-degree-of-freedom system.

Results by other authors (Hardin et al., 1994; Avramidis and Saxena, 1990) have suggested, for a 'Drnevich' resonant column, that for stiff soils and rocks the connection between specimen and drive plate may be flexible and therefore may not represent a true single-degree-of-freedom system. Also, the support apparatus may not have sufficient mass and stiffness to prevent itself vibrating. To investigate these hypotheses, tests were conducted with accelerometers connected to differing parts of the apparatus.

Figure 4.10 shows the response of two accelerometers of different sensitivities which were independently fixed, using solvent adhesive, to the base of Aluminium Bar 4. The voltage output from the charge amplifier for the first accelerometer (Accl.1) shows no apparent peak and it is assumed that the output represents background noise within the system. The voltage output for Accelerometer 2 (Accl.2), the more sensitive accelerometer, shows a well defined peak around the resonant frequency of the bar. This suggests that the assumption of a base of the aluminium bar be fixed may be false.

Figure 4.11 shows the respective amplitudes of the drive mechanism and coil during a resonance test on Aluminium Bar 3, i.e. with accelerometers fixed to the drive mechanism and one of the coils. Table 4.2 gives the amplitude ratio between the drive mechanism and the coil for a variety of bars. Although the ratios are small there is still significant relative movement. Avramidis and Saxena, (1990) refined the flexibility of the apparatus by stiffening various components. Other authors have modelled the resonant column with greater degrees of freedom to overcome this difficulty (Min et al., 1990; Hardin et al., 1994; Ashmawy and Drnevich, 1994). As the design of the GHRC was still in the early stages several measures were taken to stiffen the drive mechanism components.

4.2.3 *Damping using the SRC*

It was noted in Section 3.5 that two techniques (forced vibration and free vibration) are available to measure the damping ratio, D. However, the measured value of material damping obtained using these techniques also includes an element of damping associated with the apparatus. In a standard resonant

column the motion of the drive mechanism is created by passing a sinusoidal current through the coils creating a magnetic field which interacts with the magnets (attached to the drive mechanism) causing motion. However, the motion of the magnets also induces an electro-motive force (EMF) in the coils. This force opposes the motion of the magnets (termed back-EMF) thereby causing an additional loss of energy in the system above the intrinsic material damping of the specimen. This is termed the *equipment damping.*

One method that has been adopted (Laird, 1994; Stokoe et al., 1999; Wang et al., 2003) is to quantify the value of the equipment damping and produce correction curves so that the equipment damping can be subtracted from the measured damping. This is achieved by measuring the damping ratio for a range of calibration bars, since the material damping for an aluminium bar is deemed negligible (standard tables give $Q = 350,000$ for aluminium), therefore it is assumed that the damping measured is that of the equipment.

Figure 4.12 shows measurements of equipment damping for brass and aluminium calibration bars using the SRC. The results show that the equipment damping is inversely proportional to the loading frequency with a maximum value over 1% for the lowest frequency bar tested. This value is large when compared to the inherent damping of sand specimens at higher frequencies (Figure 3.7). In flexure, the resonant frequency is approximately 40% of the torsional frequency (Cascante, 1996), which may then lead to measurements of damping (using flexure) dominated by the equipment damping.

To reduce the possibility of equipment damping dominating the measured damping a method had to be adopted to reduce the equipment damping. A method which has recently been adopted for reducing equipment generated damping has been developed by using a current-mode source instead of the more commonly used voltage-mode source (Meng and Rix, 2003; Cascante et al., 2003). However in the testing undertaken during this research the equipment damping was reduced by the implementation of an open circuit arrangement to the coils during free vibration decay, which is outlined in Section 4.3.3.

4.3 The Gas Hydrate Resonant Column

4.3.1 *Introduction*

The construction of the new Gas Hydrate Resonant Column was undertaken by GDS Instruments Ltd, Hook, Hampshire[1] with the design being the joint responsibility of both the writer and GDS Ltd. The GHRC consists of two independent systems: the pressure/temperature system and its controls, and the resonant column drive system and its controls.

4.3.2 *Pressure Cell and Environmental Chamber*

The pressure cell and environment chamber were designed to provide the conditions necessary for hydrate growth. The following describes the differing components; the pressure control systems; and a brief outline of the instrumentation available.

System components

The pressure cell consists of a base and cell top, made from stainless steel, and designed to a maximum working pressure of 25MPa. The cell top and base are connected by two removable 'C'-clamps which are bolted together, with the apparatus connected to the frame of the environmental chamber through the base. An electrically operated lifting frame was provided to allow the safe lowering and raising of the cell top. Figure 4.13 shows these components.

The cell base was designed with five ports into the base to allow for the application of suction; water back pressure; two separate gas back pressures; and an atmospheric vent to the soil specimen. Two ports were provided into the cell chamber for application of cell pressure and saturation of the specimen via the top cap. Eight ports were also provided through the cell base (Figure 4.14) for electrical connections to the drive mechanism, axial transducer, thermistors and accelerometer. One port was provided in the cell top for emergency pressure release (not shown).

[1]GDS Ltd were formerly located at Egham, Surrey.

Environmental conditions were controlled by two separate cooling systems. An air conditioning unit provides air cooling within the environmental chamber, and a separate jacket (fluid-cooled, using pumped glycerol), is attached to the cell top (Figure 4.15) with the heat exchanger for the fluid-cooled jacket and electronic control systems being situated below the chamber (Figure 4.16). This allowed the chamber to be situated at a practical working height. The temperature for both cooling systems could either be operated manually from the console attached to the apparatus, or remotely via a computer. The separate systems allow temperature control from -20^0C to $+50^0$C with a resolution of 0.1^0C.

Pressure control systems

Both the cell pressure (nitrogen) and gaseous back pressure (methane) are supplied by gas 'J'-bottles with a maximum bottle pressure of 30MPa and 20MPa, respectively. Regulation of pressure from the bottles to the cell is controlled via a 25:1 ratio loader (RL), which in turn is controlled by a proportional air valve (PAV) using an RS232 interface. A motorised valve allows controlled pressure release from the system via flow control regulators. A schematic diagram of the pressure system layout is shown in Figure 4.17.

The control of the pressures (via the PAV) was achieved using a commercial software package, GDSLab, designed by GDS Instruments Ltd, which was modified to suit the requirements of the GHRC. The RL operated at approximately 25 times the PAV pressure. Therefore, to allow a pressure of 12.5MPa out of the gas bottles, the pressure set by the PAV was 500kPa.

Instrumentation

As the application of pressure via the control software relies on proxy measurements (PAV pressure to RL) the true applied pressure to the specimen is measured via inline 5000psi rated (approximately 35MPa) pressure transducers identified in the schematic diagram (Figure 4.17).

Further instrumentation includes a LVDT, supported by the support ring of the GHRC drive mechanism, to measure axial deformation of the speci-

men during the testing, and two thermistors attached to the membrane on opposite sides of the specimen, to measure the temperature within the cell. The GDSLab software allows real-time acquisition and storage of these test data throughout the test.

4.3.3 *Drive Mechanism*

The design of the drive mechanism, as shown in Figure 4.18, was based on that of the 'Stokoe' resonant column (Figure 4.1) but with modifications (Figures 4.19) made to increase the overall stiffness of the apparatus (based on the results obtained in Section 4.2.2). In addition, software controlled electronics were designed to provide both torsional and flexural excitation. In addition, the inherent back EMF damping was removed by creating an open-circuit during the free vibration decay to remove the back EMF.

Design improvements to apparatus stiffness

- **Stiffening of coils.**
  - In the 'Stokoe' resonant column apparatus each individual coil is fixed in place by resin to the support ring(Figure 4.19(d)). In the GHRC each coil is mounted in an acrylic frame which is mechanically fixed by four M4 bolts to the support ring. Also, a circular aluminium plate was fixed to the top of all the coil frames to link them together and provide additional rigidity (Figure 4.19(c)).
- **Increasing restraint of support ring.**
  - In the 'Stokoe' resonant column apparatus the support ring is held onto the support frame by clamping the support ring to the frame using two M4 screws (Figure 4.19(b)). This was improved by using four M5 screws instead (Figure 4.19(a)) .
- **Strengthening the support frame.**

- The support frame of the GHRC was strengthened by omitting the large holes that were machined out of the 'Stokoe' resonant column apparatus support frame (Figure 4.1).

- **Strengthening the drive plate.**

  - The drive plate was strengthened by increasing the thickness of the section from 6.6mm to 10mm, Also the number and size of the screws holding the plate to the top platen were increased from four to six, and M4 to M5, respectively.

- **Fixity of base platen.**

  - To ensure that the base platen (and calibration bar) were adequately fixed during testing the base plate of the GHRC was fixed to the cell base with eight M5 bolts, instead of four M4 bolts as in the 'Stokoe' resonant column apparatus.

The effect that these improvements had on the calibration tests to determine I_0 and I_y are discussed in Section 4.4.

Electronic and software control systems

A computer program, written using TestPoint[2], integrated with a 16 bit, high speed, data acquisition and control card (DT3016)[3], residing on the PCI bus of the acquisition and control computer, provided for complete automation of the resonance test. TestPoint is a programming tool which aids the creation of custom written programs for testing and data acquisition. Predefined objects and modelling of the system components for the test are combined with a variety of associated actions (using drop and drag mouse operations) to create the test. Figure 4.20 shows a schematic presentation of system components. The DT740 screw terminal, identified in Figure 4.20, links all the system components to the DT3016 card using cables which provide both digital and analogue inputs and outputs.

[2]TestPoint is a trademark of Capital Equipment Corporation, Billerica, MA
[3]DT3016 is manufactured by Data Translations Inc, Marlboro, MA

To enable both torsional and flexural excitation to the specimen using the designed drive mechanism, an electronic control pad was designed by GDS Instruments Ltd to allow switching of the voltage applied to the coils from outside the cell. This switching arrangement also allowed for all the coils to be disconnected (open circuit) during free vibration decay. The provision of an open circuit prevents a back EMF being induced in the coils and therefore its inertial effect on the vibrating system. The operation of each excitation mode and disconnection of all coils was initiated through the computer program using digital input/output signals.

During a test the computer program creates a sinusoidal waveform with a predefined output voltage and frequency which is sent to the GDS control box in prescribed frequency steps. Data is acquired from the accelerometer (via the charge amplifier) for each frequency step and the peak output determined and stored along with its corresponding excitation frequency. At the end of the test the acquired data are plotted with peak output against excitation frequency (as shown in Figure 3.11). The resonant frequency of the specimen corresponds to the peak output observed. Two tests are undertaken to find the resonant peak. A broad sweep, at 1Hz intervals with a maximum 100 cycles per step, is undertaken to define the resonance region. A fine sweep is then undertaken with a minimum step interval of 0.1Hz, with data acquisition starting after the specimen has reached steady state (approximately 2 seconds of excitation).

Damping measurements are undertaken once the resonant frequency has been found. The specimen is excited at its resonant frequency until a steady state is achieved and then the coils are open circuited. The data acquisition is started immediately before the open circuit is formed and the whole free vibration decay waveform is acquired. Post processing of the waveform defines the peak for each cycle and then calculates the logarithmic decay, δ, from which D and Q can be calculated.

4.4 Calibration of the new GHRC drive system

To calculate the values of V_s and V_{lf}, obtained from torsional and flexural vibration respectively, certain properties of the drive system are required (see Section 3.4 and 3.6). Section 4.2.1 outlined a method that could be used to measure I_0 which could also be adapted to calibrate the flexural mode which requires the effective height of the drive system. The following section therefore presents results obtained in calibrating the GHRC drive system for both torsional and flexural vibration. Results are also presented for the equipment damping that is inherent in the system for each vibrational mode.

4.4.1 *Calibration of* I_0

Based on the results from Section 4.2.1 it was decided that only the four aluminium bars would be used during the calibration of the GHRC, since these gave consistent results in both static and dynamic tests.

Figure 4.21 show the results of the calibration using the adopted method. Figure 4.22 compares the value of I_0 against frequency obtained during the calibration of the GHRC drive system with that of the 'Stokoe' resonant column apparatus. It should be noted that the value of I_0 for the GHRC system includes the top cap. The results show that the spread of values of I_0 for the GHRC system is 75.7% of those for the 'Stokoe' resonant column apparatus system, which suggests that the modifications made to the GHRC system have been moderately successful in reducing the error in I_0.

Work on frozen soil samples using the resonant column (Al-Hunaidi et al., 1996) had showed a large increase in resonant frequency over the unfrozen state. Therefore, an increase in frequency would be expected for hydrated specimens and so additional aluminium bars, named GHRC Bars 1-4 and Elkin bars 1-4 (Figure 4.23), were made to cover the range of resonant frequencies similar to those which might occur in hydrated specimens. The GHRC bars were designed to connect directly to the drive plate, whereas the Elkin bars were designed to have the top cap connected as well. This would

allow the effect of the top cap and potential issues with the connections to be addressed. The range of values of I_0 from the calibration of the GHRC bars was from 3.657x10^{-3}kgm^2 for 200.6Hz to 5.553x10^{-3}kgm^2 for 456Hz as shown in Figure 4.24. Table 4.3 highlights the errors in the computed values of V_s and G_{max} for all the aluminium bars when compared with the specified values given for the grade of material used. It can be seen that using the GHRC bars, with the additional fixings at the base and connecting directly to the drive plate, reduces the error in V_s and G_{max} even though the bars are much stiffer. However, there is still an increasing error, 4.1% and 8.3% for V_s and G_{max}, respectively (for the stiffest bar), as the bar stiffness increases.

Considering Eq 4.1 and the results of the static tests undertaken in Section 4.2.1 it can be seen that the derivation of I_0 is a function of the bar stiffness (k), and the resonant column overestimates this value with increasing stiffness. To try to eliminate the dependency of I_0 on k, a procedure was adopted whereby the value of I_0 was derived using the known material properties of the aluminium bars and the measured resonant frequencies and substituting these values into Eq's 3.29 and 3.30. The derived values of I_0 using this method are shown in Figure 4.25. By applying a least squares regression curve to this data and using the equation of the line obtained, a value of I_0 corresponding to measured frequency can be calculated. Table 4.4 highlights the reduction in the error values of V_s and G_{max} by using this calculated value of I_0 to recalculate V_s and G_{max}. The results suggest that by using an empirical solution to define a value of I_0 a higher degree of accuracy is obtained with a maximum error of -1.12% in the calculation of V_s and a maximum error of -2.03% for G_{max}. This overcomes the difficulty of trying to model the resonant system with higher degrees of freedom.

4.4.2 *Calibration of* I_y

It can be seen from Eq 3.58 that the position of the drive mechanism is fundamental to determining the frequency of first mode of vibration of flexure. Eq 3.60, which allows the equivalent height to be determined for each mass, is difficult to use for masses with a complicated geometry. It can therefore be

rewritten to allow the equivalent height of the drive mechanism ($h(y_{ci}, I_{yi})$) to be expressed in terms of I_{yi} and y_{ci} which are the area moment of inertia and the centre of gravity of the added mass respectively:

$$h(y_{ci}, I_{yi}) = 1 + \frac{3y_{ci}}{L} + \frac{9}{4L^2}\left[\frac{I_{yi}}{m_i} + y_{ci}^2\right]. \tag{4.3}$$

To determine the equivalent height of the drive mechanism using Eq 4.3, values of m_i, y_{ci} and I_y are required for the drive system. If it is assumed that y_{ci} is at the geometric centre, and m_i can be measured, then the only unknown is I_y.

Calibration for flexure is similar to that for torsion. The resonant frequency of the system with and without an added mass is measured. Using Eq 3.60 the equivalent height for the top bar, top cap (if fitted) and added mass can be computed. Using Eq 3.58 and substituting in the measured and derived values for each test, two simultaneous equations can be formed. Solving to find the equivalent height of the drive mechanism, substituting into Eq 4.3 and rearranging, the value of I_y can be found. Cascante (1996) suggests that a test is conducted with the drive mechanism raised by a known value, to check that the stiffness of the bar ($3EI_b\text{Ł}^3$) is constant for the two tests. This is achieved by measuring the resonant frequency after raising the drive mechanism, a known distance, and using the computed value of I_y to determine the stiffness of the bar.

Figure 4.26 and Table 4.5 shows the results of tests conducted on different calibration bars to determine I_y. The results from these tests show a variation in I_y from 0.56x10^{-3}m^4 to 4.80x10^{-3}m^4. The value of I_y is neither constant nor falls onto a single line (as the value for I_0 does). The stiffness ratio, before and after raising the drive mechanism, shows an increasing difference from 1.01 to 1.05 for increasing bar stiffness. The largest error however is between the computed stiffness, using the results from the tests, and the stiffness calculated from the material properties. This shows a maximum error of 72% for bar GHRC 4. The difference between the GHRC bars and the Elkin bars is that the latter is designed to allow the top cap to be attached. Figure 4.27 show the results of undertaking a regression calculation starting with the

known material properties and measured frequency to calculate I_y, which is also included in Table 4.5.

These results suggest that the determination of I_y using either method is problematic. It can be seen that the value of I_y is a function of not only the bar stiffness, but also of the added masses and bar geometry. In the derivation of Eq 3.58 it was assumed that the strain energy of shear was negligible and could be disregarded. However this may not be true when the ratio of specimen dimensions l/d> 6 (Gere and Timoshenko, 1991). The implications of the measured variation is discussed in Section 5.4.2.

4.4.3 *Damping Calibration*

Improvements to the GHRC included the design of electronic hardware to provide an 'open circuit' during free vibration decay of the specimen to negate the effect of the back-EMF. The success of this can be seen in Figure 4.28, which shows the free vibration decay curves, for one of the calibration bars, obtained with an 'open circuit' and a 'closed circuit'. It can be seen that the induced back-EMF substantially increases the damping of the bar.

The effect of this back-EMF on the measured damping of the bar can be quantified by comparing the damping values obtained, for the calibration bars, using the half power method (HPD), which includes the back-EMF, and the free vibration decay (FVD), which has no back-EMF. This is shown in Figure 4.29 for torsion and flexure. The general trend for HPD method shows a slight reduction in damping with increasing frequency from approximately, 0.88% to 0.82%, and 1% to 0.77%, for torsional and flexural excitation, respectively. The FVD method however, shows a marked reduction in damping overall with the measured damping increasing with frequency from, 0.045% to 0.197%, and 0.089% to 0.243%, for torsion and flexure, respectively. The result of using the 'open circuit' arrangement is that the increase in stiffness of the bar and its effect on D can now be clearly seen (Figure 4.29), which otherwise would have been masked by the increased damping due to the back-EMF and its frequency dependency. This increase in damping helps reinforce the hypothesis that the idealisation of the resonant column drive

system as a single degree of freedom may not be strictly true as the bar stiffness increases. As the aluminium bar can be assumed to have a very low attenuation, the increase in damping with bar stiffness might possibly be due to frictional losses occurring between the various component connections.

The value of the equipment damping can be quantified and deducted from the measured value obtained during testing by using a correction curve obtained by applying a regression analysis to the damping calibration data as shown in Figure 4.30

4.5 Calibration of transducers

To ensure that the transducer measurements were representative of the true values observed, calibration of the transducers was undertaken to quantify their accuracy and precision. A calibration methodology was adopted (Heymann, 1998), which provided a stepwise approach to ensure consistency of the calibration. These steps can be summarised as:

1. Calibration of the entire transducer system (transducer, signal conditioners, A/D converters, etc.) with a suitably accurate reference, ensuring that sufficient data points were measured over the calibration range (a minimum of 10).

2. Performance of a regression analysis of the data to determine the least squares fit to the data.

3. Use of the regression analysis to calculate the error between the applied value and the measured value.

4. Plotting of the errors to allow a visual assessment of the error (maximum error, non-linearity, hysteresis of the transducer).

5. Determine a 95% confidence limits for the errors assuming a normal distribution.

Table 4.6 provides a summary of the transducers used during the testing programme and their calibration details. Calibration of the transducers

was performed at the beginning of the testing program. Further calibration checks were made on all transducers after the testing program and results (see Abstract) show that no significant changes had occurred.

4.5.1 *Pressure transducer calibration*

The calibration of the pressure transducers was undertaken using an hydraulic dead-weight tester manufactured by DH Budenburg Ltd. This apparatus works on the principal of balancing pressures between applied dead weights and an outlet port connected to the transducers. The accuracy of the apparatus is given as 0.02% for a pressure range of 1200-12000kPa (Gräbe, 2002)

The calibration of the transducer was undertaken for a load and unload cycle with 500kPa steps for the whole range of the testing apparatus. Atmospheric pressure was taken as 100kPa. Figure 4.31 shows a typical calibration result, with the regression, accuracy and error for each data point indicated. The accuracy of the pressure transducer over the calibration range can be expressed as a ratio of the maximum error and the range. This value for the pressure transducers varied from $0.11\% - 0.08\%$. The weight limitation of the calibration rig meant that during hydrate formation the applied pressure was outside the calibrated range, however independent calibration of the transducers prior to installation gave an accuracy of 0.06% for the full range of 34MPa.

4.5.2 *LVDT calibration*

The axial LVDT was used to measure the axial deformation of the drive plate which is connected to the top of the sample. Figure 4.18 shows the LVDT body connected to the top plate of the GHRC. The central core of the LVDT was free to move with the drive plate. The LVDT was calibrated against a micrometer (Mitutoyo series 152-348), which was housed in a purpose made frame to ensure alignment of the LVDT and the micrometer (Figure 4.32). The accuracy of the micrometer over its full range ($25mm$) was quoted at $\pm 2\mu$m. Figure 4.33 shows the calibration results with the regression, accuracy

and error for each data point indicated. The accuracy of the LVDT was better than 0.2% of full scale output.

4.5.3 *Thermistor calibration*

Two resistance-temperature curved-matched thermistors were used to measure the ambient temperature on the outside face of the membrane enclosing the specimen. These thermistors had a temperature range from -50^{0}C to +150^{0}C with a tolerance of $\pm$0.2^{0}C. Calibration was achieved using a ELE conductivity meter, with a temperature probe (resolution 0.1^{0}C), immersed in a water bath with the thermistors. A typical calibration result is shown in Figure 4.34. It can be seen that the response of the thermistor was non-linear and was generally described by a 5th order polynomial. As a result of this response, raw data (mV) was converted to temperature, within GDSLab, by using a 'look up' table based on interpolation of points derived during the calibration of the thermistors.

Table 4.1: *Results of calibration tests on the Stokoe resonant column. Note - For brass bars the dimensions given are for outside diameter and inside diameter of the brass tubes used respectively.*

Bar No	Material	Dimensions, (mm)	Resonant frequency, (Hz)	Static torsional stiffness, (10^3Nm)	Dynamic torsional Stiffness (10^3Nm)	Calculated stiffness, GIp/L (10^3Nm)	Moment of inertia for drive system, I_0 (10^{-3}kgm^2)
1	Brass 1	12.7-10.9	47.6	0.259	0.281	0.258	2.96
2	Aluminium 1	13	59.8	0.432	0.438	0.417	2.99
3	Brass 2	15.88-14.04	68.5	0.519	0.575	0.534	2.91
4	Nylon 1	40	71.9	0.442	0.613	0.577	2.93
5	Brass 3	17.46-14.36	96.9	1.12	1.18	1.09	3.00
6	Aluminium 2	18	111.7	1.53	1.55	1.53	2.98
7	Brass 4	20.64-18.2	112.3	1.63	1.57	1.55	3.01
8	Nylon 2	40	124.7	1.46	1.98	1.82	3.17
9	Brass 5	25.4-23.2	139.6	2.51	2.59	2.73	3.183
10	Aluminium 3	23	175.2	3.83	4.23	4.08	3.39
11	Nylon 3	50	185.7	3.69	4.91	3.68	3.54
12	Brass 6	25.4-22.2	203.6	5.81	6.33	3.74	3.67
13	Brass 7	28.5-22.2	231.6	-	9.06	9.00	4.08
14	Aluminium 4	28.1	244.3	8.8	10.52	9.09	4.32

Table 4.2: *Comparison of relative coil and magnet movement during RC tests for various calibration bars.*

Bar Number	Frequency Hz	Peak coil displacement x10^{-6} m	Peak magnet displacement x10^{-6} m	ratio of coil & magnet displacement
Aluminium Bar 4	245.2	0.019	7.020	1/3625
Aluminium Bar 3	175.1	0.042	16.39	1/395
Brass Bar 4	111.7	0.054	28.36	1/525
Aluminium Bar 1	59.8	0.120	38.33	1/319

Table 4.3: *Computed values of V_s and G_{max} and their errors (when compared to material property values for aluminium, $V_S = 3097ms^{-1}$ and $G = 25.9GPa$) for all calibration bars using derived value of I_0.*

Bar Number	Frequency Hz	Computed V_s ms^{-1}	Error %	Computed G_{max}, GPa	Error %
Aluminium Bar 1	52.6	3143	+1.46	26.8	-2.62
Aluminium Bar 2	99.5	3154	+1.79	26.9	+0.28
Aluminium Bar 3	157.3	3221	+3.83	28.1	+2.79
Aluminium Bar 4	235.5	3388	+8.59	31.1	+8.25
GHRC Bar 1	200.6	3054	-1.42	25.3	-2.62
GHRC Bar 2	308	3098	+0.03	26.0	+0.28
GHRC Bar 3	385	3137	+1.29	26.7	+2.79
GHRC Bar 4	456	3229	+4.10	28.3	+8.25
Elkin Bar 1	191.8	3020	-2.55	24.7	-4.93
Elkin Bar 2	296.2	3073	-0.79	25.6	-1.35
Elkin Bar 3	369	3148	+1.62	26.9	+3.43
Elkin Bar 4	426	3233	+4.20	28.3	+8.44

Table 4.4: *Regressed values of V_s and G_{max} and their errors using the Eq of 'best fit' line obtained in Figure 4.25 to derive I_0 for all bars.*

Bar Number	Frequency Hz	Computed V_s ms^{-1}	Error %	Computed G_{max} GPa	Error %
Aluminium Bar 1	52.6	3114	+0.53	26.3	+1.29
Aluminium Bar 2	99.5	3089	-0.26	25.9	+0.28
Aluminium Bar 3	159.2	3069	-0.90	25.5	-1.58
Aluminium Bar 4	233.7	3102	-0.15	26.1	+0.53
GHRC Bar 1	200.6	3098	+0.04	26.0	+0.30
GHRC Bar 2	308	3098	+0.04	26.0	+0.32
GHRC Bar 3	385	3113	+0.52	26.3	+1.27
GHRC Bar 4	456	3083	-0.44	25.8	-0.66
Elkin Bar 1	191.8	3091	-0.21	25.9	-0.19
Elkin Bar 2	296.2	3084	-0.41	25.8	-0.60
Elkin Bar 3	369	3064	-1.10	25.4	-1.99
Elkin Bar 4	426	3063	-1.12	25.4	-2.03

Table 4.5: *Results of flexural calibration test for GHRC.*

Bar No	Resonant frequency, (Hz)	Computed I_y, (10^{-3}m^4)	Calculated I_y from material properties, (10^{-3}m^4)	Computed stiffness, k (10^6N/m)	Calculated stiffness, (10^6N/m)	Stiffness ratio for lifted mechanism	Error in stiffness, %
Aluminium 3	56.6	0.56	8.94	0.44	0.53	1.01	-21.8
Aluminium 4	82.6	4.8	10.14	1.02	1.18	1.012	-15.9
GHRC 1	149.3	1.77	4.31	1.88	2.38	1.02	-26.7
GHRC 2	224.2	2.67	6.20	4.39	6.24	1.04	-42.1
GHRC 3	274.8	2.44	8.07	6.88	10.07	1.06	-54.0
GHRC 4	331.4	2.89	10.09	9.69	16.70	1.05	-72.4
Elkin 1	91.3	1.18	7.60	1.85	2.38	—	-28.7
Elkin 2	142.1	2.16	10.21	4.66	6.25	—	-33.9
Elkin 3	179	3.72	12.75	7.88	10.65	—	-35.3
Elkin 4	209.8	3.20	14.27	10.72	15.25	—	-42.23

Table 4.6: *Calibration details for transducers.*

Transducer	Measurement	Company & Type	Design range	Calibration range	Resolution	Accuracy	$\frac{\text{Accuracy}}{\text{calib. range}}(\%)$
Pressure trans.	Cell pressure	Maywood P102	34MPa	12MPa	0.525kPa	4.98kPa	0.08
Pressure trans.	CH_4 Back pressure	Maywood P102	34MPa	12MPa	0.525kPa	5.58kPa6	0.09
Pressure trans.	Pore pressure	Maywood P102	34MPa	12MPa	0.525kPa	6.50kPa6	0.11
LVDT	Axial disp	RDP M5	$\pm 12.5mm$	$\pm 12.5mm$	1μm	19μm	0.16
Thermistor	Sample temp	RS 151 – 215	$-50 - +150^0$C	$-10 - +30^0$C	0.003^0C	—	—
Thermistor	Sample temp	RS 151 – 215	$-50 - +150^0$C	$-10 - +30^0$C	0.003^0C	—	—

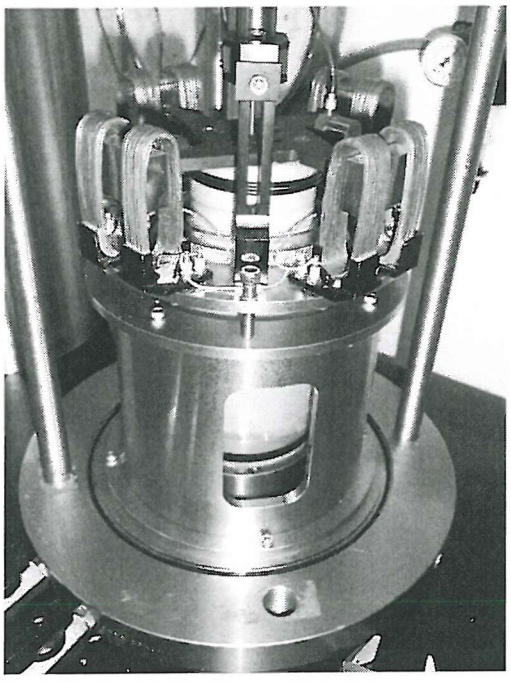

Figure 4.1: *SRC without pressure jacket showing electromagnetic drive system. Isotropic stresses are applied by compressed air acting on the silicone fluid surrounding the specimen.*

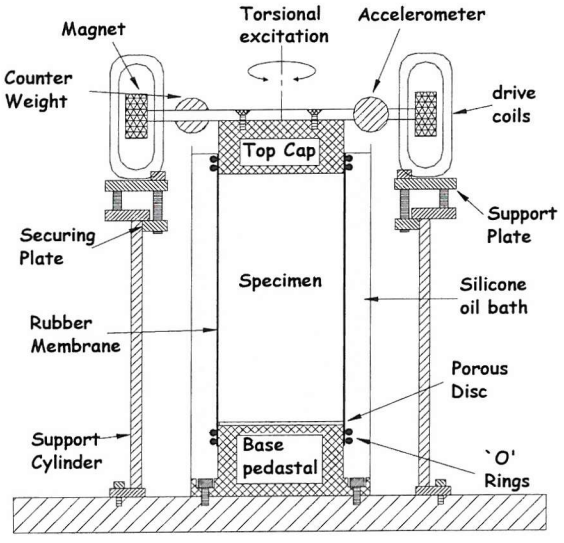

Figure 4.2: *Cross-section through the SRC resonant column (without pressure confinement jacket). Modified from Stokoe et al. (1999).*

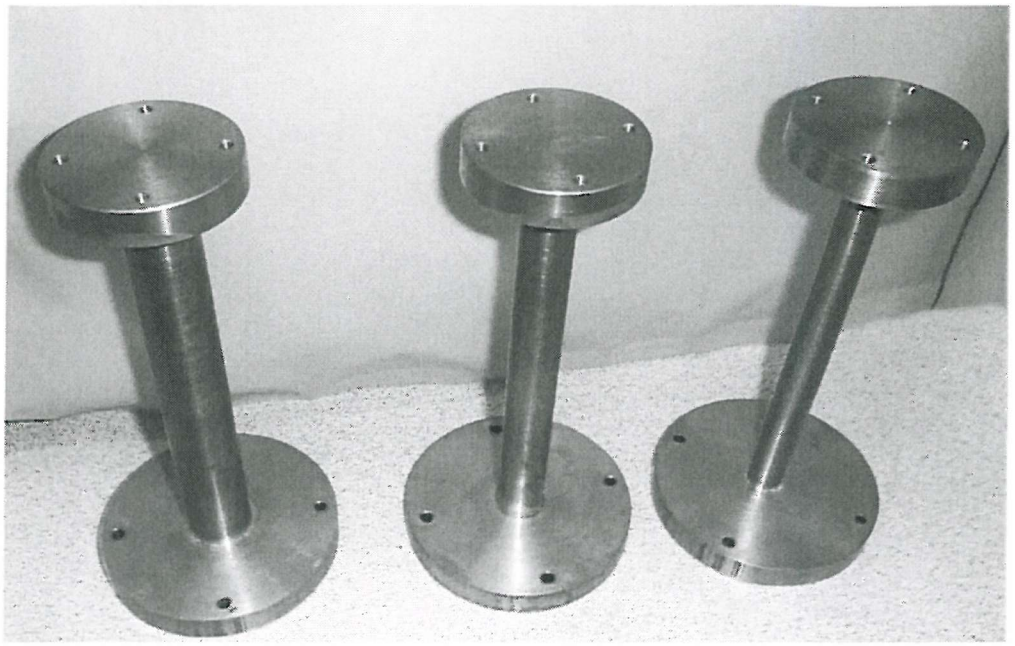

Figure 4.3: *Examples of the brass calibration bars used in the calibration of the resonant column.*

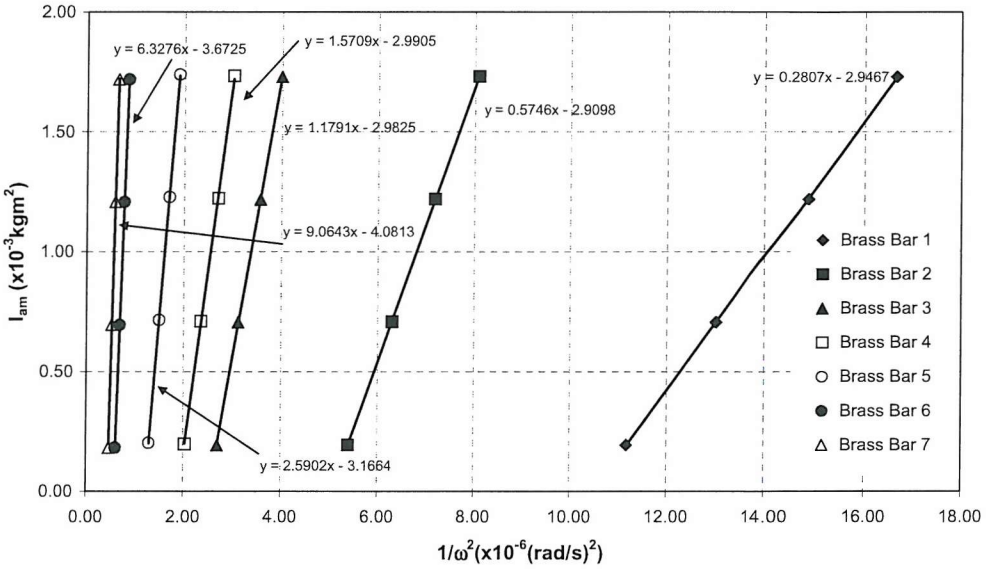

Figure 4.4: *Plot of I_{am} versus $1/\omega^2$ for brass calibration bars.*

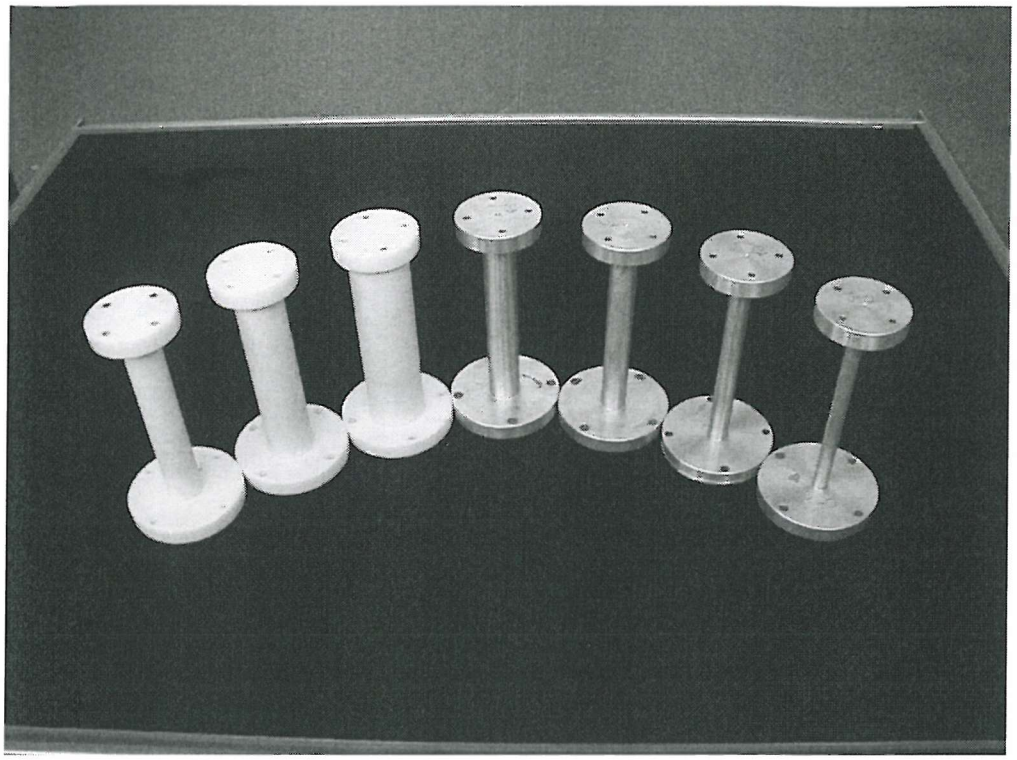

Figure 4.5: *Aluminium and nylon calibration bars.*

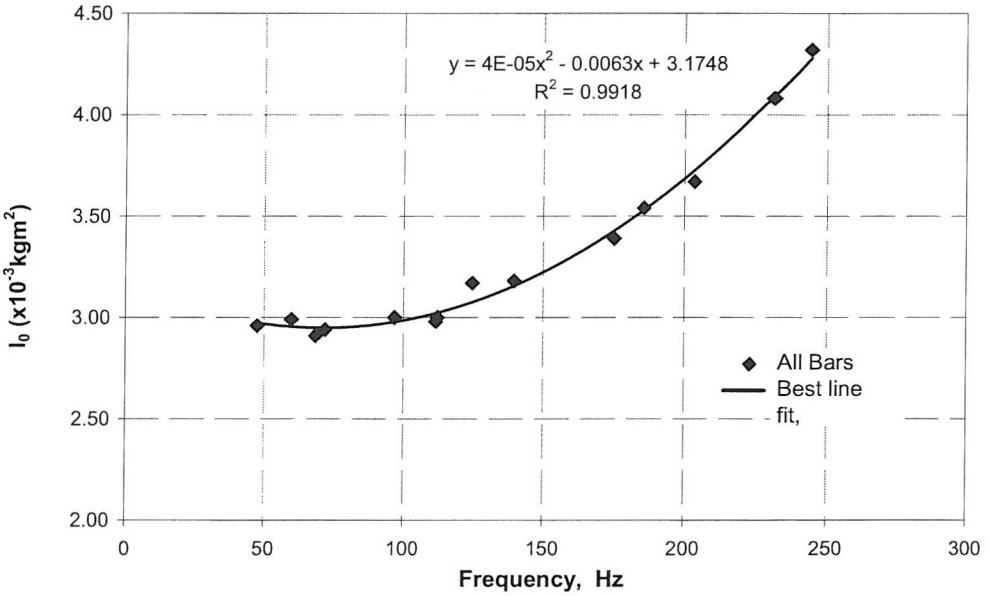

Figure 4.6: *Plot of frequency versus I_0 for all calibration bars.*

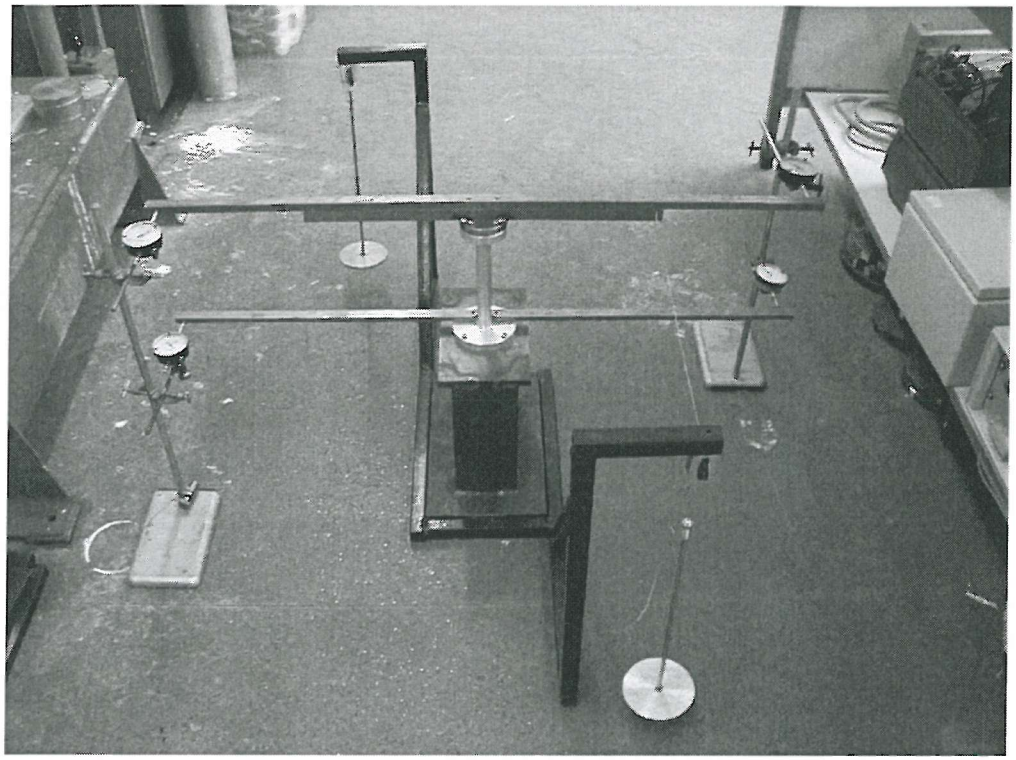

Figure 4.7: *Calibration frame for undertaking static torsional tests.*

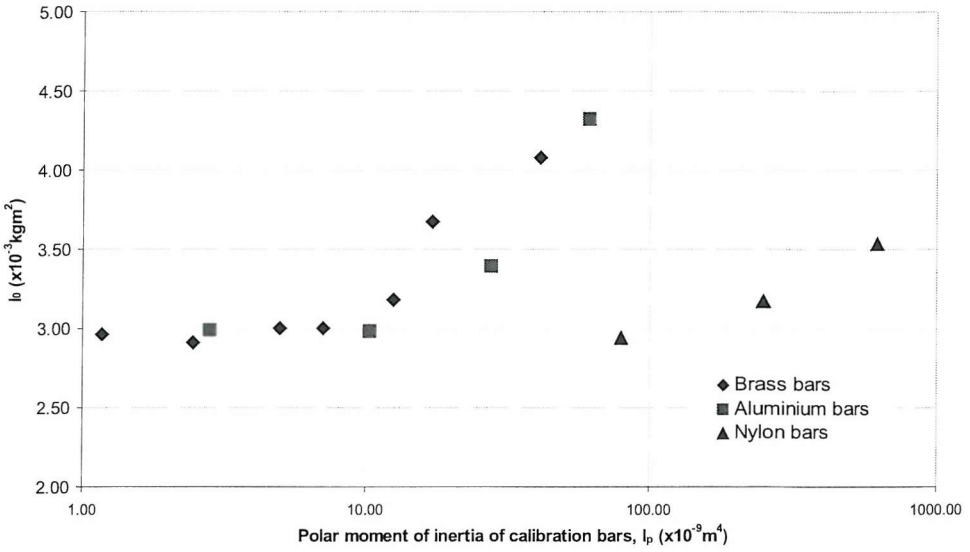

Figure 4.8: *Comparison of polar moment of inertia of calibration bars and mass polar moment of inertia of drive system.*

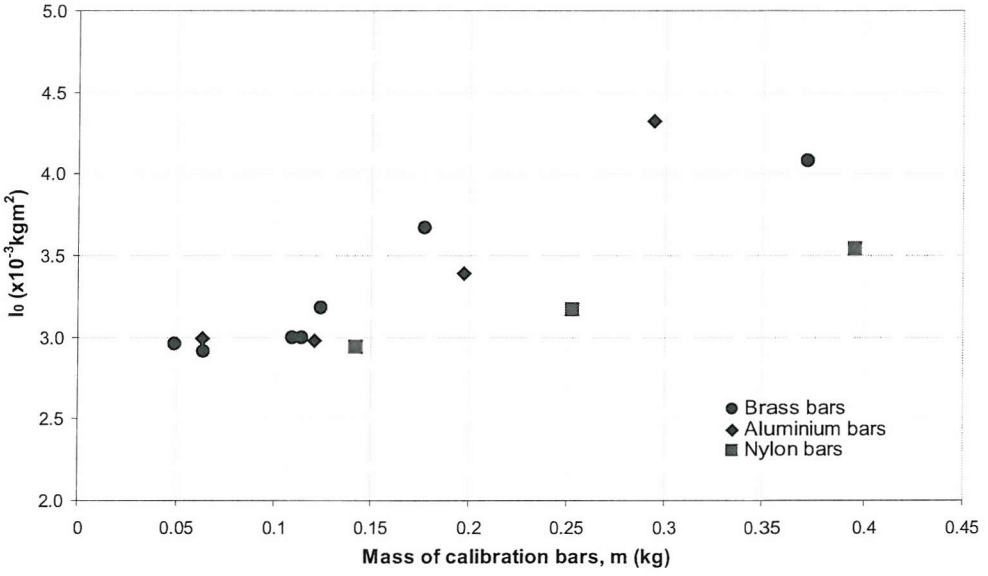

Figure 4.9: *Comparison of mass of calibration bars and mass polar moment of inertia of drive system.*

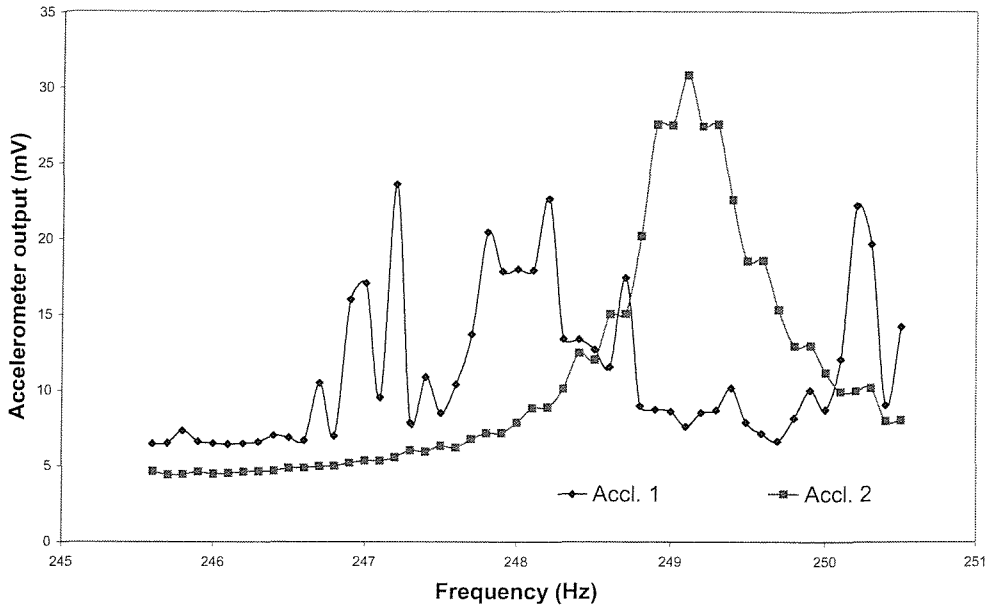

Figure 4.10: *Frequency response curve for Aluminium Bar 4 with different sensitivity accelerometers (Accl. 1 and Accl. 2) independently fixed onto the base plate of the calibration bar.*

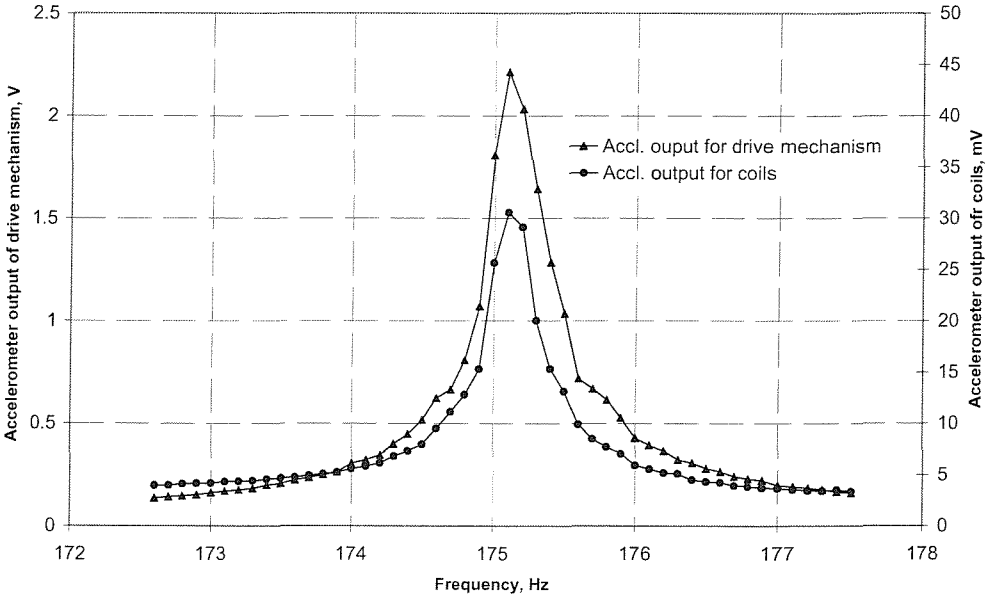

Figure 4.11: *Comparison of movement between coil and drive mechanism during test on Aluminium Bar 3.*

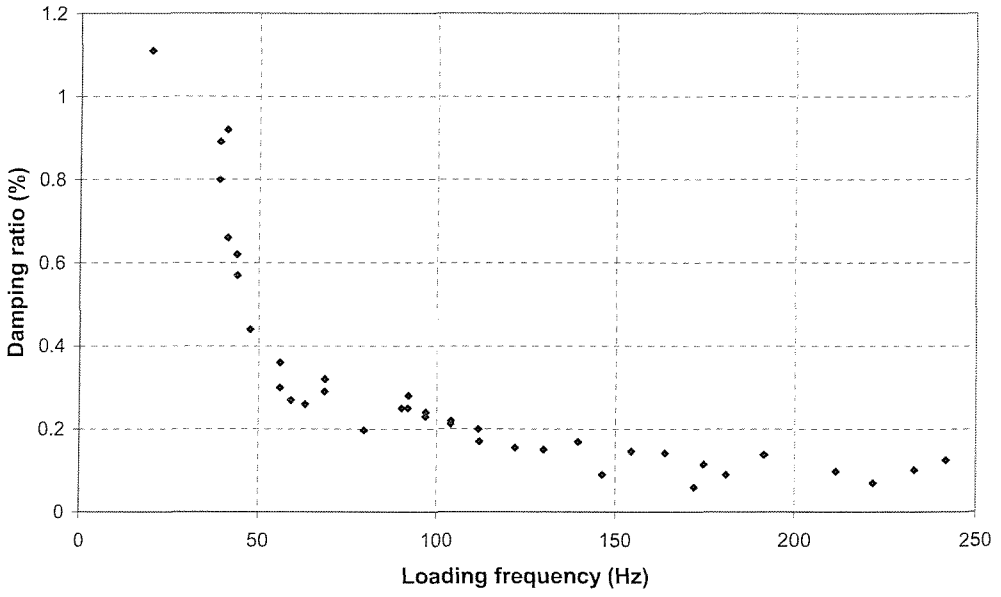

Figure 4.12: *Equipment damping for SRC as a function of frequency.*

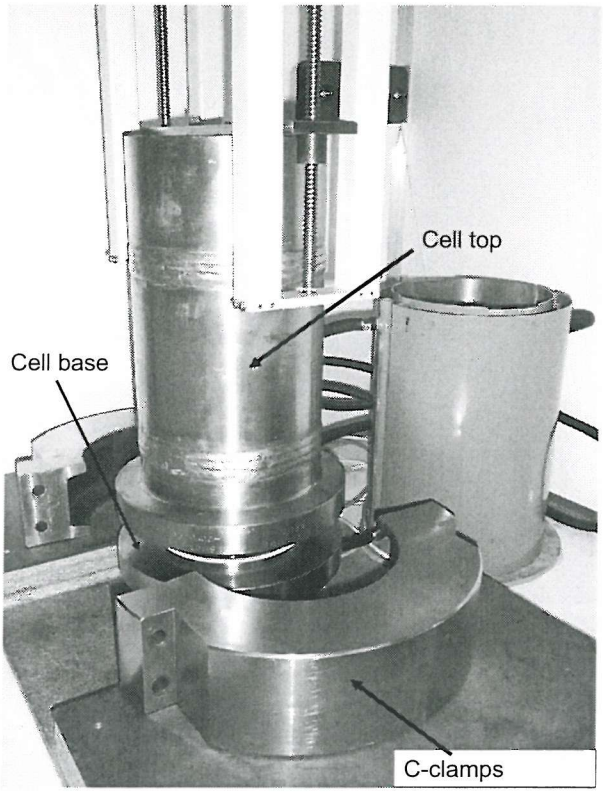

Figure 4.13: *GHRC pressure cell base, and top, with 'C'-clamps.*

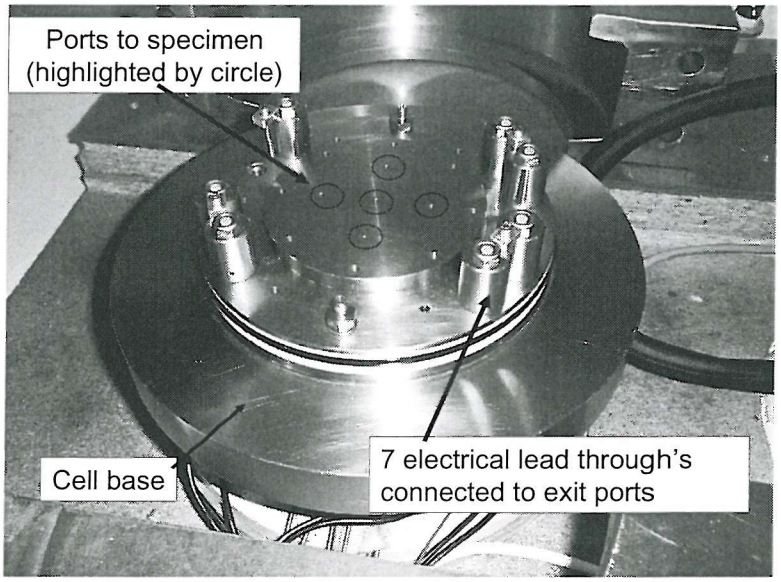

Figure 4.14: *GHRC cell base showing 5 ports to the specimen and 7 electrical connection ports around the perimeter of the cell base.*

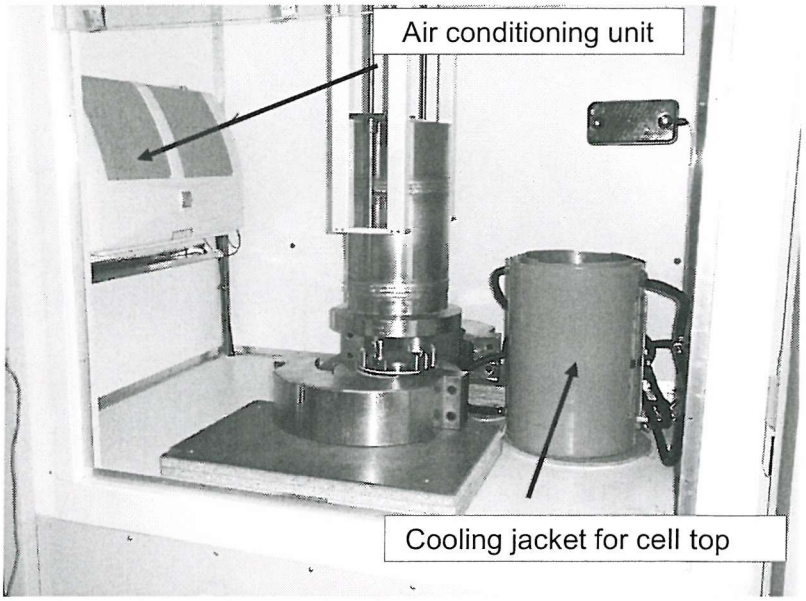

Figure 4.15: *Environmental chamber showing air conditioning unit and fluid cooled jacket for cell top.*

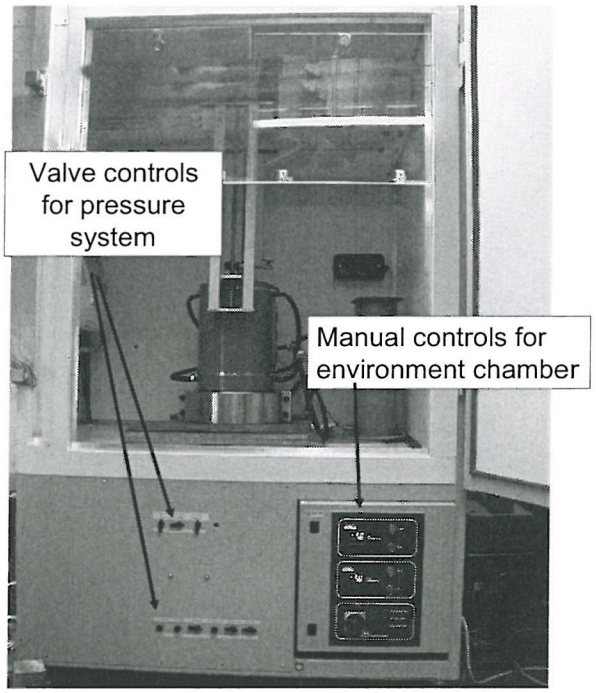

Figure 4.16: *Environmental chamber with manual controls mounted below the working space.*

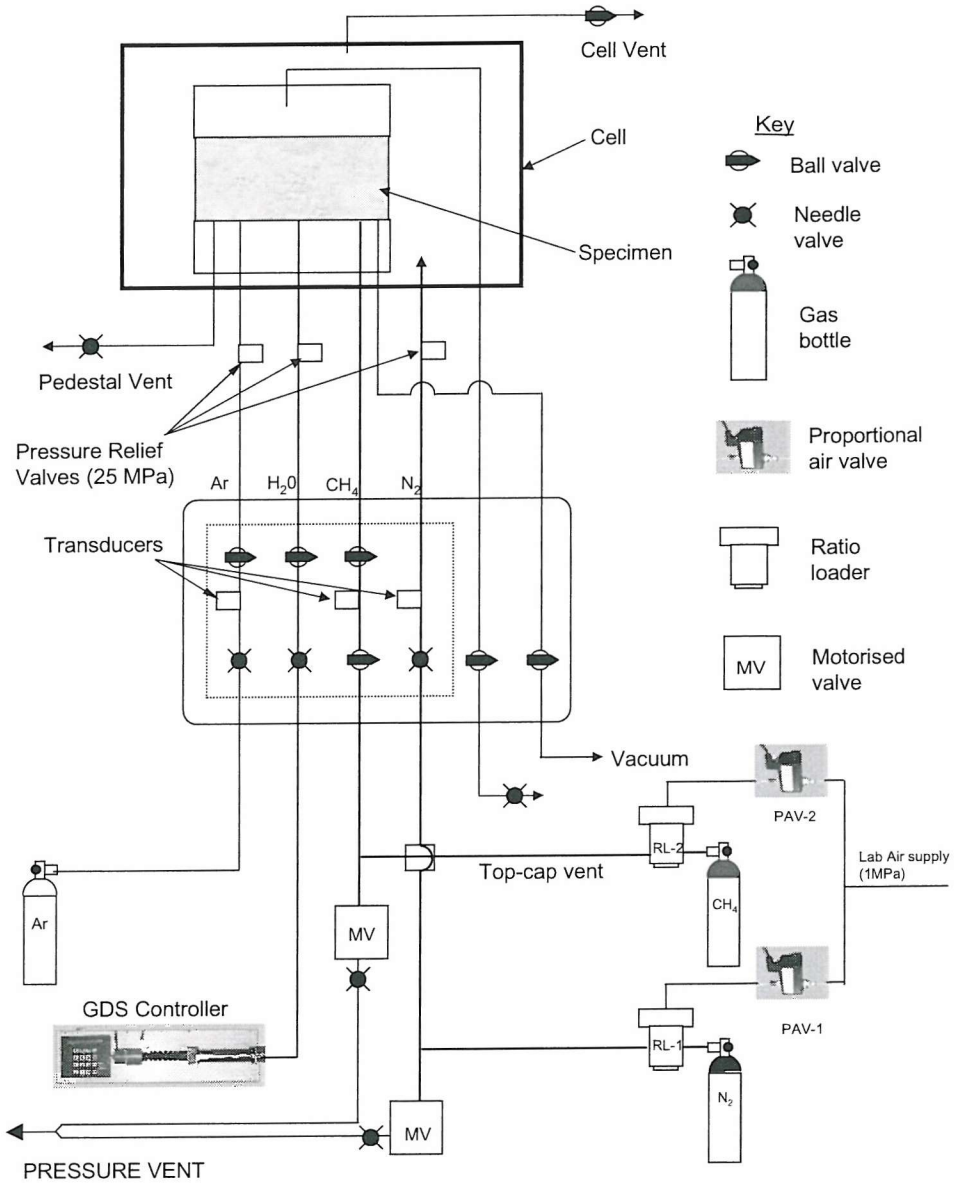

Figure 4.17: *Schematic diagram of pressure system for GHRC.*

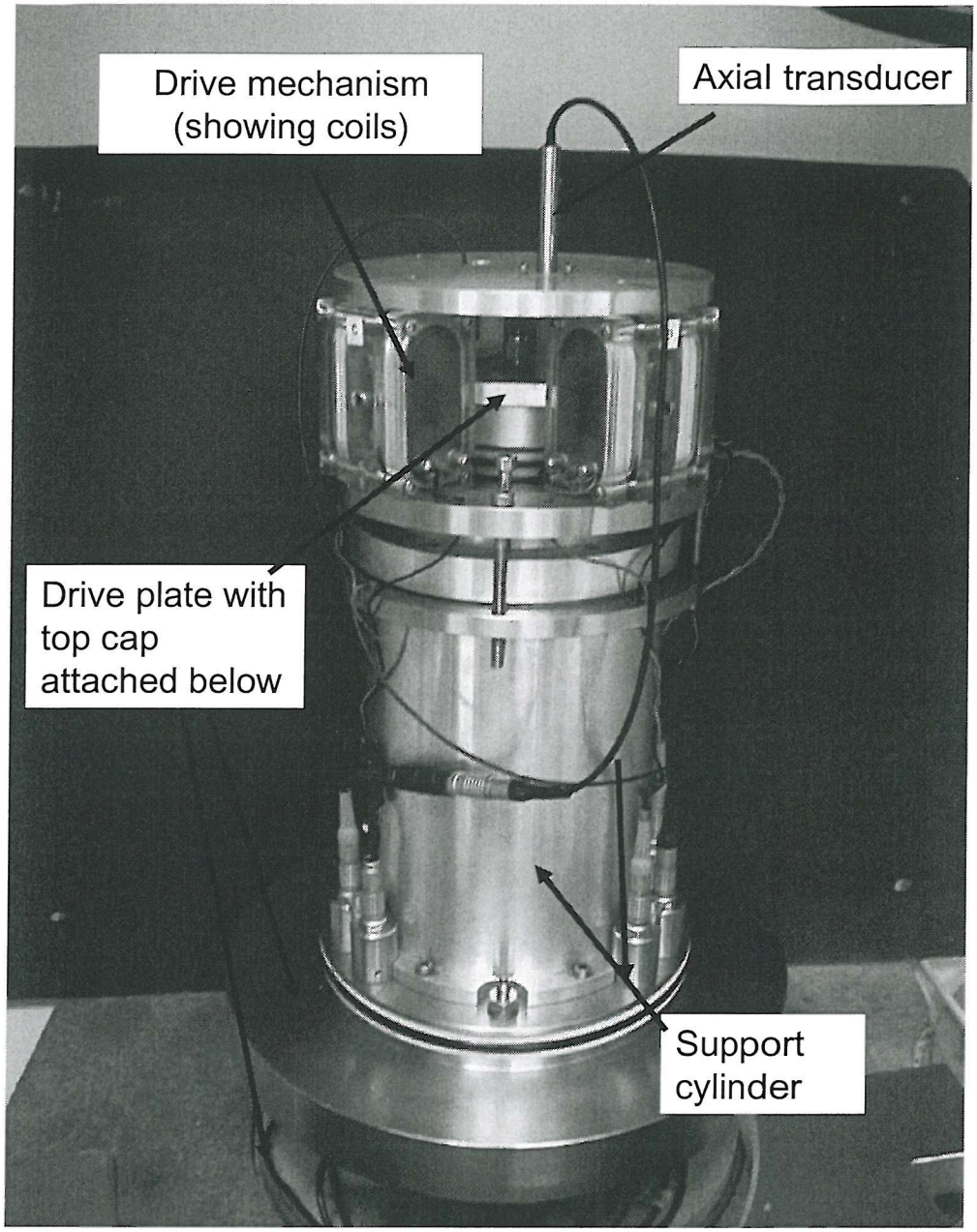

Figure 4.18: *GHRC drive system showing support cylinder.*

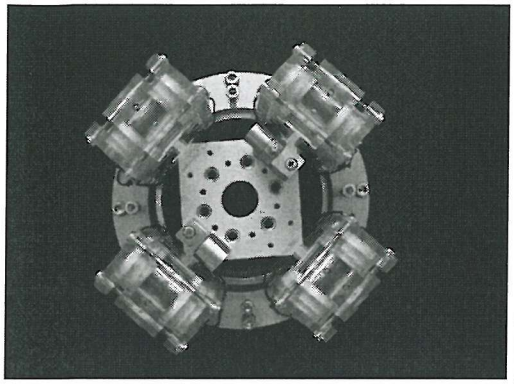

(a) Plan of GHRC drive system.

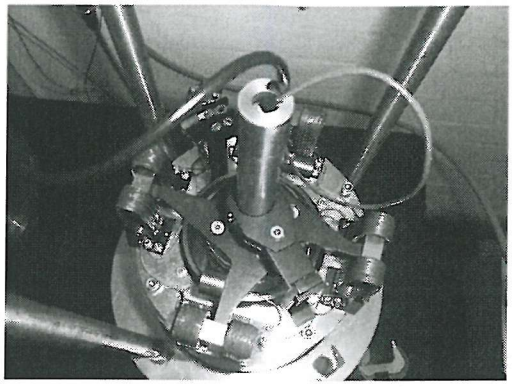

(b) Plan of SRC drive system.

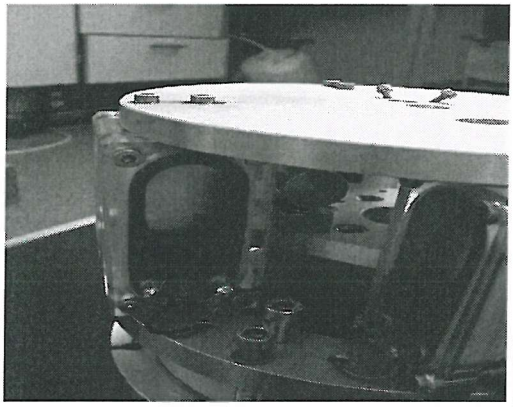

(c) Side view of GHRC drive system.

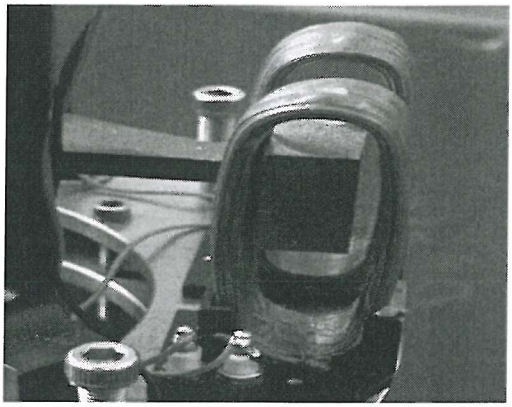

(d) Side view of SRC drive system.

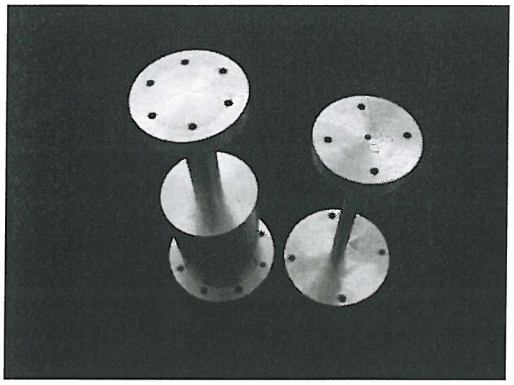

(e) Comparison of GHRC(left) and SRC calibration bars.

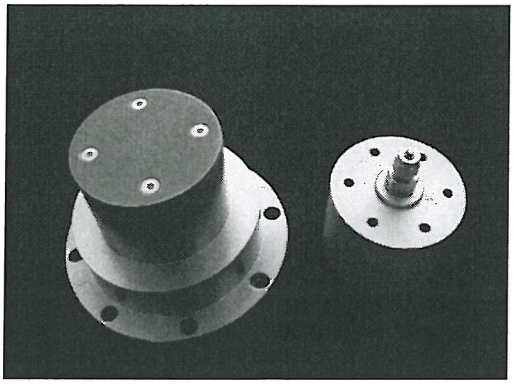

(f) Top cap and base platen for GHRC.

Figure 4.19: Comparison of GHRC and SRC to highlight design improvements.

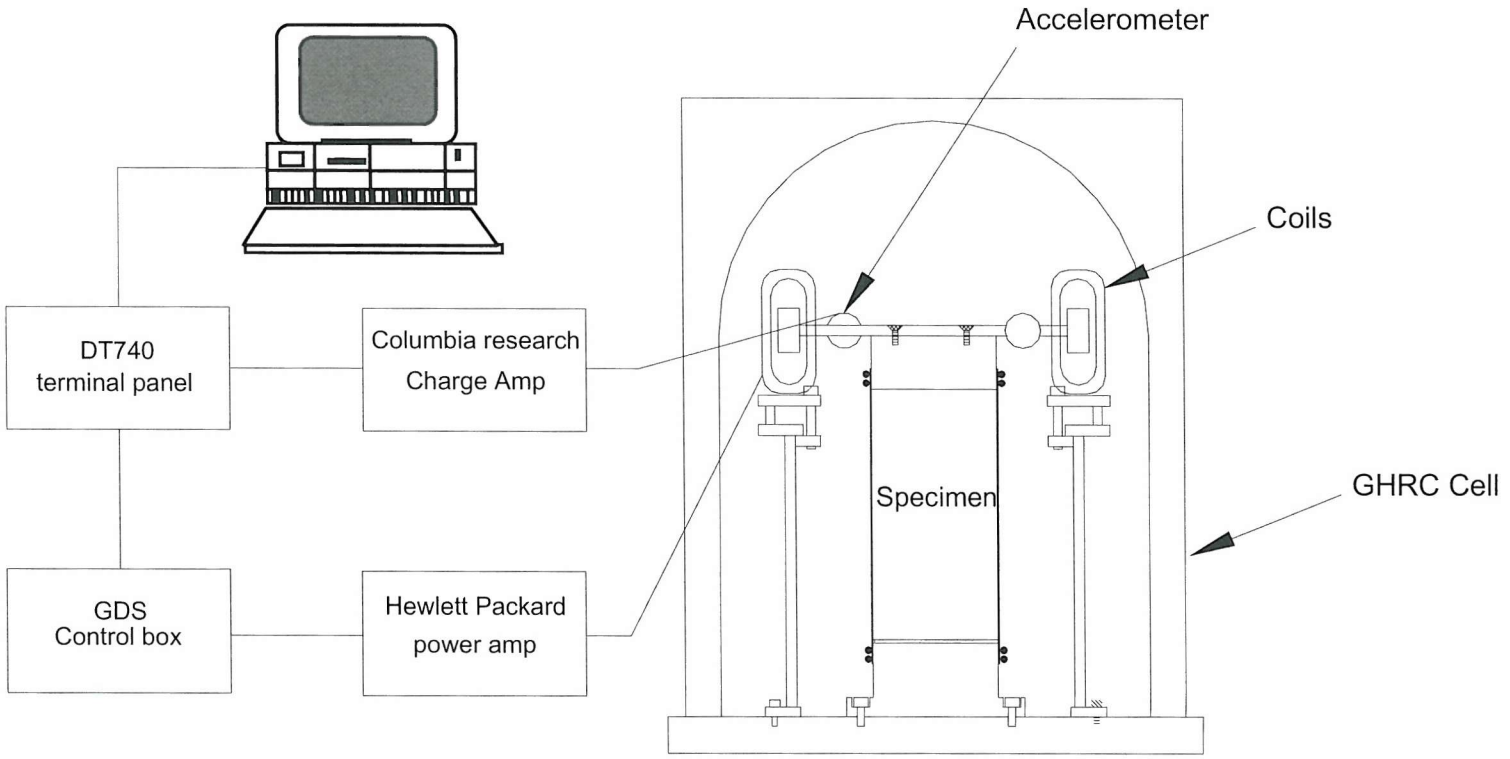

Figure 4.20: *Schematic of GHRC set-up for resonance testing.*

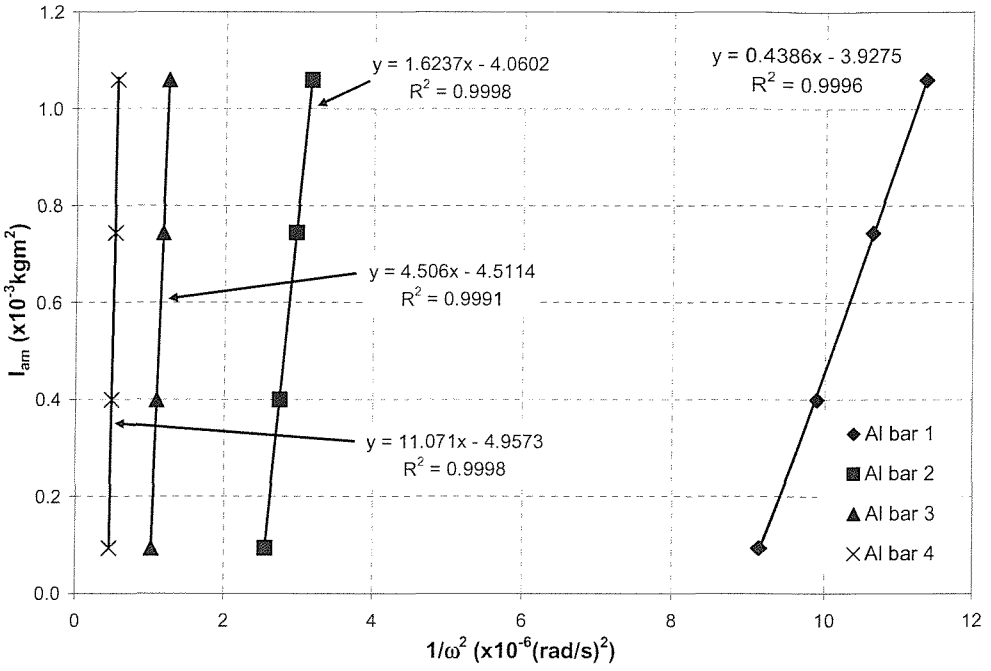

Figure 4.21: *Plot of I_{am} with $1/\omega^2$ for GHRC using aluminium bars.*

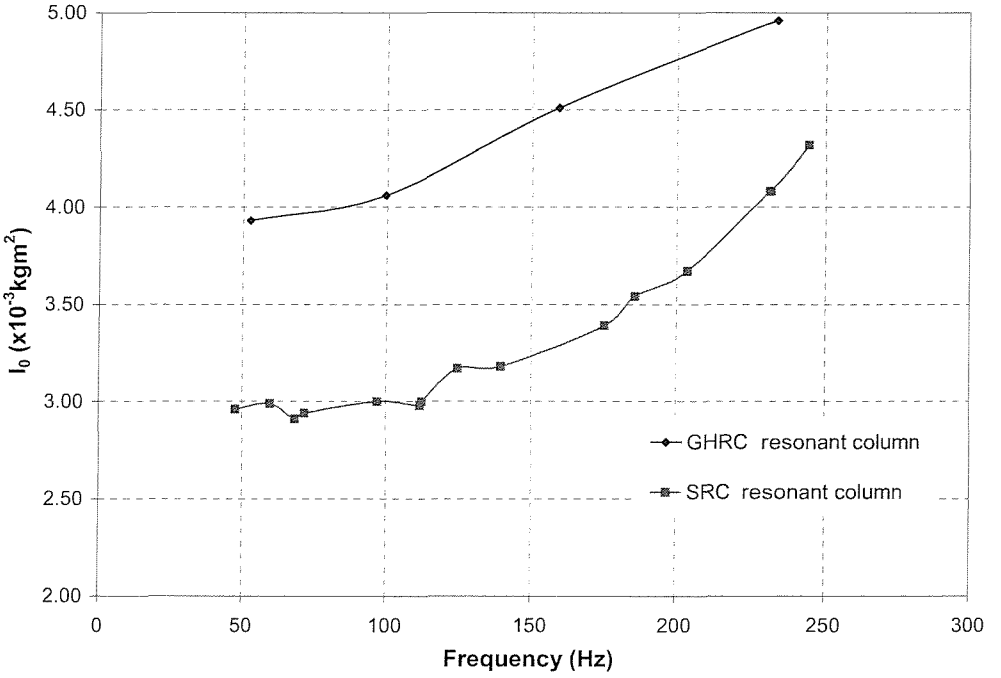

Figure 4.22: *Comparison of I_0 values obtained during calibration test for GHRC and SRC.*

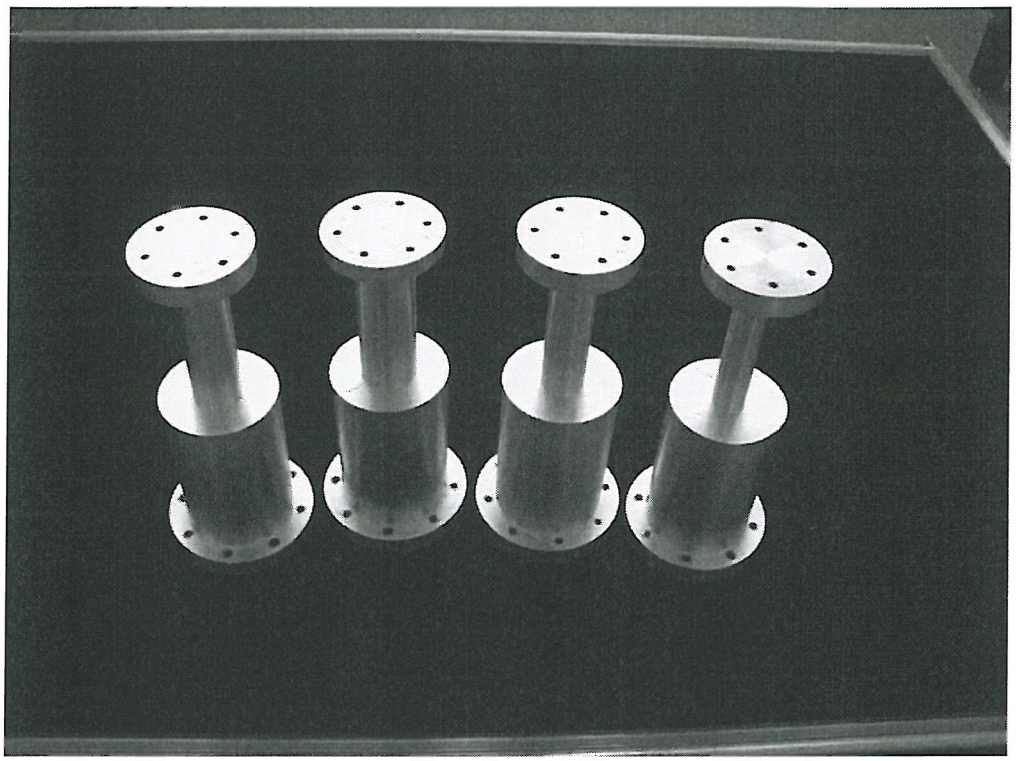

Figure 4.23: *Photograph of new aluminium calibration bars for GHRC with additional fixing points.*

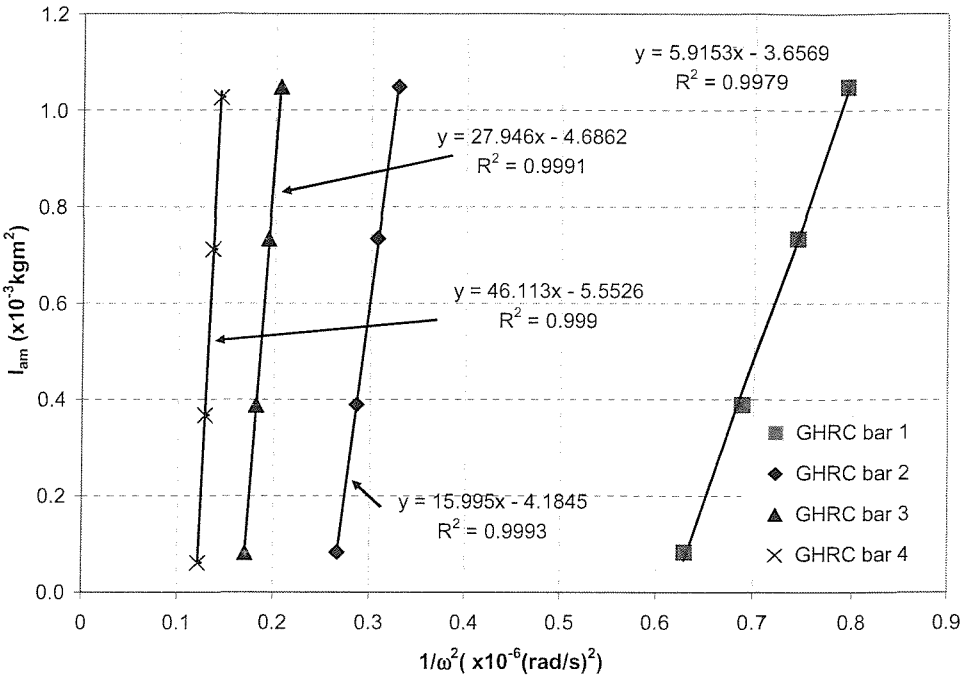

Figure 4.24: *Plot of I_{am} with $1/\omega^2$ for GHRC using new GHRC calibration bars.*

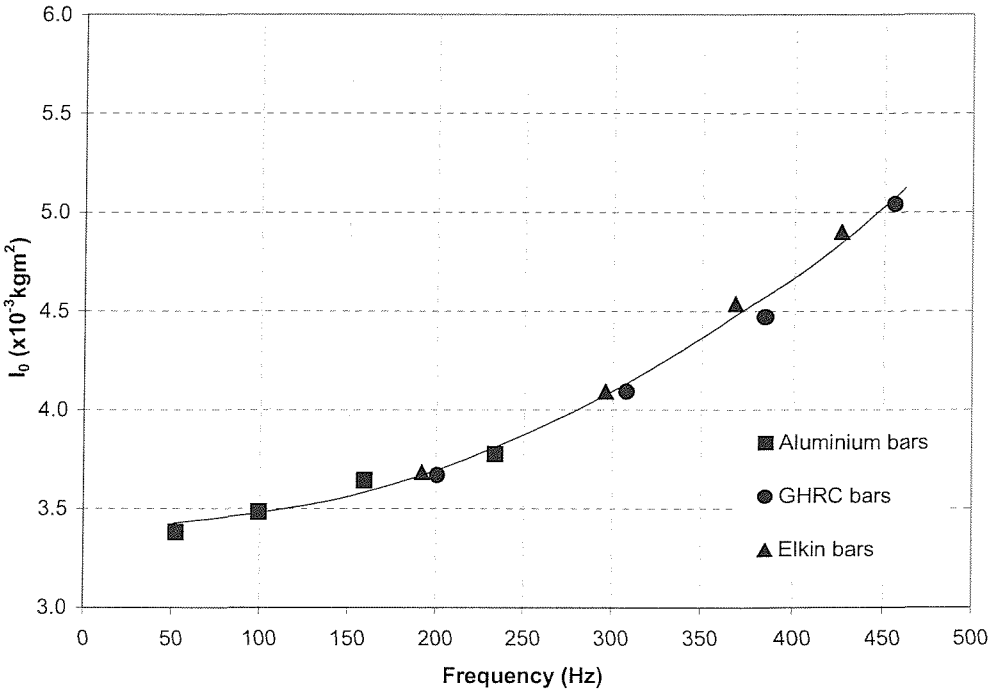

Figure 4.25: *Calibration curve for GHRC using regression analysis.*

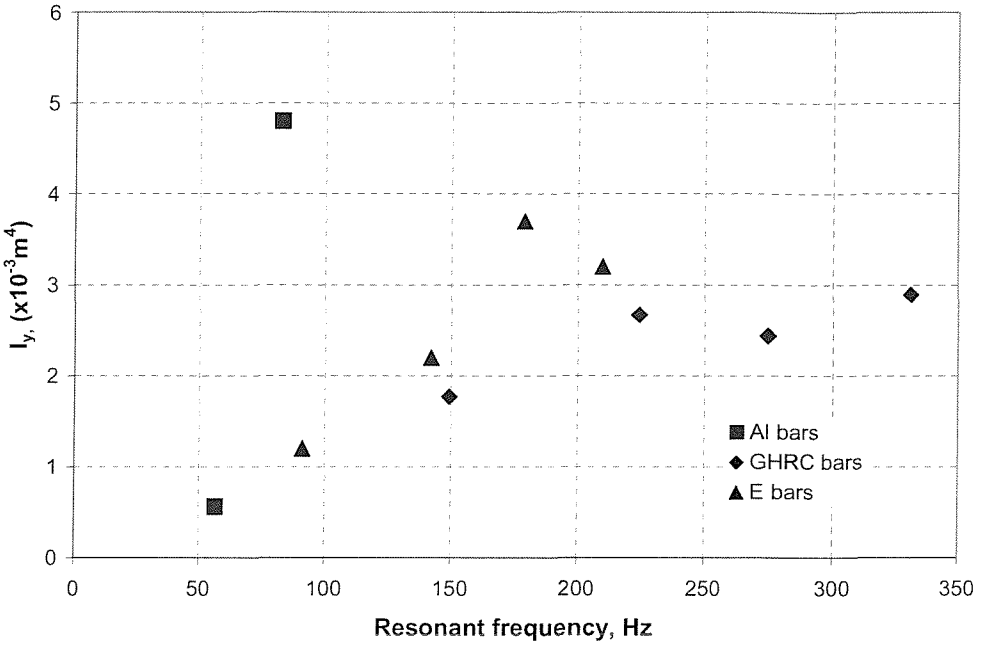

Figure 4.26: *Plot of computed I_y values against frequency for flexural vibration using Cascante's method.*

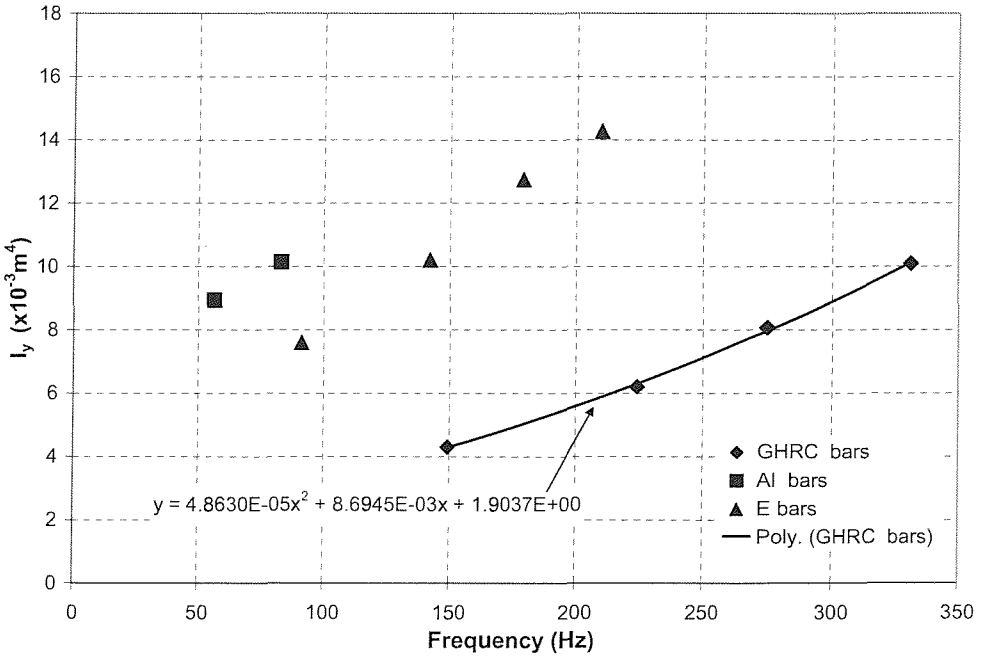

Figure 4.27: *Flexural calibration for GHRC using regression analysis.*

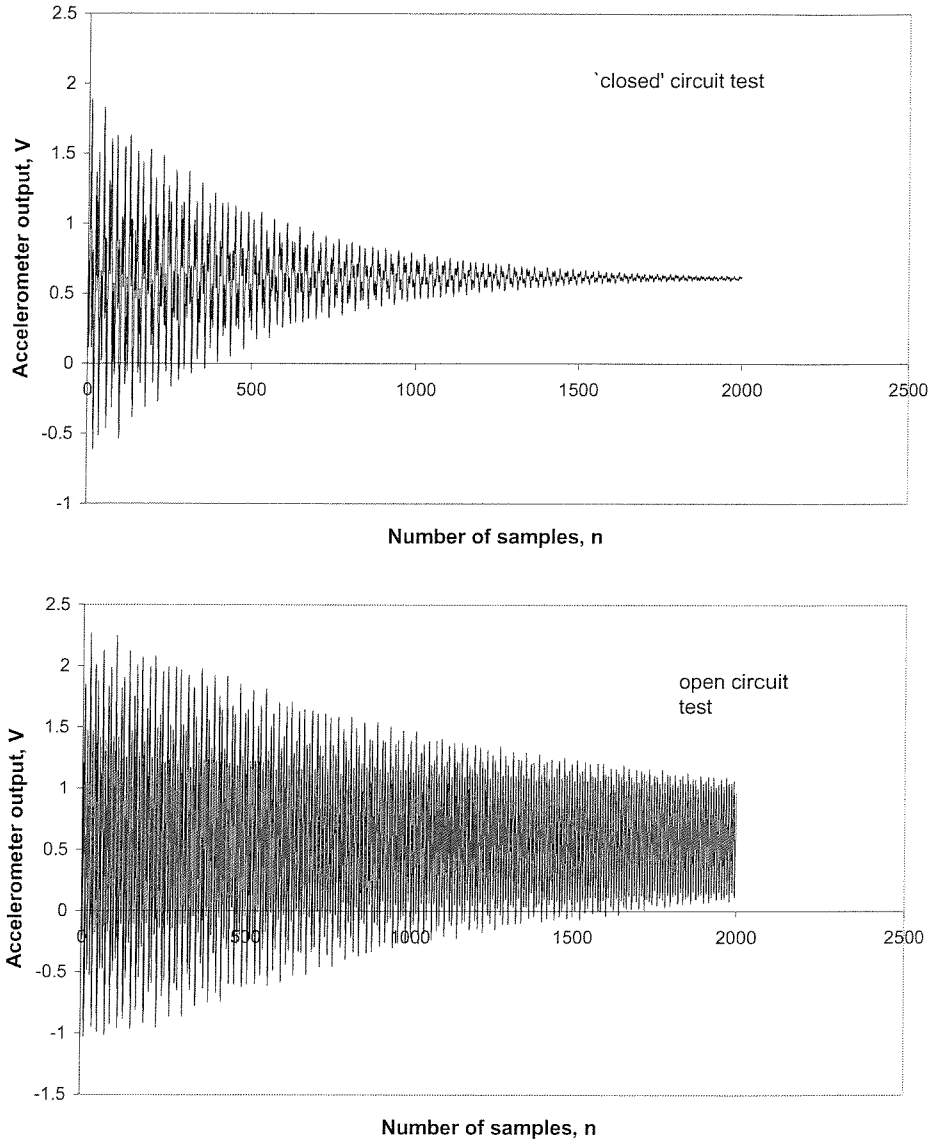

Figure 4.28: *Comparison of free vibration decay plots using an 'open-circuit' and 'closed-circuit' arrangement for aluminium bar 4.*

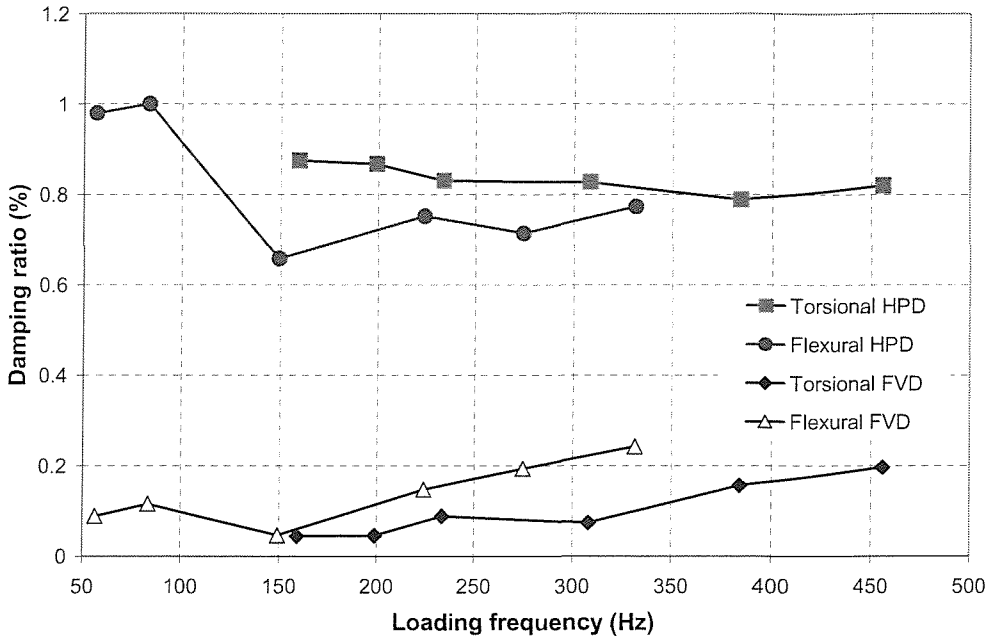

Figure 4.29: *Measurement of damping using the half-power method (HPD) and free vibration decay method (FVD) in torsional and flexural excitation for different calibration bars.*

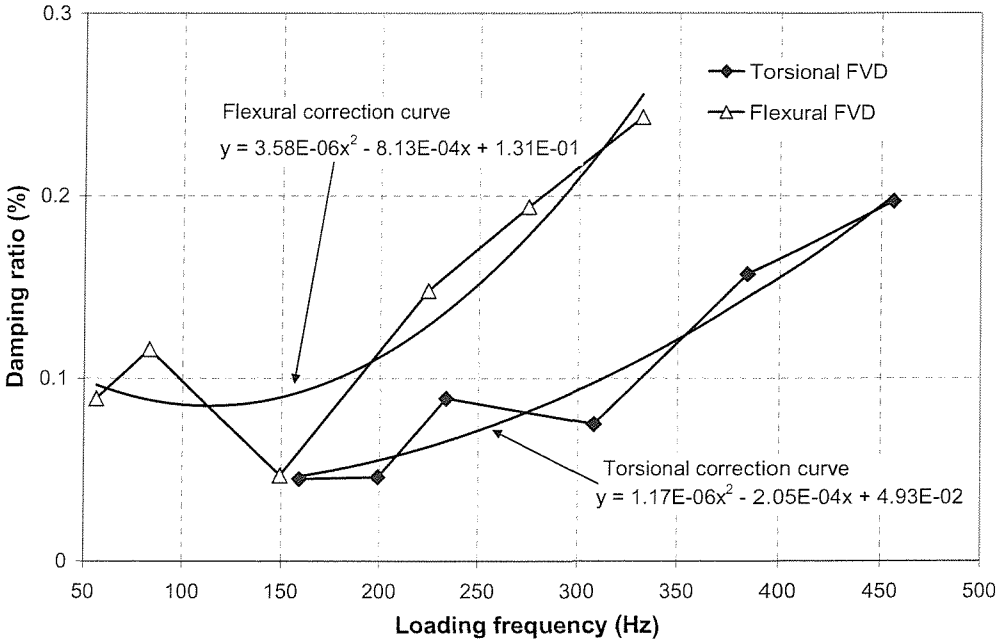

Figure 4.30: *Flexural and torsional damping correction curves from regression analyses of FVD damping data obtained for aluminium calibration bars.*

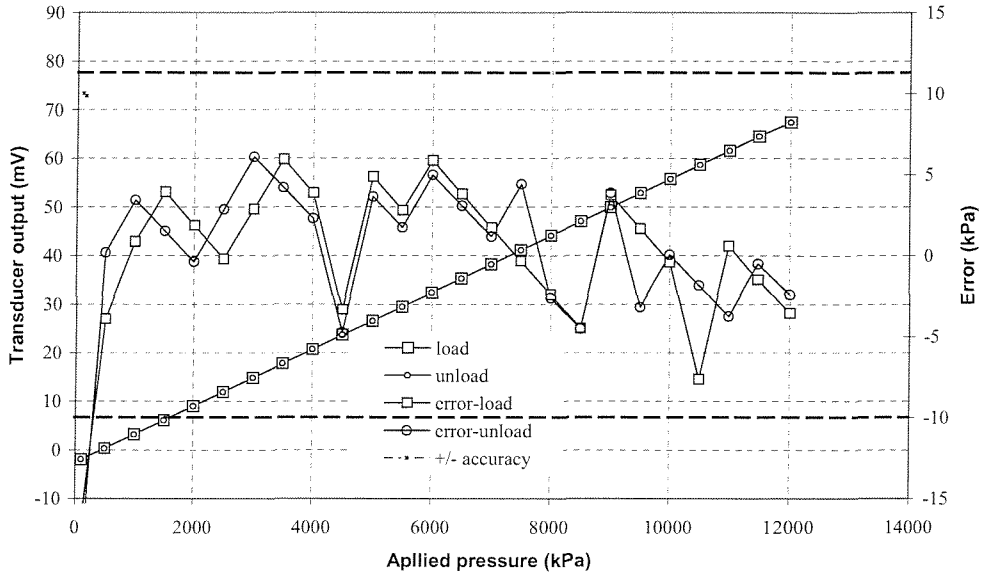

Figure 4.31: *Typical pressure transducer calibration graph (Cell pressure).*

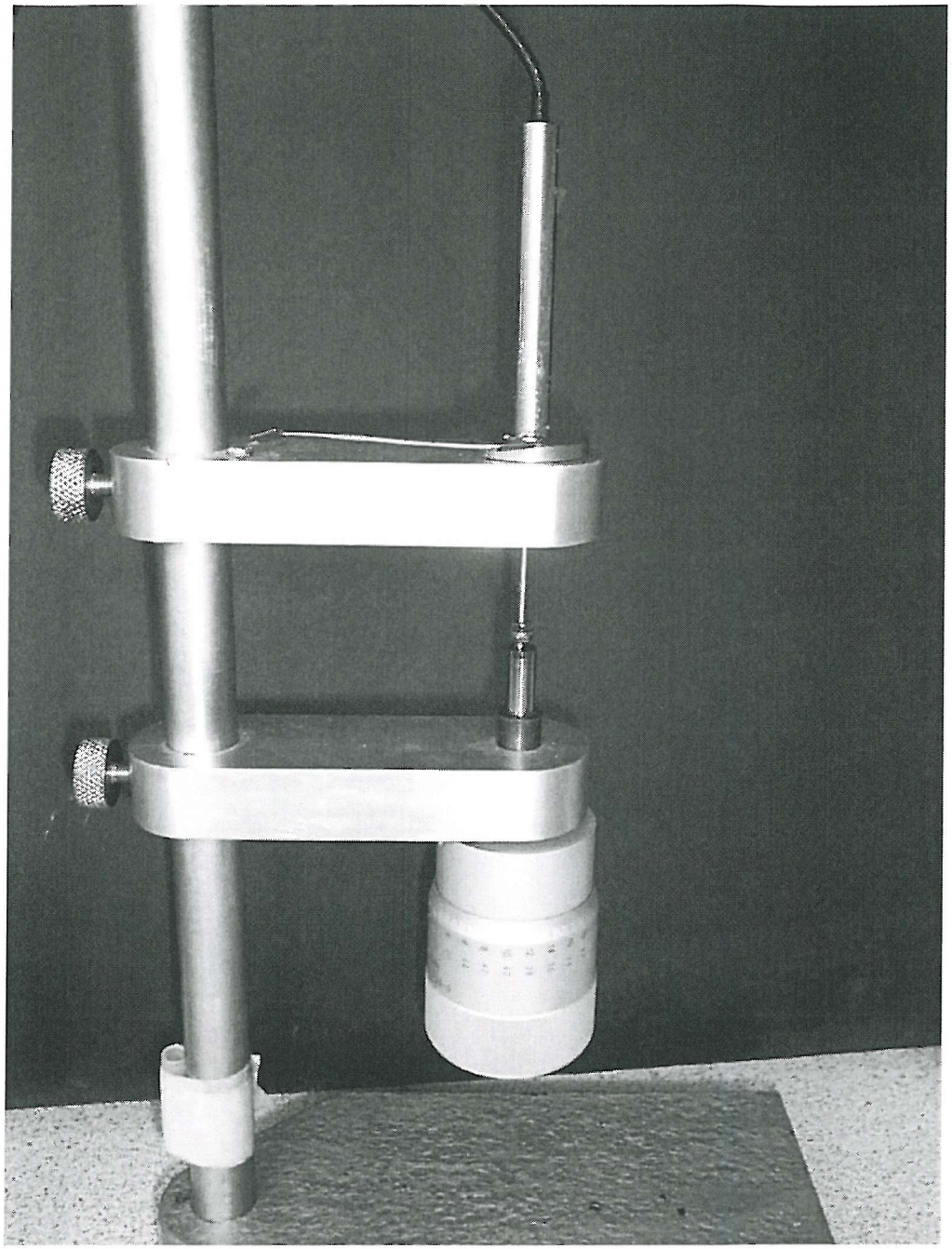

Figure 4.32: *Micrometer and frame for the calibration of axial LVDT.*

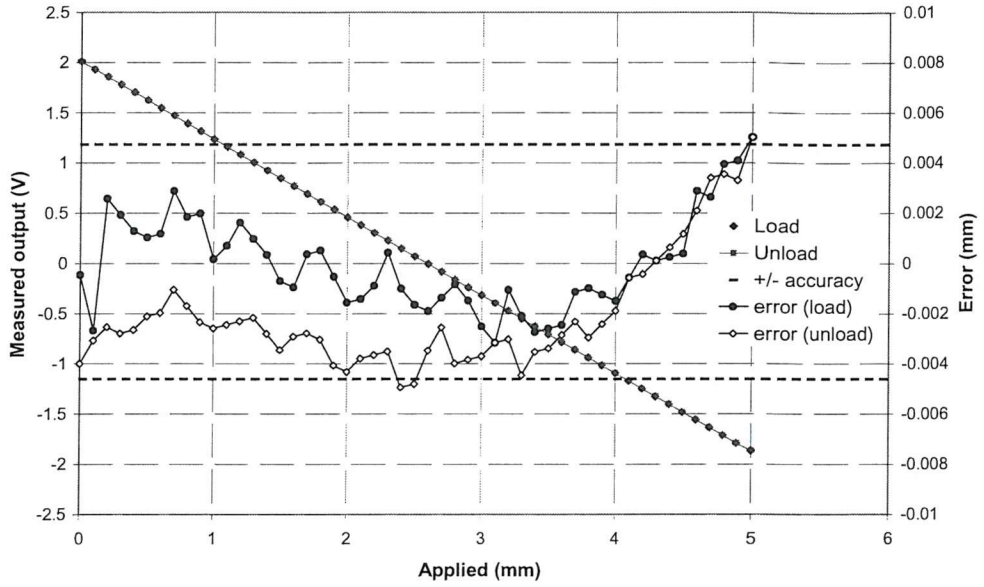

Figure 4.33: *Calibration graph for LVDT.*

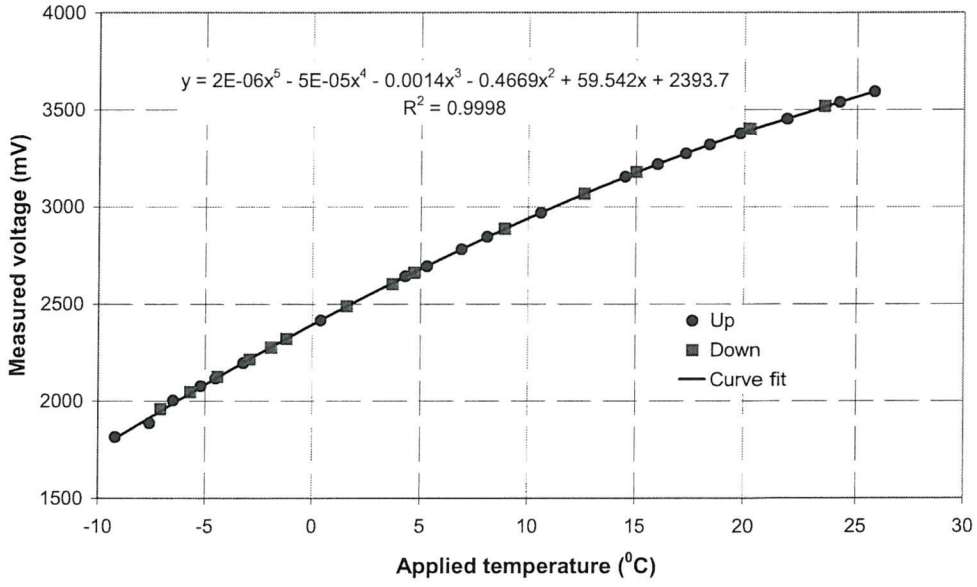

Figure 4.34: *Typical calibration graph of thermistor showing non-linearity.*

Chapter 5

LABORATORY TESTING

This chapter describes the formation and testing of numerous sand specimens containing varying proportions of methane gas hydrate in the pore space to determine their geophysical properties using the GHRC. The methodology for specimen preparation, containing sand/ice mixtures, and the subsequent hydrate formation procedure are highlighted. The procedure for resonant column testing is described and typical results for the tests undertaken are shown. Resonant column testing was also undertaken on the same specimens once the hydrate has been allowed to dissociate.

5.1 Material properties

The material used throughout this research was a Leighton Buzzard sand[1] of fraction E. Leighton Buzzard sand is a natural, uncrushed, rounded to sub-rounded silica sand, which is free from silt, clay or organic matter. The sand is classified as being part of the Lower Greensand sequence and outcrops at Leighton Buzzard, Bedfordshire, UK.

Fraction E is a fine sand with a particle size in the range $90 - 150\mu$m with a minimum 85% of the supplied sand being in the range. A maximum of 15% is either larger or finer. The specific gravity (G_s) of the sand was determined to be 2.65 (Method 8, BS1377:Part2:1990).

[1]Supplied by the David Ball group, Cambridge, U.K.

The maximum density of the sand was determined using the dry pluviation technique (Cresswell et al., 1999; Kolbuszewski, 1948; Rad and Tumay, 1987) which involves slowly raining sand down through diffuser meshes into a collecting pot. The pot was also situated on a vibrating table during the raining of sand. This method produced a maximum dry density of 1624kg/m^3. The minimum dry density was obtained using the tube method devised by Walter et al. (1982). This involves slowly raising a sand filled tube, situated in a collecting pot, and allowing the sand to exit the base. This allows air to be entrained in the sand leading to a minimum density. The minimum density, using this method was found to be 1331kg/m^3. Maximum and minimum void ratios, e, using the above techniques were calculated as $e_{max} = 0.993$ and $e_{min} = 0.633$.

5.2 Specimen preparation

The original methodology developed to form hydrate bearing sediments, using a modified version of the technique developed by Stern et al. (1996), proposed that the specimens would be prepared by raining a mixture of sand and ice grains, using the pluviation method, into a sample mold within the environment chamber at temperatures of -20^0C. The volume of hydrate could be controlled by the volume of ice added to the air dried sand. However, initial tests had shown that the sealing of the environment chamber to the ingress of warm moist air was problematic and ice formed on the cold surfaces preventing pluviation and also accurate determination of ice within the formed specimen.

The following description therefore identifies the steps adopted to allow the controlled mixing of sand and known volume of ice, where the distribution of ice within sand could be defined. Once this was achieved the ice was allowed to melt within the sand. The melting of the ice allowed individual sand grains within the vicinity of the ice grain to become water wet. Surface tension and capillarity restricted the migration of water within the fine sand ensuring an even distribution of moisture within the sand prior to specimen preparation. Once the specimens were prepared the pore water was frozen to prevent the

migration of water under high pore pressure.

5.2.1 *Sand and ice mixture*

The sand/ice mixture used in the formation of hydrate-bearing sands was formed by mixing known masses of sand and ice. The mass of sand was sufficient to make 70mm dia and 140mm long specimens. The volume of hydrate within either recovered or laboratory prepared specimens is historically defined as a percentage of the pore space. As the density of ice, 917kgm^{-3}, approximately equals the density of methane hydrate, 910kgm^{-3}(Sloan, 1998), the mass of ice required to fill a known volume of the specimen pore space, assuming a maximum dry density and complete conversion of ice to hydrate, could be estimated. The true volume of ice in the pore space is calculated from the specimen geometry after the specimen is formed.

The 'seed' ice is produced from triply distilled, de-aired water. The water was frozen in a single block which was subsequently ground using a domestic food blender. The grinding of the ice was carried out inside a chest freezer at -20^0C, in a number of 15 second cycles, to prevent melting and annealing of the ice grains. The ice grains were then sieved to 125-300μm grain size and stored in air tight freezer bags at the base of the chest freezer. The ground ice remains as individual grains if kept at temperatures below -12^0C (Stern, 2002). Therefore, to prevent the annealing of ice grains during their mixing with the sand, the sand was kept in air tight bags at the base of the same freezer.

A riffle box (Figure 5.1) was used to mix the ice and sand together. A riffle box is designed to produce two equal sub-samples, in the base trays, when the constituents are emptied through the top grill. By repeating this procedure several times an evenly distributed mix of sand and ice was produced. To ensure that uniform mixing was being achieved, thin sections from prepared specimens were obtained (using polypropylene beads as a replacement for the ice - polypropylene beads were chosen as they had approximately the same particle size and density as ice). Digital images were made of the thin sections

and analyzed (using Image-Pro Plus[2]) to compare the area fractions of the constituent parts that are visible. Table 5.1 provides details of these analyses for thin sections obtained from specimens containing 5%, 10% and 20% plastic beads by total volume. Figure 5.2 shows the digital images obtained from the thin sections for 5% specimens. The black spots are the plastic beads, the white spots are the sand grains and the light grey is the pore space filled with resin. It can be visually observed from Figure 5.2, which contains 5% plastic bead fraction, and Figure 5.3, which contains 20% plastic bead fraction, and Table 5.1 that the plastic beads are randomly distributed throughout the samples.

The hydrate content within the pore space was directly calculated from the mass of added ice and the dimensions of the prepared specimen. The sand that was used throughout this research was initially stored in a large plastic container, with a loose fitting lid, within the laboratory prior to being frozen in air tight bags. The humidity of this sand prior to being placed in individual airtight bags was assessed by oven drying (110^0C for 24hrs) three samples of sand. These were obtained from different positions within the container as the airtight bags were filled. The mass of absorbed water was found to be 2.33g/1000g of sand, 2.35g/1000g and 2.39g/1000g giving an average mass of the absorbed water of 2.36g/1000g of sand. This value of absorbed water was excluded from the calculation to determine the volume of hydrate within the pore space. Towards the end of the research programme further sand was taken from the container and the mass of absorbed water was measured at 2.58/1000g of sand (This was in July whereas the previous tests were conducted in the January). Calculations had shown that this volume of absorbed water was insufficient to completely cover the individual sand grains in a monolayer of water. Once the testing was complete the moisture content for some the samples were checked to see if any drying occurred during the test. For the samples tested it was found that on average 1.94g of additional moisture was present than that which was added. This suggests that no appreciable drying occurred during the hydrate formation, testing

[2]Image-Pro Plus is a computer programme designed by Media Cybernetics L. P., Silver Springs, M.D., U.S.A. for the analysis of digital images

and dissociation stages

5.2.2 *Specimen preparation*

Once the ice and sand were mixed, placed in air tight bags, and the ice allowed to completely melt specimens were prepared by tamping the 'moist' sand into a sample mold to produce dense sand samples. Dense sand specimens were formed to limit variations in void ratio between specimens since this has been shown to have a major influence on the small strain stiffness of sands. Visible observations of the sand, after the ice had melted and on subsequent freezing of the specimens (moisture contents of 5%), showed uniform distribution of the water.

The specimen preparation followed a sequence of steps, for all specimens tested, which were as follows;

- A thin film of silicone-based lubricant was applied to the base pedestal and a butyl membrane placed over it, ensuring a smooth fit.
- A split sample mould was placed around the membrane, with the membrane being turned over at the top edge.
- The sample mould was filled with pre-weighed 'moist' sand in 7-8 equal layers with each layer being tamped, using a timber rod with a flat rubber end cap. This allowed a dense specimen to be formed, which would also reduce any possible sample disturbance during set up. Care was taken to capture any spilled sand.
- The top cap was carefully placed on top of the sand ensuring it was horizontal. A thin film of lubricant was applied to the top cap and the membrane turned up to provide a seal. A negative back pressure was applied to the specimen (-50kPa, via a vacuum - once at -50kPa the vacuum valve is closed) to facilitate the removal of the split mold and help reduce any free air. This was left on the specimen for 1hr to identify any leakage in the membrane or between the membrane and the base pedestal, or the membrane and top cap.

- Any 'moist' sand left over was weighed, oven-dried and reweighed to ascertain the mass of water remaining in the left over sand.
- The diameter of the specimen was measured (±0.02mm) and recorded for three separate points along the length of the sample with measurements taken at two orthogonal points at each section. The height of the specimen was taken (±0.5mm) at two orthogonal points and recorded.
- A thin fihn of lubricant was applied to the membrane and a layer of aluminium foil was placed over it. The foil was lubricated and then a latex membrane was placed over it to keep aluminium foil in place. Two 'o' rings were placed over the membranes onto the base pedestal and top cap respectively. Although the butyl membrane was sealed sufficiently to hold a vacuum without the 'o'rings it was thought prudent to have them attached when the high cell and back pressures were being used.

Table 5.2 highlights the initial properties of the specimens tested during this research. Two specimens were prepared without any ice in the pore space and at differing relative densities (loose specimen (H0L) and dense specimen (H0D)). These were used to explore the effects that density variations alone might have on the seismic properties of the specimens. Specimens H0L through to H40 were initially prepared and tested with specimens H3-2 to H5-2 being subsequently prepared, and tested, to validate the results obtained for specimens H3-1 to H5-1.

During the commissioning of the GHRC apparatus and the development of the testing program several issues were highlighted. These included: the diffusion of gases through the membranes; and the damping effects of viscous oils used as a cell fluid. It has been shown (Bishop and Henkel, 1962) that standard latex membranes are air permeable. As both the cell pressure and pore pressure are provided by gases it was thought likely that gas interaction and possible loss of effective stress might be possible. The use of silicone oil as a barrier, between the cell pressure and pore pressure(Figure 4.2), would be ineffective as tests had shown large outgassing of the oil after high cell pressures were applied. It was also considered likely that the inertial effect of the viscous cell fluid might affect the measured damping properties in flexure.

Therefore butyl membrane were used to encapsulate the specimen as these were considered to have a very low gas permeability. As an added precaution aluminium foil was also placed between the butyl membrane and a standard latex membrane to help hinder the migration of gases into, and out of, the specimen. During testing no loss in the value of effective stress was recorded with time suggesting that use of butyl membrane and aluminium foil was effective.

Calculation on the torsional and flexural stiffness of the aluminium foil and two membranes had shown the ratio of specimen stiffness (for a loose sand) to combined membrane stiffness to be in the order of 3800 and 5600 for flexural and torsional stiffness respectively. Therefore no corrections were made to the test data to take account of the additional stiffness of the membranes. The difference in membrane stiffness to specimen stiffness was deemed high enough to present no significant loss in accuracy to the measured values.

5.2.3 *Apparatus set-up*

Once the specimen was formed the GHRC apparatus was set up to allow testing of the specimens once hydrate formation was complete. Again, a sequence of events was followed, to ensure correct alignment of the drive plate and coils, and that all electrical connections were made. The steps were:

- Thermistors were attached to each side of the specimen at mid-height using rubber bands.
- The drive mechanism and support frame were gently lowered over the specimen, ensuring that the drive plate rested gently on the top cap and that the thermistor leads were not trapped. The drive mechanism position was adjusted until the fixing holes for the top cap and the drive plate were aligned and the magnets attached to the arms of the drive plate were centred in the middle of the coils. The support ring for the coils was then clamped to the support frame by four M5 machine screws. The drive plate was then attached to the top cap by six M5 countersunk screws. Finally the support frame for the drive mechanism was attached to the base of the cell with eight M5 screws

- The thermistors were connected to the correct electrical lead through and the accelerometer cable was connected to the accelerometer. The unattached end of the accelerometer cable was pulled through the coil restraining plate and connected to its lead through. The coil retaining plate was then fixed to the top of the coils using eight M4 screws.
- The LVDT was connected to the retaining plate and adjusted to give sufficient vertical movement to the centre core. The LVDT lead was connected to its lead through and the given value, using the GDSLab computer system, was altered until zero displacement was read.
- The electrical connections for the four coils are connected to their individual lead through's and a broad sweep, using a low input voltage, was undertaken to test the that the coils are working.
- The cell top was lowered and the 'C'-clamps secured by four M16 bolts.
- A nitrogen gas cell pressure of 250kPa was applied to the specimen whilst slowly releasing the vacuum.

5.3 Hydrate Formation

After the application of the nitrogen gas cell pressure the temperature of the cooling systems (environment chamber and the cooling jacket as shown in Figure 4.15) were set to -15^0C and left overnight to allow the formation of ice within the pore space of the specimen. Once frozen, a methane gas back pressure was applied to the specimen and slowly raised, with cell pressure increasing, accordingly, to maintain an effective pressure of 250kPa$\pm$50kPa on the specimen, over 1-1.5hrs up to 15MPa using GDSLab. This high pressure, which is well within the methane gas hydrate phase boundary (Figure 1.1) was applied to the specimen to allow the complete formation of gas hydrates in a reasonable time span (Section 2.7). Once the target pressures had been reached, these values were maintained for a further 30mins to allow for any relaxation in the pressure system that might occur. After this period both applied pressures were 'locked off', using the ball valves below the pressure

transducers (Figure 4.17). The recorded values from the pressure transducers were monitored for 15mins to ensure no leaks within the systems were evident. The temperature of the environment chamber was then set to 10^0C, which caused a slow warming of the specimen. Due to the large mass of the cell base, and cell top, the time taken to raise the specimen temperature to the target value was approximately 15mins per degree centigrade. Once the specimen temperature was at 10^0 the temperature was maintained overnight to allow for the full conversion of ice to hydrate. Once full ice/hydrate conversion was deemed to have occurred the specimen temperature was reduced to 3^0C and, once achieved, the pore pressure was reduced to 5MPa, whilst maintaining a 250kPa$\pm$50kPa effective stress on the specimen. Once stabilised the specimen was ready to undergo resonant column testing.

Figure 5.4 shows a typical temperature/pressure plot obtained during the hydrate formation phase. The graph shows the initial application of methane back pressure up to 15MPa and then the subsequent rise in the methane gas pressure as the specimen temperature was raised.

5.4 Resonant column testing

The testing program was designed to characterize the dynamic response of dry sand specimens, containing differing volumes of gas hydrate within the pore space under isotropic loading and unloading. Isotropic loading was applied in steps of 250kPa up to a total effective confining pressure of 2000kPa, with the unloading steps following the same sequence in reverse. Torsional and flexural resonant frequencies and attenuations were measured at each loading and unloading step. Each load step was maintained for thirty minutes to allow for any initial consolidation of the specimen to occur as a result of the application of the load/unload step, before resonant testing was undertaken.

5.4.1 *Strain measurement*

To ensure that the seismic properties measured were comparable to those that are measured during geophysical surveys, the strain amplitude experienced by the specimen was kept below γ_t^e. From tests conducted on dry specimens of pluviated Leighton Buzzard sand (Figure 3.7) the value of γ_t^e was estimated as $1x10^{-3}\%$ since for any given strain below this point shear modulus is a maximum (G_{max}) and damping is a minimum (D_{min}) as discussed in Section 3.3. From Eq's 3.70 and 3.78, the amount of strain that a specimen undergoes during torsional, or flexural excitation respectively, is directly related to the voltage output from the accelerometer via the charge amplifier. By rearranging Eq's 3.70 and 3.78, and substituting in the assumed specimen dimensions, the maximum voltage output during a test, to ensure that γ_t^e is not exceeded, can be estimated as a function of frequency. This allowed a quick measurement to be undertaken during a broad sweep of applied frequencies (Section 4.3.3) to ensure that γ_t^e was not exceeded before a fine sweep around resonance was undertaken.

5.4.2 *Resonant column testing results*

Velocity measurement

Figure 5.5 and Figure 5.6 show the typical response curve for both torsional and flexural excitation respectively. It can be seen from these figures that the resonance peak is well defined and easily identified. The data in Figures 5.5 and Figure 5.6 was obtained by following the methodology identified in Section 4.2.

Once the resonant frequency was obtained the respective velocities, for each mode of vibration, can be computed. The value of V_s is obtained from Eq's 3.29 and 3.30 with the substitution of the relevant measured resonant frequency and the specimen dimensions. The value of I_0 for use in Eq 3.29 was determined using the regression curve obtained from Figure 4.25 to correct for the frequency dependency of I_0 identified during calibration. An estimate of the systematic errors, due to the resolution of individual measurements

(length, diameter, mass, frequency,etc.), was undertaken and the results show that the error, within a 95% confident limit, was $\pm 5.2 \text{ms}^{-1}$, $\pm 11 \text{ms}^{-1}$ and $\pm 20 \text{ms}^{-1}$ at 130Hz, 370Hz and 550Hz respectively. This gave a maximum percentage error of approximately 1% at any point.

The value of V_{lf} was obtained from Eq's 3.58, Eq 4.3 and Eq 3.61 following substitution of the relevant data. Section 4.4.2 highlighted the difficulty in determining the value of I_y for use in Eq 4.3. It was shown that I_y was dependent on various parameters including the method used to determine its value. Therefore in the computation of I_y the regression curve obtained from Figure 4.27 was used to correct for the possible frequency dependency of I_y. An estimation of the systematic errors and the possible uncertainties that may occur in the computation of V_{lf} as a result of using the regression curve was conducted. Estimates of the uncertainties were obtained by applying differing values of I_y in the analysis. For a minimum value of I_y the average of the computed values given in Table 4.5 were used while the maximum value was obtained from the average of the calculated values given in Table 4.5.

The computed value of V_{lf}, at a frequency of 65.5Hz (corresponding to the resonant frequency for specimen H0D at $\sigma' = 500$kPa), was $530 \pm 4.4 \text{ms}^{-1}$ and $577 \pm 4.6 \text{ms}^{-1}$ when the minimum and maximum value of I_y was used respectively. The small deviations for each reading is the computation of the possible systematic error with a 95% confidence limit. At 157Hz (specimen H3-1) the computed values were $1409 \pm 9 \text{ms}^{-1}$ and $1505 \pm 9.1 \text{ms}^{-1}$ and at 273Hz (specimen H40) the values were $2384 \pm 26 \text{ms}^{-1}$ and $2546 \pm 27 \text{ms}^{-1}$. These values provide lower and upper bounds to the computed velocity, with the derived value, using the regression curve, being constrained within these values. Figure 5.7 shows a typical plot of computed shear wave velocity (V_s), and longitudinal wave velocity (V_{lf}), versus effective confining pressure, σ', for an unconsolidated sand.

Attenuation measurement

Figure 5.8 shows a typical free vibration decay curve for a hydrated specimen. The decay curve was obtained by taking 50 samples per decay cycle for up to 60 cycles. The logging of data points was commenced prior to the formation

of an 'open circuit' to ensure the whole decay curve was captured. The value of δ was determined from the gradient of a fitted regression curve by plotting peak amplitude for each successive cycle (Figure 5.9). The attenuation, or damping, can then be calculated using the relationships given by Eq 3.42. The values of the attenuation parameters were corrected to take account of the inherent apparatus damping, as a function of frequency, which was shown to exist (Figure 4.29). The correction factor was determined by fitting a least squares curve to each of the free vibration decay damping sets in Figure 4.29, and using the equation of each line to calculate the correction factor for a given frequency. Figure 5.10 presents typical results for the shear wave damping coefficient, D_S, and attenuation, Q_S^{-1}, both as a function of effective confining pressure while 5.11 presents longitudinal wave damping coefficient, D_E, and attenuation, Q_E^{-1}, with effective confining pressure.

5.5 Hydrate dissociation

To consider the effect that hydrate formation and hydrate dissociation may have on sediment properties resonant column tests were performed on dissociated specimens. Once resonant column testing was completed on a hydrated sand specimen, the hydrate, within the pore space, was dissociated by increasing the specimen temperature. The rise in temperature forced the hydrate outside its phase boundary thereby inducing hydrate dissociation. As the hydrate dissociated the pore pressure rose more than that which would occur due to temperature alone. The cell pressure was controlled to maintain an effective stress of 250kPa on the sample throughout the dissociation stage.

Once the sample was completely dissociated the pore pressure was reduced to 5MPa and the specimen temperature held at 20^0C to enable resonant column testing to be undertaken at the same pressure conditions as for the hydrated sediment. The resonant column testing procedure was similar to that previously described for the hydrate-bearing sediment except that only 250kPa, 500kPa, 1000kPa and 2000kPa effective confining pressures were applied and tested. The unloading sequence mirrored the loading sequence in reverse.

Table 5.1: *Digital analysis of thin sections with different estimated volumes of plastic beads within sand samples. Samples are split into thirds (Base, Middle and Top) with thin sections obtained across each section (T) and down each section(L)*

Thin section	Area of plastic grains (pixels)	Total area of image (pixels)	The % of beads within total area
5% sample			
Base-L	106,728	1,818,190	5.87
Base-T	101,621	1,806,415	5.63
Middle-L	78,879	1,524,119	5.17
Middle-T	110,719	1,822,974	6.07
Top-L	106,515	1,809,458	5.89
Top-T	96,426	1,819,187	5.29
10% sample			
Base-L	178,045	1,826,894	9.7
Base-T	213,343	1,819,786	11.7
Middle-L	175,190	1,790,097	9.8
Middle-T	172,459	1,807,639	9.5
Top-L	188,177	1,815,623	10.4
Top-T	158,016	1,812,518	8.7
20% sample			
Base-L	335,425	1,805,944	18.6
Base-T	291,390	1,599,752	18.2
Middle-L	229,536	1,142,487	20.1
Middle-T	311,326	1,545,870	20.1
Top-L	321,625	1,481,580	21.7
Top-T	308,801	1,553,756	19.9

Table 5.2: *Initial properties of prepared specimens of Leighton Buzzard sand.*

Specimen No.	% of ice in pore space)	Relative density, Dr (%)	Void ratio	Porosity	moisture content (%)
H0L	0	34.15	0.867	0.465	0
H0D	0	78.12	0.712	0.416	0
H1	1.07	90.48	0.667	0.400	0.253
H2	2.16	75.26	0.722	0.419	0.537
H3-1	3.03	75.27	0.728	0.419	0.748
H4-1	3.77	72.17	0.733	0.423	0.939
H5-1	4.94	75.06	0.722	0.419	1.199
H10	9.67	64.65	0.76	0.432	2.497
H20	18.06	67.72	0.749	0.428	4.579
H40	35.63	68.16	0.748	0.428	8.075
H3-2	2.72	56.80	0.795	0.443	0.728
H4-2	3.85	66.43	0.754	0.430	0.987
H5-2	4.91	72.08	0.734	0.423	1.222

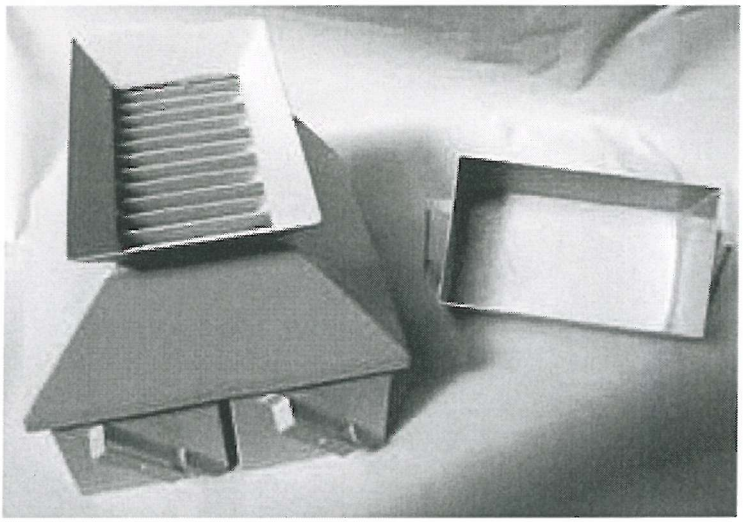

Figure 5.1: *A riffle box for mixing of sand and ice.*

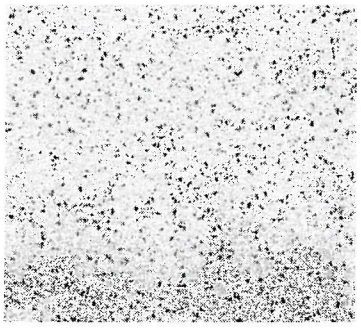

(a) longitudinal slice of base section

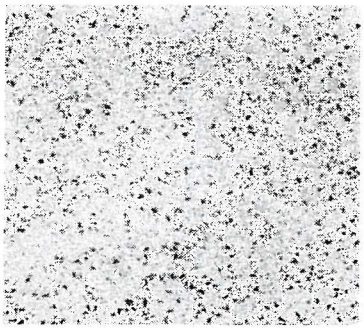

(b) transverse slice of base section

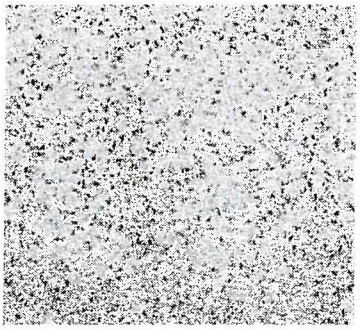

(c) longitudinal slice of middle- section

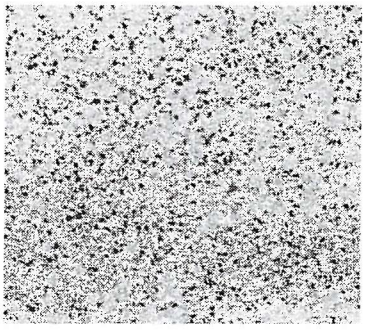

(d) transverse slice of middle section

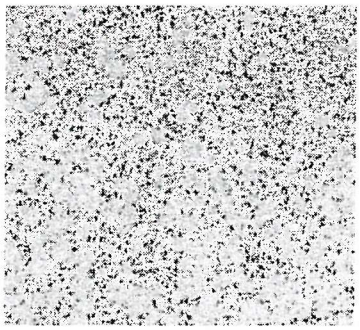

(e) longitudinal slice of top section

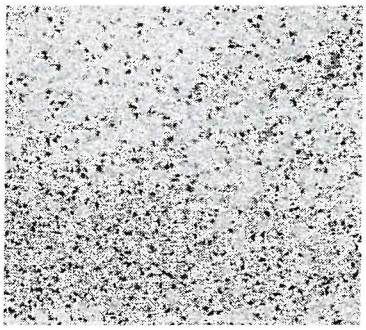

(f) transverse slice of top section

Figure 5.2: *Digital images of thin sections for sand sample containing 5% plastic beads.*

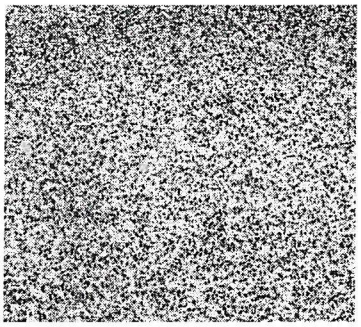

(a) longitudinal slice of base section

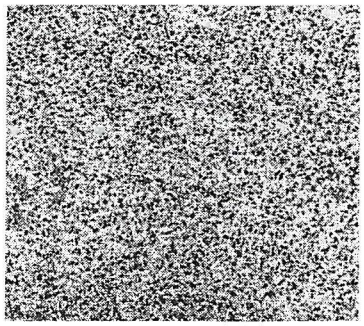

(b) transverse slice of base section

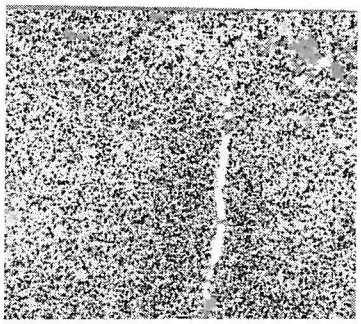

(c) longitudinal slice of middle- section

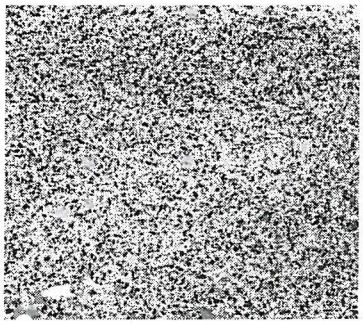

(d) transverse slice of middle section

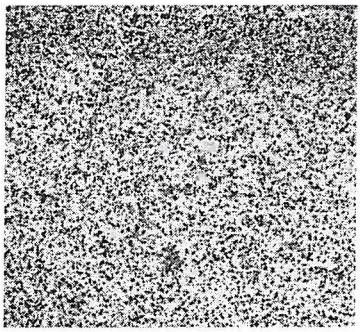

(e) longitudinal slice of top section

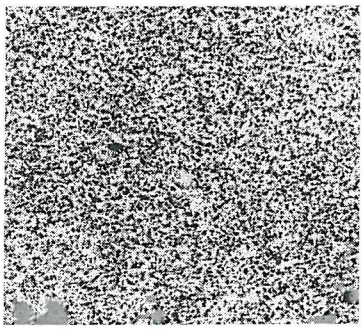

(f) transverse slice of top section

Figure 5.3: *Digital images of thin sections for sand sample containing 20% plastic beads.*

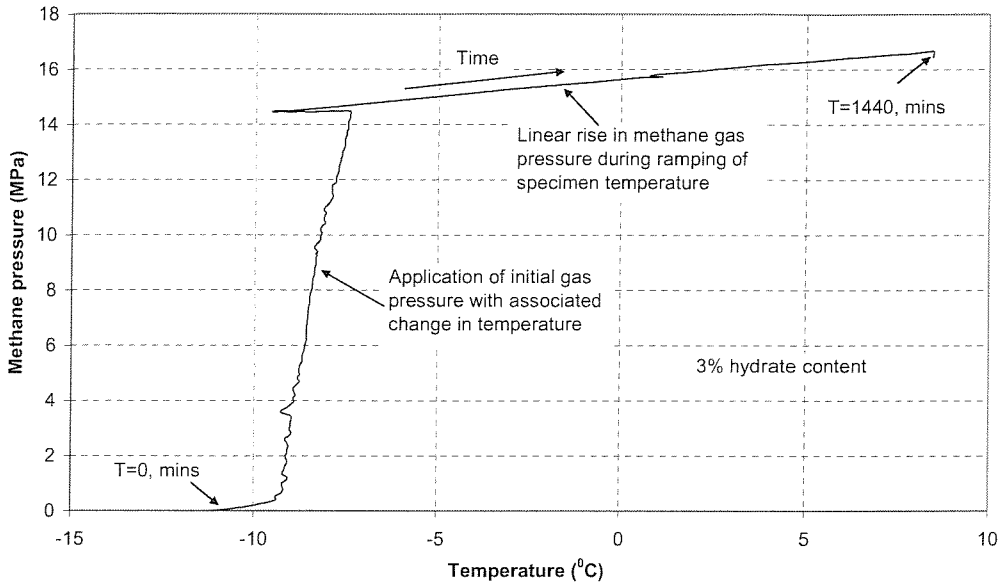

Figure 5.4: *Typical P-T for history for specimen H3-2. The graph shows the initial application of methane back pressure up to 15MPa and then the subsequent rise in the methane gas pressure as the specimen temperature was raised.*

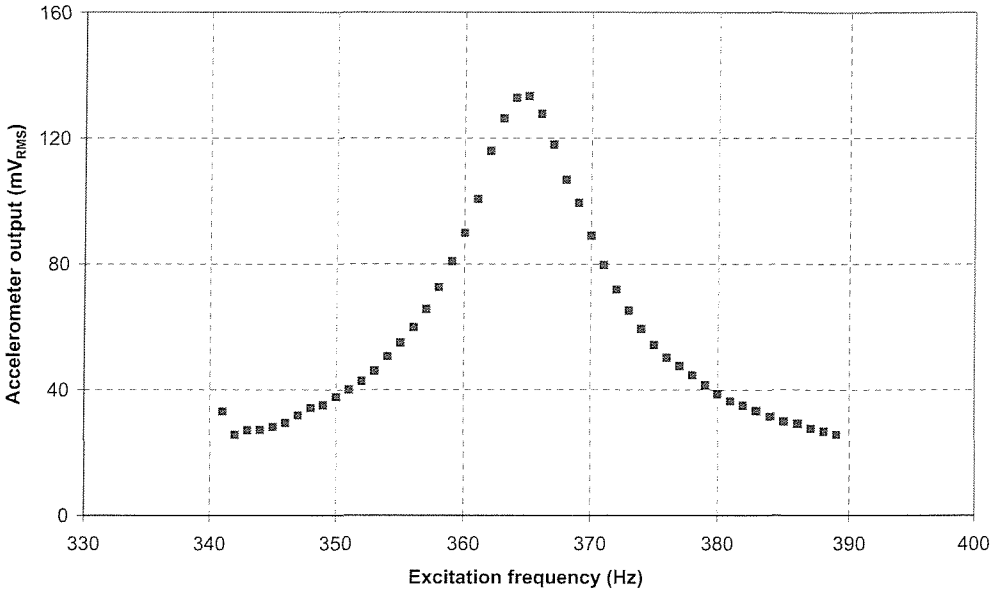

Figure 5.5: *Typical frequency response curve for hydrated specimen H3-2 under torsional excitation.*

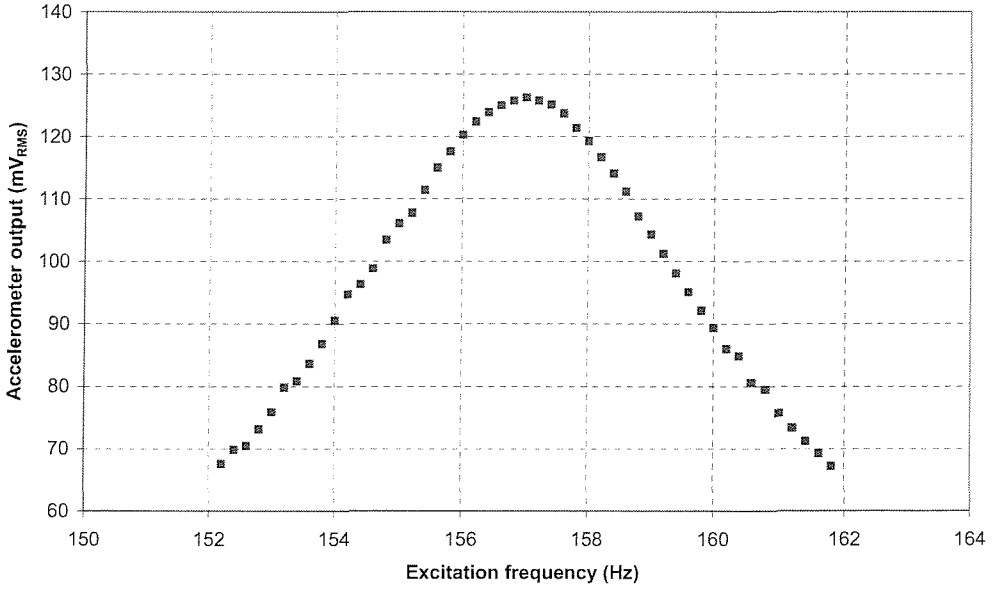

Figure 5.6: *Typical frequency response curve for hydrated specimen H3-2 under flexural excitation.*

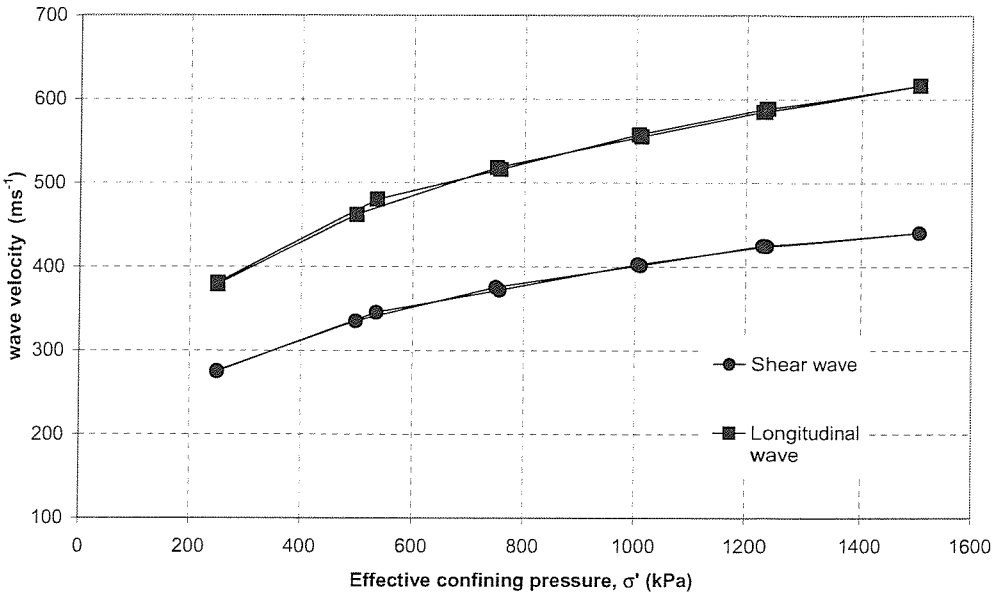

Figure 5.7: *Typical wave velocities for specimen H0L with effective confining pressure.*

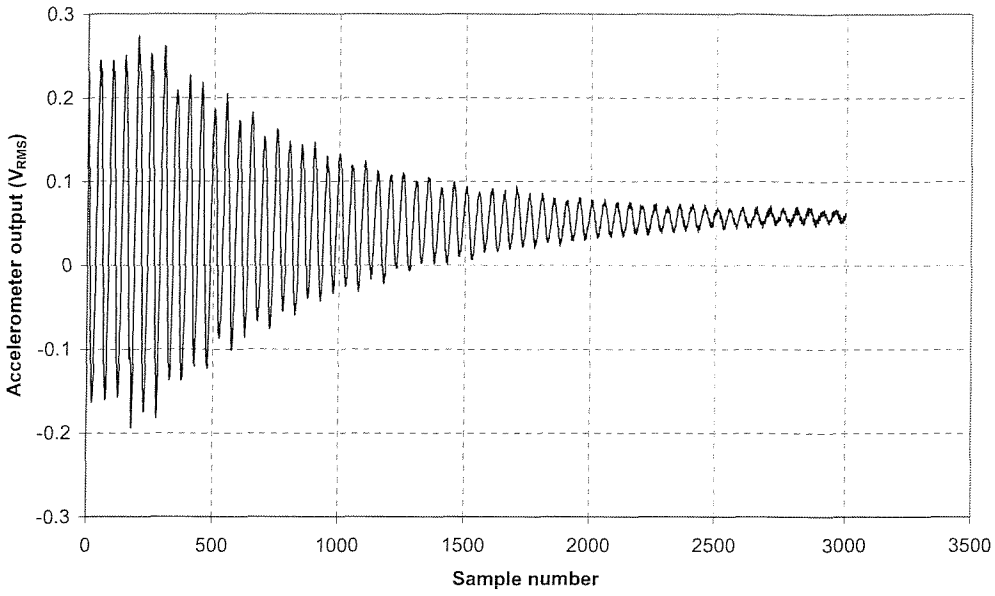

Figure 5.8: *Typical free vibration decay curve for hydrated specimens.*

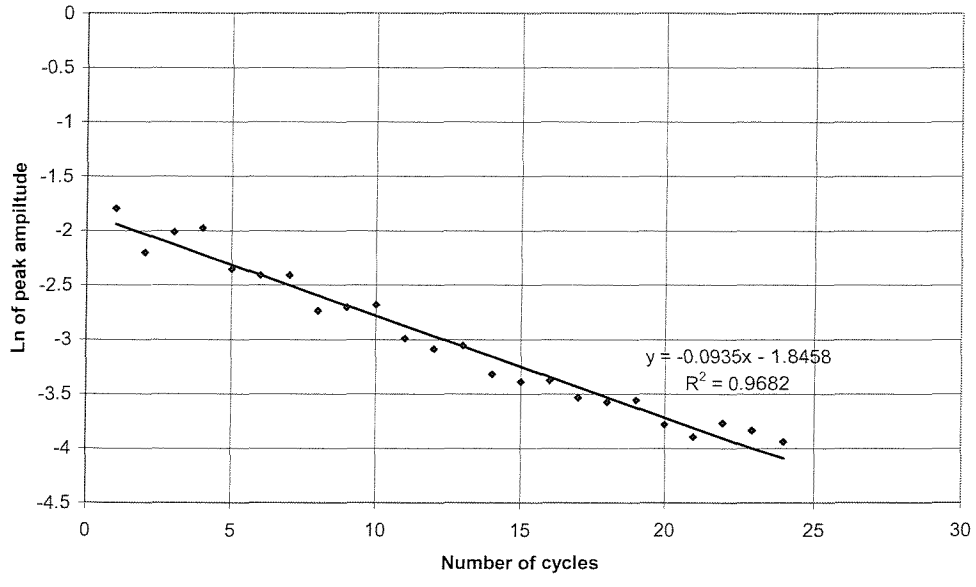

Figure 5.9: *Plot of peak amplitude versus number of cycles obtained from Figure 5.8.*

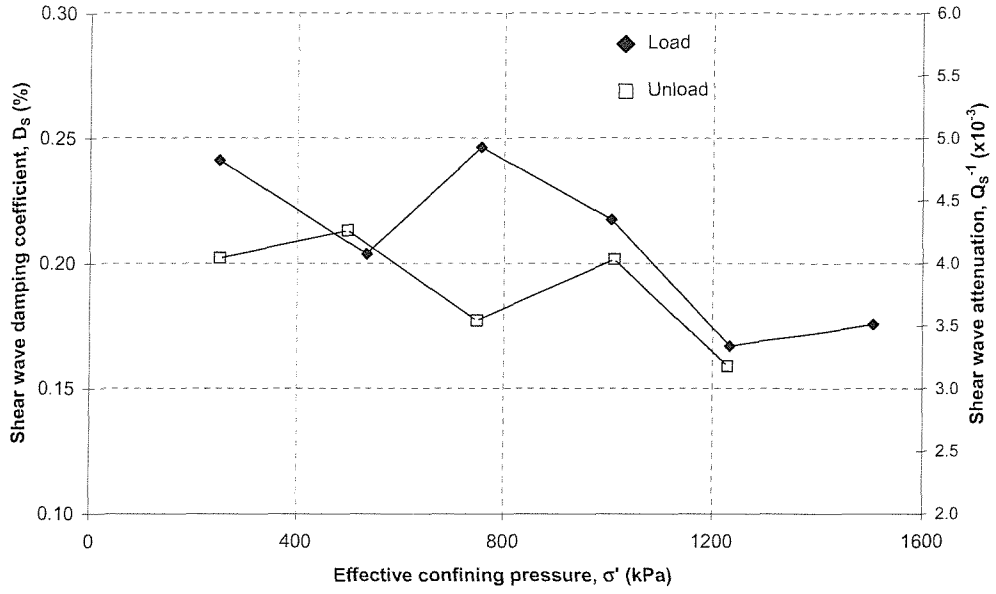

Figure 5.10: *Damping coefficient, D_S, and attenuation, Q_S^{-1} with effective confining pressure, σ' for specimen H0L.*

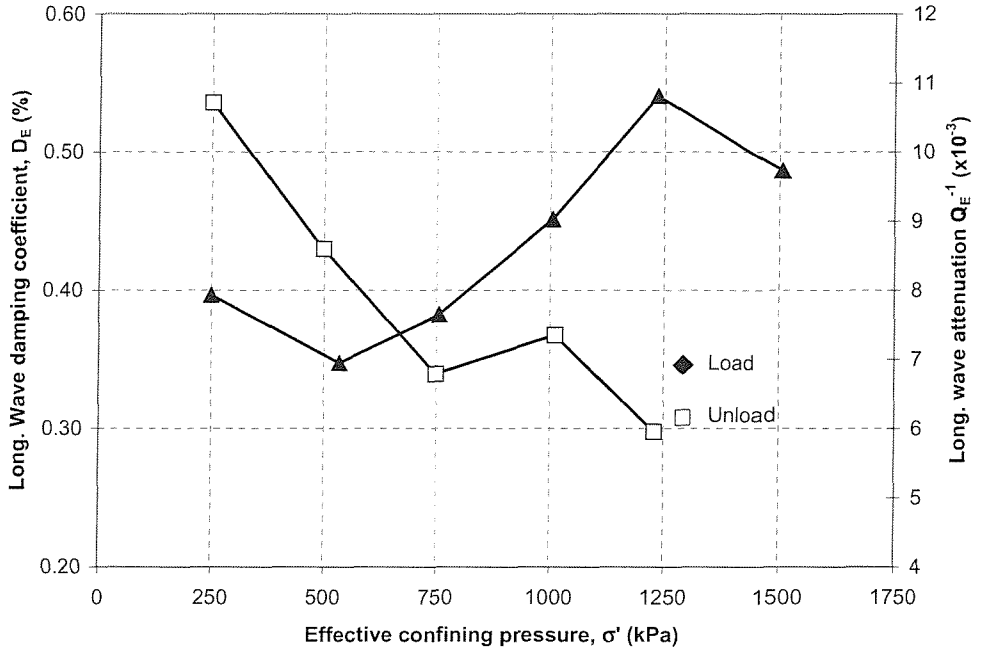

Figure 5.11: *Damping coefficient, D_E, and attenuation, Q_E^{-1} with effective confining pressure, σ' for specimen H0L.*

Chapter 6

Discussion

6.1 Introduction

A new laboratory apparatus, the GHRC, has been designed and constructed to determine the seismic properties of dry[1] sand specimens containing differing volumes of methane hydrate in the pore space. The methane hydrate was formed from ice in the presence of methane gas, within the sand specimen, with the volume of hydrate directly linked to the volume of ice added during specimen preparation. After the formation of the hydrate, specimens were subjected to resonant column testing from which the seismic properties (V_p, V_s, Q_p and Q_s) were derived.

This chapter presents and discusses the results obtained from the formation and subsequent testing of 13 sand specimens containing methane gas hydrates. Firstly, results of hydrate formation tests are discussed with regard to the estimation of hydrate content. Secondly, the results of the resonant column testing are discussed with emphasis on the effect of hydrate content on seismic velocities and attenuation properties of sand specimens. Finally the results of resonant column testing on the sand specimens after hydrate dissociation, are discussed and compared to the results on hydrated specimens.

[1]The term 'dry' is used based on the assumption that all the added water, in the form of ice, is converted to hydrate and the initial absorbed water remains on the sand grains at grain contacts

6.2 Hydrate formation

Methane hydrate was formed by melting ice in the presence of methane gas at high pressure. The methane pressure was set at 15MPa prior to assumed hydrate formation, which is well within the methane hydrate phase boundary given by Figure 1.1. The temperature of the specimen was then raised from an initial value of -15^{0}C to +10^{0}C at approximately 1^{0}C/15mins. As described previously, work by Stern et al (1996) and Stern et al.(1998) had shown that the formation of hydrate, from melting seed ice, caused a reduction in the thermal expansion gradient of the methane gas as the H_2O liquidus line is passed (Figure 6.1). In the formation tests undertaken for this research no visible change in the thermal expansion gradient of the methane gas was evident for specimens containing up to 5% ice (Figure 6.2) in the pore space. However, there was a noticeable change for specimens with an initial high ice content (Figure 6.3). Figure 6.4 shows a comparison of the pressure gradients for differing tests. After the initial application of the methane gas back pressure the gradient of the slope, relating to pore pressure rise as a function of temperature, for specimen H40, was smaller than specimens H1 to H5-2 where the ice content was low.

As no apparent change in the thermal expansion gradient of the methane gas was evident for specimens with low ice contents, it can be proposed that the majority of hydrate growth (hydrate nucleation (Stage 1) and hydrate formation through diffusion (Stage 2)) occurred during the raising of the methane back pressure and continued during the controlled raising of the specimen temperature. The high pore pressure helps the nucleation and diffusion process when the specimen temperature is below 0^{0}C (Salamatin and Kuhs, 2002; Staykova et al., 2002; Staykova et al., 2003).

Another contributing factor is the size of the ice grains. In the work of Stern et al. (1996); Stern et al. (1998) and Stern et al. (2000) the individual ice grains were between 180- and 250μm. In the work of Salamatin and Kuhs (2002); Staykova et al. (2002) and Staykova et al. (2003), the ice grains had a typical diameter of 40-80μm. In our research the ice, formed during sample preparation, reside within the pore space of the sand specimen, or for low

moisture contents are preferentially formed at grain contacts. Therefore, for specimens formed from typically 100μm diameter sand grains, the pore size is much smaller than those mentioned above. Therefore hydrate growth will be much quicker once the hydrate stability conditions are attained. Also, although the temperature of the environment chamber is kept constant during the application of cell pressure and back pressure, a rise in specimen temperature was observed. This may have been partly due to: the adiabatic expansion of both the methane gas within the specimen, and the nitrogen gas supplying the confining pressure; and due to the temperature of both gases applied to the cell being at $+20^0$C. Although the slow application of gas pressure ensures that bulk melting of the specimen is not induced, it may cause surface melting of the ice grains, during their application, inducing hydrate nucleation to occur more rapidly than the suggested bulk temperature may of suggest.

Stern et al. (1996) and Stern et al. (2000) stated that the volume of hydrate produced could be calculated by measuring the reduction in methane pressure (Figure 6.1) as the temperature was reduced. By reducing their pressure vessel temperature below 0^0C, after hydrate formation, any pressure drop could be measured and used to compute the volume of gas used up in the hydrate formation process. Also the volume of gas consumed can be used to estimate the cage occupancy of the hydrate crystals (Section 2.2). However, in this research this technique was unavailable due to hydrate nucleation and diffusion-led conversion occurring whilst the pressure was being applied, and continuing while the bulk specimen temperature was below 0^0C. Therefore, the success of the hydrate formation procedure could only be assessed qualitatively by the possible rise in seismic velocity of the hydrated sand specimen or the pore pressure rise due to dissociation of the gas hydrate at the end of the test.

6.2.1 *Hydrate dissociation*

Due to the difficulty of assessing the hydrate content from pressure anomalies during hydrate formation, qualitative assessment of hydrate formation and

its volume was undertaken during hydrate dissociation. Figure 6.5[2] shows the dissociation curves for a variety of specimens tested. Each dissociation curve is formed by two distinct effects:

1. The increase in pore pressure as a function of hydrate dissociation;
2. The increase in pore pressure due to the temperature-induced thermal expansion of the free gas .

Table 6.1 highlights the pressure rise obtained from the dissociation of each hydrated specimen. It can be noted that the ratio of initial ice content to the rise in pore pressure ($I_c/\Delta P$) is approximately constant for all tests, with the ratio slightly reducing for the higher hydrate contents. These results suggest that relating the hydrate content to the initial volume of ice added, is reasonably justified for determining a quantitative estimate of hydrate content for each test. The reduction in $I_c/\Delta P$, at the high ice content, was assumed to result from the overestimation of the pore pressure obtained during the dissociation stage. It can also be noted in Figure 6.5 that as the hydrate content increases the maximum temperature obtained before complete hydrate dissociation increases. This broadening of the observed temperature range leads to an overestimation of the hydrate dissociation-induced pore pressure rise since some of the additional pore pressure rise can be attributed to the increasing thermal expansion of free gas. Also, the porosity of the specimen reduces (from approximately 40% for specimen H0D to 28% for specimen H40) with increasing ice contents and therefore specimens with high hydrate contents will experience higher pore pressure rises due to the reduction in volume available to the free gas.

The broadening of the temperature range also suggests that the hydrate is stable outside the hydrate stability field (shown in Figure 6.5) for pure methane gas hydrates, especially for specimens with an initial high ice content. This could be due to anomalous preservation of the hydrate, as reported

[2]The rise in pore pressure for specimen H10 was halted due to the pore pressure and cell pressure equalizing during the dissociation stage, and so these data cannot be used to assess hydrate volume

by other researchers (Stern et al., 1996; Stern et al., 2000; Stern et al., 2002; Tohidi et al., 2001; Tohidi et al., 2002).

6.3 Effect of hydrate on seismic velocity

This section discusses the influence of hydrate content on the seismic velocities of 13 dry sand specimens subjected to isotropic loading. Figures 6.6 and 6.7 show the relationships between velocity (V_s and V_{lf}, respectively) and effective confining pressure (σ') during isotropic loading and unloading for test specimens H0L through to H40 (as described in Section 5.2.2). Two important conclusions can be drawn from these results reported in these figures: the pressure dependency of both velocities is reduced once the hydrate content is 3% or above; and both V_s and V_{lf} generally increase as the degree of hydrate within the pore space increases. The results also show that for specimens H4-1 and H5-1 a reduction in V_s occurs compared to specimen H3-1, while for V_{lf} a reduction in H4-1 is evident. During the hydrate formation stage for specimens H4-1 and H5-1, the effective confining pressure was for a period of time (up to 30 minutes) much greater than 250kPa, which was the target value for all tests. Therefore, specimens H3-2 - H5-2 were prepared and hydrate formed under the correct effective confining pressure for the whole duration of the formation procedure. These were subsequently tested to determine the possible variability in velocity at these hydrate contents. Figures 6.8 and 6.9 compare the velocity profiles from specimens H3-2 - H5-2 and specimens H3-1 - H5-1 for V_s and V_{lf} respectively. The results show that V_s and V_{lf} for specimens H4-2 and H5-2 are higher than those for specimens H4-1 and H5-1. However, Figure 6.9 shows that V_{lf} is lower for specimen H5-2 than for H4-2.

Figure 6.10 shows the increase in both V_s and V_{lf} as a function of hydrate content, for all test specimens, at discrete stages of the isotropic loading phase. Two distinct regions can be identified. Initially, a steep rise in both velocities is observed probably due to the addition of small amounts of hydrate within the pore space of the specimen. Above a critical volume of hydrate, between 3%-5%, the rate of increase in velocity as a function of

hydrate content reduces substantially. The vertical bars in Figure 6.10 show the uncertainty in the computed values due to systematic errors in the measured values for specimens under an effective confining pressure of 500kPa. The vertical bars for V_{lf} in Figure 6.10 also contain the uncertainties with regard to the computation of I_y as highlighted in 5.4.2. The results suggest a bi-partite relationship between velocity and hydrate content with a 'transition zone' situated between 3%-5% hydrate volume. A hypothesis can be developed to describe the effect of hydrate content on the computed seismic velocity by considering the relationship between the seismic velocity and effective confining pressure as shown in Figures 6.6 and 6.7.

6.3.1 *Variation in velocity with effective confining pressure*

In Section 3.3.1, factors affecting the value of G_{max} (shear modulus obtained at small strain) were discussed, with Eq 3.4 showing that σ' is one of the main factors that has an influence on the value of G_{max}. It was also noted in Section 3.4 that G is related to V_s by Eq 3.13 with E and V_{lf} following the same form. In unconsolidated soils subjected to isotropic loading Eq 3.4 can be simplified to express the relationship between shear wave velocity and effective confining pressure:

$$V_s = A\sigma'^{b}, \tag{6.1}$$

where A and b are constants.

The power exponent (b) represents both the nature of contact stiffness and fabric change as a function of isotropic stresses (Cascante, 1996). Cascante (1996) also showed that the longitudinal wave velocity, obtained from flexural excitation in the resonant column, also followed the standard power relationship for shear wave velocity. The power exponent is given the subscript b_S for shear wave velocity and b_L for longitudinal wave velocity. Therefore, by applying a power law regression curve through the test data (Figures 6.11 and 6.12), the value of the exponent can be found for each wave velocity. Table 6.2 lists the values obtained from the regression curves (for loading and unloading) for all tests, with Figures 6.13 and 6.14 showing the variation of

the b_S and b_L exponent during isotropic loading and unloading, respectively, as a function of hydrate content.

The results from the non-hydrated dry sand specimens (Table 6.2) show $b_S = 0.27$ and $b_L = 0.27$ for the loose sand specimen (H0L) during isotropic loading and unloading, while the dense sand specimen (H0D) has $b_S = 0.23$ and $b_L = 0.22$. These values are consistent with published data on remoulded clean sand specimens (Cascante, 1996; Hardin and Richart, 1965). The reduction in b_S and b_L from specimen H0L to H0D can be attributed to more stable contacts and smaller changes in specimen fabric during isotropic consolidation. This is supported by the greater axial strain, ε_z, that specimen H0L underwent during consolidation (under the same load conditions) compared to specimen H0D, as shown in Figure 6.15.

The values of the power exponent, shown in Figures 6.13 and 6.14 and Table 6.2 for specimens H0D to H3-2, show that the addition of small amounts of hydrate into the pore space has a dramatic influence on the values of b_S and b_L. The values for b_S and b_L reduce from 0.23 to 0.01 for both exponents. Figure 6.16 shows the maximum axial strain, ε_{max}, experienced by each test specimen. The value of ε_{max} shows little variation between the specimens implying that fabric change is limited between differing specimens. Therefore the increase in velocity can be assumed to be related to the contact stiffness. As all specimens were subjected to the same loading conditions the reduction in b_S and b_L, coupled with the increase in velocity from specimen H0D to H3-2, suggests that the increase in contact stiffness is due to the increasing cementation of the sand grains by hydrate at grain contacts. Dvorkin and Nur (1993) showed that small amounts of cement at grain contacts (frozen capillary water in one test and epoxy resin in another) can dramatically increase wave propagation velocity. Their results showed a large increase in velocity for low cement saturation ($< 10\%$, where the value is defined as a percentage of the pore space) with the velocity increase reducing with increasing cement saturation. Similar results were also obtained by Saxena et al. (1988) studying cementation effects of Portland cement on sand properties.

The slight increase in the b_S and b_L exponents during unloading for all hydrated specimens suggests a reduction in contact stiffness possibly caused

by brittle fracture of the hydrate cement.

Examination of b_S and b_L values for specimens H4-1 to H40 shows that increasing the hydrate content has little effect on the b_S exponent and causes a slight increase in b_L. This implies that the increase in velocity from specimen H4-1 to H40 is not a function of the contact stiffness and is due to the reduction in porosity through the increasing hydrate phase within the sand specimen (Han et al., 1986). In the initial calculation of porosity, the volume of water in the pore space during specimen preparation is counted as part of the void space. However, after hydrate formation the hydrate becomes part of the solid phase and therefore a reduction in porosity occurs. Figure 6.17 highlights the axial strain experienced by specimens H4-1 to H40 showing the reduction in axial strain as the volume of hydrate increases. This suggests that for specimens with high hydrate content more stress is carried by the hydrate phase.

6.3.2 *Axial deformation*

Figures 6.16 and 6.17 also show that the residual strain, ε_r (defined as the value of axial strain remaining at the end of the load/unload cycle), increases with hydrate content. During testing of all specimens a period of 30 minutes was left after the application of each load and unload step, to allow for any deformation to occur and the axial displacement to stabilize. Figure 6.18 shows the axial deformation for each load step, for specimen H3-2, showing that all of the load is carried almost immediately and all measurable displacement cease before resonant column testing is undertaken. However, Figure 6.19, which shows the axial deformation with time for specimen H40, clearly identifies a time dependent creep continuing, after an initial consolidation due to the application of each load step. Therefore it is possible that the reduction in ε_{max}, and increasing ε_r for specimens H20 and H40 may be due to the time dependent deformation behaviour of the hydrate. The value of ε_r for specimen H40 was shown to be 0.083% at the end of the test (Figure 6.17), but had reduced to 0.054% some 2hrs after the removal of the last unload step.

6.3.3 *Comparison of V_{lf} and saturated V_p*

In the resonant column V_{lf} was obtained from the small-strain Young's Modulus (E_{max}) using Eq 3.61. In single phase particulate materials, such as dry sands, the Young's Modulus computed from flexural excitation is the same as that obtained from longitudinal excitation. Therefore, the compressional wave velocity, V_p, can be determined using Eq 3.62 and 3.63. However, in saturated particulate materials the interaction between the fluid and the solid phase is different for flexural and longitudinal vibration.

During flexural excitation the strain field within the specimen has a triangular-Navier distribution in cross-section between tension and compression (Cascante et al., 1998). If the rate of pore pressure dissipation is greater than the period of vibration of the flexural mode then the computed Young's Modulus is dependent on the compressional stiffness of the soil frame alone, since the pore water is able to move to equilibrate the pore pressure. In longitudinal vibration the imposed strain is constant in cross section, and therefore the stiffness of both the frame and the water is considered. Figure 6.20 shows the longitudinal velocity response of a saturated dense sand specimen, specimen H0D and loose sand specimen H0L. The maximum value for V_{lf} is shown to be just under 700ms^{-1} which is comparable to the velocity for the dry dense specimen H0D. The compressional velocity of pure water alone, without any sediment is approximately 1500ms$^-$1 and saturated sands should be expected to have a value higher than that of water (Hamilton, 1971).

Although V_p can be computed from the elastic constants E and ν (using Eq 3.62 and 3.63), it can also be computed using,

$$V_p = \sqrt{\frac{(K + \frac{4}{3}G)}{\rho}}, \tag{6.2}$$

where K is the bulk modulus of the soil. In a dry soil, K can be computed (assuming isotropy) from,

$$K = \frac{EG}{3(3G - E)}. \tag{6.3}$$

The bulk modulus of a fluid saturated soil, however, is dependent on the

bulk moduli of the soil and the fluid. Gassmann (1951) derived an equation to compute the bulk modulus of a fluid saturated porous medium using the bulk moduli of the constituent parts,

$$K = K_d + \frac{(1 - \frac{K_d}{K_m})^2}{\frac{n}{K_f} + \frac{1-n}{K_m} - \frac{K_d}{K_m^2}}; \tag{6.4}$$

where: K = saturated bulk modulus of the soil,
K_f = bulk modulus of the fluid,
K_m= average bulk modulus of the soil grains,
K_d = bulk modulus of the dry frame (from RC tests),
n = porosity of the rock.

The soil grain bulk modulus (K_m) is the effective modulus for an aggregate of grains when taken as a single grain, which is based on the mineralogy making up the soil. In the tests conducted on hydrated specimens it was shown that hydrate becomes part of the solid phase. Therefore, in the case of mixed mineralogy, the effective K_m, for the solid phase (hydrate and quartz), can be calculated from the individual components of the soil using Hill's average formula (Hill, 1952),

$$K_m = \frac{1}{2}\left[\sum_{i=1}^{N} \varphi_i K_i + (\sum_{i=1}^{N} \varphi_i / K_i)^{-1}\right] \tag{6.5}$$

where N is the number of mineral constituents, φ is the volumetric fraction of the i-th constituent and K_i is the bulk modulus of the mineral constituents. Tests on bulk gas hydrate have determined the bulk modulus of methane gas hydrate to be 7.9GPa (Waite et al., 2000). The bulk modulus of a quartz sand grain is given as 36.6GPa (Mavko et al., 1998) and water as 2.25GPa. The density of the saturated soil can be determined, using

$$\rho = \rho_d + n\rho_f \tag{6.6}$$

where ρ_d is the density of the soil frame =(1-n)ρ_m, where ρ_m is the density of the solid mineral phase and ρ_f is the density of the pore fluid.

Therefore, using Eq's 6.3, 6.4, 6.5 and 6.6, substituting in the known values of bulk moduli and the computed porosity, the compressional velocity of

a saturated medium can be computed using data from the resonant column tests. Figure 6.21 presents the computed V_p values for the test specimens H0L to H40 as a function of hydrate content along with the computed saturated V_s and V_{lf} for comparison. The vertical bars show the uncertainty in the computed values for V_p (for an effective confining pressure of 500kPa) due to systematic errors and the uncertainty in the determination of I_y, as previously highlighted. The vertical bars are omitted for V_s and V_{lf} for clarity as they are as previously shown in Figure 6.10. As the shear modulus of the specimen is unaffected by fluid saturation, the saturated V_s values are computed from Eq 3.13 using the computed saturated soil density. The results show an increase in velocity from V_{lf} to V_p as expected due to the increase in bulk modulus computed from Eq 6.4 as a result of the inclusion of K_f. The difference in values between the dry bulk modulus K_d and the saturated bulk modulus (K) can be seen in Figure 6.22. The vertical bars shown in Figure 6.22 show the potential deviation in K and K_d due to systematic errors and the uncertainty with I_y. It can been seen in Figure 6.21 that for specimens with no hydrate, or a low hydrate content (less than 3%), a large velocity offset and a reduction in the velocity slope for V_p is observed compared to that for V_{lf}. This is due to the bulk modulus of the modelled saturated sediment being dominated by the bulk modulus of the fluid (Figure 6.22). As the hydrate content increases (3% and above) the cementation of the sand grains by hydrate, and the reduction in porosity (less water required to fill pore space) leads to a reduction in the influence of K_f and so a reduction in the velocity offset is observed between V_p and V_{lf} which reduces as the hydrate content approaches the maximum hydrate content (Specimen H40), i.e. in Figure 6.21.

6.3.4 V_p/V_s ratios

Figure 6.23 shows the computed V_p/V_s ratios for all the specimens tested. The ratio for non-hydrated specimens was 5.53 and 3.91 for the loose and dense specimen respectively. These values are comparable to those that have been measured for near surface marine sediments, including sands (Hamilton,

1979). The addition of hydrate into the pore space causes a large reduction in the V_p/V_s ratio from 5.53 to 2.25 from specimen H0L to H3-2 ($\sigma' = 500$kPa) with a slight reduction to 1.9 at the maximum hydrate content (specimen H40). The value for V_p/V_s ratio at high hydrate contents is comparable to values given in the literature for rocks, such as mudstones, limestones and sandstones (Castagna et al., 1984; Hamilton, 1979; Wilkens et al., 1984).

This reinforces the suggestion made in Section 6.3.1 that the addition of hydrate into the pore space of the sand specimens tested in this research causes cementation of the sand grains, leading to a change in the lithology of the sand from an unconsolidated particulate material to a bonded rock-like material.

6.3.5 *Velocity model*

The results of the research undertaken show that the addition of hydrate into the pore space causes cementation of the sand grains, which leads to a dramatic increase in the seismic velocity of the sand specimens. It has been shown that both shear wave velocity and longitudinal wave velocity increase rapidly with hydrate content up to a critical hydrate content value of 3-5% with the increase in velocity with hydrate content thereafter being more subdued.

Figure 6.24 shows a hypothetical model for differing volumes of hydrate in the pore space. Figure 6.24(a) shows sand grains with no hydrate in the pore space. In this case the velocity is a function of the inherent fabric and normal frictional contact stiffness and follows the standard power law for velocity vs. effective confining pressure for particulate materials with the power exponent, b ranging from 0.27-0.23.

As hydrate forms in the pore space, 'patchy' cementation at grain contacts occur as shown in Figure 6.24(b). Both the shear wave and longitudinal wave velocities increase dramatically as the hydrate content approaches the critical hydrate volume where all grain contacts become cemented. The wave velocities become less pressure dependent (as highlighted by a reduction in the power exponent b), emphasizing the change from a frictional contact

stiffness to a cemented grain contact stiffness for the sand.

At the critical hydrate volume (Figure 6.24(c)) all sand grains are fully cemented at grain contacts and the b exponent is a minimum. At this point the specimen stiffness becomes sensitive to the distribution of hydrate in the pore space and could be the cause for some of the variations in measured velocity between the specimens H3-1 to H5-2.

Increased additions of hydrate in the pore space above the critical hydrate volume causes an enlargement in the volume of the hydrate cement at grain contacts, and a subsequent infilling of the pore space as shown in Figure 6.24(d). This leads to a more gradual increase in velocity with increasing hydrate content.

6.3.6 *Comparison of research results with previous studies*

This research has shown that gas hydrate can act as a cementing agent in particulate materials and that the concentrations of hydrate required to fully cement sand grains are quite low. This is a significant departure from previous reported studies on gas hydrates. Work by Berge et al. (1999) had shown that CCL_3F hydrate acts as a cement for concentrations above 35% while Kunerth et al. (2001) concluded that THF-hydrate grows within the pore space. However, both these hydrates were synthetic and may have had differing forms and material properties to methane gas hydrates. Tohidi et al. (2001) and Tohidi et al. (2002), using glass micromodels, inferred that methane hydrates formed from free gas infilled the pore space and left liquid water wetting the surface of the glass. This is to be expected since hydrate grows at the gas-water interface (in a three-phase system), and since no intergranular contacts were formed in the glass micromodels, the methane bubbles sat in the pore space. The methodology adopted in this research inevitably forces the hydrate to form at grain contacts since it is here through surface tension and capillarity that the free water sits prior to be refrozen. Therefore the cementation of grain contacts may only exist due to the testing procedure adopted. However Tohidi et al. (2002) also showed that hydrates from

dissolved methane gas could only grow in the pore space by the nucleation of the hydrate being initiated by silica 'flour' particles (2μm) in the pore fluid. It is therefore possible that in nature the formation of gas hydrates from dissolved methane gas will preferentially occur at grain contacts due to the availability of nucleation sites.

Several recent studies of hydrate-bearing sediments using seismic survey data and effective medium model theories have also come to the conclusion that hydrate grows preferentially in the pore space (Ecker, 2001; Jakobsen et al., 2000; Helegrud et al., 1999; Lee and Collett, 2001; Sakai, 2000) and does not act as a cementing agent. Some of the seismic survey data that was modelled in reaching these conclusions was obtained from clay-rich sediments. Theoretical models suggest that capillary pressures prevent the formation of gas hydrates in small pores associated with clay particles (Clennell et al., 1999; Henry et al., 1999) and therefore leads to preferential formation of gas hydrates in larger pore spaces associated with silts and sands (Ginsburg et al., 2000; Kraemer et al., 2000; Matsumoto, 2002; Shipboard Scientific Party, 2002; Winters et al., 1999). It is therefore possible that in clay rich sediments, zones of hydrate-cemented silts or sands exist where the affected areas are smaller than the spatial resolution of the seismic survey. This can lead to an average velocity being measured within this zone of resolution which is then modelled. Some means of accounting for the spatial averaging/scaling problems is needed to accurately interpret the field seismic data.

Although the testing adopted in this research was on gas saturated hydrated sediments the results are applicable to values derived from seismic surveys from water saturated sediments. This is because in the resonant column both V_s and V_{lf} measure the velocity of the soil matrix and are virtually unaffected by the presence of the free gas, apart from the change in density between the gas filled pore space and the water filled pore space in seismic surveys. Density variations between the laboratory and filed measurements can be easily corrected for. The use of the Gassmann's equation also allows the difference between gas or fluid filled specimen to be compared.

6.4 Attenuation

Attenuation was measured for all test specimens using the free vibration decay method as previously described, for each mode of vibration. The inherent attenuation of the apparatus was computed, using the regression curves shown in Figure 4.29 for each measurement and deducted from the presented values. In the presentation of data the intrinsic attenuation inherent in the specimen is defined as Q_S^{-1} and Q_E^{-1}, for torsional and flexural vibration. Presenting the data in this format allows a comparison to be made between the measured attenuation and the attenuation for Q_P^{-1} and Q_K^{-1}, computed using Eq 3.43,

6.4.1 *Attenuation and hydrate content*

Figures 6.25 and 6.26 show the variation of intrinsic attenuation, Q^{-1} (for both torsional and flexural excitation respectively) with σ' for all test specimens. The inclusion of hydrate into the pore space causes a large increase in attenuation for both modes of vibration. Although the attenuation values as a function of σ' (Figures 6.25 and 6.26) show a high degree of scatter for each specimen, the general trend exhibits a low sensitivity to σ'. Figures 6.27 and 6.28 show the attenuation, for torsional and flexural excitation respectively, for selected specimens (H0D, H3-2 and H40) with error bars showing the 95% confidence limits for the measured data. The values for the error bars were obtained by applying a 95% confidence limit to the regression curve fitted through the measured values of peak amplitude per cycle for each free vibration decay test. Although the error bars are large for certain measurements, the results show that the increase in attenuation is a real effect of the hydrate inclusion and not a function of possible errors arising from the measurement technique. A comparison of attenuation between Figures 6.25 and 6.26 shows that the longitudinal wave attenuation is more variable than shear wave attenuation and shows up as an increased sensitivity to changes in effective confining pressure within each specimen.

A comparison of Q_S^{-1} and Q_E^{-1} with hydrate content at an effective confining pressure of 500kPa is shown in Figure 6.29. The trendline for the

attenuation values show that small amounts of hydrate at grain contacts have a major influence on attenuation with a clearly defined peak observed around the 3-5% hydrate content. This attenuation peak occurs at the same hydrate percentage as the transition zone identified in the velocity analysis (Section 6.3). An increasing hydrate content for specimens H10-H40 shows a steady reduction in attenuation, but with the measured value still 2-3 times higher than that for specimens with no hydrate content (H0L and H0D). These trends are consistent for each load and unload step. Similar attenuation peaks have also been reported for sand/cement samples where the attenuation peak corresponded to a 5-8% cement content (by mass of the sample) and decreased thereafter (Saxena et al., 1988).

Figures 6.30 and 6.31 presents the computed attenuations for Q_P^{-1} and Q_K^{-1}, derived using Eq 3.63, for all test specimens at an effective confining pressure of 500kPa. These derived values must be viewed with caution based on the discussion in Section 3.6.2. Error bars are shown which highlight the range of possible values due to systematic errors and the uncertainties in I_y as previously described. The added trend lines show that Q_P^{-1} and Q_K^{-1} follow the same trend identified for Q_S^{-1} and Q_E^{-1} as highlighted in Figure 6.29. However, it can be seen that the values of Q_P^{-1} and Q_K^{-1} obtained for specimens H4-1 and H5-1 lie considerably outside these trend lines. The values of Q_P^{-1} and Q_K^{-1} are dependent on the value of Poisson's ratio, computed from Eq 3.63 using derived velocity values, and the measured values of Q_S^{-1} and Q_E^{-1} at each load step. Figure 6.32 shows the computed Poisson's ratio for each specimen as a function of hydrate content at an effective confining pressure of 500kPa. Again, error bars are provided to show the range of possible values due to systematic errors and the uncertainty with I_y. The results show that the Poisson's ratio computed for H5-1 to be much higher than the other specimens with low hydrate contents, with specimen H4-1 being only slightly higher. The high values of Poisson's ratio, coupled with the low attenuation values of Q_E^{-1}, observed for both specimens, result in the very low attenuation values for both Q_P^{-1} and Q_K^{-1}.

Uncertainty in I_y has a large effect on the estimated errors for Poisson's ratio which then directly leads to the errors in both Q_P^{-1} and Q_K^{-1}. It is

also noted that the largest errors in both Q_P^{-1} and Q_K^{-1} are situated at the critical hydrate content where the sand grains start to be fully bonded, with specimens H4-1 and H5-1 generally having the largest errors. However it can still be seen that the attenuation peak is real and not an affect of systematic errors or the uncertainty in I_y. The value of Q_K^{-1} is generally 2-3 times greater than Q_S^{-1} (except for specimens H4-1 and H5-1) which suggests that the cause of attenuation is related to 'squirt flow' as opposed to frictional losses (Mavko and Nur, 1979).

6.4.2 *Attenuation model*

It is generally assumed that the presence of gas hydrates in the pore space of marine sediments causes a reduction in attenuation (Guerin and Goldberg, 2002; Pecher and Holbrook, 2000) due to a reduction in porosity, based on experimental results by Hamilton (1972). This hypothesis is dependent on frictional losses at grain contacts being the main source of attenuation. However it has been shown (Section 3.3.2) that at small strains (less than 10^{-6}), attenuation is constant (with strain) and thought to result from viscous flow effects (Winkler and Nur, 1979). Wood et al. (2000) also assumed that gas hydrates would reduce attenuation based on the reduction of attenuation in frozen soils (Toksöz et al., 1979) although work by Al-Hunaidi et al. (1996) found the opposite.

A conceptual model to describe attenuation in hydrated sediments has therefore been developed here by utilizing the partially saturated attenuation model of Mavko and Nur (1979). The model for attenuation developed by Mavko and Nur (1979) is dependent on fluid being present in the pore space. Literature on frozen porous media have shown that the surfaces of soil particles remain liquid water wet in the presence of water ice (Handa et al., 1992; Overloop and Van Gerven, 1993; Tsytovich, 1975; Valiullin and Furo, 2002). As many physical characteristics of ice and hydrate are similar, it can be assumed that after hydrate formation some liquid water remains as absorbed water on the sand grains. All measurements of attenuation undertaken as part of this research were performed at strains less than 10^{-6} which

is below the strain level where frictional losses occur (Winkler et al., 1979).

Figure 6.33 idealizes the differing stages of hydrate formation and their possible effect on grain contacts and attenuation (see also Figure 6.24). When no hydrate is present in the pore space, fluid flow occurs at grain contacts, due to absorbed water on the sand. Due to the short contact zone, fluid flow is relatively easy and energy losses are small and so attenuation is minimal (Figure 6.33(a)). As the density of the sand increases the number and stability of particle contacts increase, leading to a reduction in attenuation as seen in Figures 6.25 and 6.26.

Figure 6.33(b) shows hydrate growth in the pore space at grain boundaries causing cementation of grain contacts, and this increases the effective area of the grain contact. By assuming that the cementation of the sand grains by hydrate is not perfect across the whole region (Murphy et al., 1986), the area between the hydrate cement and grain is now analogous to a long flat crack filled with water (due to absorbed water on sand grains). As a seismic wave passes, particle motion causes deformation of the crack and fluid squirts from the crack into the pore space, with the resultant loss in mechanical energy causing increased attenuation. As hydrate content increases up to the critical hydrate value (Section 6.3) the number of cemented grain contacts increases, with a corresponding increase in attenuation.

At the critical hydrate content all sand grains are cemented and attenuation is at a maximum. Above the critical hydrate content, increasing hydrate leads to an encasement of the sand grains and an infilling of the pore space (Figure 6.33(c)). As the sand grains become encased the potential for squirt flow into the pore space is reduced, or impeded, which in turn leads to a reduction in attenuation.

The attenuation measured for specimens containing higher hydrate concentrations is twice that measured for the air dry specimens, suggesting only partial impediment of the squirt flow phenomena occurs, or equally there are less crack-like pores of the correct geometry/thickness to facilitate squirt flow. This suggests that as the hydrate seals around the sand grains and reduces the squirt flow through the flat cracks, squirt flow is still possible though the equant pores within the hydrate structure or as mentioned previously the

number of flat cracks is reduced.

Attenuation data, from the Malik 2L-38 well in the Mackenzie Delta, Canada (Guerin and Goldberg, 2002), had shown a monotonic increase in attenuation up to 80% hydrate content. But, it can also be inferred from their data that at low hydrate contents, 5-10%, an initial maximum occurred and then increased monotonically, although there is some scatter in the data due to the resolution of the survey (Goldberg, 2003). Although their data was obtained under saturated conditions, one can apply the same conceptual model of attenuation, herein developed, to their data set. At low hydrate concentrations squirt flow through flat cracks occurs at cemented grain boundaries causing the initial maximum in attenuation. As the hydrate concentration increases the grain boundaries are sealed and quirt flow occurs, either through the equant pores, or through a reduced number of flat cracks within the hydrate structure. This causes an initial fall off in attenuation, since flat cracks have higher dissipation potential than equant pores. As hydrate concentrations increase a corresponding increase in the number, and length, of pores being available to the dissipative motion occur, and so attenuation increases monotonically. Although the results of this research do not show increasing attenuation with hydrate content after the initial maximum, this could be explained by the finite volume of liquid water that was available in each test.

6.5 Dissociated hydrate specimens

After undertaking resonant column tests on hydrated specimens the hydrate was dissociated, as described previously, and resonant column testing was undertaken on the dissociated specimens. Tests were undertaken at the same effective confining pressure, and total pressure, as the hydrated specimens.

6.5.1 *Velocity comparison*

Figures 6.34 and 6.35 show the relationships between velocity (V_s and V_{lf} respectively) and effective confining pressure during isotropic loading and unloading for the majority of test specimens (H1 was not tested and H10

was affected by pressure equalization). The results show that hydrate formation and dissociation had no appreciable lasting effect on the velocity curves. The response of previously hydrated specimens approximately follow the same path as specimen HOD for both velocity modes. The small discrepancies can be attributed to the initial variation in density and void ratios, as shown in Table 5.2. The V-σ' exponent is $b_S = 0.23$ and $b_L = 0.23$ for all tested specimens during loading and unloading. The effects of overpressurisation of specimens H4-1 and H5-1 during hydrate formation are not evident in the dissociated specimens, suggesting that variations in velocities, when hydrated, are due to the hydrate formation itself.

Comparing the data in Table 5.2, specimen HOD should have the highest velocity due to its relative density, D_r being higher. Also, the addition of water in the pore space increases the density of the specimen. Therefore, considering Eq 3.13, the measured velocity of the specimens should reduce due to the increasing density for specimens H0D to H40 (Table 5.2). However, Figures 6.34 and 6.35 show that specimen H2 has the highest V_s of all the specimens, while specimen H3-1 shows the highest V_{lf}. This suggests that surface tension and capillary effects cause a stiffening of the frame matrix (Ingles, 1962) with increasing water content. As the water content increases, the increased density of the specimen has a greater effect on velocity than the surface tension and capillary effects and so a reduction in velocity occurs as shown by the results for H20 and H40.

6.5.2 *Attenuation of dissociated sediments*

The addition of water in to the pore space due to the dissociation of the hydrate causes a slight increase in shear wave attenuation compared to the dry specimens as shown in Figure 6.36. A sensitivity of the measured attenuation to σ' is evident possibly due to closure of micro-cracks (at grain contacts) as pressure is applied (Best, 1997). This trend is also generally shown for longitudinal wave attenuation as shown in Figure 6.37.

Attenuation did not significantly increase as the volume of water, as a function of pore space, was increased from 2% to 40%. Mavko and Nur (1979)

suggest that as saturation increases, the number of flat cracks filled by water (which dominate the attenuation properties of the rock), also increases and causes a rise in attenuation. However, this hypothesis is based on rocks with low porosity and cracks with low aspect ratios. In these tests, with uniform sand grains, the addition of small volumes of water enables saturation of the grain contact (due to surface tension and capillarity), and therefore an increase in attenuation was measured. Increasing the water content further did not effect saturation at the grain contacts and so had no appreciable effect on attenuation thereafter.

Figure 6.36 also shows the measured attenuation for the hydrated specimen H3-2, which corresponds to the measured attenuation peak observed in Figure 6.29. This clearly shows that the formation of hydrate at grain contacts had a major effect on attenuation compared to the effect of increased water at grain contacts in the dissociated specimens.

Table 6.1: *Pore pressure rise during dissociation, from data shown in Figure 6.5.*

Specimen number	Ice content, I_c (% of pore space)	Pore pressure rise, δ P (MPa)	$I_c/\delta P$
H1	1.07	0.13	8.23
H2	2.15	0.25	8.57
H3-2	3.02	0.37	7.32
H4-2	3.83	0.48	7.98
H5-2	4.89	0.63	7.76
H10	9.62	—	—
H20	18.06	2.67	6.76
H40	35.45	5.79	6.12

Table 6.2: *Values of b_s and b_L as a function of hydrate content for sand specimens obtained during isotropic loading and unloading.*

Specimen number	b_s (Loading)	b_s (Unloading)	b_L (Loading)	b_L (Unloading)
H0L	0.27	0.27	0.27	0.27
H0D	0.23	0.23	0.22	0.22
H1	0.16	0.19	0.16	0.20
H2	0.11	0.12	0.09	0.11
H3-1	0.01	0.06	0.01	0.06
H3-2	0.02	0.04	0.02	0.04
H4-1	0.07	0.06	0.07	0.06
H4-2	0.02	0.04	0.02	0.04
H5-1	0.06	0.06	0.05	0.06
H5-2	0.03	0.02	0.03	0.02
H10	0.03	0.03	0.04	0.05
H20	0.01	0.02	0.02	0.04
H40	0.02	0.03	0.06	0.06

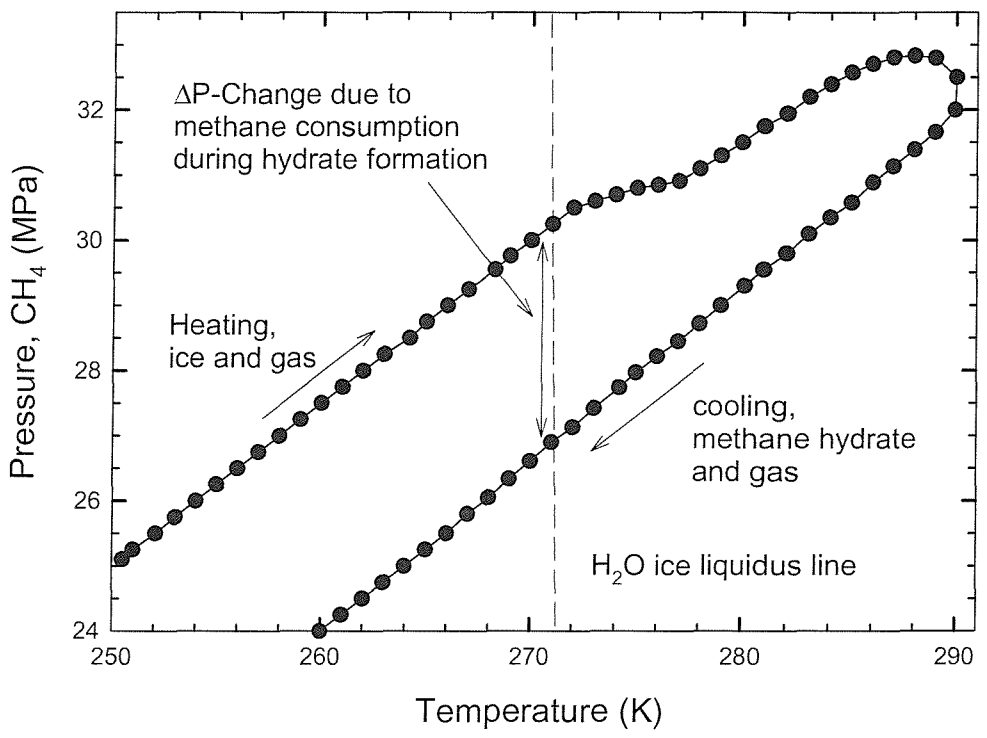

Figure 6.1: *P-T history of a methane hydrate synthesis run. Redrawn from Stern et al., (2000).*

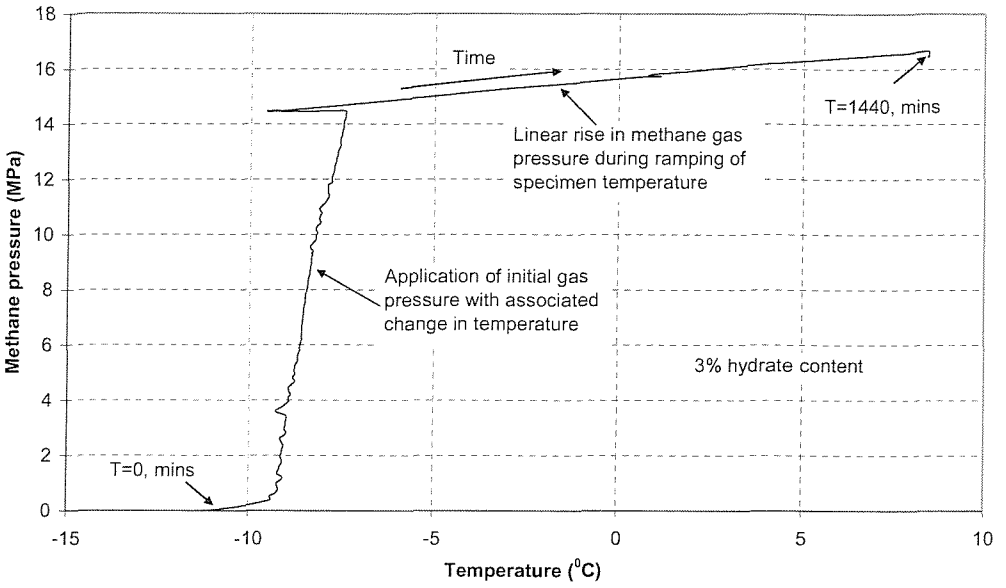

Figure 6.2: *P-T history of hydrate specimen H3-2 during hydrate formation test.*

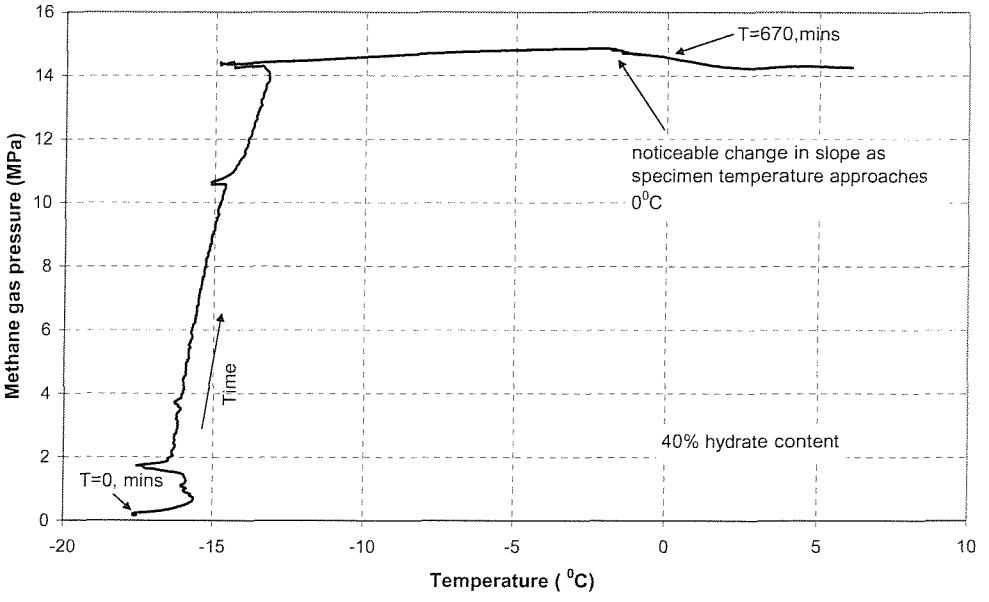

Figure 6.3: *P-T history of specimen H40 during hydrate formation.*

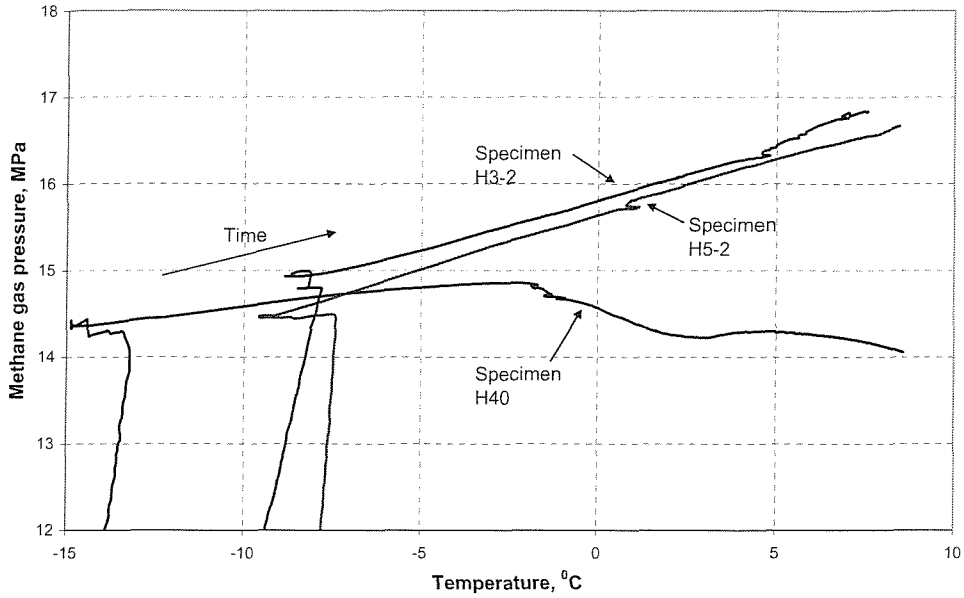

Figure 6.4: *Comparison of P-T histories for specimens with differing initial ice volumes within the pore space. Specimen H3-2 = 3% of pore space, H5-2 = 5% and H40 = 35% as highlighted in Table 6.1*

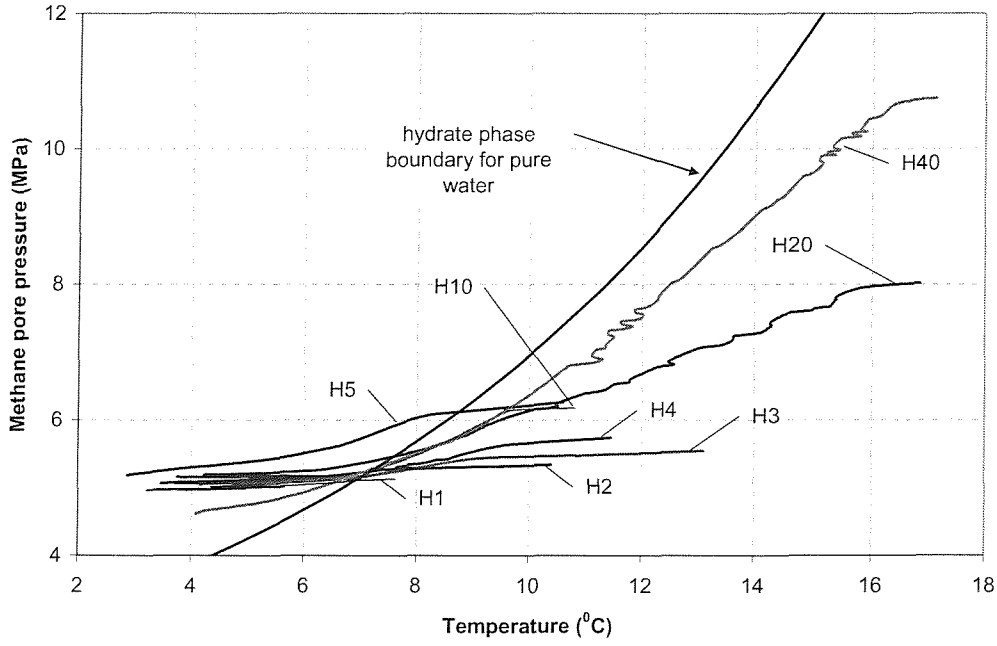

Figure 6.5: *Dissociation curves for differing hydrated specimens. Note: The dissociation curve for specimen H10 was truncated due to the pore pressure rising above the cell pressure.*

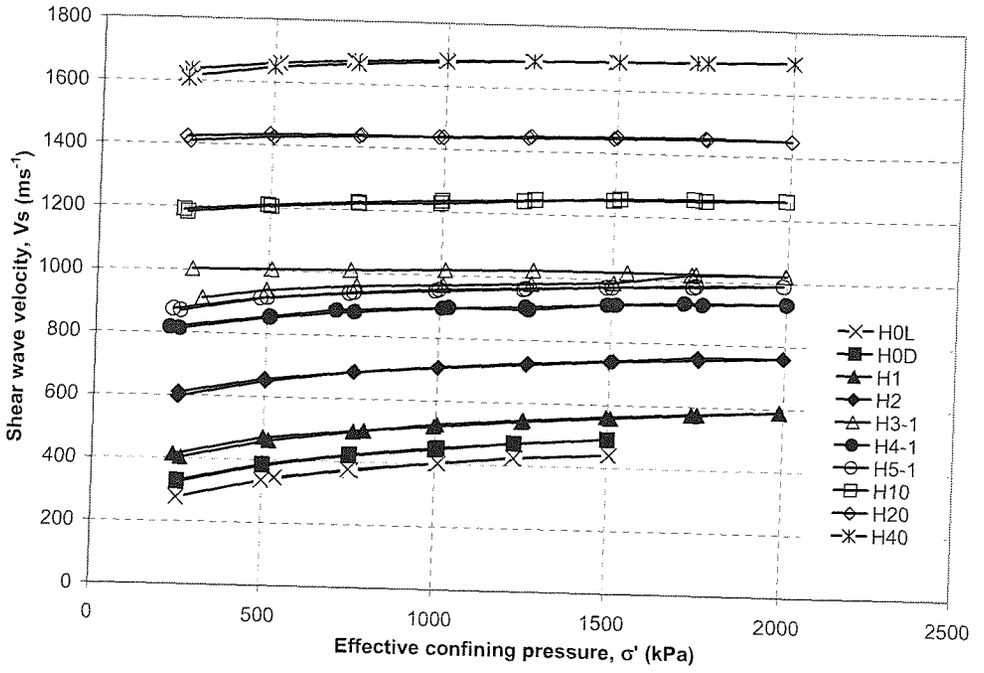

Figure 6.6: *Shear wave velocity (V_s) against effective confining pressure (σ') for specimens H0L to H40 during the load/unload cycle.*

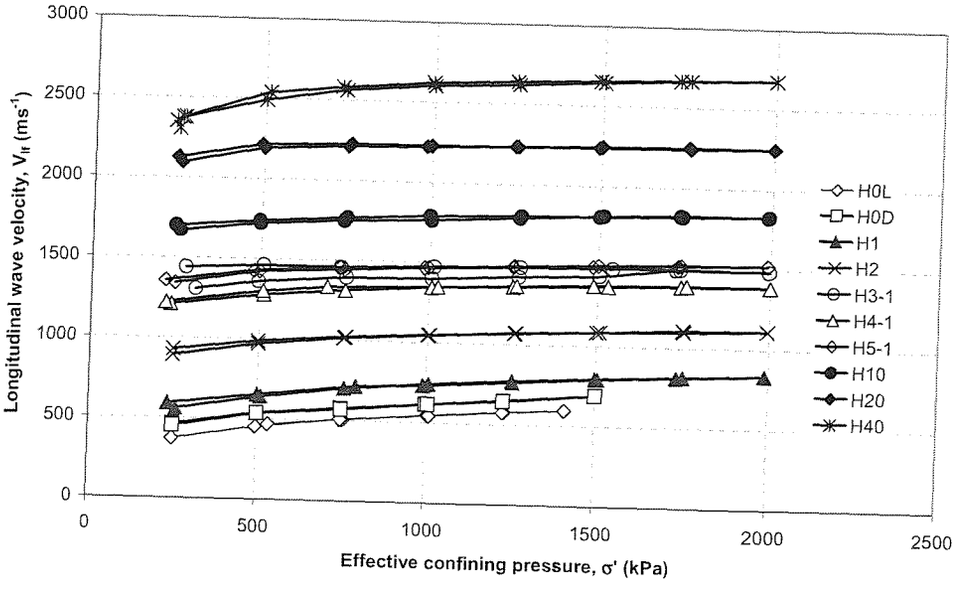

Figure 6.7: *Longitudinal wave velocity (V_{lf}) against effective confining pressure (σ') for specimens H0L to H40 during the load/unload cycle.*

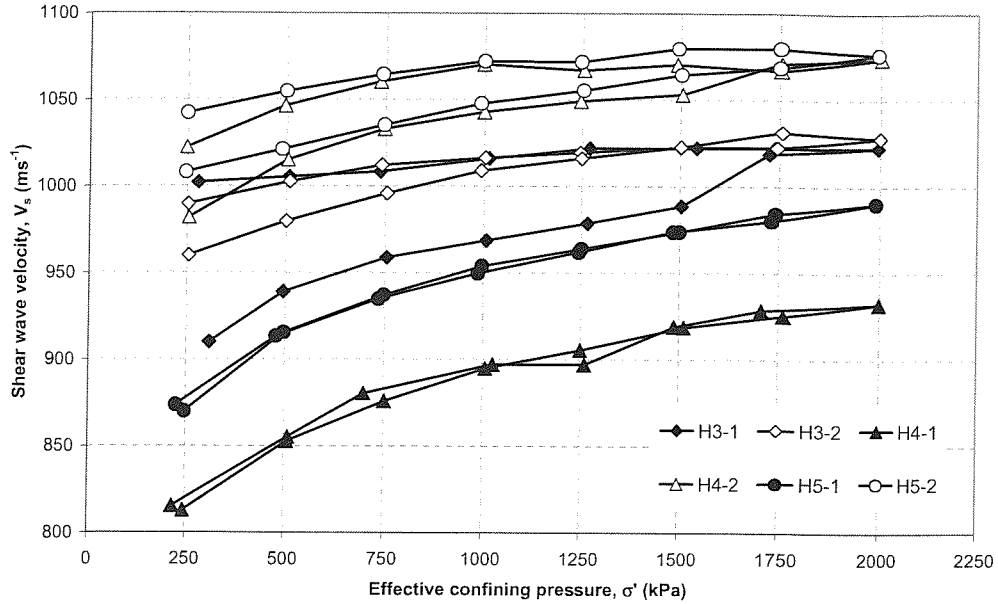

Figure 6.8: *Shear wave velocity (V_s) against effective confining pressure (σ') for specimens H3-1 - H5-1 and H3-2 - H5-2 during the load/unload cycle.*

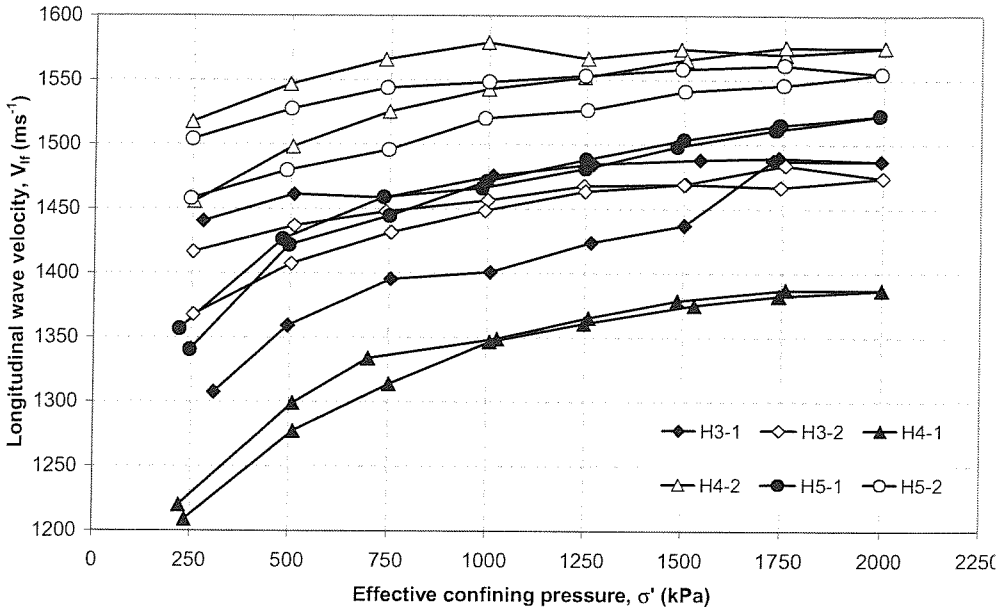

Figure 6.9: *Longitudinal wave velocity(V_{lf}) against effective confining pressure (σ') for specimens H3-1 - H5-1 and H3-2 - H5-2 during the load/unload cycle.*

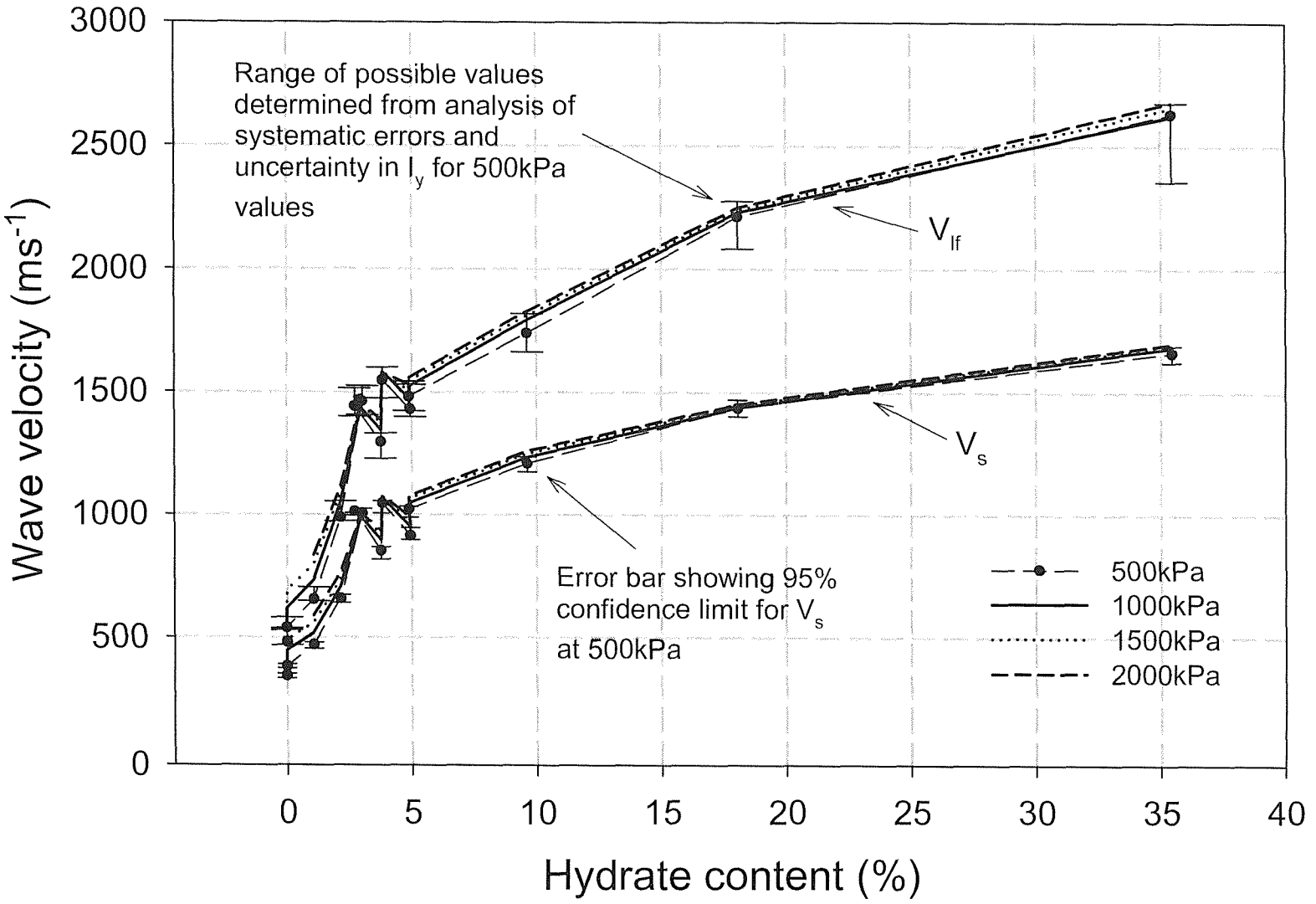

Figure 6.10: *Variations in V_s and V_{lf} as a function of hydrate content.*

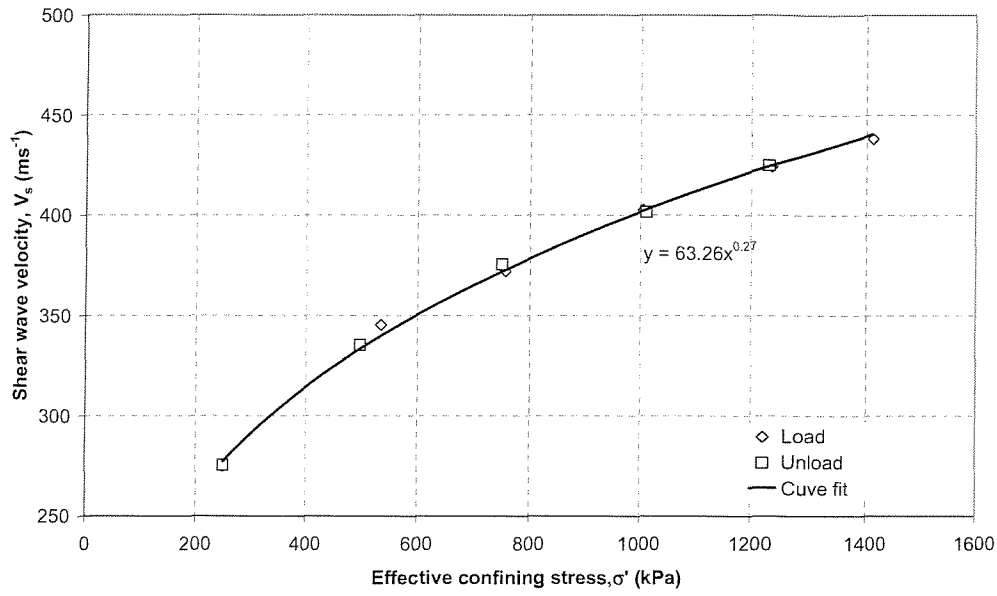

Figure 6.11: *Shear wave velocity (V_s) against effective confining pressure (σ') for specimen H0L with plotted regression curve showing b_S component.*

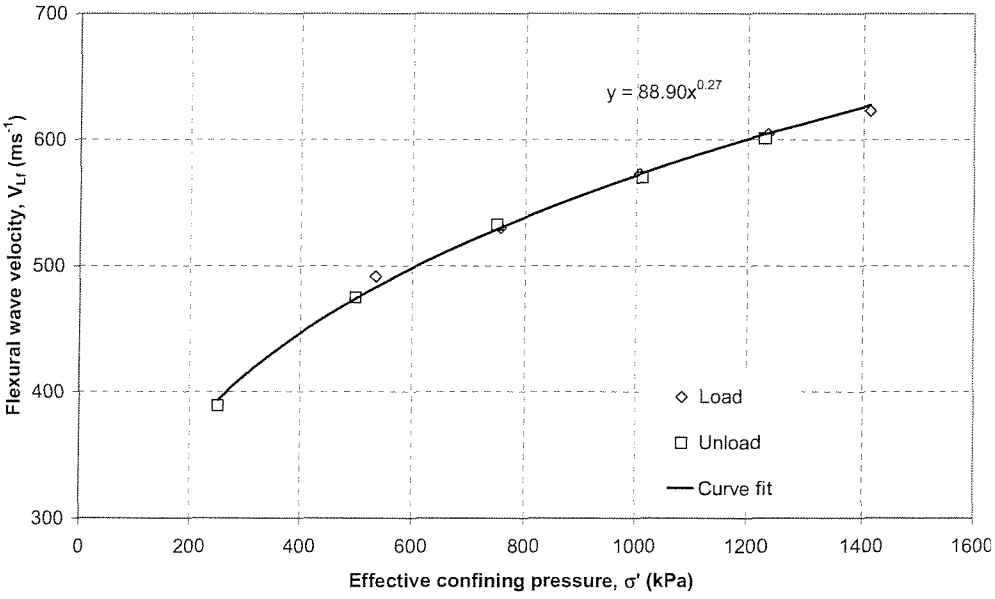

Figure 6.12: *Longitudinal wave velocity (V_{lf}) against effective confining pressure, (σ') for specimen H0L with plotted regression curve showing b_L component.*

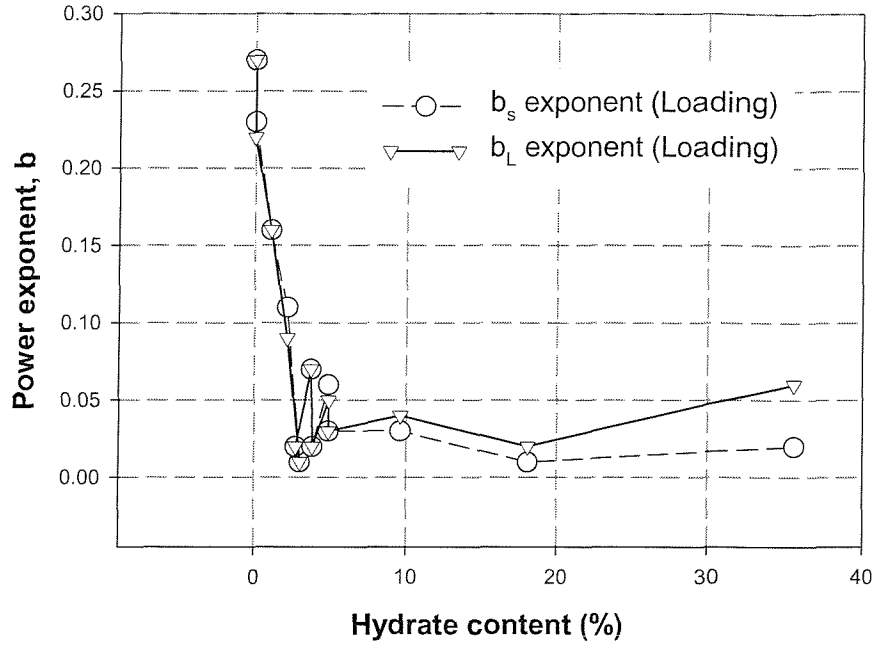

Figure 6.13: *Power law regression curve exponent, b as a function of hydrate content obtained during isotropic loading.*

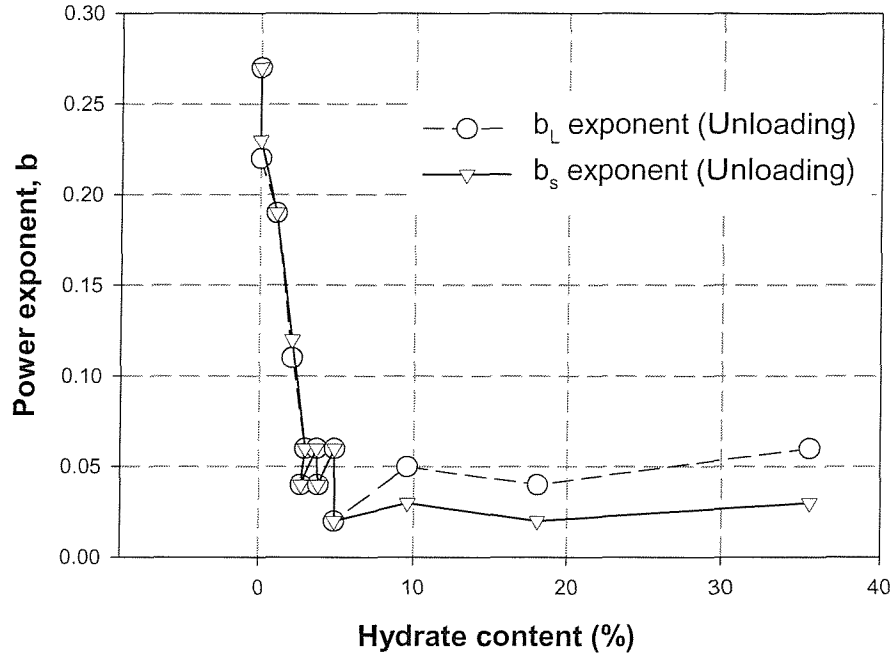

Figure 6.14: *Power law regression curve exponent, b as a function of hydrate content obtained during isotropic unloading.*

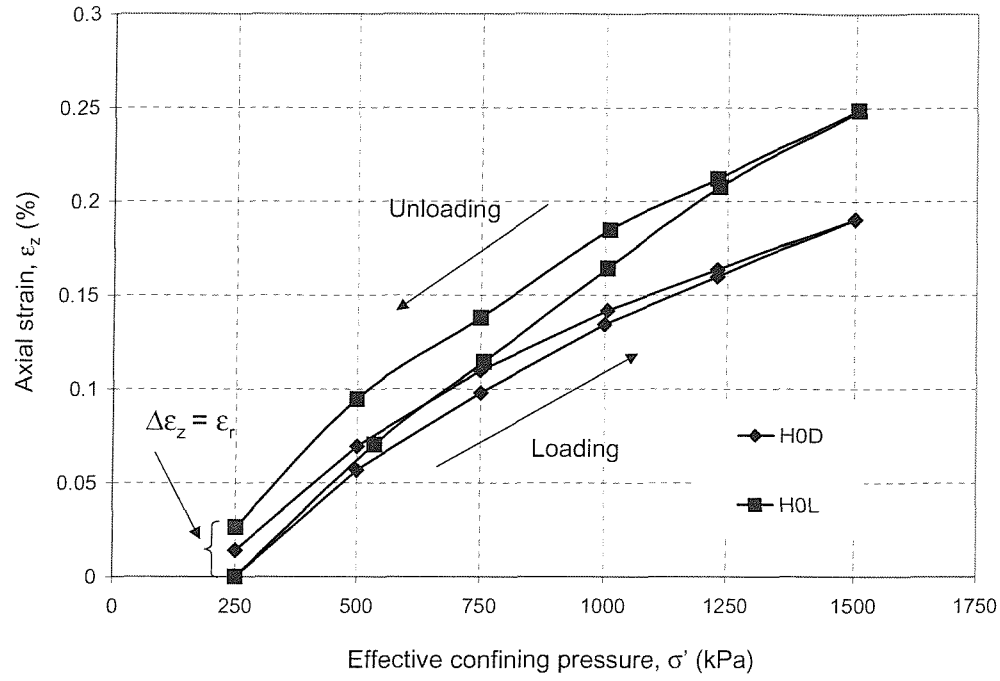

Figure 6.15: *Effective confining pressure (σ') with axial strain (ε_z) for specimens H0L and H0D.*

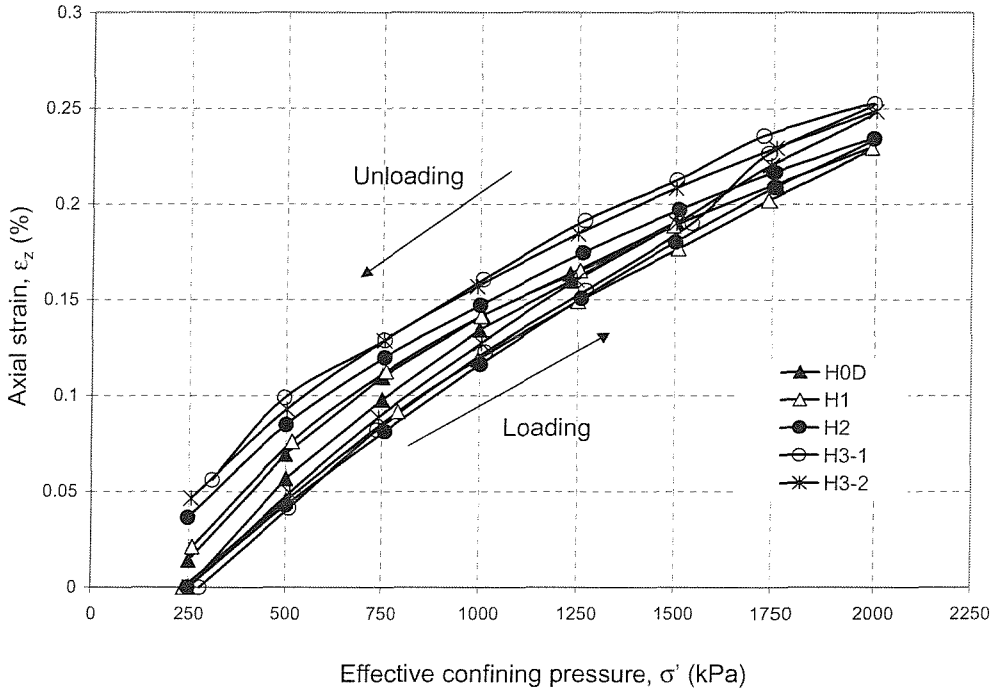

Figure 6.16: *Effective confining pressure (σ') with axial strain (ε_z) for specimens H0D to H3-2.*

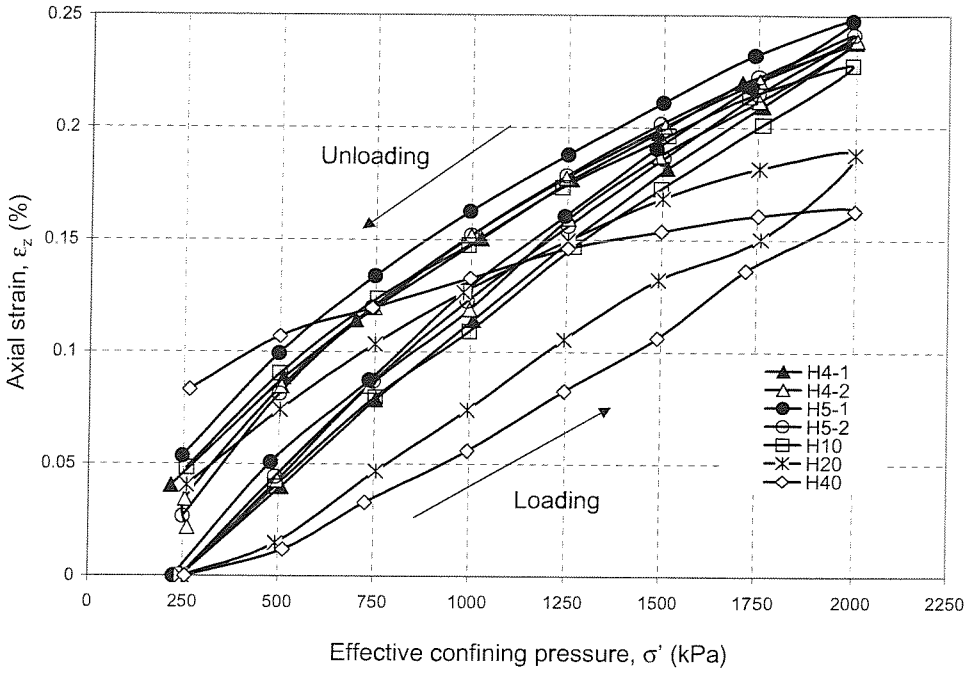

Figure 6.17: *Effective confining pressure (σ') with axial strain (ε_z) for specimens H4-1 to H40.*

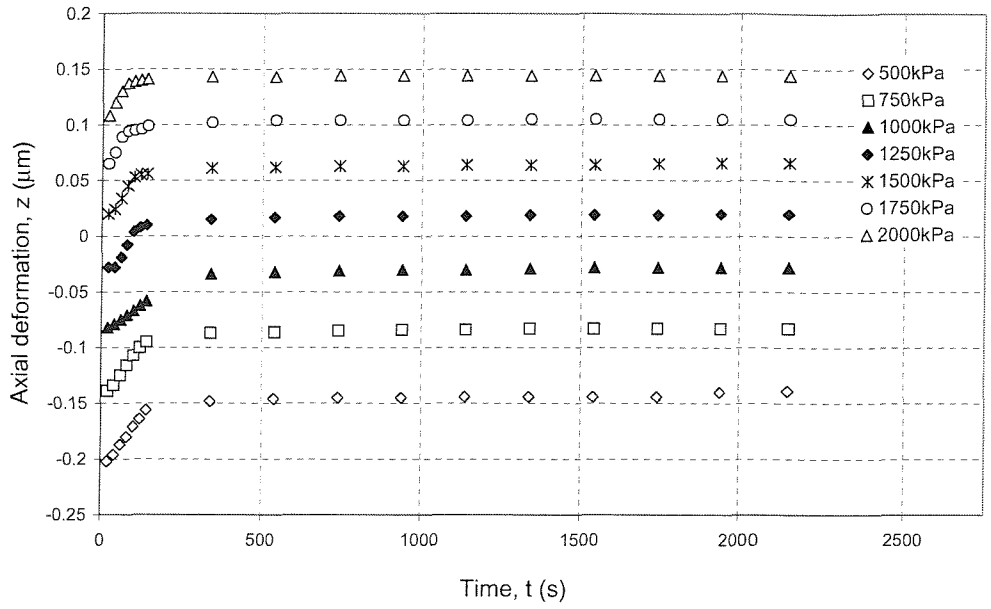

Figure 6.18: *Axial deformation measured during isotropic loading of specimen H3-2 for each loading step.*

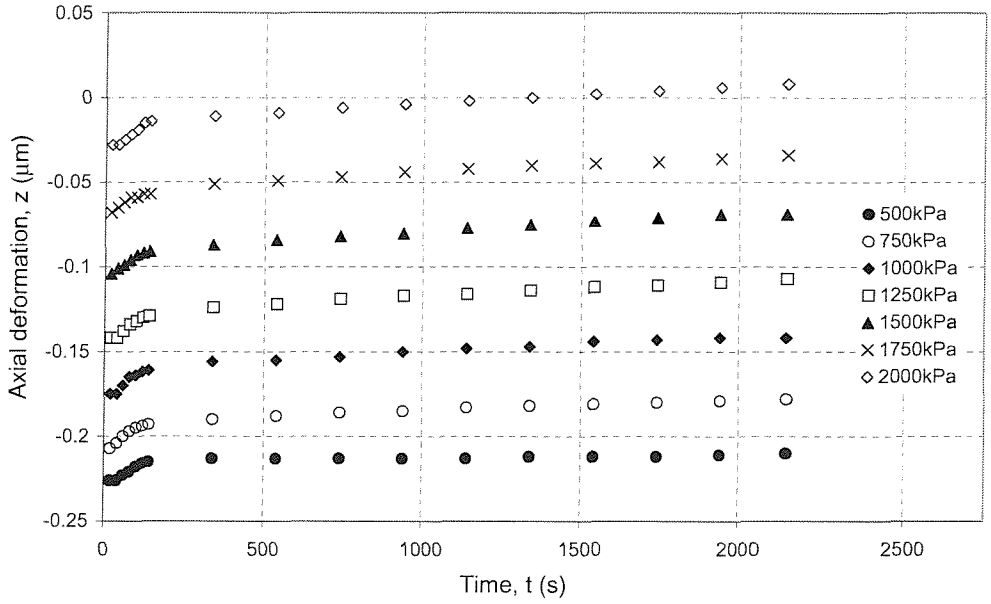

Figure 6.19: *Axial deformation measured during isotropic loading of specimen H40 for each loading step.*

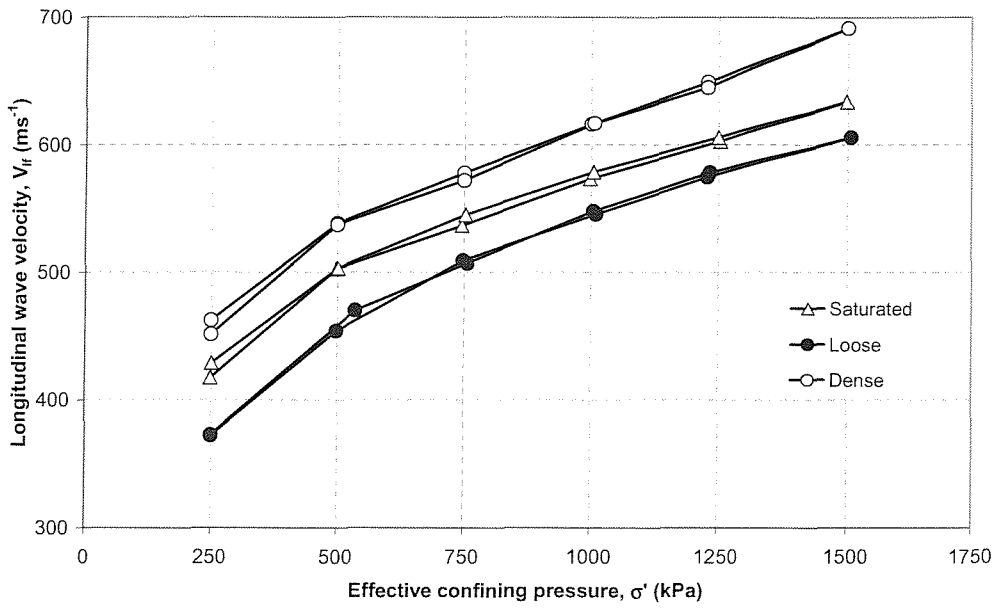

Figure 6.20: *Comparison of V_{lf} between a saturated dense sand and specimens H0L and H0D with σ'.*

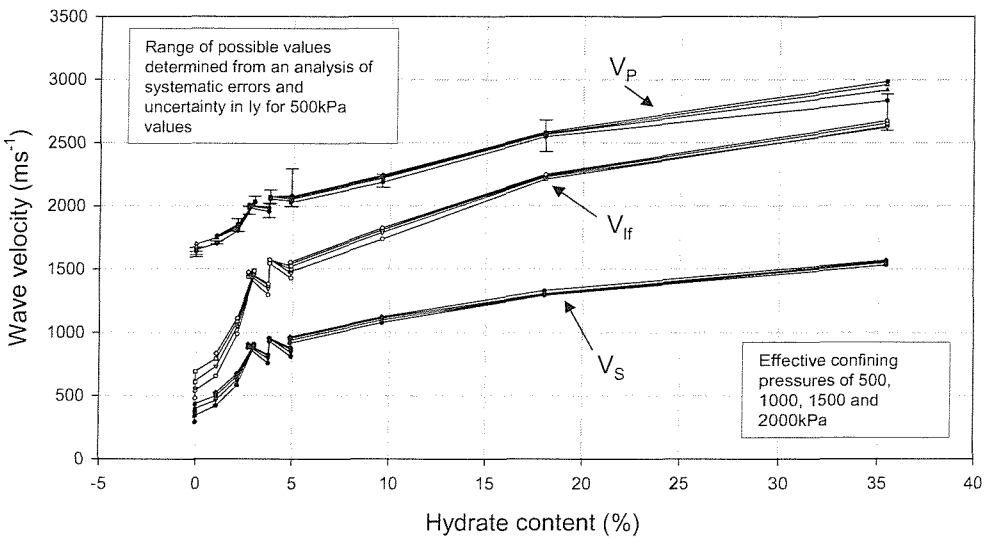

Figure 6.21: *Comparison of differing wave velocities as a function of hydrate content for all specimens.*

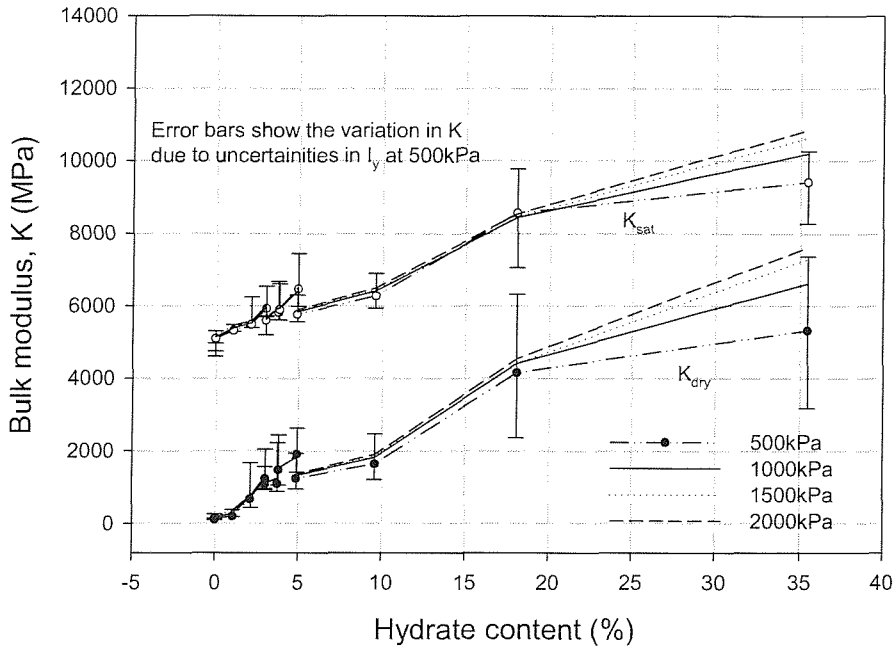

Figure 6.22: *Variation between measured dry bulk modulus (K_d) and saturated bulk modulus (K) as a function of hydrate content for all specimens.*

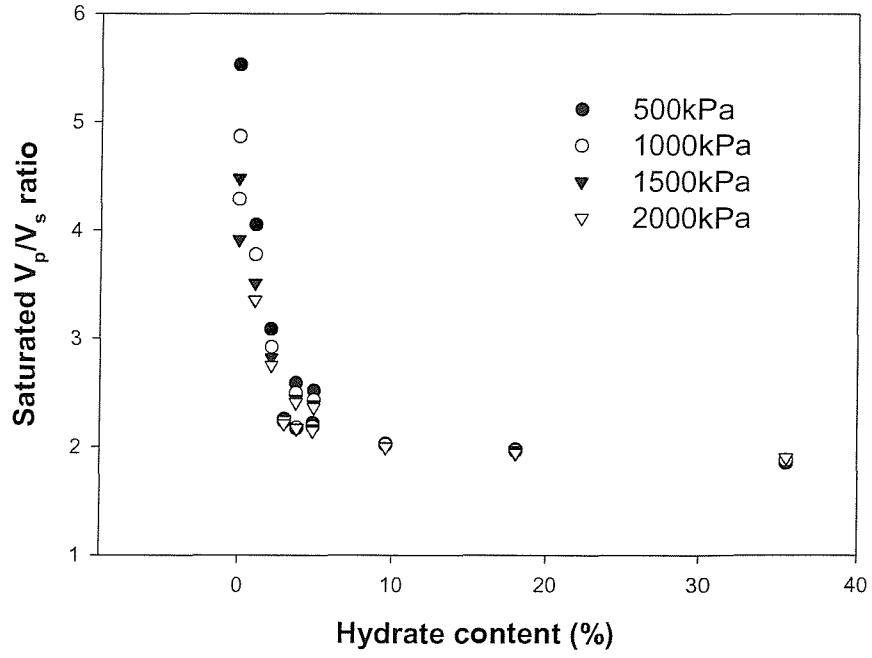

Figure 6.23: *Variation in saturated V_p/V_s ratio as a function of hydrate content for all specimens at differing effective confining pressures (500, 1000, 1500 and 200kPa).*

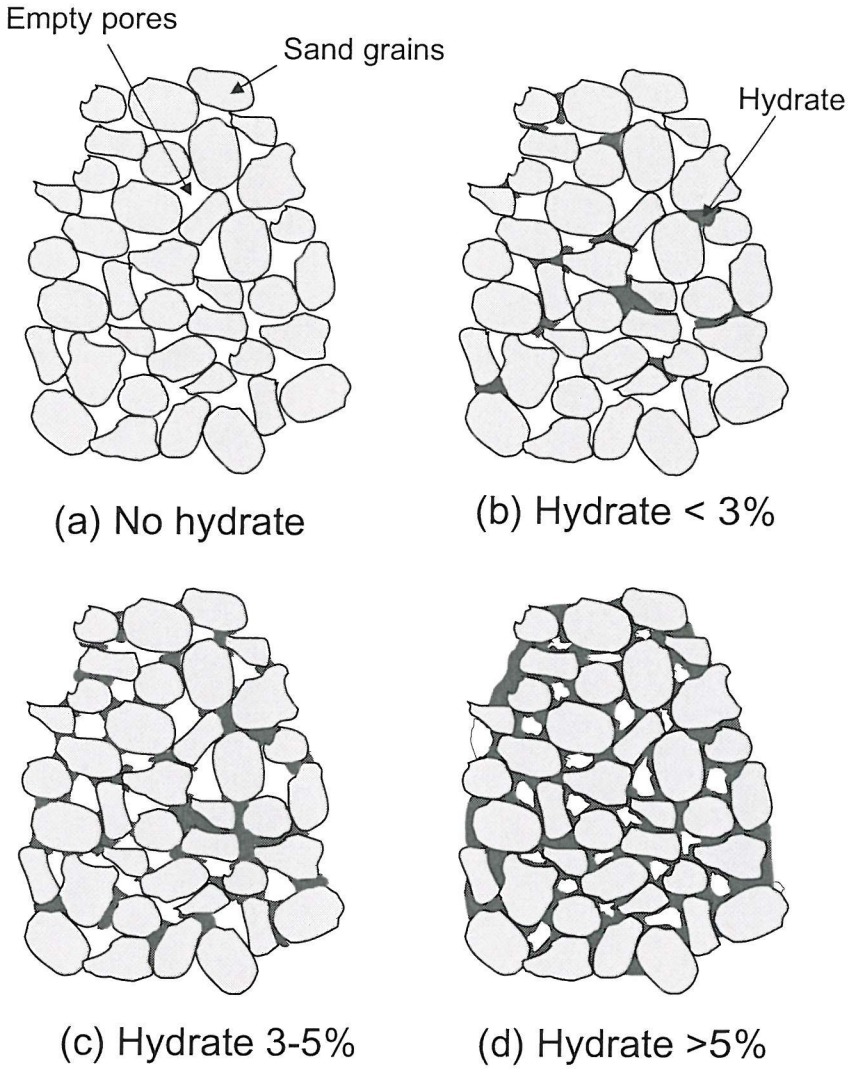

Figure 6.24: *Idealised model showing cementation and void filling as a function of increasing hydrate content. See text.*

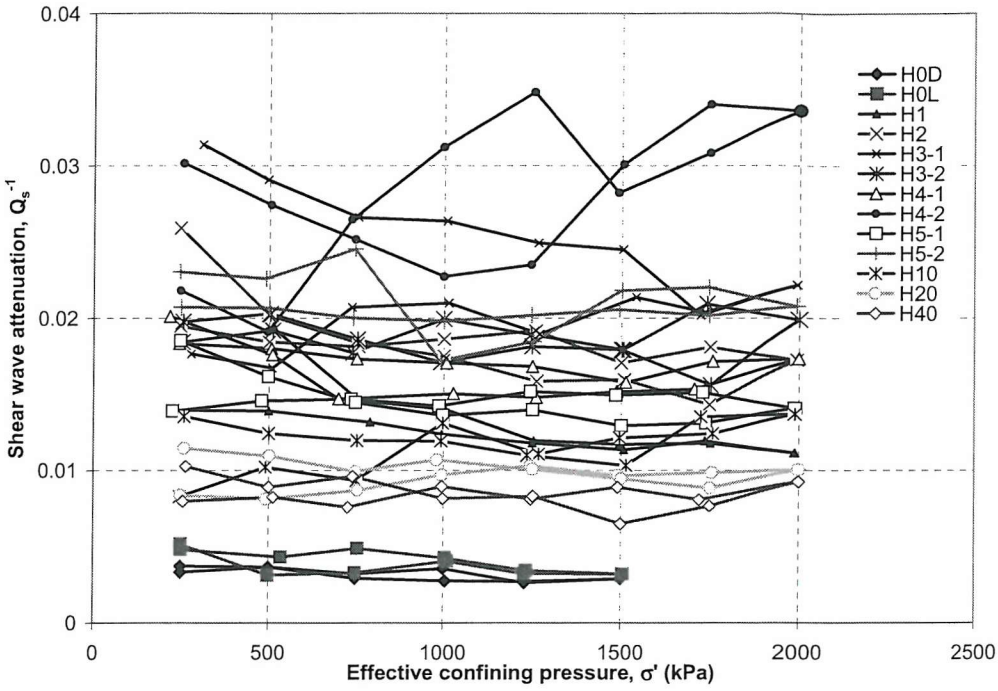

Figure 6.25: *Shear wave attenuation (Q_S^{-1}) against effective confining pressure (σ') for all specimens.*

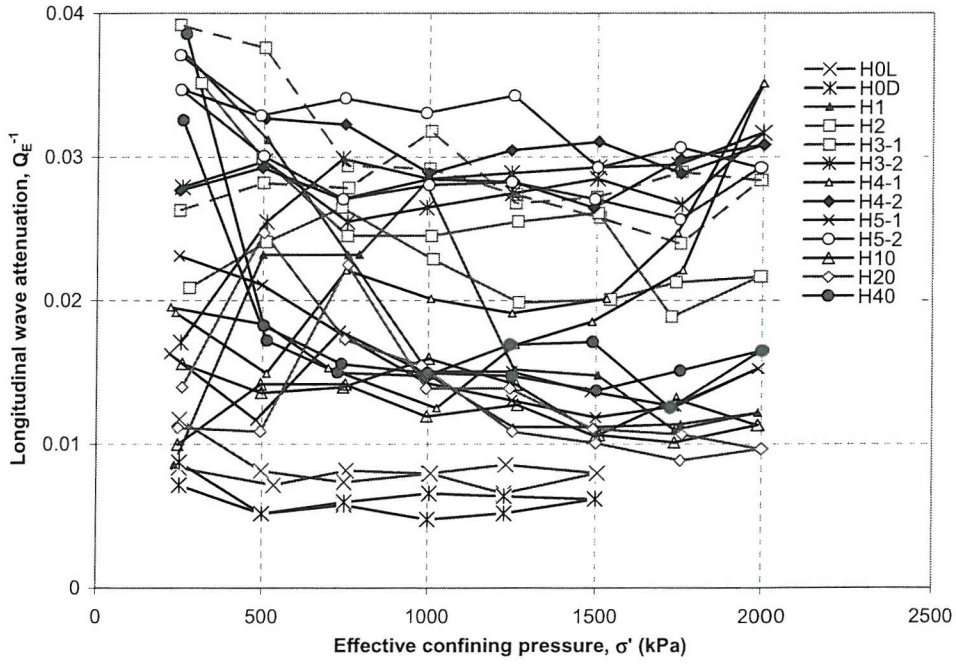

Figure 6.26: *Longitudinal wave attenuation (Q_E^{-1}) against effective confining pressure (σ') for all specimens.*

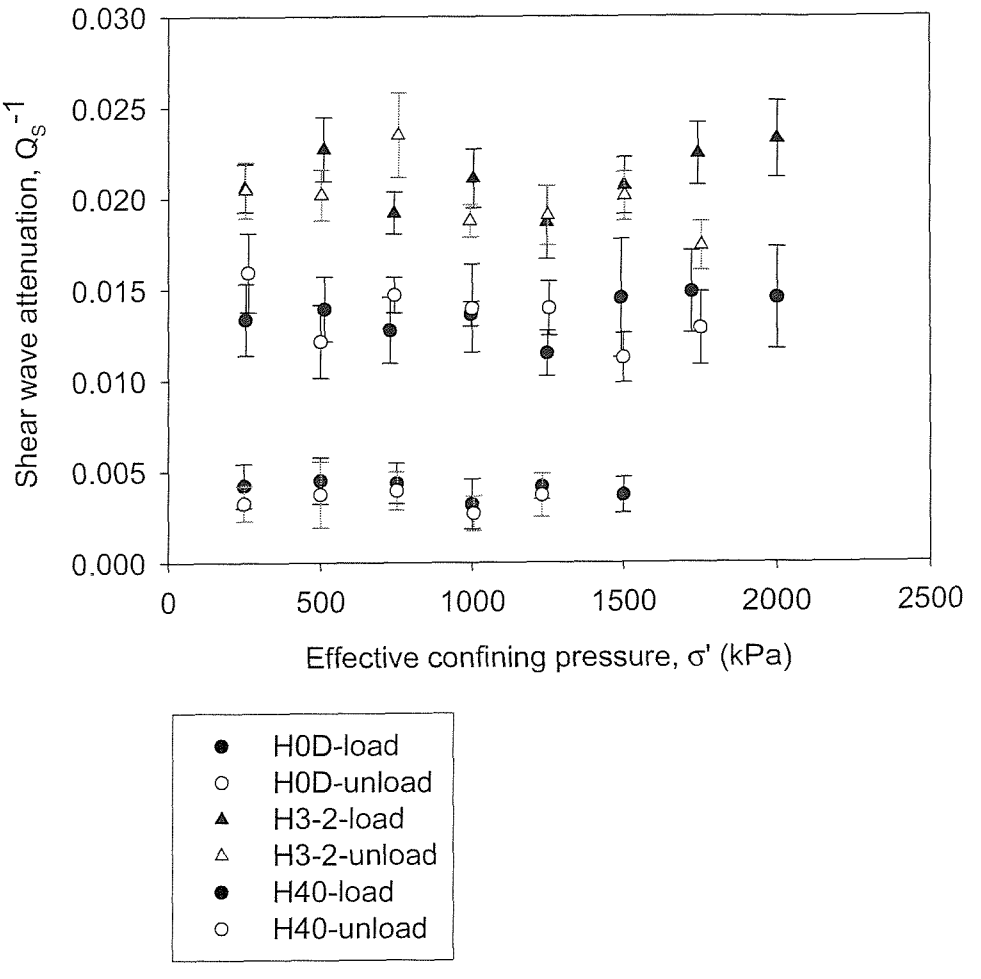

Figure 6.27: *Shear wave attenuation (Q_S^{-1}) against effective confining pressure (σ') for specimens H0D, H3-2 and H40 with error bars.*

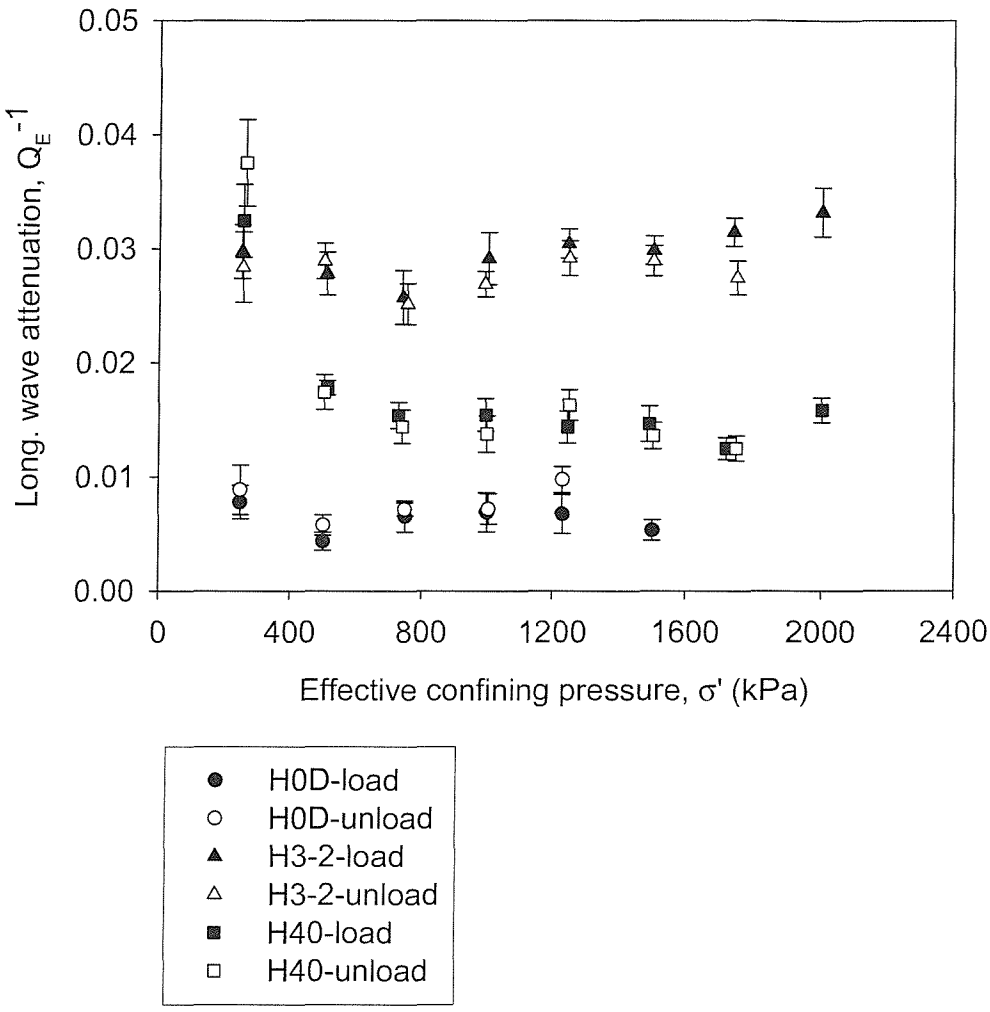

Figure 6.28: *Longitudinal wave attenuation (Q_E^{-1}) against effective confining pressure (σ') for specimens H0D, H3-2 and H40 with error bars.*

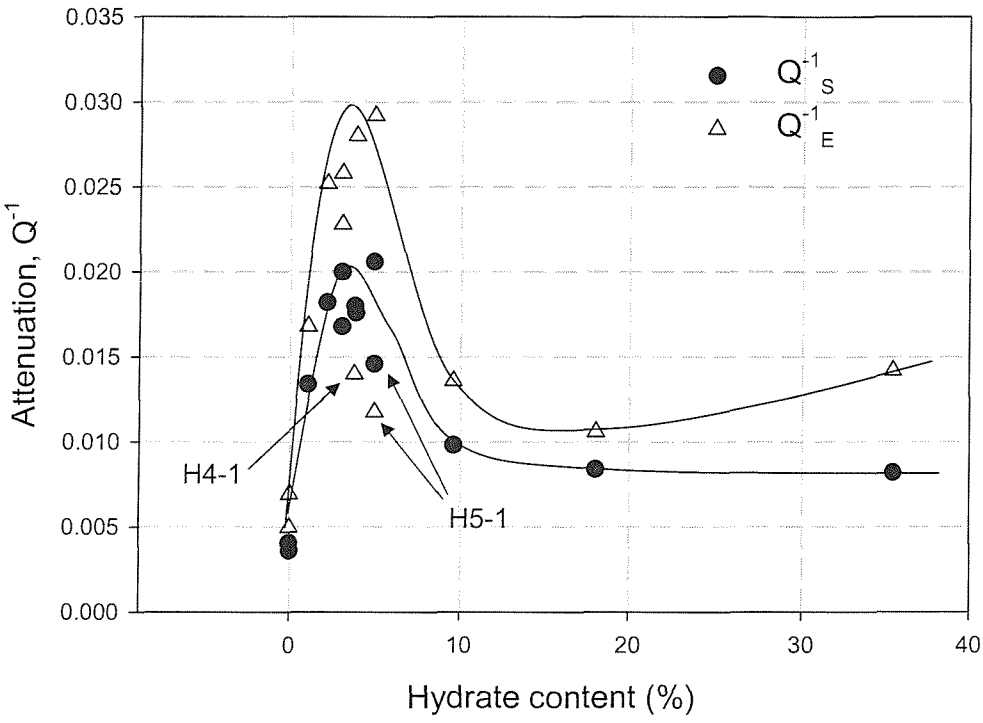

Figure 6.29: *Shear wave (Q_S^{-1}) and longitudinal wave attenuation (Q_E^{-1}) as a function of hydrate content for all specimens at an effective confining pressure of 500kPa.*

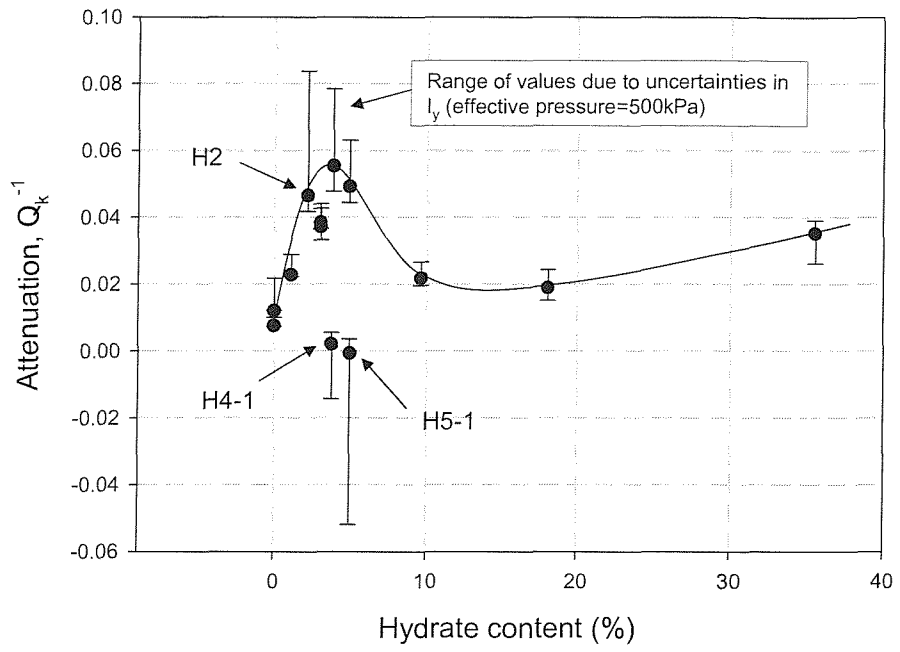

Figure 6.30: *Attenuation (Q_K^{-1}) as a function of hydrate content at σ'=500kPa for all specimens.*

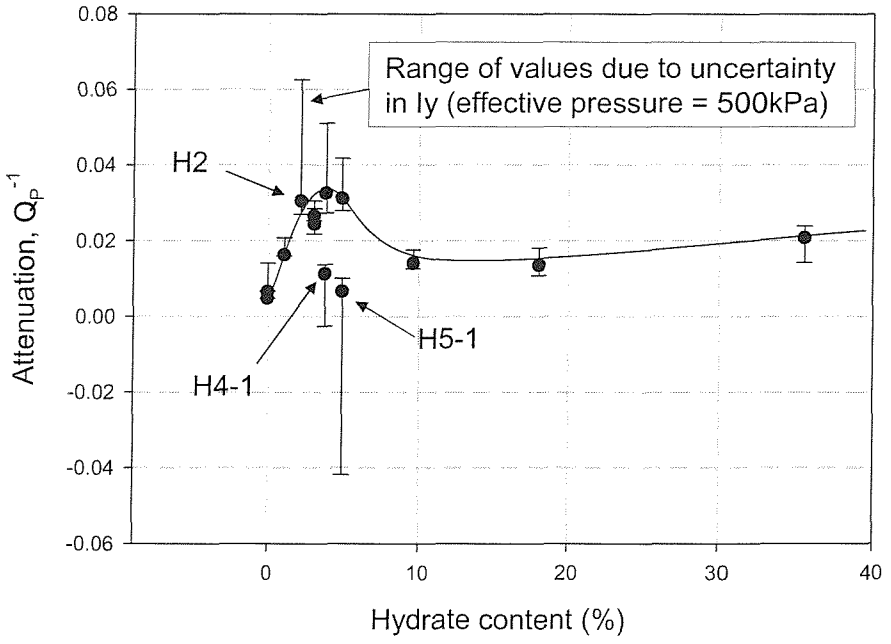

Figure 6.31: *Attenuation (Q_P^{-1}) as a function of hydrate content at σ'=500kPa for all specimens.*

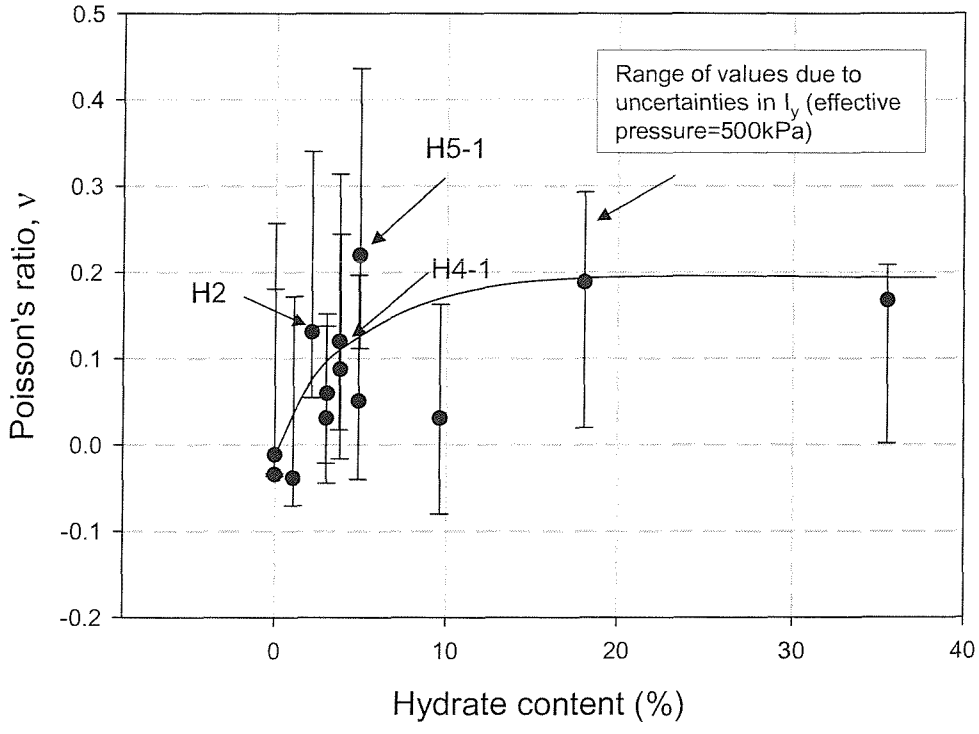

Figure 6.32: *Poisson's ratio derived from V_s and V_{1f} measurements for all specimens as a function of hydrate content at σ'=500kPa.*

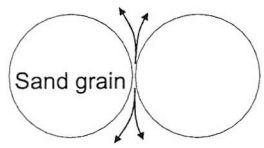

Squirt flow at particle contacts through bound water

(a) Idealised view of grain contacts with no hydrate.

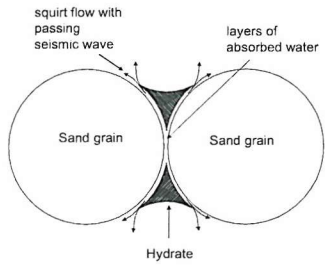

(b) Idealised view of grain contacts with hydrate at grain boundaries.

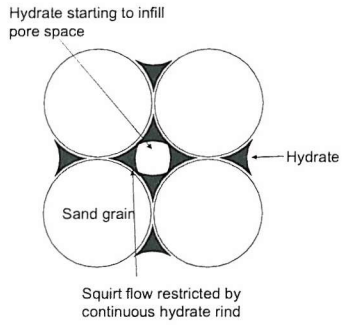

(c) Connected hydrate cemented grain contacts with commencement of pore filling.

Figure 6.33: *Conceptual model of grain contacts with increasing hydrate cement.*

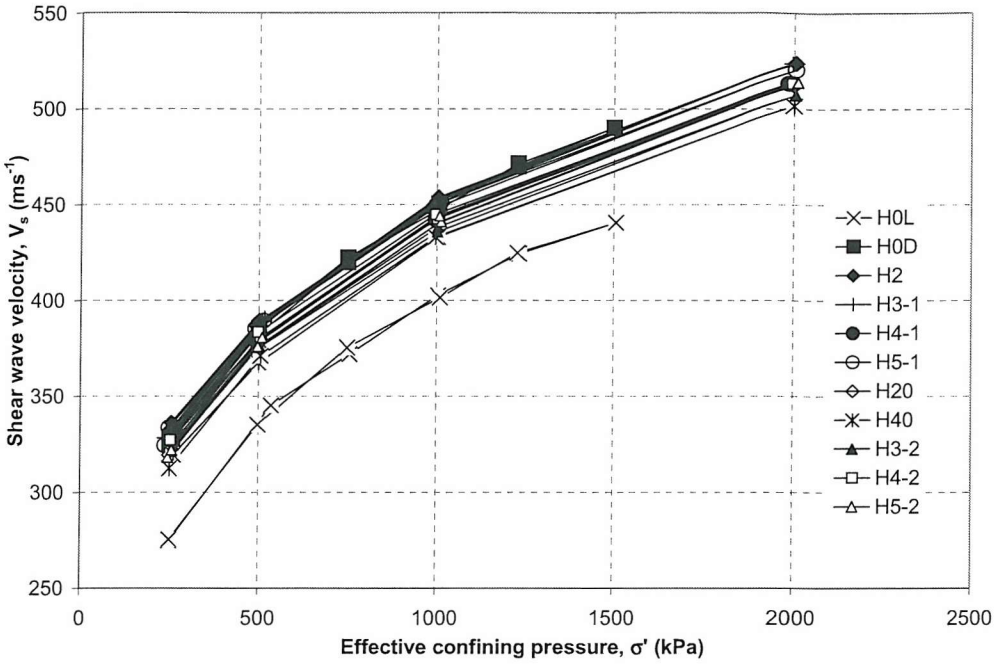

Figure 6.34: *Shear wave velocity,v_s with effective confining pressure, σ' for all dissociated specimens*

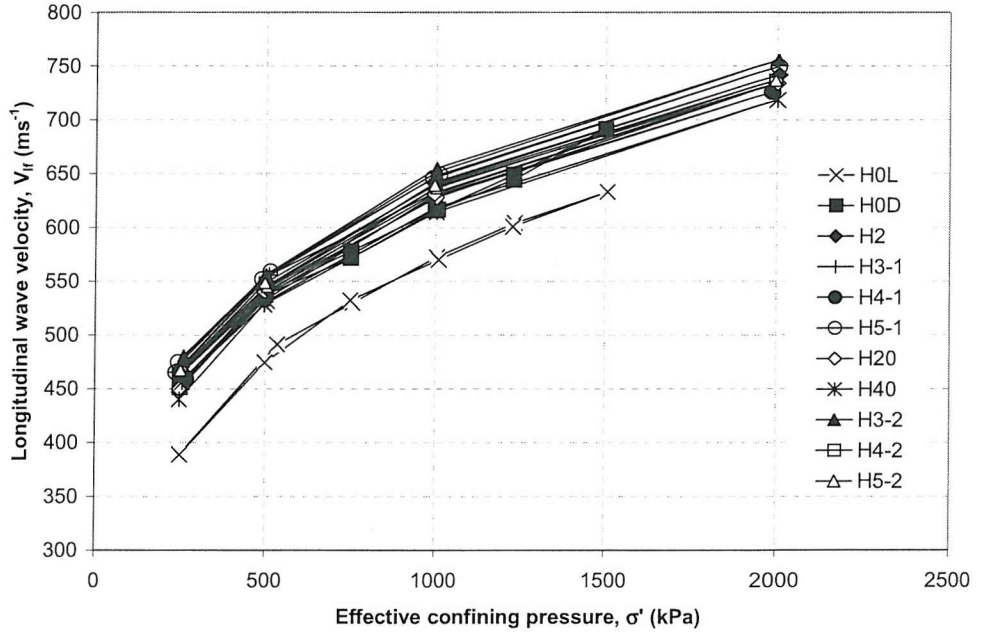

Figure 6.35: *Longitudinal wave velocity,v_{lf} with effective confining pressure, σ' for all dissociated specimens. Note: each dissociated specimen has a different water content.*

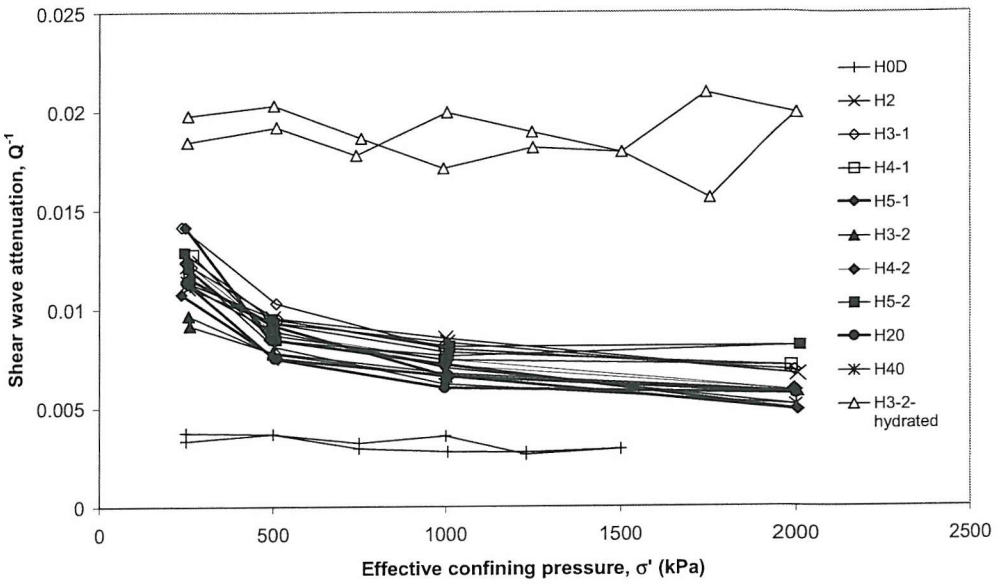

Figure 6.36: *Shear wave attenuation (Q_S^{-1}) as a function of effective confining pressure (σ') for dissociated specimens.*

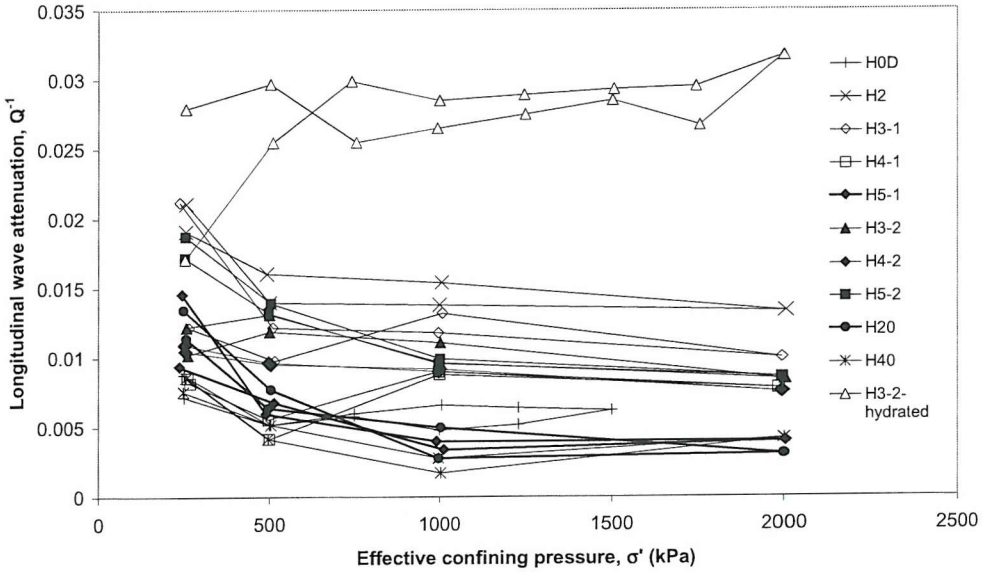

Figure 6.37: *Longitudinal wave attenuation (Q_S^{-1}) as a function of effective confining pressure (σ') for dissociated specimens.*

Chapter 7

Conclusions and Recommendations

7.1 Conclusions

Assessing the importance of gas hydrates with regard to its potential as an energy resource; its influence on global warming; or the potential of hydrate dissociation causing a geotechnical hazard, requires an estimation of the distribution and concentration of gas hydrate within the sediment column. The effective use using seismic surveys to provide such estimates will depend on the elastic properties of hydrate bearing sediments being understood.

The effect of gas hydrate on the elastic properties of ocean bottom sediment is poorly understood (Chapter 2). A laboratory apparatus, the resonant column, was identified as an effective apparatus (Chapter 3) for measuring the dynamic (and therefore seismic) properties of laboratory prepared specimens of hydrated soils. Due to the formation conditions of gas hydrate a new gas hydrate resonant column (GHRC) was developed to enable the testing of hydrated particulate materials (Chapter 4). Thirteen laboratory sand specimens, with different volumes of hydrate formed in the pore space, were tested to investigate their dynamic properties (Chapter 5), and were subsequently retested after the hydrate had dissociated. The results of these tests were analyzed to quantify the effect that gas hydrate had on the dynamic properties of sand specimens (Chapter 6). The main conclusions drawn from

the research are as follows.

7.1.1 *Gas hydrate and sediments*

- Gas hydrates are stable under certain thermobaric (temperature and pressure) conditions. Within the sediment column these thermobaric conditions exist in two distinct regions. These are: permafrost regions where stability conditions exist at the base of the permafrost layer (high pressure-low temperature); and continental margins and deep inland seas where water column depth and cold ocean bottom temperature provide suitable pressure and temperature conditions. In both cases increased burial causes hydrate stability temperature to be exceeded due to the geothermal gradient, leading to hydrate dissociation.

- Gas hydrates are thought, from the limited samples obtained, to occur in a number of forms. These are: nodular, veins, sheet and disseminated in the pore space of the rock or soil. The formation of the differing structures is dependent on the morphology of the sediment. Disseminated hydrate is more frequently associated with more coarse particulate sediments. In fine, clay rich, sediments the small pore size restricts disseminated growth and leads to veins forming along fissures with the larger pore sites giving rise to nodular forms. Growth will continue until the hydrate forming species are exhausted.

- Gas hydrates can occur with different crystal structures depending on the gas facies available. The main form of gas hydrate found in the sediment column is sI, with biogenic methane gas being the dominate gas.

- The most cost effective methods of determining the extent and distribution of gas hydrates are geophysical surveys. The effectiveness of these techniques is reliant on the elastic properties of gas hydrate bearing sediments being accurately defined. The recovery of intact

samples of hydrated sediment from the field is problematic due to the pressure reduction induced dissociation of hydrate samples during core recovery. The characterization of laboratory prepared specimens, containing gas hydrate, has also been hampered by the lack of control in the formation of hydrate, within specimens, in laboratory experiments.

7.1.2 *Development of GHRC*

- A laboratory apparatus, the resonant column, was identified which would allow the elastic properties of specimens to be determined. The resonant column can perform measurements of velocity and attenuation at strains and frequencies that are relevant to those that are measured during offshore seismic surveys (strain $< 10^{-6}$, frequency range 30-500Hz). This is important because certain seismic properties are strain and frequency dependent.

- A specially designed resonant column (GHRC) was constructed to enable the thermobaric conditions for hydrate formation and stability conditions to be applied to the specimen, thus allowing hydrate formation and dynamic testing in a single apparatus. Modifications were also made to the design to allow the application of differing excitation modes to allow for both V_p and V_s to be determined along with there respective attenuations.

- Investigations into the calibration of a 'Stokoe' resonant column (SRC) have shown that certain fundamental properties of the resonant column (I_0 and I_y) were a function of specimen stiffness (related to resonant frequency). Modifications were implemented to increase the apparatus stiffness for the GHRC to reduce this variability and was found to be partially successful. Extensive calibration of the apparatus has allowed empirically derived curves to be developed which allow corrections to be made to the obtained values to overcome the effect of increasing specimen stiffness. The

error in the values obtained using the derived correction factor was shown to be less than 0.1% for shear wave velocity and between ±2.15% (at resonant frequency of 53Hz) and ±4.8% (at resonant frequency of 273Hz) for longitudinal velocity.

- Improvements were made to the apparatus to reduce the degree of attenuation that was inherent in the original (SRC) apparatus. This allowed the intrinsic attenuation of bonded specimens to be measured without the large back-EMF induced attenuation masking the measurements.

7.1.3 *Specimen preparation and hydrate formation*

- A methodology has been developed to allow the formation of gas hydrate within the pore space of fine sands from seed ice. The volume of gas hydrate is directly linked to the volume of ice added during specimen preparation.

- Riffling of sand and ice together enabled a random and homogeneous distribution of ice throughout the sand. This was confirmed by digital analyses of thin sections obtained from prepared specimens, where the ice was replaced by polypropylene beads which had an equivalent density and grain size to the ice. Due to capillarity and surface tension it is assumed that the subsequent melting of the ice, prior to specimen preparation, prevented gravitational migration of the water away from localized sites.

- The use of butyl rubber membranes prevented migration of gases between the cell and the specimen evidenced by the constant pore pressure over time during testing.

- Hydrate nucleation and formation was shown to commence during application of methane back pressure and continue while specimen temperature was below the water liquidus line. The observation of hydrate formation by the reduction of methane pore pressure as

specimen temperature was raised was only evident for the highest hydrate content. This prevented the quantitative assessment of hydrate content based on the assumed reduction in methane pore pressure due to the formation of hydrate which was assumed to occur after the water liquidus was passed.

- The rise in methane pore pressure during dissociation was used to qualitatively assess the different volumes of hydrate formed between specimens.

7.1.4 *Dynamic properties of sands containing gas hydrates*

- Tests showed that the presence of hydrate increased the seismic velocity of sand specimens, with shear velocity and longitudinal velocity following the same trend. A transition zone was found to exist around the 3-5% hydrate content region. This region marked an abrupt change in the relationship between seismic velocity and hydrate content with a reduction in the gradient after the transition zone.

- The power law exponents b_S and b_L obtained from regression analyses of the velocity vs. effective confining pressure plot, for each specimen during loading and unloading, showed a sharp reduction from 0.23 to 0.01 when the hydrate content increased from 0-3%. This suggests that the velocity increase was the result of cementation of individual sand grains with all the sand grains being fully bonded, at grain contacts, at the 3% hydrate content. This leads to the seismic velocity becoming pressure independent. The value of b was reasonably constant above the critical hydrate content of 3% suggesting that the measured increase in velocity is due to widening of the hydrate cement at grain contacts and infilling of the void space leading to a reduction in porosity as the hydrate content increases up to the maximum value tested.

- A slight increase in the b_S and b_L exponents during unloading for all hydrated specimens suggests a reduction in contact stiffness possibly caused by brittle fracture of the hydrate cement.

- The addition of hydrate to sand specimens was shown to have a drastic effect on the saturated V_p/V_s ratio (assuming the soil behaves isotropically). The value of the V_p/V_s ratio sharply reduces from the non-hydrated sediment (6-7) to a value similar to that of consolidated rock when fully cemented (< 2 for hydrate content of 3% and above). These results suggest that the V_p/V_s ratio can be used as a diagnostic tool in the identification of hydrate content in shallow subsurface sediments.

- Axial deformation measurements, obtained from the axial transducer attached to the drive plate, during the loading/unloading cycle, for each specimen, shows an increasing residual strain for increasing hydrate content. For specimens with the highest hydrate content (18% and 35%) a time-dependent creep effect was visible after the application of each load step. This was manifested as a large residual strain for these specimens at the end of the load/unload cycle.

- Whilst the formation of hydrate within the specimen led to significant changes in the mechanical behaviour of the sand, both in terms of increased overall stiffness and reduced effective stress dependency of stiffness, subsequent dissociation led to a complete reversal of the process.

7.1.5 *Attenuation*

- The addition of small amounts of hydrate at grain contacts had a major influence on attenuation, with a clearly defined peak observed around the 3-5% hydrate content. This attenuation peak occurred at the same hydrate percentage as the transition zone identified in the velocity analysis. Increasing hydrate content above the critical value

caused a slight reduction in attenuation, although still larger than that measured in the dry specimens.

- It is hypothesised that the attenuation peak occurs due to squirt flow of bound water between sand grains and hydrate cement at grain contacts which reduces as the hydrate increases and causes a sealing of the whole grain.

- The measured attenuation showed low sensitivity to confining pressure for the hydrated specimens and dry specimens. This is in contrast to the attenuation for dissociated hydrate specimens which showed a sensitivity to confining pressure. This suggests differing mechanisms for attenuation when the specimens are hydrated and subsequently dissociated. For dissociated specimens, increasing confining pressure leads to frustration of particle rotation and so lower squirt flow, as opposed to the squirt flow between hydrate cement and sand grains which is not pressure dependent.

- The use of attenuation, determined for different modes of wave propagation, can be used to validate the hydrate formation procedure since Q_K and Q_P are sensitive to variation in hydrate formation and can therefore be used as a diagnostic tool.

7.2 Recommendations

Several areas of further work have been identified to help build on the success of the research reported in this thesis. These are: further development of laboratory apparatus; hydrate formation in more realistic sediments; and extending the range of tests undertaken.

7.2.1 *Further development of the GHRC*

Through the development of the GHRC and the subsequent calibration of the apparatus, and testing of hydrated specimens, several shortcomings were identified. Therefore the following suggestions are offered:

- Calibration of the apparatus should be conducted using bars of the same geometry as the specimen to remove the possible affects of bar shape on the derived values of I_0 and I_y.

- Development of mathematical models to fully describe the system during torsional and flexural excitation. This will enable the rigidity of connections and the shear energy that is neglected in the derivation of I_y to be accounted for and so help improve the correlation of I_0 and I_y, for bars of different stiffness.

- Incorporation of ultrasonic P-wave transducers to allow the direct measurement of P-wave velocities in saturated media and the tracking of flexure vibration-derived longitudinal velocity in dry media.

- Provision of a thermistor within the specimen, to enable actual specimen temperature rather than the temperature of the surrounding gas to be measured. Cooling of methane and nitrogen gas prior to admittance into the cell would enable hydrate formation to be restricted until formation pressures were achieved.

7.2.2 *Formation of hydrate in sediments*

The formation of hydrates using the developed methodology was shown to significantly increase the velocity of propagating waves within the sand specimens, which is not seen in natural sediments. Therefore the following suggestions are made:

- The development of methodologies to enable the controlled formation of gas hydrates in specimens containing an increasing clay content to reproduce formation conditions found in oceanic soils. The use of zeolite particles to introduce methane gas in saturated specimens is a possible mechanism.

- To develop a methodology to enable saturation of hydrated sand specimens to allow their attenuation properties to be investigated.

7.2.3 *Laboratory testing procedure*

In this research programme only the small strain dynamic response of different hydrate specimens, during isotropic loading and unloading, were investigated with each velocity and attenuation measurement undertaken 30 minutes after the application of each load step. Therefore the following are suggested:

- As the specimens containing a higher hydrate content were shown to exhibit creep behaviour, an investigation into the creep dependency of these specimens should be undertaken.
- The stiffness of soils under dynamic excitation is amplitude dependent. Therefore an investigation into the possible strain dependency of hydrate bearing soils will lead to a better understanding of the role that tectonic activities, and hydrates, may play in marine slope failures.

Bibliography

Al-Hunaidi, M. O., Chen, P. A., Rainer, J. H., and Tremblay, M. (1996). Shear moduli and damping in frozen and unfrozen clay by resonant column tests. *Can. Geotech. J.*, 35:510–514.

Allen, J. C. and Stokoe, K. H. (1982). Development of resonant column apparatus with anisotropic loading. *Geotechnical Engineering Report GR82-28*, Civil Engineering Dept., Univ. of Texas at Austin.

Anderson, D. G. and Stokoe, K. H. (1978). Shear modulus, a time-dependent material property. *Dynamic Geotechnical Testing, ASTM 654*, pages 66–90.

Anstey, V. (1991). Velocity in thin section. *First Break*, 9:449–457.

Ashi, J. (1999). Large submarine landlides associated with decomposition of gas hydrates. *Landslide News*, 12:17–19.

Ashmawy, A. K. and Drnevich, V. P. (1994). A general dynamic model for the resonant column/quasi-static torsional shear apparatus. *Geotechnical Testing Journal*, 17(3):337–348.

Avramidis, A. S. and Saxena, S. K. (1990). A modified "stiffened" Drnevich resonant column. *Soils and Foundations*, 30(3):56–68.

Barrer, R. M. and Edge, M. A. (1967). Gas hydrates containing argon, krypton and xenon: kinetics and energetics of formation and equilibria. In *Proc. R. Soc. London A*, volume 300, pages 1–24.

Bathe, M., Vagle, S., Saunders, G. A., and Lambson, E. F. (1984). Ultrasonic wave velocities in the structure II clathrate hydrate $THF{\cdot}17H_2O$. *J. Mater. Sci. Letts.*, 3:904–906.

Bellotti, R., Jamiolkowski, M., Lo Presti, D. C. F., and O'Neill, D. A. (1996). Anisotropy of small strain stiffness in Ticino sand. *Geotechnique*, 47(1):115–131.

Berge, L. I., Jacobsen, K. A., and Solstad, A. (1999). Measured acoustic wave velocities of R11 (CCL_3F) hydrate samples with and without sand as a function of hydrate concentration. *J. Geophys. Res.*, 104:15,415–15,424.

Berndt, C., Meinert, J., Vanneste, M., Bunz, S., and Bryn, P. (2002). Submarine slope-failure offshore Norway triggers rapid gas hydrate decomposition. In *Proc. Fourth Int. Conf. On Gas Hydrates, Yokohama, May 19-23*, pages 71–74.

Best, A. I. (1997). The effect of pressure on ultrasonic velocity and attenuation in near-surface sedimentary rocks. *Geophs. Prospect.*, 45(2):345–364.

Bily, C. and Dick, J. W. L. (1974). Natural occuring gas hydrates in the Mackenzie Delta, Northwest Territories. *Bulletin of Canadian Petroleum Geology*, 22(3):340–352.

Bishop, A. W. and Henkel, D. J. (1962). *The Measurement of Soil Properties in the Triaxial Test.* Edward Arnold, London, 2 edition.

Booth, J. S. and O'Leary, D. W. (1991). A statistical overview of mass movement characteristcs on the North American Atlantic outer continental margin. *Marine Geotechnology*, 10:1–18.

Brandt, H. (1960). Factors affecting compressional wave velocity in unconsolidated marine sand sediment. *J. Acoust. Soc. Am*, 32:171–179.

Brewer, P. G., Orr, F. M., Freidrich, K. A., Orange, D. L., McFarlane, J., and Kirkwood, W. (1997). Deep-ocean field test of methane formation from a remotely operated vehicle. *Geology*, 25(5):407–410.

Brooks, J. M., Anderson, A. L., Sassen, R., McDonald, I. A., II, M. C. K., and Guinasso, N. L. (1994). Hydrate occurences in the shallow subsurface cores from the Continental Slope sediments. In Sloan Jr, E. D., .Happel, J., and Hnatow, M. A., editors, *Natural gas hydrates*, volume 715, pages 381–391. New York Academy of Science, New York.

Brooks, J. M., Jeffery, A., McDonald, T., Plaum, R., and Kvenvolden, K. (1985). Geochemistry of hydrate gas and water from site 570, Deep Sea Drilling Project Leg 84. In von Huene, R., Aubouin, J., et al., editors, *Initial Reports of the Deep Sea Drilling Project*, volume 84, pages 699–703. U.S. Government Printing Office, Washington, D. C.

Buffett, B. A. and Zatespina, O. Y. (2000). Formation of gas hydrate from dissolved gas in natural porous media. *Marine Geology*, 164:69–77.

Bugge, T., Befring, S., Belderson, R., and et al. (1987). A giant three-stage slide off Norway. *Geo-Marine Letters*, 7:191–198.

Cascante, G. (1996). Low strain measurements with mechanical waves in geomaterials - experimental miceomechanics. *PhD Dissertation*, University of Waterloo, Waterloo, Ont.

Cascante, G., Santamarina, C., and Yassir, N. (1998). Flexural excitation in a standard torsional-resonant column. *Can. Geotech. J.*, 35:478–490.

Cascante, G., Vanderkooy, J., and Chung, W. (2003). Difference between current and voltage measurements in resonant-column testing. *Can. Geotech. J.*, 40:1–15.

Castagna, J. P., Batzle, M. L., and Eastwood, R. L. (1984). Relationship between compressional-wave and shear-wave velocities in clastic rocks. *Geophysics*, 50:571–581.

Chen, A. T. F., Lee, S. H. H., and Stokoe, K. H. (1979). Interpretation of strain dependent modulus and damping from torsional soil tests. *Report No. USGS-GD-79-002, NTIS No PB-298479*, U. S. Geological Survey.

Chuvilin, E. M., Makhonina, N. A., Titenskaya, O. A., and Boldina, A. O. (2002). Petrophysical investigations on frozen sediments artifically saturated by hydrate. In *Proc. Fourth Int. Conf. On Gas Hydrates, Yokohama, May 19-23*, pages 734–739.

Claypool, G. and Kaplan, I. (1974). The origin and distribution of methane in marine sediments. In Kaplan, I., editor, *Natural Gases in Marine Sediment*, pages 99–139. Plenume, New York.

Clayton, C. R. I., Matthews, M. C., and Simons, N. E. (1997). *Site investigation.* Blackwell Sciences Ltd, Oxford, England, 2nd edition.

Clennell, B. M., Hovland, M., Booth, J., Henry, P., and Winters, W. J. (1999). Formation of natural hydrates in marine sediments: 1. Conceptual model of gas hydrate growth conditioned by host sediment properties. *Journal of Geophysical Research*, 104:22,985–23,003.

Collett, T. S. (1983). Detection and evaluation of natural gas hydrates from well logs, Prudhoe Bay, Alaska. In *Proc. Fourth Int. Conf. On Permafrost*, pages 169–174.

Collett, T. S. (1993). Natural gas hydrates of the Prudhoe Bay and Kuparuk River area, North Slope, Alaska. *AAPG Bulletin*, 77:793–812.

Collett, T. S. and Ladd, J. (2000). Detection of gas hydrates with downhole loge and assessment of gas hydrate concentrations (saturations) and gas volume on the Blake Ridge with Electrical Resistivity log data. In Paull, C., Matsumoto, R., Wallace, P., et al., editors, *Pro.ODP.Results, 164*, pages 179–191. College Station, TX Ocean Drilling Program.

Cresswell, A., Barton, M. E., and Brown, M. R. (1999). Determining the maximum dry density of sands by pluviation. *Geotechnical Testing Journal*, 22(4):324–328.

Dickens, R. G., Paull, C. K., Wallace, P., and the ODP Leg 164 Scientific Party (1997). Direct measurement of insitu methane quantities in a large gas-hydrate reservoir. *Nature*, 385:426–428.

Dillon, W. P., Hutchinson, D. R., Drury, R. M., Taylor, M. H., and Booth, J. S. (1998). Evidence for faulting related to dissociation of gas hydrates and release of methane gas off the Southeastern United States. In Henriet, J. P. and Meinert, J., editors, *Gas hydrates: Relevance to world margin stability and climate change*. Geological Society, London, Special Publications, 137, 364-380.

Dillon, W. P., Lee, M. W., and Coleman, D. F. (1994). Identification of marine hydrates insitu and their distribution off the Atlantic Coast of the United States. In Sloan Jr, E. D., Happel, J., and Hnatow, M. A., editors, *Natural gas hydrates*, pages 362–380. New York Academy of Science, New York.

Dobry, R. and Vucetic, M. (1987). State of the art report: Dynamic properties and seismic response of soft clay deposits. *International Symposium on Geotech. Eng of Soft Soils,* Mexico City, vol 2:51–87.

Drnevich, V. P. (1967). Large Amplitude Vibration Effects on the Shear Modulus of Sand. *PhD Dissertation*, University of Michigan.

Drnevich, V. P. (1978). Resonant column testing - problems and solutions. *Dynamic Geotechnical Testing, ASTM 654*, pages 394–398.

Drnevich, V. P., Hall, J. R., and Richart, F. (1967). Effects of amplitude vibration on the shear modulus of sand. *Proc. of the International Symposium on Wave Propagation and Dynamic Properties of Earth Material,* Albuquerque, N. M., pages 189–199.

Drnevich, V. P., Hardin, B. O., and Shippy, D. J. (1978). Modulus and damping of soils by the resonant column method. *Dynamic Geotechnical Testing, ASTM 654*, pages 91–121.

Dutta, N. C. (1987). Geopressure. *Geophysics Reprint Series* No. 7, Society of Exploration Geophysicists, Tulsa, Oklahoma.

Dvorkin, J., Mavko, G., and Nur, A. (1995). Squirt flow in fully saturated rocks. *Geophysics*, 60:97–107.

Dvorkin, J. and Nur, A. (1993). Rock physics for the characterisation of gas hydrates. In *The Future of Energy Gases*, volume 84, pages 699–703. Geol. Surv. Prof. Pap., US., 1570.

Eastwood, R. L. and Castagna, J. P. (1987). Interpretation of vp/vs ratios from sonic logs. In Danbom, S. H. and Domenico, S. N., editors, *Shear wave exploration*, volume 1. Society of Exploration Geophysics, Tulsa, Oklahoma.

Ecker, C. (2001). Seismic characterisation of methane hydrate structures. *PhD Dissertation*, Stanford University.

Embly, R. and Jacobi, R. (1977). Distribution and morphology of large sediment slides and slumps on Atlantic continental margins. *Marine Geotechnology*, 2:205–208.

Englezos, P., Kalogerakis, N., Dholabhai, P. D., and Bishnoi, P. R. (1987). Kinetics of formation of methane and ethane gas hydrate. *Chem. Engng. Soc.*, 42:2647–2658.

Franklin, L. J. (1980). In-situ gas hydrates - a potential energy source. *Petoleum Engineer International*, Nov:112–122.

Gassmann, F. (1951). Uber die elastizitat poroser medien. *Vieteljahrsschrift der Naturforschenden Gesselschaft*, 96:1–21.

Gere, J. M. and Timoshenko, S. P. (1991). *Mechanics of Materials*. Chapman & Hall, London, 3rd edition.

Gettrust, J., Wood, W., and Lindwall, D. (1999). New seismic study of deep sea hydrates results in greatly improved resolution. *Eos Trans*, 80:439–442.

Ginsburg, G., Soloviev, V., Matveeva, T., and Andreeva, I. (2000). Sediment grain size control on gas hydrate presence, sites 994, 995 and 997. In Paull, C., Matsumoto, R., Wallace, P., et al., editors, *Pro.ODP.Results, 164*, pages 237–245. College Station, TX Ocean Drilling Program.

Ginsburg, G. D. (1998). Gas hydrate accumulation in deep-water sediments. In Henriet, J. P. and Meinert, J., editors, *Gas hydrates: Relevance to world margin stability and climate change.* Geological Society, London, Special Publications, 137, 51-62.

Ginsburg, G. D., Guseynov, R., Dadshev, A., et al. (1992). gas hydrates of the southern Caspian. *International Geology Review*, 34:765–782.

Goldberg, D. (2003). Private communication. Borehole Research Group, Lamount-Doherty Earth Obsevatory, Palisades, N.Y.

Gräbe, P. J. (2002). Resillient and permanent deformation of railway foundations under principal stress rotation. *PhD Dissertation*, University of Southampton.

Guerin, G. and Goldberg, D. (2002). Sonic waveform attenuation in gas hydrate-bearing sediments from the Malik 2L-38 research well, Mackenzie Delta, Canada. *J. Geophs. Research*, 107(B5):EPM 1–EPM 11.

Hall, J. R. and Richart, F. E. (1963). Dissipation of elastic waves in granular soils. *J. of Soil Mech. and Found. Div*, 89(SM6).

Hamilton, E. L. (1971). Elastic properties of marine sediments. *J. Geophys. Res.*, 76(2):579–604.

Hamilton, E. L. (1972). Compressional-wave attenuation in marine sediments. *Geophysics*, 37:620–646.

Hamilton, E. L. (1979). v_p/V_s and Poisson's ratios in marine sediments and rocks. *J. Acoust. Soc. America*, 66(4):1093–1101.

Han, D., Nur, A., and Morgan, D. (1986). Effects of porosity and clay content on wave velocities in sandstone. *Geophysics*, 51:2093–2107.

Handa, Y. P. (1986). Composition, enthalpies of dissociation and heat capacities in the range 85 to 270k for clathrate hydrates of methane, ethane and propane and the enthalpy of iso-butane hydrate, as determined by a heat-flow calorimeter. *J. Chem. Thermodynamics*, 18:915–921.

Handa, Y. P. and Stupin, D. (1992). Thermodynamic properties and dissociation characteristics of methane and propane hydrates in 70$\dot{A}$ radius silica gel pores. *J. of Phys. Chem.*, 96:8599–8603.

Handa, Y. P., Zakrzewski, M., and Fairbridge, C. (1992). Effect of restricted geometries on the surface and thermodynamic properties of ice. *J. of Phys. Chem.*, 96:8594–8599.

Hardin, B. O. (1978). The nature of stress-strain behaviour of soils. *Proc.* ASCE *Geotech. Engrg. Div. Speciality Conf. on Earthquake Engineering and Soil Dynamics*, vol 1:3–90.

Hardin, B. O. and Black, W. L. (1968). Vibration modulus of normally consolidated clays. *J. of Soil Mech. and Found. Div.,* ASCE, Vol 94, No. SM2, Proc. Paper 5833,, pages 353–369.

Hardin, B. O. and Drnevich, V. P. (1972a). Shear modulus and damping in soils: Design equations and curves. *J. of Soil Mech. and Found. Div.*, 98(7):667–691.

Hardin, B. O. and Drnevich, V. P. (1972b). Shear modulus and damping in soils: Measurement and parameter effects. *J. of Soil Mech. and Found. Div.*, 98(7):603–624.

Hardin, B. O. and Music, J. (1963). Apparatus for the vibration of soil specimens during the triaxial test. *J. of Soil Mech. and Found. Div.,* ASCE (SM1), 89:33–63.

Hardin, B. O. and Richart, F. E. J. (1965). Elastic wave velocities in granular soils. *Symposium on Instrumentation and Apparatus for Soils and Rocks,* ASTM STP 392, ASTM, pages 55–74.

Hardin, K. O., Drnevich, V. P., Wang, J., and Sams, C. E. (1994). Resonant column testing up to 3.5 mpa (500psi). In Ebelhar, R. J., Drnevich, V. P., and Kutter, B. L., editors, *Dynamic Geotechnical Testing II,* ASTM STP 1213, pages 222–233. American Society of Testing and Materials, Philadelphia.

Harrison, W. E. and Curialle, J. A. (1982). Gas hydrates in sediment of holes 497 and 498a, Deep Sea Drilling Project Leg 67. In von Huene, R., Aubouin, J., et al., editors, *Init. Repts. DSDP, 67*, pages 591–595. U.S. Government Printing Office, Washington, D. C.

Helgerud, M. B. (2001). Wave speed in gas hydrates and sediments containing gas hydrates: A laboratory and modelling study. *PhD Dissertation*, Stanford University.

Helgerud, M. B., Dvorkin, J., Nur, A., Sakai, A., and Collett, T. (1999). Elastic-wave velocity in marine sediments with gas hydrates: Effective medium modeling. *Geophys. Res. Lett.*, 26:2021–2024.

Henry, P., Thomas, M., and Clennell, B. M. (1999). Formation of natural hydrates in marine sediments: 2. Thermodynamic calculations of stability conditions in porous media. *Journal of Geophysical Research*, 104:23,005–23,022.

Hesse, R. (1986). Diagnesis#11. early diagenetic pore water/sediment interaction: Modern offshore basins. *Geoscience Canada*, 14(3):165–196.

Hesse, R. and Harrison, W. (1981). Gas hydrate (clathrate) causing pore water freshening and oxygen isotropic fractionation in deep-water sedimentary sections of terrigenous continental margins. *Earth and Planetary Sci. Lett.*, 55:453–462.

Hesse, R., Lebel, J., and Gieskes, J. (1995). Interstitial water chemistry of gas hydrate bearing sections on the Middle America Trench slope, Deep Sea Drilling Project Leg 84. In von Huene, R., Aubouin, J., et al., editors, *Iinitial Reports of the Deep Sea Drilling Project*, volume 84, pages 727–736. U.S. Government Printing Office, Washington, D. C.

Heymann, G. H. (1998). Stiffness of soils and weak rocks at very small strains. *PhD Dissertation*, University of Surrey.

Hill, R. (1952). The elastic behaviour of crystalline aggregate. *Proc. Phys. Soc., London*, A65:349–354.

Holbrook, W. S., Hoskins, H., Wood, W. T., Stephen, R. A., Lizzarralde, D., and the Leg 164 Science Party (1996). Methane gas-hydrate and free gas on the Blake Ridge from vertical seismic profiling. *Science*, 273:1840–1843.

Hunt, J. M. (1979). *Petroleum geochemistry and geology*. W. H. Freeman, San Francisco.

Hwang, M. J., Wright, D. A., Kapur, A., and Holder, G. D. (1990). An experimental study of crystallization and crystal growth of methane hydrates from melting ice. *J. Inclusion Phenom.*, 8:103–116.

Hyndman, R. and Davis, E. (1992). A mechanism for the formation of methane hydrate and sea-floor bottom-simulating reflectors by vertical fluid expulsion. *J. Geophy. Res.*, 97(7):7025–7041.

Ingles, O. G. (1962). Bonding forces in soils, Part 3:A theory of tensile strength for stabilised and naturally coherent soils. In *Proceedings of the 1st Conf. of the Australian Research Board.*, volume 1, pages 1025–1047.

Isenhower, W. M. (1980). Torsional Simple Shear/Resonant Column Properties of San Francisco Mud. *MSc Thesis*, University of Texas at Austin.

Ishimoto, M. and Iida, K. (1937). Determination of elastic constants of soils by means of vibration methods. *Bulletin of the Earthquake Research Institute*, 15:67.

Jakobsen, M., Hudson, J. A., Minshull, T. A., and Singh, S. C. (2000). Elastic properties of hydrate-bearing sediments using effective medium theories. *J. Geophys. Res.*, 105:561–577.

Jenden, P. and Gieskes, J. (1983). Chemical and isotopic compositions of interstitial water from Deep Sea Drilling Project sites 533 and 534. In Sheridan, R., Gradstein, F., et al., editors, *Initial Reports of the Deep Sea Drilling Project*, volume 76, pages 453–461. U.S. Government Printing Office, Washington, D. C.

Johnson, D. H. (1981). Attenuation: A state-of-the-art summary. In Toksoz, M. N. and Johnson, D. H., editors, *Seismic wave attenuation, Geophysics reprint series, No.2*, pages 1–5. Society of Exploration Geophysics, Washington, D. C.

Johnson, D. H. and Toksoz, M. N. (1981). Definitions and terminology. In Toksoz, M. N. and Johnson, D. H., editors, *Seismic wave attenuation, Geophysics reprint series, No.2*, pages 1–5. Society of Exploration Geophysics, Washington, D. C.

Kayen, R. E. and Lee, H. J. (1991). Pleistocene slope instability of gas hydrate-laden sediment on the Beaufort Sea margin. *Marine Geotechnology*, 10:125–141.

Keary, P. and Brooks, M. (1991). *Introduction to geophyscial exploration.* Blackwell Science, Oxford, 2 edition.

Kiefte, H., Clouter, M. J., and Gagnon, R. E. (1985). Determination of acoustic velocities of clathrate hydrates by Brillouin spectroscopy. *J. of Phys. Chem.*, 89:3103–3108.

Kolbuszewski, J. J. (1948). An experimental study of the maximum and minimum porosities of sands. In *Proceedings of the Second International Conference of Soil Mechanics and Foundation Engineering,* Rotterdam, Vol 1,, pages 158–165.

Kolsky, H. (1953). *Stress waves in solids.* Clarendon Press, Oxford.

Konrad, J. C. and Duquennoi, C. (1993). A model for water transport and ice lensing in frozen soils. *Water Resour. Res.*, 29:3019–3024.

Kraemer, L. M., Owen, R. M., and Dickens, G. R. (2000). Lithology of the upper gas hydrate zone, Blake Outer Ridge: A link between diatoms, porosity and gas hydrate. In Paull, C., Matsumoto, R., Wallce, P., et al., editors, *Proc. ODP. Results, 164*, pages 229–236. College Station, TX, Ocean Drilling Program.

Kunerth, D. C., Weinberg, D. M., Rector, J. W., Scott, C. L., and Johnson, J. T. (2001). Acoustic laboratory measurement during the formation of a THF-hydrate in unconsolidated porous media. *J. Seismic Explor.*, 9:337–354.

Kuwano, R. and Jardine, R. J. (2002). On the applicability of cross-anisotropic elasticity to granular materials at very small strains. *Geotechnique*, 52(10):727–749.

Kvenvolden, K. (1988). Methane hydrate a major reservoir of carbon in the shallow geosphere? *Chem. Geol.*, 71(1):41–51.

Kvenvolden, K. (1998). A primer on the geological occurrence of gas hydrates. In Henriet, J. P. and Meinert, J., editors, *Gas hydrates: Relevance to world margin stability and climate change*. Geological Society, London, Special Publications, 137, 9-30.

Kvenvolden, K. and Barnard, L. (1983). Gas hydrates of the Blake Outer Ridge, site 533, Deep Sea Drilling Project leg 76. In Sheridan, R., Gradstein, F., et al., editors, *Initial Reports of the Deep Sea Drilling Project*, volume 76, pages 353–365. U.S. Government Printing Office, Washington, D. C.

Kvenvolden, K. and Kastner, M. (1990). Gas hydrates of the Peruvian outer continental margin. In Suess, E., von Huene, R., et al., editors, *Proceedings of the Ocean Drilling Program, Scientific Results*, volume 112, pages 517–526. College Station, TX, Ocean Drilling Program.

Kvenvolden, K. and McDonald, T. (1985). Gas hydrates of the Middle America Trench, Deep Sea Drilling Project Leg 84. In von Huene, R., Aubouin, J., et al., editors, *Iinitial Reports of the Deep Sea Drilling Project*, volume 84, pages 664–682. U.S. Government Printing Office, Washington, D. C.

Laird, J. P. (1994). Linear and Nonlinear Dynamic Properties of Soils at High Confining Pressures. *MSc Thesis*, University of Texas at Austin.

Lee, M. W. and Collett, T. S. (2001). Elastic properties of gas hydrate-bearing sediments. *Geophysics*, 66:763–771.

Lee, M. W., Dillon, W. P., and Hutchinson, D. R. (1992). Estimating the amount of gas hydrates in marine sediments in the Blake Ridge area, Southeastern Atlantic Margin. Technical Report 92-275, US Geological Survey.

Lodde, P. F. (1982). Dynamic response of San Francisco Bay mud. Technical Report GT82-2, Civil Engineering Dept, University of Texas at Austin.

LoPresti, D. C. F., Jamiolkowski, M., Pallara, O., Cavallaro, A., and Pedroni, S. (1997). Shear modulus and damping of soils. *Geotechnique*, 47(3):603–617.

Makaogon, Y. (1981). *Hydrates of Natural Gas*. PennWell Publishing, Tulsa, Oklahoma.

Malone, R. D. (1985). Gas hydrates. Technical Report DOE/METC/SP-218, U.S. Dep. of Energy, Washington, DC.

Maslin, M., Mikkelsen, N., and Haq, B. U. (1998). Sea level controlled catastraphic failure of the Amazon Fan. *Geology*, 26:1107–1110.

Matsumoto, R. (2002). Comparison of marine and permafrost gas hydrates: Examples from Nankai Trough and Mackenzie Delta. In *Proc. Fourth Int. Conf. On Gas Hydrates, Yokohama, May 19-23*, pages 19–23.

Matsumoto, R., Uchida, T., Waseda, A., Uchida, T., Takeya, S., Hirano, T., Yamada, K., Maeda, Y., and Okui, T. (2000). Occurence, structure and composition of natural gas hydrate recovered from the Blake Ridge, Northwest Atlantic. In Paull, C., Matsumoto, R., Wallce, P., et al., editors, *Proc. ODP. Results, 164*, pages 13–28. College Station, TX, Ocean Drilling Program.

Matthews, M. (1986). Logging characteristics of methane hydrate. *The Log Analyst*, 27:26–63.

Mavko, G. and Nur, A. (1979). Wave attenuation in partially saturated rocks. *Geophysics*, 44:161–178.

Mavko, G. M., Mukerji, T., and Dvorkin, J. (1998). *The rock physics handbook: Tools for seismic analysis in porous media.* Cambridge University Press, New York.

Mehta, A. P. and Sloan, E. D. (1993). Structure H hydrate phase equilibria of methane + liquid hydrocarbon mixtures. *Journal of Chem. Eng. Data*, 38:887–890.

Meinert, J., Posewang, J., and Baumann, M. (1998). Gas hydrates along the northeastern Atlantic margin: possible hydrate-bound margin instabilities and possible release of methane. In Henriet, J. P. and Meinert, J., editors, *Gas hydrates: Relevance to world margin stability and climate change.* Geological Society, London, Special Publications, 137, 275-291.

Meng, J. and Rix, G. J. (2003). Reductiopn of equipment-generated damping in resonant column measurements. *Geotechnique*, 53(5):503–512.

Menq, F. and Stokoe, K. H. (1998). Linear dynamic properties of sandy and gravelly soils from large-scale resonant tests. In Benedetto, D., editor, *Deformation characteristics of geomaterials*, pages 63–71. Swets and Zeitlinger, Lisse.

Min, T., Drnevich, V. P., and J.Wang (1990). Effects of imperfect fixity in spring-top resonant column tests. *Geotechnical Testing Journal*, Vol 13(4):351–360.

Minshull, T., Singh, S., and Westbrook, G. (1994). Seismic velocity structure of a gas hydrate reflector, offshore Western Columbia, from full waveform inversion. *Journal of Geophysical Research*, 99:4715–4734.

Murphy, W. F. (1982). Effects of partial saturation on attenuation in massilon sandstone and vycor porous glass. *J. Acoust. Soc. Am*, 71(6):1458–1468.

Murphy, W. F., Winkler, K. W., and Kleinberg, R. L. (1986). Acoustic relaxation in sedimentary rocks: Dependence on grain contacts and fluid saturation. *Geophysics*, 5:757–766.

Overloop, K. and Van Gerven, L. (1993). Freezing phenomena in absorbed water as studied by NMR. *J. Magn. Reson.*, Ser: A, 101:179–187.

Palmer, I. D. and Traviola, M. L. (1980). Attenuation by squirt flow in undersaturated gas sands. *Geophysics*, 45:1780–1792.

Pandit, B. I. and King, M. S. (1983). Elastic wave velocities of propane hydrates. In Cox, J. L., editor, *Natural gas hydrates: properties, occurrence and recovery*, pages 49–61. Butterworth, Boston.

Paull, C. K., Matsumoto, R., Wallace, P. J., et al. (1996). *Proc. ODP. Init. Repts. 164*. Ocean Drilling Program, College Station,TX.

Paull, C. K., Ussler III, W., and Borowski, W. (1994). Sources of methane to form marine gas hydrates. In Sloan Jr, E. D., .Happel, J., and Hnatow, M. A., editors, *Natural gas hydrates*, volume 715, pages 392–409. New York Academy of Science, New York.

Pearson, C. F., Murphy, J. R., and Hermes, R. (1986). Laboratory ultrasonic and resistivity measurements on sedimentary rocks contining tetrahyrofuran hydrates. *J. Geophys. Res*, 91, Ser: B14:14,132–14,138.

Pecher, I. A. and Holbrook, W. S. (2000). Seismic methods for detecting and quantifying marine methane hydrate/free gas reservoirs. In Max, M. D., editor, *Natural gas hydrates in oceanic and permafrost environments*, pages 275–294. Kluwer Academic Press.

Popenoe, P., Schmuck, E., and Dillon, W. (1993). The Cape Fear landslide: Slope failure associated with salt diapirism and gas hydrate decomposition. In Schwab, W., editor, *Submarine Landslides: Selective studies in the U.S. exclusive economic zone*, pages 40–53. US Geological Survey Bulletin 2002.

Porovic, E. (1995). Investigaions of soil behaviour using a resonant-column torsional-shear hollow-cylinder apparatus. *PhD Dissertation*, University of London, Imperial College of Science Technology and Medicine.

Powrie, W. (1997). *Soil Mechanics: Concepts and Applications*. E & FN Spon, London.

Rad, N. S. and Tumay, M. T. (1987). Factors affecting sand specimen preparation by raining. *Geotechnical Testing Journal*, 10(1):31–37.

Richart, F. E., Hall, J. R., and Woods, R. D. (1970). *Vibration of soils and foundations*. Prentice Hall, New Jersey.

Ripmeester, J. (1991). The role of heavier hydrocarbons in hydrate formation. Paper presented at the 1991 *American Institute of Chemical Engineering Spring Meeting*, Houston,TX.

Ripmeester, J., Tse, J., Ratcliffe, C., and Powell, B. (1987). A new hydrate structure. *Nature*, 325:135.

Ruppel, C. (1997). Anomalouly low temperatures observed at the base of the hydrate stability zone on the US Alantic passive margin. *Geology*, 26:699–702.

Sakai, A. (2000). Can we estimate the amount of gas hydrate by seismic methods? In Holder, G. D. and Bishnoi, P. R., editors, *Gas hydrates: Challenges for the future*, volume 912, pages 374–391. New York Academy of Sciences, New York.

Salamatin, A. N. and Kuhs, W. F. (2002). Formation of porous gas hydrates. In *Proc. Fourth Int. Conf. On Gas Hydrates, Yokohama, May 19-23*, pages 673–677.

Sassen, R. and McDonald, I. R. (1994). Evidence for Structure H hydrate, Gulf of Mexico continental slope. *Organic Geochemistry*, 22(6):1029.

Saxena, S. K., Avramidis, A. S., and Reddy, K. R. (1988). Dynamic moduli and damping ratios for cemented sands at low strains. *Can. Geotech. J.*, 25:353–368.

Scherer, G. W. (1993). Freezing gels. *J. Non-Crystalline Solids*, 155(1):1–25.

Seed, H. B. and Idriss, I. M. (1970). *Soil Moduli and Damping Factors for Dynamic Response Analyses.* Report No EERC 70-10. Earthquake Engineering Research Centre, Universtiy of California, Berkley, California.

Seed, H. B., Wong, R. T., Idriss, I. M., and Tokimatsu, K. (1986). Moduli and damping factors for dynamic analyses of cohesionless soil. *J. of Geotech. Eng.* ASCE, 112(11):1016–1032.

Sheridan, R., Gradstein, F., et al. (1983). *Initial Reports of the Deep Sea Drilling Program,* Vol 76. US Government Printing Office, Washington, D.C.

Shibuya, S. and Tanaka, H. (1996). Estimate of elastic shear modulus in holocene soil deposits. *Soils and Foundations*, 36(4):45–55.

Shipboard Scientific Party (2002). Leg 204 Preliminary Report. *ODP Prel. Rep.*, 204[Online]:Available from the World Wide Web: http://www-odp.tamu.edu/publications/prelim/204_prel/204PREL.PDF.

Shipley, T., Houston, M., Buffler, R., et al. (1979). Seismic evidence for widespread possible gas hydrate horizons on the continental slopes and rises. *AAPG Bulletin*, 63(12):2204–2213.

Singh, S. C., Minshull, T. A., and Spence, G. D. (1993). Velocity structure of a gas hydrate reflector. *Science*, 260:204–207.

Sloan, E. D. (1998). *Clathrate hydrates of natural gases.* Marcel Dekker, New York, 2nd edition.

Staykova, D. K., Hansen, T., Salamatin, A. N., and Kuhs, W. F. (2002). Kinetic diffraction experiments on the formation of porous gas hydrates. In *Proc. Fourth Int. Conf. On Gas Hydrates, Yokohama, May 19-23*, pages 537–542.

Staykova, D. K., Kuhs, W. F., Salamatin, A. N., and Hansen, T. (2003). Formation of porous gas hydrates from ice powders: Diffraction experiments and multistage model. *J. Phys. Chem. B*, 107:10299–10311.

Stern, L. (2002). Private communication. U. S. Geological Survey, Menlo Park, USA.

Stern, L. A., Circone, S., Kirby, S. H., and Durham, W. B. (2002). New insights into the phenomenon of anomalous or "self" preservation of gas hydrates. In *Proc. Fourth Int. Conf. On Gas Hydrates, Yokohama, May 19-23*, pages 673–677.

Stern, L. A., Hogenboom, D. L., Durham, W. B., Kirby, S. H., and I-Ming Chou (1998). Optical-cell evidence for superheated ice under gas-hydrate-forming conditions. *J. Phys. Chem. B*, 102:2627–2632.

Stern, L. A., Kirby, S. H., and Durham, W. B. (1996). Perculiarities of methane clathrate hydrate formation and solid-state deformation, including possible superheating of water ice. *Science*, 273:1843–1848.

Stern, L. A., Kirby, S. H., Durham, W. B., Circone, S., and Waite, W. F. (2000). Laboratory synthesis of pure methane hydrate for suitable for measurement of physical properties and decompostion behaviour. In Max, M. D., editor, *Natural gas hydrates in oceanic and permafrost environments*, pages 323–348. Kluwer Academic Press.

Stokoe, K. H., Darendeli, M. B., Andrus, R. D., and Brown, L. T. (1999). Dynamic soil properties: laboratory, field and correlation studies. In *2nd International conference on Earthquake Geotech. Eng.*, volume 3, Lisbon, Portugal.

Stoll, R. D. (1974). Effects of gas hydrate in sediments. In Kaplan, I., editor, *Natural Gases in Marine Sediment*, pages 235–248. Plenume, New York.

Stoll, R. D. and Bryan, G. M. (1984). Physical properties of sediments containing gas hydrates. *J. Geophy. Res*, 84(B4):1629–1634.

Stoll, R. D., Ewing, J., and Bryan, G. M. (1971). Anomalous wave velocities in sediments containing gas hydrates. *J. Geophy. Res*, 76:2090–2094.

Suess, E., Bohrmann, G., Rickert, D., Werner, W. F., Torres, M. E., Trehu, A., and Linke, P. (2002). Properties and fabric of near-surface methane

hydrates at Hydrate Ridge, Cascadia Margin. In *Proc. Fourth Int. Conf. On Gas Hydrates, Yokohama, May 19-23*, pages 740–744.

Summerhayes, C., Bornhold, B., and Embley, R. (1979). Superficial slides and slumps on the continental slope and rise of South West Africa: A reconnaissance study. *Marine Geology*, 31:265–277.

Tatsuoka, F. and Kohata, Y. (1995). Stiffness of hard soils and soft rocks in engineering applications. In *Proc. 1st Int. Symp. Pre-Failure Deformation Characteristics of Geomaterials, Sapporo*, volume 2, pages 947–1063.

Telford, W. M., Geldart, L. P., and Sheriff, R. E. (1990). *Applied Geophysics.* Cambridge University Press, New York, 2nd edition.

Thompson, W. T. (1988). *The theory of vibrations with applications.* Prentice Hall, Englewood Cliffs, N.J.

Timoshenko, S. P. (1953). *The history of strength of materials.* McGraw Hill, New York.

Tohidi, B., Anderson, R., Clennell, M. B., Burgass, R. W., and Biderkab, A. B. (2001). Visual observation of gas-hydrate formation and dissociation in synthetic porous media by means of glass micromedels. *Geology*, 29(9):867–870.

Tohidi, B. H., Anderson, R., Clennell, B., Yang, J., Bashir, A., and Burgess, R. W. (2002). Application of high pressure glass micromodels to gas hydrate studies. In *Proc. Fourth Int. Conf. On Gas Hydrates, Yokohama, May 19-23*, pages 761–765.

Toksöz, M. N., Johnston, D. H., and Timur, A. (1979). Attenuation of seimic waves in dry and saturated rocks: 1. Laboratory measurements. *Geophysics*, 44(4):681–690.

Tsytovich, N. A. (1975). *The mechanics of frozen ground.* Mcgraw Hill, Washington, D.C.

Valiullin, R. and Furo, I. (2002). The morphology of coexisting liquid and frozen phases in porous material as revealed by exchange of nuclear spin magnetization followed by ^1H nuclear magnetic resonance. *J. Chem. Phys.*, 117:2307–2316.

von Huene, R., Aubouin, J., et al. (1985). *Initial Reports of the Deep Sea Drilling Program,* Vol 84. US Government Printing Office, Washington, D.C.

Vrettos, C. and Savidis, S. (Jun 1999). Shear modulus and damping for Mediterranean Sea clays of medium plasticity. In *2nd International conference on Earthquake Geotech. Eng.*, volume 2, Lisbon, Portugal.

Vucetic, M. and Dobry, R. (1991). Effect of soil plasticity on cyclic response. *Journal of Geotechnical Engineering,* ASCE, 117(1):89–107.

Waite, W. F., Helegrud, M. B., Nur, A., Pinkston, J. C., Stern, L. A., and Durham, W. B. (2000). Laboratory measurement of compressional and shear waves through methane hydrate. In Holder, G. D. and Bishnoi, P. R., editors, *Gas hydrates: Challenges for the future*, volume 912, pages 323–348. New York Academy of Sciences, New York.

Walter, J. E., Highter, W. H., and Vallee, R. P. (1982). Determining the maximum void ratio of uniform cohesionless soils. *Transportation Research Record 897*, pages 42–51.

Wang, Y. H., Cascante, G., and Santamarina, J. C. (2003). Resonant column testing: the inherent counter EMF effect. *Geotech. Testing. J.*, 26(03):342–352.

Westbrook, G. K., Carson, B., Musgrove, R. J., et al. (1994). *Proc. ODP. Init. Repts*, volume 146. College Station, TX, Ocean Drilling Program.

Whiffen, B. L., Kiefte, H., and Clouter, M. J. (1982). Determination of acoustic velocities in xenon and methane hydrates by brillouin spectroscopy. *Geophys. Res. Letts*, 9:645–648.

White, R. S. (1979). Gas hydrate layers trapping free gas in the Gulf of Oman. *Earth Planet. Sci. Lett.*, 42:114–120.

Whitmarsh, R. B., Miles, P. R., and Pinheiro, L. M. (1990). The seismic velocity of some NE Atlantic continental rise sediments: or lithication index? *Geophys. J. Int.*, 101:367–378.

Wilkens, R., Simmons, G., and Caruso, L. (1984). The ratio V_p/V_s as a discriminant of composition of silliceous limestones. *Geophysics*, 49:1850–1860.

Wilson, S. D. and Dietrich, R. J. (1960). Effect of consolidation pressure on elastic and strength properties. *Proc. ASCE Research Conference on Shear Strength of Cohesive Soils,* Boulder, Colo, pages 419–435.

Winkler, K. (1985). Dispersion analysis of velocity and attenuation in Berea sandstone. *J. Geophys. Res.*, 90(B8):6793–6800.

Winkler, K. and Nur, A. (1979). Pore fluids and seismic attenuation in rocks. *Geophys. Res. Lett.*, 6:1–4.

Winkler, K., Nur, A., and Gladwin, M. (1979). Friction and seismic attenuation on rocks. *Nature*, 277:528–531.

Winters, W. J., Dallimore, S. R., Collett, T. S., Katsube, J. T., Jenner, K. A., Cranston, R. E., Wright, J. F., Dixon, F. M., and Uchida, T. (1999). Physical properties of sediments from JAPEX/JNOC/GSC Malik 2l-28 gas hydrate research well. *Geol. Surv. Bull.*, 544:95–100.

Winters, W. J., Dillon, W. P., Pecher, I. A., and Mason, D. H. (2000). Ghastli-determining physical proerties of sediment containing natural and laboratory formed gas hydrates. In Max, M. D., editor, *Natural gas hydrates in oceanic and permafrost environments*, pages 311–322. Kluwer Academic Press.

Winters, W. J., Waite, W. F., Mason, D. H., Dillon, W. P., and Pecher, I. A. (2002). Sediment properties associated with gas hydrate formation. In

Proc. Fourth Int. Conf. On Gas Hydrates, Yokohama, May 19-23, pages 722–727.

Wood, W. T., Holbrook, W. S., and Hoskins, H. (2000). In situ measurements of p-wave attenuation in methane hydrate and gas bearing sediemnts on the Blake Ridge. In Paull, C., Matsumoto, R., Wallce, P., et al., editors, *Proc. ODP. Results, 164*, pages 265–272. College Station, TX, Ocean Drilling Program.

Wood, W. T. and Ruppel, C. (2000). Seismic and thermal investigation of the Blake Ridge gas hydrate area: A synthesis. In Paull, C., Matsumoto, R., Wallce, P., et al., editors, *Proc. ODP. Results, 164*, pages 253–264. College Station, TX, Ocean Drilling Program.

Yamamoto, S., Alcauskas, J., and Crozier, T. (1976). Solubility of methane in distilled water and sea water. *Journal of Chemical and Engineering Data*, 21:78–80.

Appendix A

Calibration of transducers

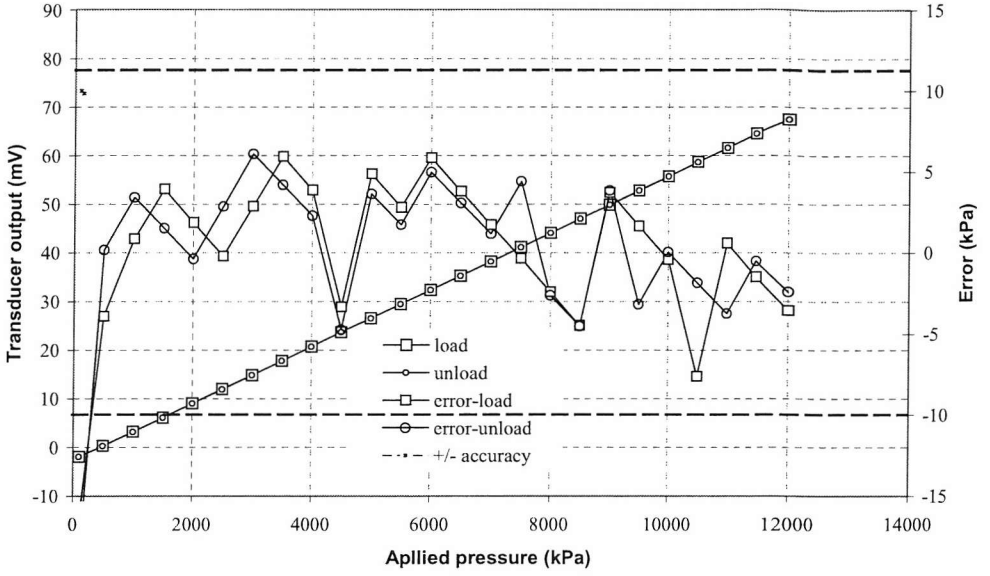

Figure A.1: *Transducer calibration graph for cell pressure before testing*

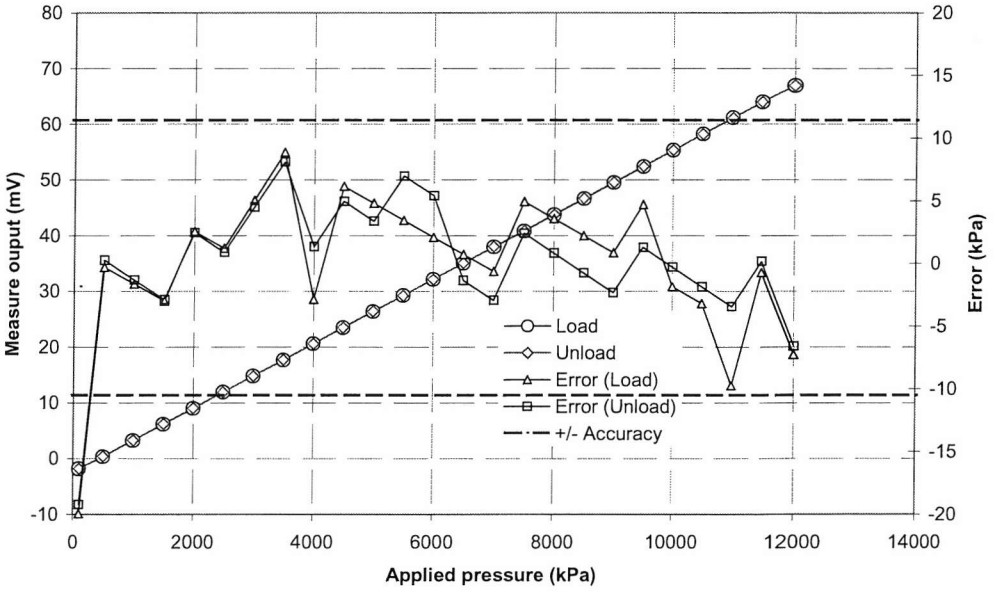

Figure A.2: *Transducer calibration graph for cell pressure after testing.*

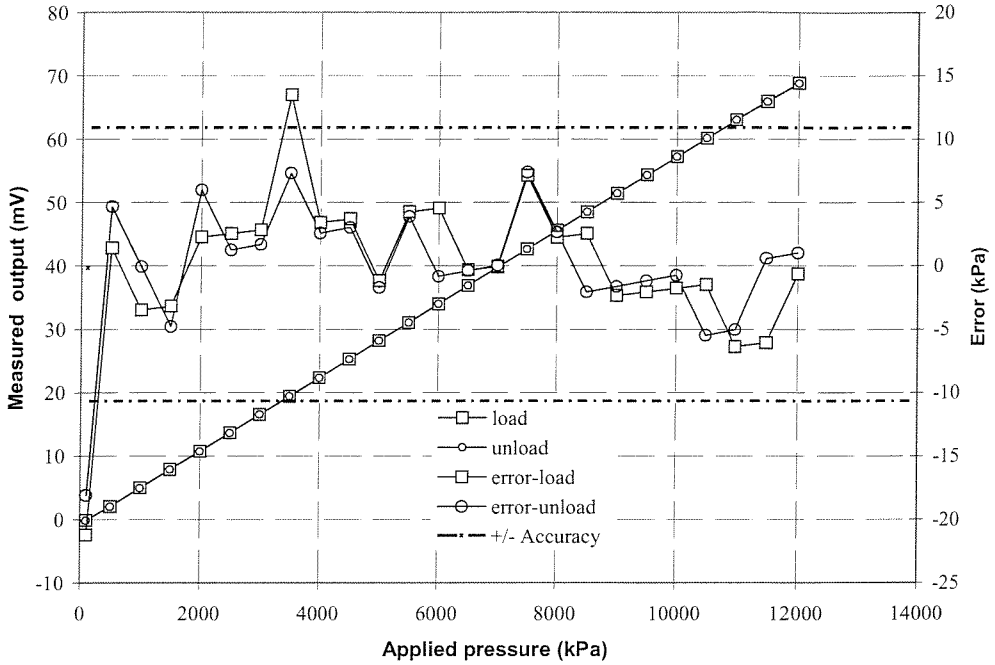

Figure A.3: *Transducer calibration graph for CH_4 back pressure before testing.*

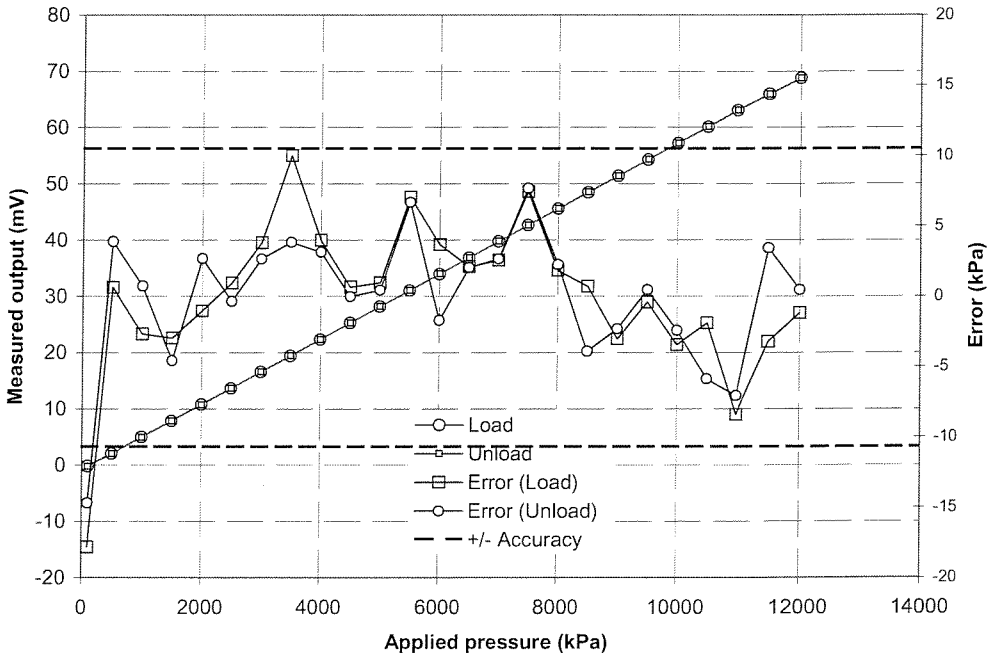

Figure A.4: *Transducer calibration graph for CH_4 back pressure pressure after testing.*

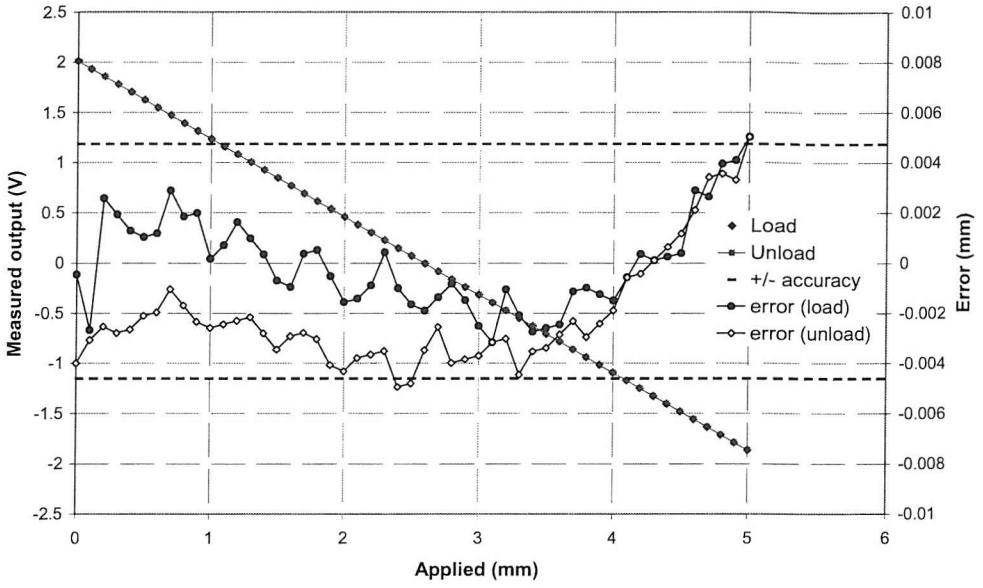

Figure A.5: *Axial transducer calibration graph before testing over 5mm range.*

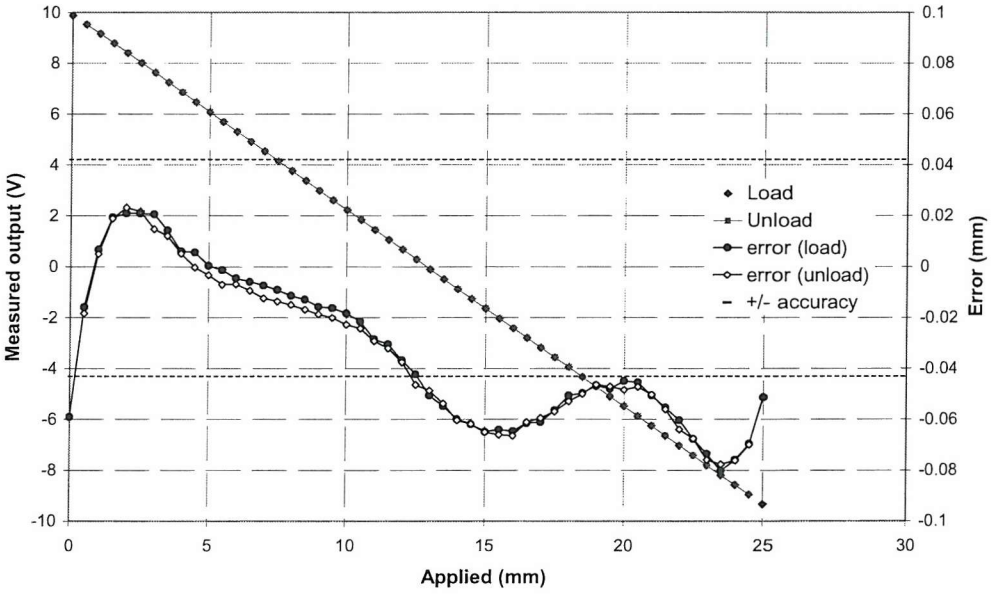

Figure A.6: *Axial transducer calibration graph before testing over 25mm range.*

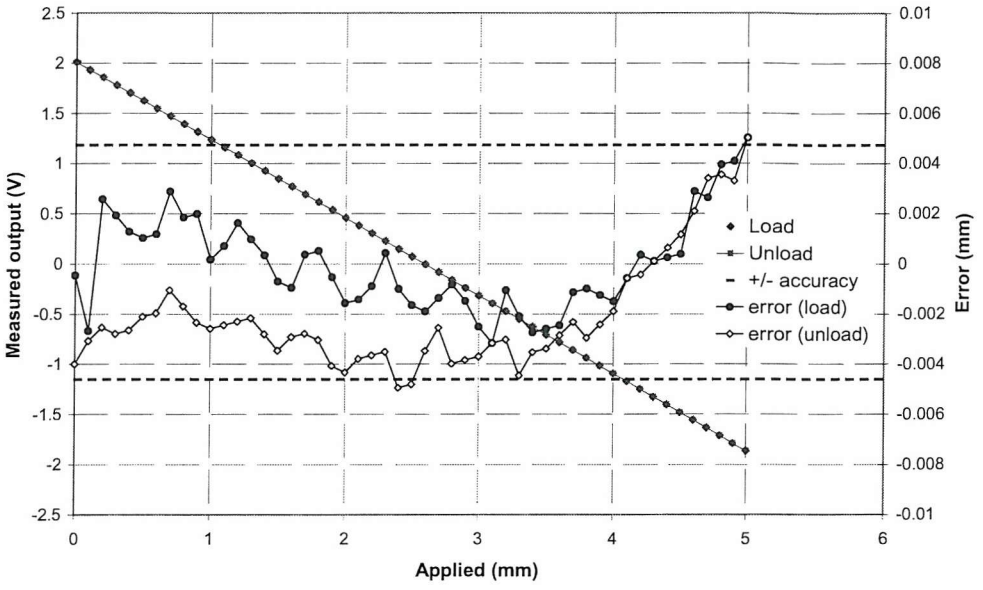

Figure A.7: *Axial transducer calibration graph after testing over 5mm range.*

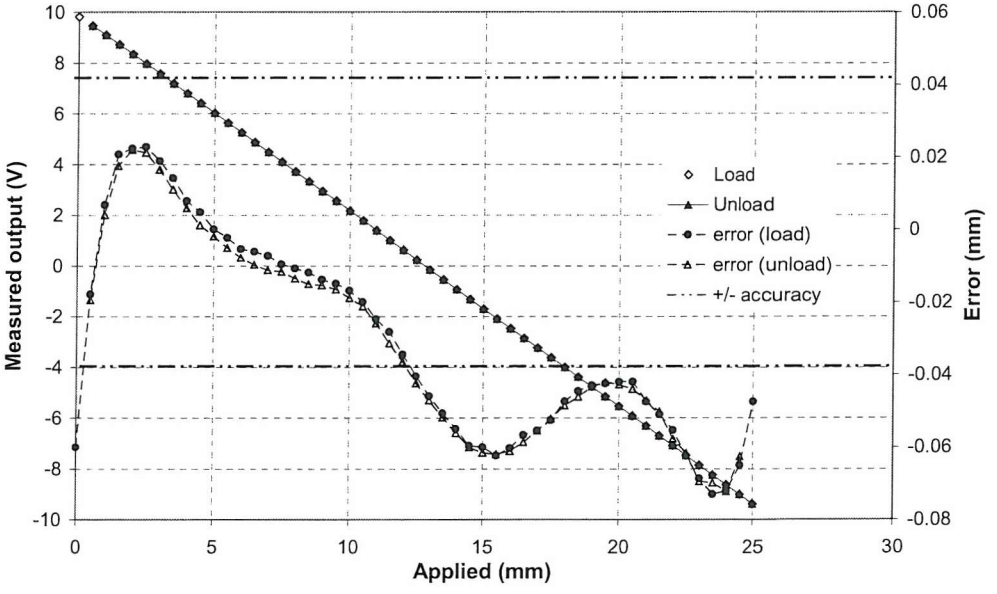

Figure A.8: *Axial transducer calibration graph after testing over 25mm range.*

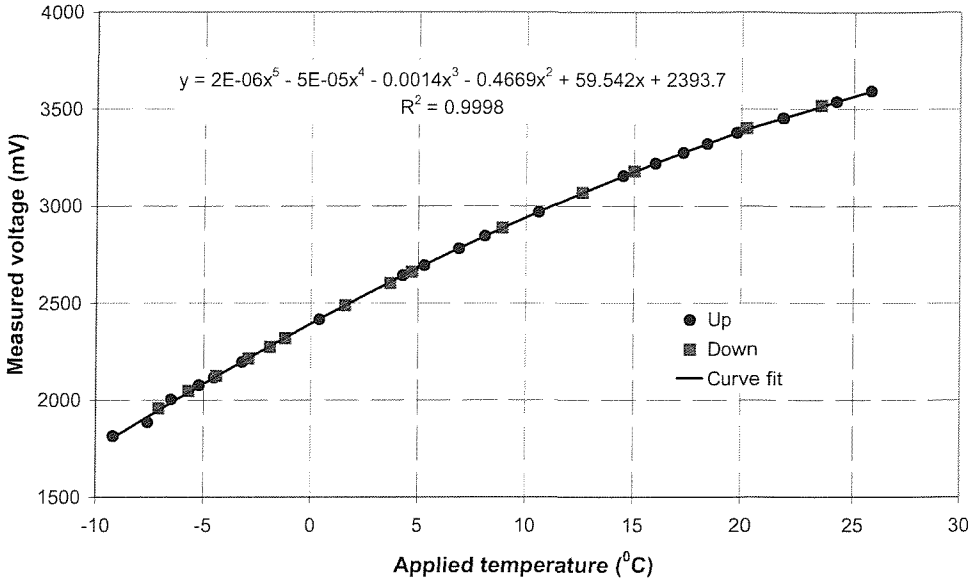

Figure A.9: *Thermistor transducer (01) calibration graph before testing.*

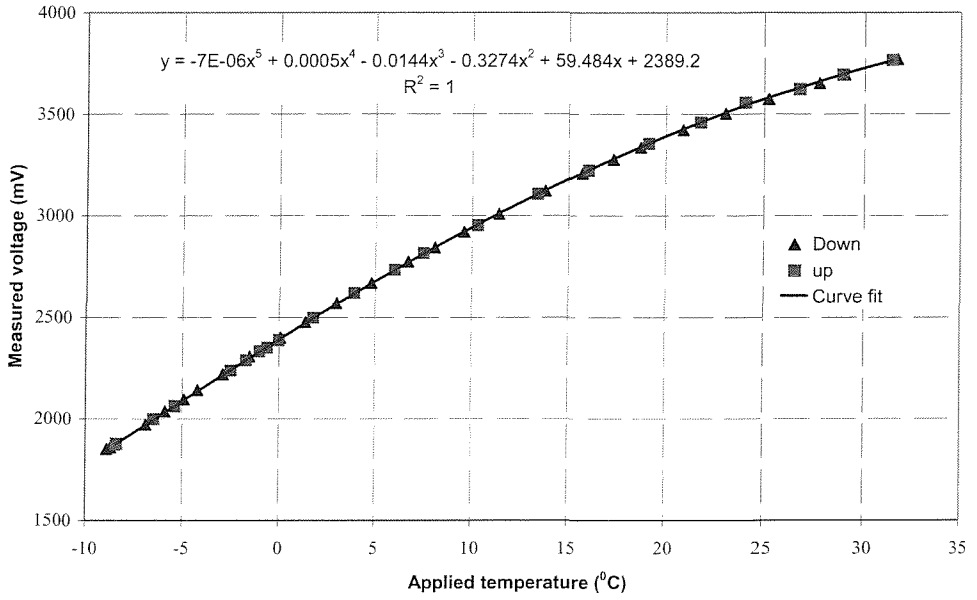

Figure A.10: *Thermistor transducer (01) calibration graph after testing.*

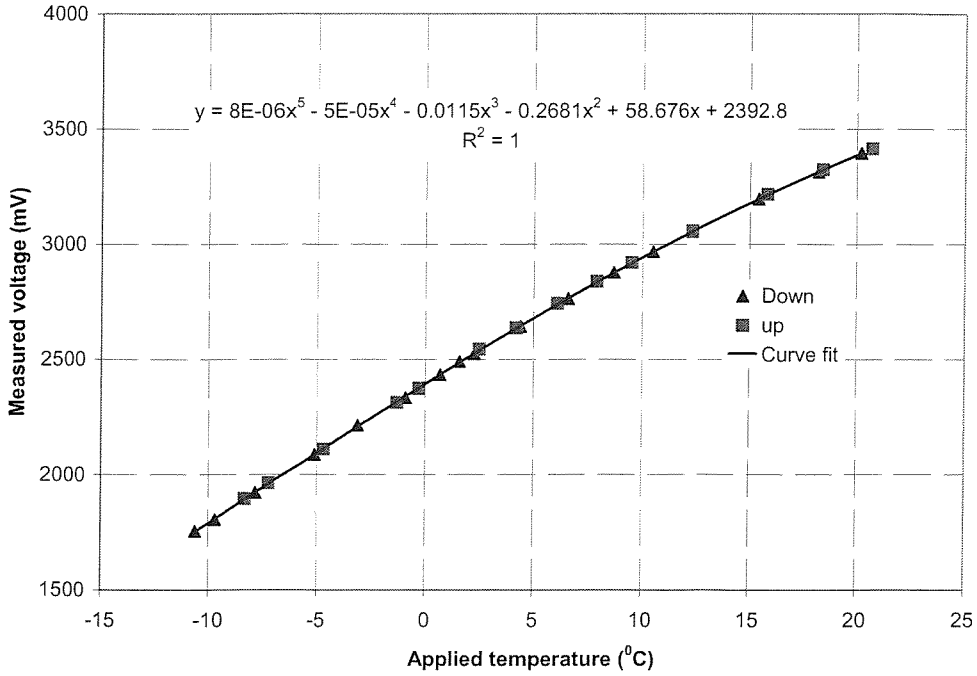

Figure A.11: *Thermistor transducer (02) calibration graph before testing.*

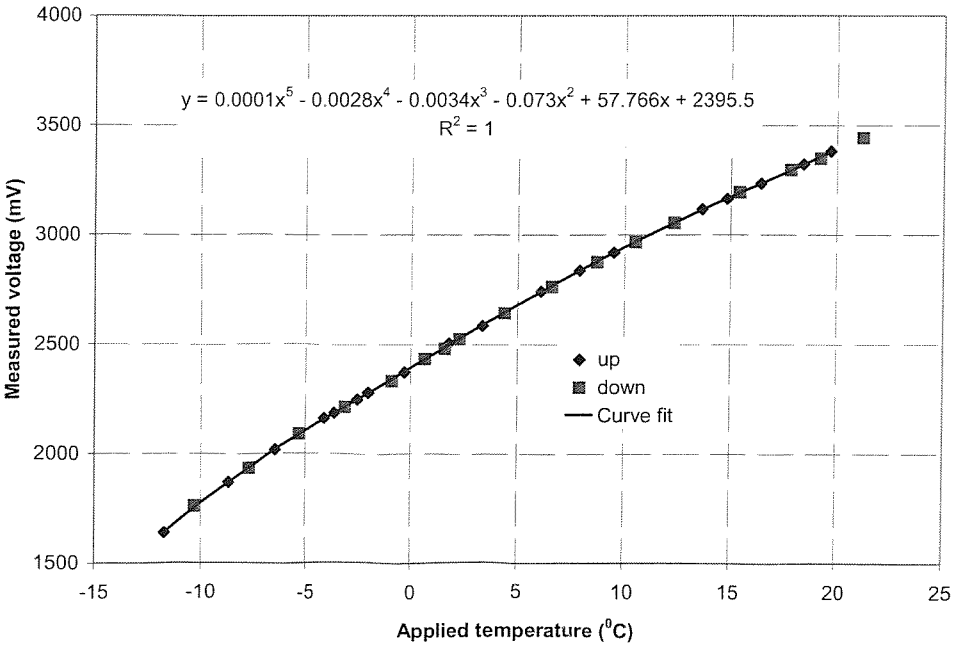

Figure A.12: *Thermistor transducer (02) calibration graph after testing.*